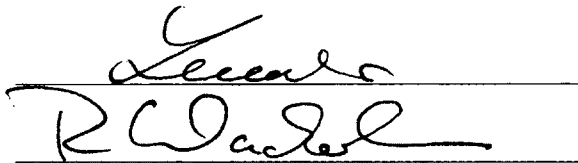


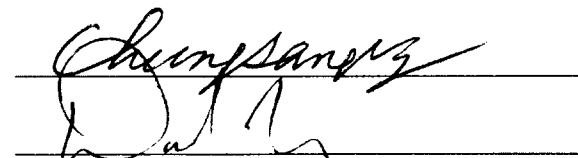
MAGNETOHYDRODYNAMIC SIMULATIONS OF PLASMA DYNAMICS
IN THE MAGNETOSPHERIC CUSP REGION

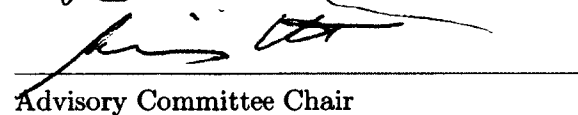
By

Eric T. Adamson

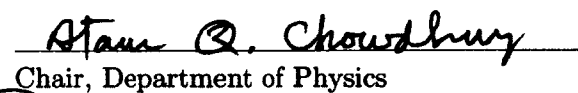
RECOMMENDED:





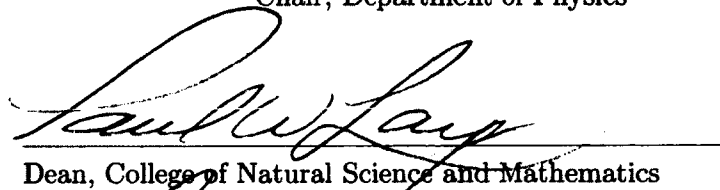


Advisory Committee Chair

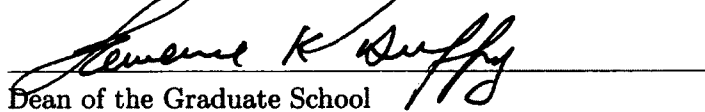


Chair, Department of Physics

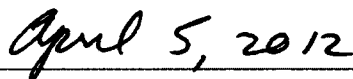
APPROVED:



Dean, College of Natural Science and Mathematics



Dean of the Graduate School



Date

**MAGNETOHYDRODYNAMIC SIMULATIONS OF PLASMA DYNAMICS
IN THE MAGNETOSPHERIC CUSP REGION**

A
THESIS

Presented to the Faculty
of the University of Alaska Fairbanks
in Partial Fulfillment of the Requirements
for the Degree of

DOCTOR OF PHILOSOPHY

By
Eric T. Adamson, B.S.

Fairbanks, Alaska

May 2012

UMI Number: 3528852

All rights reserved

INFORMATION TO ALL USERS

The quality of this reproduction is dependent upon the quality of the copy submitted.

In the unlikely event that the author did not send a complete manuscript and there are missing pages, these will be noted. Also, if material had to be removed, a note will indicate the deletion.

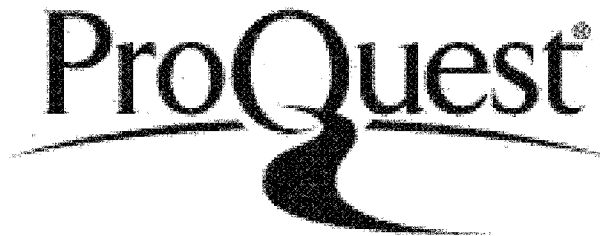


UMI 3528852

Published by ProQuest LLC 2012. Copyright in the Dissertation held by the Author.

Microform Edition © ProQuest LLC.

All rights reserved. This work is protected against unauthorized copying under Title 17, United States Code.



ProQuest LLC
789 East Eisenhower Parkway
P.O. Box 1346
Ann Arbor, MI 48106-1346

Abstract

The Earth's magnetospheric cusp regions are rich in interesting plasma physics. The geomagnetic cusps offer solar wind plasma a relatively easy entry point into the magnetosphere through magnetic reconnection with the interplanetary magnetic field. The cusp regions are characterized by various interesting and important observations such as low energy particle precipitation, significant outflow of ionospheric material, and the frequent presence of energetic particles in regions of depressed magnetic field strength. The physical mechanisms which lead to these observations are often unresolved. For instance, the acceleration mechanism for energetic cusp populations is not understood, nor is it known what implications they may have on magnetospheric dynamics. It is however, well accepted that magnetic reconnection plays a critical role in the vicinity of the cusps and is likely responsible for much of the dynamics in the region.

Modeling of the geomagnetic cusps is notoriously challenging. Global magnetospheric models have proven indispensable in the study of the interaction of the solar wind plasma with the Earth's magnetosphere, however, the exterior cusp region poses a significant challenge for these models due to their relatively small scale. I have developed a mesoscale cusp-like magnetic field model in order to provide a better resolution (up to 300 km) of the entire cusp region than is possible in these global models.

Typical observational features of the high-altitude cusps are well reproduced by the simulation. Results for both strongly northward and strongly southward interplanetary magnetic field indicate extended regions of depressed magnetic field and strongly enhanced plasma β (cusp diamagnetic cavities). The Alfvénic nature of the outer boundary between the cusp and magnetosheath, in addition to the flow characteristics in the region, indicate that magnetic reconnection plays an important role in structuring the high-altitude cusp region. The inner boundaries with magnetosphere are gradual transitions forming a clear funnel. These cavities further present a unique configuration in which reconnecting magnetic flux tubes may gain a significant amount of flux tube entropy ($H = p^{1/\gamma}V$) through topological changes due to magnetic reconnection.

Table of Contents

	Page
Signature Page	i
Title Page	ii
Abstract	iii
Table of Contents	iv
List of Figures	vii
List of Tables	ix
Acknowledgements	x
Dedication Page	xi
1 Introduction	1
1.1 Earth's Magnetosphere	1
1.2 The Magnetospheric Cusps	4
1.3 Cusp Diamagnetic Cavities	6
1.4 CDC Boundaries	9
1.5 Plasma Transport Through the Cusps	10
1.6 Cusp Simulations	12
1.7 Methodology	14
1.8 Overview of Thesis	18
Bibliography	21
2 3D Mesoscale MHD Simulations of a Cusp-Like Magnetic Configuration:	
Method and First Results	29
2.1 Abstract	29
2.2 Introduction	29
2.3 Numerical Simulation	32
2.3.1 Numerical Method	32
2.3.2 Model	33
2.4 Relaxation Method	37
2.5 Results	41
2.5.1 Dynamic Simulation	41
2.5.2 Comparison with Cluster 2 Data	43

2.6	Discussion and Conclusion	47
2.7	Acknowledgements	49
	Bibliography	50
3	3D Mesoscale MHD Simulations of Magnetospheric Cusp-like Configurations: Cusp Diamagnetic Cavities and Boundary Structure	55
3.1	Abstract	55
3.2	Introduction	55
3.3	Numerical Procedure	58
	3.3.1 Numerical Method	58
3.4	Results	60
	3.4.1 CDC dependence on IMF orientation	61
	3.4.2 Northward IMF	63
	3.4.2.1 Cusp Overview	64
	3.4.2.2 Dayside Plasma Sheet/CDC Boundary	67
	3.4.2.3 Lobe/CDC Boundary	67
	3.4.2.4 CDC/Magnetosheath Boundary	67
	3.4.2.5 Discussion of Northward IMF cusp	71
	3.4.3 Southward IMF	72
	3.4.3.1 Cusp overview	72
	3.4.3.2 Dayside Plasma Sheet/CDC Boundary	74
	3.4.3.3 Lobe/CDC Boundary	77
	3.4.3.4 CDC/Magnetosheath Boundary	79
	3.4.3.5 Discussion of Southward IMF cusp	81
3.5	Discussion and Conclusion	82
3.6	Acknowledgements	86
	Bibliography	87
4	Entropy Change Through Reconnection in the Vicinity of Magnetic Cusps	93
4.1	Abstract	93
4.2	Introduction	93
4.3	Numerical Procedure	95

4.3.1 Numerical Method and Model	95
4.4 Results	96
4.5 Discussion and Conclusion	101
4.6 Acknowledgements	101
Bibliography	102
5 Conclusions	103
5.1 Limitations of the Model and Future Considerations	107
Bibliography	110
Appendix	113

List of Figures

	Page
1.1 Chapman Ferraro sketch of the Magnetosphere.	2
1.2 Illustration of the Earth's Magnetosphere.	3
1.3 Illustration of the magnetic reconnection process.	6
1.4 Diagram of the magnetic field structure in the magnetospheric cusp.	7
1.5 Polar data for a CDC event seen on 20 April, 1999.	8
1.6 Plot of n (cm^{-3}) vs T (keV) for various magnetospheric plasma populations.	11
1.7 Illustration of typical reconnection geometry and resulting plasma flow.	13
2.1 Initial magnetic field configuration.	34
2.2 Illustration of the initial density (top) and pressure (bottom) distributions.	36
2.3 Illustration of the net force in the noon-midnight meridional plane.	37
2.4 Temporal evolution of the maximum force and total integrated force.	39
2.5 Distribution of the magnetic field (top) and current density (bottom).	40
2.6 Distribution of the density and pressure.	41
2.7 Plasma and magnetic field data from Cluster spacecraft 4.	45
2.8 Simulated data.	46
2.9 Distribution of the total current density, plasma beta, and velocity.	48
3.1 Illustration of the numerical grid.	59
3.2 Cusp diamagnetic cavity position indicated by plasma β	62
3.3 Total magnetic field strength indicating diamagnetic regions.	63
3.4 From top to bottom, the plots on the left display plasma density	65
3.5 Simulated data for a cut along z at $(x, y) = (-3.1, 0)$	66
3.6 Walén relation (left) and deHoffman-Teller test	68
3.7 Results of the boundary normal calculation	69
3.8 Simulated "data" for a cut along z	70
3.9 Total magnetic field ($ B $) in the y - z plane	71
3.10 From top to bottom, the plots on the left display plasma density,	74
3.11 Simulated data for a cut along z at $(x, y) = (3, 0)$	75

3.12	Walén relation and deHoffman-Teller test results	76
3.13	Simulated “data” transformed into MVAE boundary normal coordinates	78
3.14	Plasma parameters transformed into the basis given by MVAE	80
3.15	Total magnetic field ($ B $) in the y - z plane	81
4.1	Illustration of the cusp reconnection geometry.	97
4.2	Cumulative flux tube entropy (H) and volume.	99
4.3	Total flux tube volume V and field-line integrated entropy.	100
A.1	Cluster trajectory on 14th of February 2003.	118
A.2	Cluster plasma (on left) and magnetic field (on right) observations.	119
A.3	MHD simulations of the cusp for southward (left) and northward.	123
A.4	Sc4 measurements of electron (top panel), proton (middle), helium.	124
A.5	A) shows plasma (left) and magnetic field (right) observations.	128
A.6	a) shows a cartoon of reconnection topology during northward IMF.	132
A.7	MVAB (top), MVAE (middle) and MFR (bottom) hodograms.	133
A.8	a) shows plasma (left) and magnetic field (right) observations.	134
A.9	Plasma and magnetic field observations (a) and hodograms (b).	144
A.10	2-D MHD simulation of the Flux-Transfer event.	145
A.11	Ion distribution functions measured by sc4.	146
A.12	Sc4 observations at 19:08-20:00 UT.	149
A.13	Cavity structure determined from Cluster boundary normal analysis.	152
A.14	A) Presents hodograms, eigenvectors and eigenvalues of MVAB, MVAE.	158
A.15	Illustration of calculation of $\Delta\phi_{13}$	159

List of Tables

	Page
A.1 Properties of Reconnection Intervals between 18:53-19:25 UT	130
A.2 Properties of Reconnection Intervals between 19:25-20:25 UT	131
A.3 Boundary normals, average plateau eigenvalue ratios and average of.	142
A.4 Boundary normals, average plateau eigenvalue ratios and average of	143

Acknowledgements

I would like to thank a number of people for their contributions to my research and their assistance in bringing this thesis to fruition.

I have had the great fortune to have completed my graduate work under the guidance of Antonius Otto. I cannot imagine having found a more knowledgeable, patient, and understanding advisor. Not only did Antonius provide me with the three-dimensional MHD simulation code which serves as the backbone of my research, but without his guidance and endless space physics knowledge this thesis could not have been completed. I am honored to have had him as an advisor and to call him my friend.

I am also grateful to Katariina Nykyri for the invaluable data analysis from the Cluster2 spacecraft mission which appears throughout this thesis. Her friendship and cheerful optimism have remained a source of encouragement throughout my graduate career.

My thanks to my graduate advisory committee for their helpful comments and criticism which helped to shape the final form of this thesis.

I would also like to thank my close friend TJ Franklin for his constant optimism and the many discussions on science and life. He helped keep me motivated and was always available to provide me with the necessary diversions.

A special thanks to my family who's love and support has always been and remains invaluable.

My love and thanks to my wife who endured many one-sided technical discussions regarding my research; her ears were far more helpful than she believed. Raising a family while attempting a Ph.D. certainly adds a further layer of complexity and I thank my wife for being there when I could not.

And finally, I would like to thank my son for his inquisition and his laughter.

I would like to dedicate this thesis to my parents without who's love and support it would have simply never met the page. Thank you for everything.

For Mom and Dad

— Eric

Chapter 1

Introduction

1.1 Earth's Magnetosphere

The Earth's magnetosphere is the cavity carved out of the solar wind by the geomagnetic field. This field is largely dipolar in nature, resembling that of a common bar magnet with magnetic field lines converging into the polar regions. When the solar wind impacts the magnetosphere, it contracts the dayside and stretches the night side into a long "tail". The boundary between the magnetospheric magnetic field and the solar wind, referred to as the magnetopause, lies between 4.5 and 20 Earth radii ($R_E \approx 6370$ km) at the point closest to the sun (the stand-off-point), but varies depending on the speed of the solar wind. The magnetospheric tail, on the other hand, extends hundreds of R_E anti-sunward. The charged particles composing the solar wind are only able to gain entrance into the magnetosphere in specific ways, and thus, generally see the geomagnetic field as an impenetrable obstacle. It is the interaction between this field and the solar wind plasma which eventually gives rise to the aurora.

Early attempts to describe this interaction considered material emanating from the sun in isolated events and modeled the interaction with the Earth as that of an infinitely conducting slab [Chapman and Ferraro, 1931a,b]. The authors postulated that currents generated at the interface between the geomagnetic field and the advancing plasma stream would confine the Earth's magnetic field. These currents, now referred to as Chapman-Ferraro currents, were theorized according to the method of images [Jackson, 1999], in which an image dipole was placed in the conducting plane (see Figure 1.1). The resulting current systems had as their loci, two points at which the geomagnetic field was annihilated by the adjacent magnetosheath field (magnetic null-points), one in the northern and one in the southern hemisphere. These null-points were termed "horns" by the authors (labelled Q in the figure), and it was through these "horns" which plasma entry was theorized to occur.

The model of Chapman and Ferraro was based on the view that the plasma emanating from the sun was intermittent. Following the modern description of the solar wind [Parker, 1958], magnetospheric models became more physically accurate [Spreiter and Briggs, 1962; Midgley and Davis, 1963; Mead, 1964]. The modern conception of the Earth's magneto-

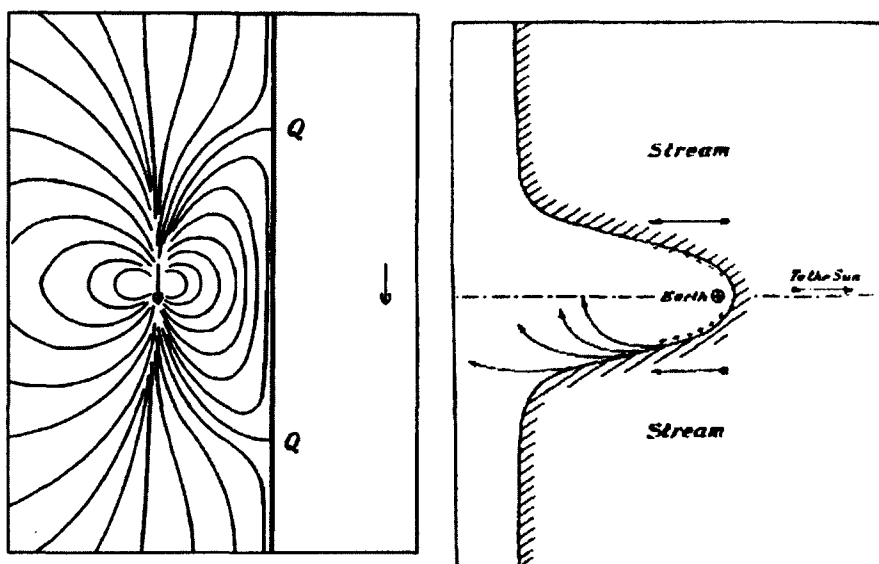


FIG. 4—Meridian section

Figure 1.1. Chapman Ferraro sketch of the Magnetosphere. The cusps are labeled “Q” in the figure on the left, with the arrow on the left indicating the Earth’s magnetic dipole, and that on the right, it’s image embedded within the conducting plane. The figure on the right illustrates the cavity carved out of the material from the sun, as envisioned by the authors [Chapman and Ferraro, 1931a,b].

sphere is illustrated in Figure 1.2. Because the solar wind is super-fast, i.e., faster than the fastest macroscopic plasma wave speed, a shock is formed where the solar wind encounters the magnetosphere. This “bow-shock” lies $\sim 2-3 R_E$ sunward of the magnetopause and slows the solar wind flow to sub-fast speeds. The region between the bow-shock and magnetopause is referred to as the magnetosheath and is filled with shocked solar wind plasma. This slowing effect in the magnetosheath is most significant at the sub-solar point and plasma flow in the magnetosheath increases with distance from the sub-solar point until super-sonic flow is regained, such that the bow-shock only exists over a limited range of latitudes in front of the Earth. Interior to the bow-shock lies the magnetopause. This boundary represents the transition between the magnetosheath field and the geomagnetic field. At high-latitudes, where the dipolar geomagnetic field lines converge, lie the magnetospheric cusps. These regions offer the shocked solar wind plasma it’s most direct point of entry into the magnetosphere.

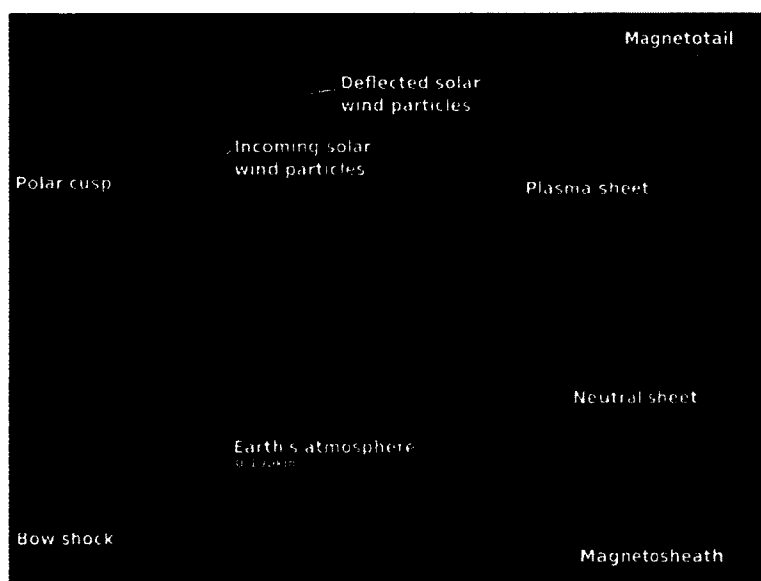


Figure 1.2. Illustration of the the Earth’s Magnetosphere [Marshall Space Flight Center, 2005].

1.2 The Magnetospheric Cusps

The cusps first appeared as a component of the magnetosphere in the model of Chapman and Ferraro [Chapman and Ferraro, 1931a,b] discussed above. The Earth's magnetospheric cusps are a complex feature, which, to a large degree, govern the entry of solar wind plasma into the magnetosphere [Heikkila and Winningham, 1971; Frank, 1971]. For such an important region, they are quite small in relation to the magnetosphere as a whole; extending from a small foot-point in the polar ionosphere toward the boundary with the magnetosheath and broadening with altitude. The magnetosphere contains two magnetic cusps; one in the northern and one in the southern hemispheres. The importance of these regions, from the perspective of magnetospheric physics, is due to the convergence of the geomagnetic field at the cusps and the consequential mapping of the entire boundary between the magnetosphere and magnetosheath (i.e., the magnetopause) into the cusps. Due to the convergence (divergence) of the magnetic field into (out of) the cusp region in the northern (southern) hemisphere, the cusps act as focal regions for plasma flow and externally generated perturbations. Such a mapping provides a means of remote sensing in which spacecraft moving through the cusp region are able to detect signatures of the dynamic interaction between the solar wind and the Earth's magnetosphere [Fuselier et al., 2000; Trattner et al., 2004].

The first measurements of the cusp were reported in 1971 [Heikkila and Winningham, 1971; Frank, 1971] with the discovery of plasma (of inferred magnetosheath origin) deep within the polar magnetosphere. Inconsistencies between the mapping of the magnetic null-point to low-altitudes and the characteristics of the high-latitude plasma precipitation, suggested that the entry process was more complex than a simple direct entry point at the magnetic null. Important advances in our understanding of the cusps have resulted from the HEOS, ISEE2, Hawkeye, Polar, and Interball missions [Paschmann et al., 1976; Gosling et al., 1991; Kessel et al., 1996; Dunlop et al., 2000]. More recently, results from the Cluster 2 mission have provided a great deal of enlightening results, furthering our understanding of the high-altitude cusp region [Lavraud and Cargill, 2005; Cargill et al., 2005; Lavraud et al., 2005].

The modern view of the cusps is that the structures represent the main pathway by which solar wind plasma is able to access the magnetosphere, not by allowing direct entry, but rather, through the process of magnetic reconnection in the vicinity of the cusps

[Reiff et al., 1977]. Magnetic reconnection is most easily discussed in the framework of magnetohydrodynamics (MHD), wherein plasma elements are “frozen-in” [Alfvén, 1943] to the magnetic field. Magnetic reconnection allows the magnetic field lines, within a limited region of space, to lose their identity and become “reconnected” to neighboring magnetic field lines. The process is illustrated in two-dimensions in Figure 1.3.

The magnetic field lines which cross through the center in the figure represent boundaries which separate distinct regions of magnetic flux. These boundaries are called separatrices as they bound topologically distinct regions. The point at which the separatrices cross is referred to as the X-point. This point is often referred to as the diffusion region because, due to micro-physical processes which are not fully understood, the frozen-in condition is violated, facilitating changes in the magnetic connection. The blue arrows in the figure represent the flow of plasma. In the upper and lower regions (the inflow regions) this flow is towards the X-point, while in the regions to the left and right of the X-point (the outflow regions), the flow is directed away from this point.

The two red spots in the figure represent arbitrary plasma elements. Initially (the top pane in the figure) these elements are connected by the same magnetic field line. According to the frozen-in condition, these plasma elements must always be connected by this field line. In the middle pane of the figure (Time 2) the elements have been convected towards the X-point such that the field line connecting them is now the separatrix. The non-ideality located in the vicinity of the X-point then breaks the frozen-in condition and the flux in this region is expelled with the outflowing plasma. The result (Time 3) is that the plasma elements are now “frozen” to two separate magnetic field lines. This process enables changes to magnetic topology and facilitates plasma transport across otherwise impenetrable boundaries, such as the magnetopause.

The general structure of the magnetospheric cusp is that of a “bent funnel” shape, extending from the polar ionosphere, along the separatrix (which defines the boundary between magnetic field-lines with both foot-points on the dayside magnetosphere, and field lines which extend tailward), to the boundary with the magnetosheath (see Figure 1.2).

The geomagnetic field in the vicinity of the cusps rotates through a complete 360° about the dipolar axis. This ensures the existence of magnetic null-points where the dipolar magnetic field is bounded at the magnetopause by an anti-parallel interplanetary magnetic field

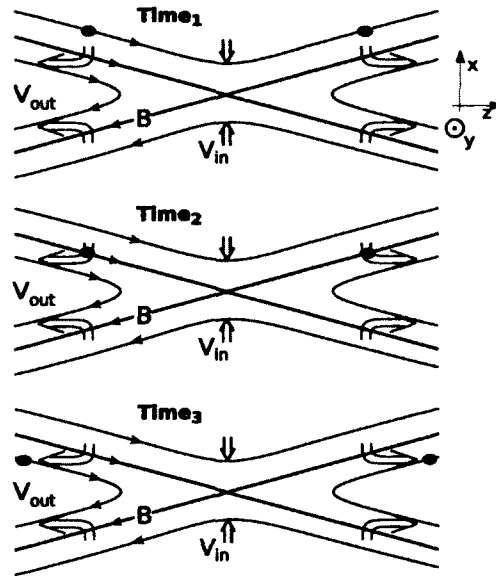


Figure 1.3. Illustration of the magnetic reconnection process [Otto, A., 2010].

(IMF) in the adjacent magnetosheath. This is illustrated for an arbitrary magnetosheath magnetic field orientation in Figure 1.4. This condition of persistent anti-parallel magnetic field, varying in location around the circumference of the cusp, suggests a dependence on IMF orientation, which is indeed well documented [Newell and Meng, 1987; Newell et al., 1989; Escoubet and Bosqued, 1989; Zhou et al., 2000; Palmroth et al., 2001; Pitout et al., 2006a]. The cusp not only exhibits a dependence on IMF orientation, but also on solar wind dynamic pressure [Zhou et al., 2000; Pitout et al., 2006b] and geomagnetic dipole tilt [Newell et al., 1989; Zhou et al., 1999; Palmroth et al., 2001; Měrka et al., 2002], changing not only location, but also in extent [Newell and Meng, 1987].

1.3 Cusp Diamagnetic Cavities

A typical feature of the high-altitude cusp is a region of extremely low magnetic field strength relative to the local magnitude. These features have been descriptively referred to as cusp diamagnetic cavities (CDC's) [Chen et al., 1998; Fritz et al., 2003] due to the diamagnetic depression of the field [Erlandson et al., 1988]. Diamagnetic currents (i.e., currents which generate a magnetic field in accordance with the induction equation which opposes the applied field) may arise in a plasma due to density or temperature gradients

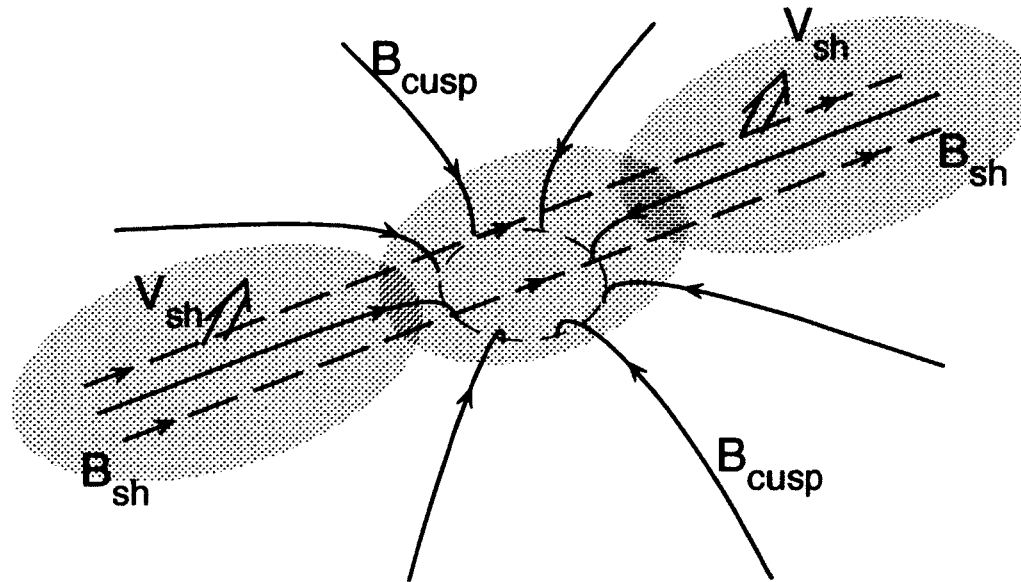


Figure 1.4. Diagram of the magnetic field structure in the magnetospheric cusp. B_{cusp} , B_{sh} , and V_{sh} represent the geomagnetic field vector on magnetospheric side of the magnetopause, magnetic field vector in the magnetosheath and the plasma velocity in the magnetosheath, respectively [Otto, 2010].

transverse to the magnetic field.

The CDC's form due to the magnetic connection between the high-altitude geomagnetic field and the magnetosheath field. Where these fields are anti-parallel, a null-point is formed, embedded within a more extensive region of strong magnetic shear. This magnetic shear defines a current sheet, bounding the geomagnetic field and enabling reconnection to transport plasma from the magnetosheath into the low field region of the high-altitude magnetosphere. Such a local accumulation of plasma, resulting from the outflow from the reconnection site towards the converging dipolar geomagnetic field, forms a region of enhanced density, generating diamagnetic currents. The diamagnetic effect in the high-altitude cusp can be so pronounced as to effectively turn off the geomagnetic field in the region.

These CDC's are characterized by magnetosheath-like plasma density, enhanced thermal pressure and low, fluctuating magnetic field strength. These features have been reported to extend up to $\sim 6 R_E$ [Fritz et al., 2003]. The regions tend to be rather shallow (on the order of 1-2 R_E) normal to the magnetopause, but quite expansive in the transverse

direction [Niehof, 2010]. An example of a CDC event as seen by the Polar spacecraft [Fritz et al., 2003] is shown in Figure 1.5. The bottom pane in the figure shows the total magnetic field measured by the Polar spacecraft over a period of ~ 6.5 hrs. The typically low and fluctuating field is seen from 12:05-17:00 UT.

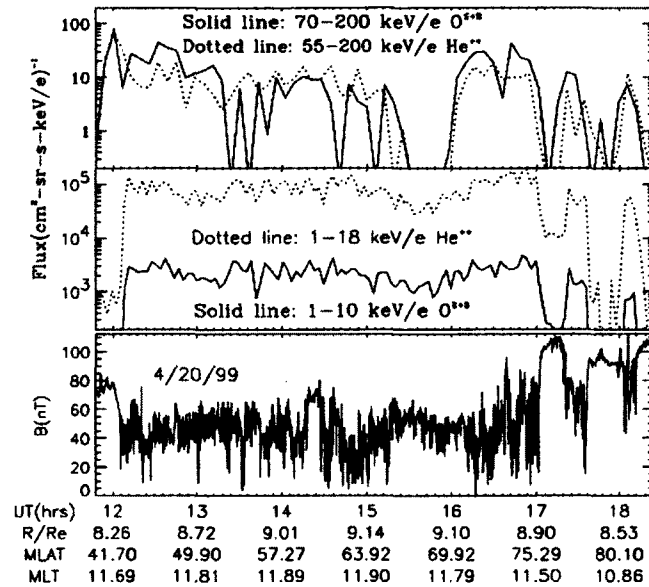


Figure 1.5. Polar data for a CDC event seen on 20 April, 1999 [Fritz et al., 2003]. Panels show (from top to bottom) variation of 70-200 keV/e $O^{\leq+2}$ (solid line) and 55-200 keV/e He^{++} (dotted line), 1-10 keV/e $O^{\geq+3}$ (solid line) and 1-18 keV/e He^{++} (dotted line) fluxes, and total magnetic field strength.

It appears that some of the fluctuations seen in Figure 1.5 are likely due to motion of the structure relative to the spacecraft [Nykyri et al., 2011a,b], particularly considering the time scale in the figure.

The top panels in Figure 1.5 display O and He ion fluxes in various high-energy channels (the typical energy of a thermal particle in this region is a few hundred to about 2 keV). The fluxes are clearly enhanced within the region of depressed and fluctuating magnetic field. These cusp energetic particles (CEP's) [Chen et al., 1998] have been found to correlate well with CDC measurements [Niehof, 2010]. CEP's of up to at least 2 MeV were first reported in the high altitude polar cusp region by Chen et al. in 1996 [Chen et al., 1997]. The energization mechanism, however, remains a topic of significant debate [Chen et al., 1998; Chang et al., 1998]. It has been suggested that these energetic particle fluxes are sufficient

to generate the so-called ring current [Fritz, 2000], which is a current consisting of energetic particles around the Earth at a radial distance of a few Earth radii. The ring current strongly intensifies during periods of high geomagnetic activity (magnetic storms).

1.4 CDC Boundaries

The exterior cusp has been shown to have three boundaries [Lavraud et al., 2004a; Paschmann et al., 1976; Haerendel et al., 1978; Onsager et al., 2001]: the day-side plasma sheet on the sunward side, the tail-lobe or mantle on the night-side, and the magnetosheath in the exterior. The exact nature of these boundaries however, is not well understood [Walters, 1966; Scarf et al., 1974; Hansen et al., 1976; Yamauchi and Lundin, 1997; Lavraud et al., 2002; Savin et al., 1998]. It appears that the inner boundaries of the high-altitude cusp form a funnel shape and thus represent an indented surface which has been labelled as the magnetopause by some [Paschmann et al., 1976; Haerendel et al., 1978; Russell, 2000]. However, it is not clear whether the same is true of the outer boundary between the cusp and magnetosheath. This question regarding the shape of the magnetopause in the vicinity of the cusp has persisted for some time. While some observational results show clear evidence of an indented surface [Zhang et al., 2007; Dunlop et al., 2005; Eastman et al., 2000], others do not [Zhou and Russell, 1997; Lavraud et al., 2004a]. This debate is further complicated by the ambiguity in the definition of the magnetopause in the vicinity of the cusp; where the traditional magnetopause [Paschmann et al., 1976; Haerendel et al., 1978; Russell, 2000] appears to coincide with the inner “funnel-shaped” boundaries, it may be more appropriate due to the apparent role of reconnection in its formation, to regard the outer boundary of the cusps as the magnetopause [Onsager et al., 2001; Lavraud et al., 2004b; Cargill et al., 2004]

Oftentimes, in magnetospheric physics, minimum variance techniques are applied to satellite data in an attempt to identify the physical nature of boundary structures. This knowledge is beneficial, as it can provide insight into physical processes responsible for the formation of such boundaries, as well as allowing for the identification of spacecraft locations with respect to well-known magnetospheric boundaries. These methods typically employ a variance analysis of the data points across a transition in plasma data, the goal being to identify the direction of minimum variance in magnetic field data (MVAB), and, or

the maximum variance in the electric field (MVAE) [Sonnerup and Cahill, 1967]. A proper determination of the boundary normal direction, then allows one to evaluate changes in the plasma parameters (under the assumptions of ideal magnetohydrodynamics (MHD)) and make comparisons with the well-known Rankine-Hugonot conditions [Baumjohann and Trueman, 1997], ideally, providing for the identification of the boundary as an established discontinuity or shock.

Definitive identification of the nature of the outer boundary between the CDC and magnetosheath, however, remains elusive. Attempts to do so have shown only partial consistency with various MHD discontinuities. It has, therefore, been suggested that the boundary, perhaps consists of a layering of adjacent discontinuities [Lavraud et al., 2002; Cargill et al., 2004]. Because of the role which magnetic reconnection is thought to play in the region, it is expected that this boundary exhibit characteristics (i.e., discontinuities in plasma parameters) typical for reconnection (i.e., a rotational discontinuity (RD) or slow-shock).

1.5 Plasma Transport Through the Cusps

As previously noted, reconnection in the vicinity of the cusps is widely accepted as the dominant pathway through which magnetosheath plasma gains entry into the Earth's magnetosphere, however, the transport of plasma deep within the magnetosphere (i.e., the plasma sheet) is more controversial.

Physical invariants have traditionally been overlooked in addressing plasma transport. Such invariants provide useful limits on plasma motion and further insights into connections within the magnetosphere. Figure 1.6 shows the distribution of various magnetospheric plasma populations plotted in terms of density (n) and temperature (T). The diagonal lines represent adiabats for $\gamma = 5/3$. The populations appear well confined within limited regions of n - T space indicating that entropy is roughly conserved. This implies, for instance, that in order for magnetosheath plasma to evolve into the near-earth plasma sheet population it would require a non-adiabatic process or processes which rarefy the plasma by a factor of ~ 30 while simultaneously heating the population by a factor of ~ 100 . Entropy may thus prove an important diagnostic tool for non-adiabatic processes participating in plasma transport [Borovsky et al., 1998; Birn et al., 2009; Wing and Johnson, 2010].

Entropy Density of Plasma-Sheet Populations

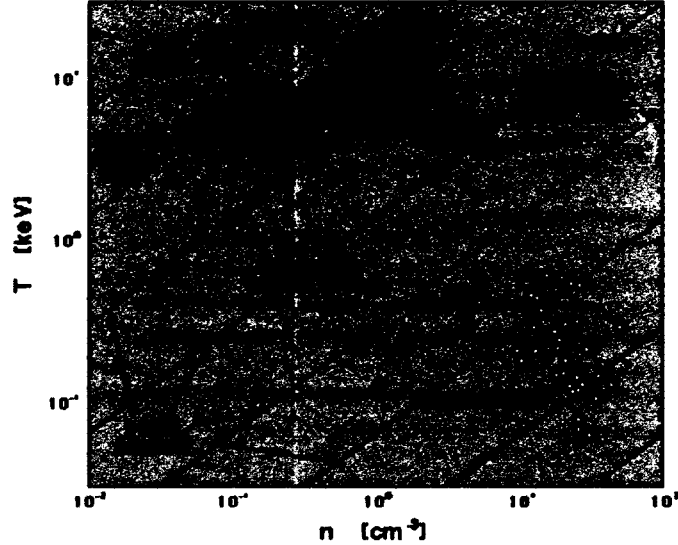


Figure 1.6. Plot of n (cm^{-3}) vs T (keV) for various magnetospheric plasma populations [Borovsky, 2006].

The frozen-in condition is of fundamental importance in the framework of ideal MHD. The concept that plasma is frozen to the magnetic field results from the assumption that the electric field in the rest frame of the plasma vanishes:

$$\mathbf{E} + \mathbf{v} \times \mathbf{B} = 0$$

This allows for the definition of a flux tube as a bundle of magnetic flux to which the constituent plasma is ideally confined. The volume of such a flux tube extending between foot-points l_1 and l_2 may be defined as:

$$V = \int_{l_1}^{l_2} \frac{dl}{B}$$

where the cross sectional area of the tube varies as $1/B$. Assuming no flux through the flux tube ends implies that the total number density is conserved. It follows that any quantity which obeys a continuity equation is likewise conserved. Consequently, a parameter may be defined which, though not precisely the entropy within a flux tube, serves as a proxy of

such:

$$H = p^{1/\gamma} V$$

The entropy on magnetic flux tubes is an important quantity for stability [Schindler and Birn, 2004; Birn et al., 2009; Johnson and Wing, 2009] and convection [Erickson, 1992] in the magnetosphere. This particularly applies to newly reconnected (closed) magnetic flux. Provided that the entropy subsequent to reconnection is approximately invariant, the entropy content of a newly re-closed flux tube determines, to some degree, the downtail distance (from Earth) to which the flux tube should relax.

Entropy may also be an important diagnostic tool for non-adiabatic processes participating in plasma transport [Borovsky et al., 1998; Birn et al., 2009; Wing and Johnson, 2010]. Knowledge of the expected flux tube entropy can aid in the identification and understanding the importance of further non-adiabatic processes and possibly their nature.

1.6 Cusp Simulations

Modeling of the geomagnetic cusps is notoriously challenging. Global magnetospheric models have proven indispensable in the study of the interaction of the solar wind plasma with the Earth's magnetosphere [Fedder and Lyon, 1995; Raeder et al., 1995; Gombosi et al., 1998; White et al., 1998; Ogino, 1986; Tanaka, 1995]. However, the exterior cusp region poses a significant challenge for these models. While global models do reproduce the high altitude magnetospheric cusps (identified by the typical enhanced density and diamagnetic field regions), the resolution is too coarse to accurately model the small scale features, specifically the relatively thin diamagnetic cavities.

As outlined above, the exterior cusp is composed of the diamagnetic region extending $1 - 2 R_E$ normal to the magnetosheath boundary but much more expansive ($\sim 6 R_E$) in the transverse direction [Niehof, 2010], populated by largely stagnant plasma and bounded by a number of small scale features which vary depending on magnetosheath plasma conditions [Zhang et al., 2007]. For northward (southward) IMF, field aligned flows have been reported along the CDC-lobe [Lavraud et al., 2004b] (CDC-dayside plasma sheet [Lavraud et al., 2005]) boundary, consistent with outflow from a high latitude (sub-solar) reconnection site (see Figure 1.7).

The magnetopause in the vicinity of the cusp region has been reported to range in

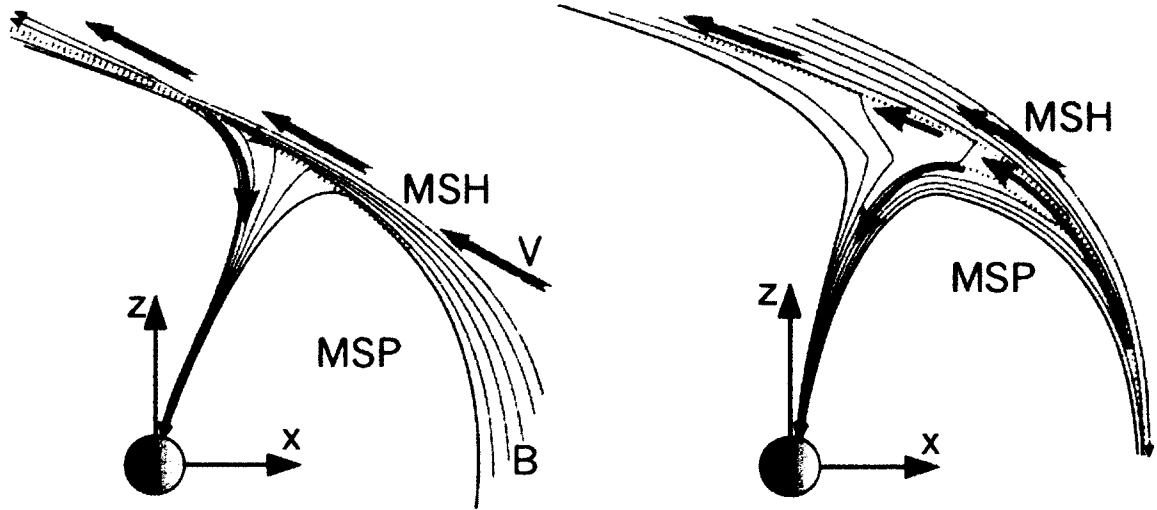


Figure 1.7. Illustration of typical reconnection geometry and resulting plasma flow. Configurations are shown for both northward IMF (left) and southward IMF(right) orientations. The orientation is such that the sun is on the right in the figure (*courtesy of Antonius Otto*).

thickness from $\sim 50 - 6000$ km, with an average thickness of ~ 1600 km and a median thickness of only 800 km [Panov et al., 2008]. Lavraud et al. [Lavraud et al., 2005] have associated sub-Alfvénic magnetosheath flows above the cusp with the existence of a so-called plasma depletion layer adjacent to the cusp-magnetosheath interface. These layers exhibit enhanced magnetic field and reduced density, such that the local Alfvén speed is enhanced, reportedly serving to stabilize the reconnection site from being swept tailward by super-Alfvénic magnetosheath flow.

Global magnetospheric models typically consider a domain of some several $100 R_E$ in the sun-tail direction and some $50 R_E$ in the transverse direction. Even with the nonuniform grids commonly used in order to reduce the required grid densities in regions where lower resolution is possible, the simulations still require something on the order of 10^8 grid points, realizing a minimum resolution of $\sim .1 - .2 R_E$. At these resolutions, the thin magnetospheric boundaries including the cusp regions pose a significant challenge for global models. It has also been noted by Siscoe et al. [Siscoe et al., 2005] that magnetic field depressions in the exterior cusp tend to be significantly greater than predicted by MHD models. This implies

that the limited resolution of global models can not sufficiently reproduce the magnetic field gradients which define the diamagnetic currents within the cusp. Considering these small-scale features which add to the complexity of the cusp, it is clear that global magnetospheric models are presented with a significant challenge in modeling the region.

1.7 Methodology

The development of a mesoscale cusp-like magnetic field model has been undertaken in order to provide a better resolution of the entire cusp region than is possible in global models. The high resolution of the local model allows for more physical reproduction of the large gradients in the various plasma parameters which define the small scale features outlined above.

The dynamic evolution of the model is examined through numerical simulations in the framework of resistive MHD. The resistive MHD equations may be derived by computing the first three macroscopic velocity moments of the Boltzman equation:

$$\frac{\partial f}{\partial t} + \mathbf{v} \cdot \nabla_{\mathbf{x}} f + \frac{q}{m} (\mathbf{E} + \mathbf{v} \times \mathbf{B}) \cdot \nabla_{\mathbf{v}} f = \frac{\partial f}{\partial t} \Big|_{coll}$$

(where, f represents the single particle distribution function, v the velocity, x the position, q the charge, m the mass, E the electric field, and B the magnetic field) which governs the evolution of a system of particles. Assuming an equation of state in order to close the system of equations, and complementing with Maxwell's equations yields the full set of MHD equations.

Typically, one or more terms are ignored in the induction equation (also referred to as generalized Ohm's law):

$$\frac{\partial \mathbf{B}}{\partial t} = \nabla \times \left(\mathbf{v} \times \mathbf{B} - \frac{1}{ne} \mathbf{j} \times \mathbf{B} + \frac{1}{ne} \nabla \cdot \mathbf{P}_e - \frac{m_e}{ne^2} \frac{\partial \mathbf{j}}{\partial t} - \eta \mathbf{j} \right)$$

in order to simplify the equations where appropriate. Here, the term in brackets on the right hand side is equal to $-\mathbf{E}$ (the electric field). The importance of the various terms in the induction equation depends on the intrinsic length scales of the system and can be addressed through a dimensional analysis [Baumjohann and Truemann, 1997].

The formulation of the equations employed in the simulation assumes an isotropic pressure (the third term on the right), and neglects the Hall (second term on the right) and

inertial (fourth term on the right) terms in the induction equation. These assumptions, as well as the neglect of the resistive term (term five on the right) are often made in first approximations to magnetospheric phenomena and are valid if the ion inertial length ($l_i = \frac{c}{\omega} \sqrt{\frac{m_i \epsilon_0}{n}}$) is much smaller than the scales typical for a given problem. The resistive term is retained here in order to facilitate reconnection, a phenomenon of established importance in the region. The MHD equations are implemented in the following form:

$$\begin{aligned} \frac{\partial \rho}{\partial t} &= -\nabla \cdot (\rho \mathbf{u}), \\ \frac{\partial(\rho \mathbf{u})}{\partial t} &= -\nabla \cdot \left[\rho \mathbf{u} \mathbf{u} + \frac{1}{2} (p + B^2) \mathbf{I} - \mathbf{B} \mathbf{B} \right], \\ \frac{\partial h}{\partial t} &= -\nabla \cdot (h \mathbf{u}) - \frac{\gamma - 1}{\gamma} h^{1-\gamma} \eta j^2, \\ \frac{\partial \mathbf{B}}{\partial t} &= -\nabla \times (\mathbf{u} \times \mathbf{B} - \eta \mathbf{j}), \\ \mathbf{j} &= \nabla \times \mathbf{B}, \end{aligned}$$

where $h = (p/2)^{1/\gamma}$ and ρ , p , η , \mathbf{u} , and \mathbf{B} represent density, pressure, resistivity, velocity, and magnetic field. The ratio of specific heats (γ) is taken to be 5/3.

The set of MHD equations are discretized according to a modified leapfrog/DuFort-Frankel method [Potter, 1973]. This method is relatively easy to implement and has a number of properties which lend it particularly attractive for this implementation. The leapfrog discretization method is applied to the continuity, momentum, and energy equations. These equations are hyperbolic in nature, i.e., they describe the propagation of various waves as well as the evolution of fluid properties as they are advected with the fluid. The leapfrog method is quite beneficial when applied to hyperbolic equations as it generates very low dispersion (on the order of $\Delta t^2, \Delta x^2$) and no numerical diffusion. This is easily illustrated through a consideration of the simple advection equation:

$$\frac{\partial f}{\partial t} + v \frac{\partial f}{\partial x} = 0 \quad (1.1)$$

The leapfrog discretization requires that the temporal and spatial differences be centered, i.e.,

$$\begin{aligned} \frac{\partial f}{\partial t} &= \frac{f_i^{n+1} - f_i^{n-1}}{2\Delta t}, \\ \frac{\partial f}{\partial x} &= \frac{f_{i+1}^n - f_{i-1}^n}{2\Delta x}, \end{aligned}$$

where n and i represent the grid location in time and space, respectively. Thus, Equation 1.1 becomes:

$$\frac{f_i^{n+1} - f_i^{n-1}}{2\Delta t} = -v \frac{f_{i+1}^n - f_{i-1}^n}{2\Delta x}. \quad (1.2)$$

The common means by which the numerical accuracy of a particular method is determined is afforded through a Taylor expansion of the variable about the location n, i . For instance,

$$\begin{aligned} f_i^{n+1} &= f_i^n + \Delta t \frac{\partial f}{\partial t} \Big|_i^n + \frac{\Delta t^2}{2} \frac{\partial^2 f}{\partial t^2} \Big|_i^n + \frac{\Delta t^3}{6} \frac{\partial^3 f}{\partial t^3} \Big|_i^n + \frac{\Delta t^4}{24} \frac{\partial^4 f}{\partial t^4} \Big|_i^n + \frac{\Delta t^5}{120} \frac{\partial^5 f}{\partial t^5} \Big|_i^n + \dots, \\ f_i^{n-1} &= f_i^n - \Delta t \frac{\partial f}{\partial t} \Big|_i^n + \frac{\Delta t^2}{2} \frac{\partial^2 f}{\partial t^2} \Big|_i^n - \frac{\Delta t^3}{6} \frac{\partial^3 f}{\partial t^3} \Big|_i^n + \frac{\Delta t^4}{24} \frac{\partial^4 f}{\partial t^4} \Big|_i^n - \frac{\Delta t^5}{120} \frac{\partial^5 f}{\partial t^5} \Big|_i^n + \dots \end{aligned}$$

Expanding the various terms in Equation 1.2 and rearranging yields:

$$\frac{\partial f}{\partial t} + v \frac{\partial f}{\partial x} + \frac{\Delta t^2}{6} \frac{\partial^3 f}{\partial t^3} + \frac{v\Delta x^2}{6} \frac{\partial^3 f}{\partial x^3} + \dots = 0. \quad (1.3)$$

Furthermore, the original differential equation (Equation 1.1) may be used in order to rewrite $\partial^3 f / \partial t^3$ in terms of the spatial derivative, ∂x , such that we are left with:

$$\frac{\partial f}{\partial t} + v \frac{\partial f}{\partial x} + \frac{v\Delta x^2}{6} \left(1 - \frac{v^2 \Delta t^2}{\Delta x^2} \right) \frac{\partial^3 f}{\partial x^3} + \dots = 0.$$

The first two terms are clearly the original differential equation. The remaining terms represent the numerical error, comprised here of only dispersive terms (i.e., odd derivatives) as all diffusive terms (even derivatives) have cancelled. The leading error term is then $\frac{v\Delta x^2}{6} \left(1 - \frac{v^2 \Delta t^2}{\Delta x^2} \right) \frac{\partial^3 f}{\partial x^3}$. It can further be shown that the method is stable as long as $v\Delta t / \Delta x \leq 1$ [Potter, 1973].

The Induction equation is parabolic due to the inclusion of the resistive term which we require in order to enable magnetic diffusion. However, the leapfrog method is unconditionally unstable for the diffusion equation [Potter, 1973]. We thus apply the DuFort-Frankel method to the induction equation. This is accomplished by rewriting the centered second spatial derivative $\frac{\partial^2 f}{\partial x^2} = f_{j-1}^n - 2f_j^n + f_{j+1}^n$ such that the $2f_j^n$ term is replaced by the average at time levels $n-1$ and $n+1$. This method takes the following form when applied to the 1-D diffusion equation, for example:

$$\frac{f_i^{n+1} - f_i^{n-1}}{2\Delta t} = \eta \left(\frac{f_{i+1}^n - f_i^{n+1} - f_i^{n-1} + f_{i-1}^n}{2\Delta x} \right).$$

The method is unconditionally stable with truncation error $\eta \Delta x^2 \left(\frac{\Delta t^2 \eta^2}{\Delta x^4} - \frac{1}{12} \right) \frac{\partial^4 f}{\partial t^4}$.

Though the combination of these two methods provides a number of desired benefits, they are both three-level discretizations. It is necessary, therefore, to employ an additional method with which to generate the initial time step. We employ the Lax-Wendroff method in order to fill this requirement. This method exhibits the same numerical dispersion characteristics as the leapfrog method, however, whereas the leapfrog method was diffusionless, the Lax-Wendroff method introduces numerical diffusion which varies as Δx^3 . This method is utilized in order to start the simulation (providing the initial integration step) and again to recouple the grids when outputting data. This recoupling is necessitated due to the "checkerboard-like" pattern by which grid points from two previous time levels are used to update the third level. This leads to solutions on two independent grids. The Lax-Wendroff method provides a convenient means by which the grids may be recoupled without introducing further dissipation. This is accomplished through iterating backwards in time from the point of the data output, thus negating any numerical effects resulting from the method, before beginning again with the leapfrog/DuFort-Frankel method. In this manner, the only numerical diffusion effects resulting from the Lax-Wendroff method are due to the initial and final time steps.

The combination of these methods also provides an effective way to control the magnetic diffusion. Whereas, many global simulations rely on numerical resistivity to enable magnetic reconnection, the explicit inclusion of resistivity afforded by the DuFort-Frankel discretization method provides an efficient means by which to control the magnetic resistivity without concern for the grid resolution thus allowing for the use of a nonuniform grid.

The simulation results presented herein employ a grid with a maximum resolution of ~ 450 km in the x - and y -directions, and ~ 320 km in z . The nonuniform grid is generated analytically according to the following function:

$$x = w + a1 * \sin \beta * w + a2 * \sin 2\beta * w + a3 * \sin 3 * \beta * w + a4 * \sin 4 * \beta * w$$

where, considering for example the x -direction, $kx = (x_{max} - x_{min}) / (nx - 3)$, $w = kx * ix$, $\beta = (2\pi) / (x_{max} - x_{min})$, with ix representing the index of a particular grid point, and nx the total number of grid points in the x -direction. The values of $a1$, $a2$, ... are then determined by requiring that $\frac{d\Delta x}{dx}|_{(x_{max}, x_{min})} = 0$ and $\frac{d^2\Delta x}{dx^2}|_{(x_{max} - x_{min})} = 0$. This series of

sine functions results in a nonuniform grid within which the grid spacing varies smoothly.

The total number of grid points used in these simulations ranges from $\sim 3.5 \times 10^6$ to $\sim 1.3 \times 10^7$. The grid sizes corresponding to particular results are indicated where relevant in the following chapters.

The MHD code used in this research was developed by Antonius Otto. It has been tested for conservation properties, various grid and system sizes and compared with other methods [Schindler and Otto, 1989; Otto, 1990, 1999]. In addition to the development of the local magnetic cusp model, which serves as the initial condition for the simulations presented herein, I have also implemented significant modifications to the original MHD code through OpenMP parallelization and the imposition of further constraints on various boundary conditions as well as the development of various diagnostics.

1.8 Overview of Thesis

The prior discussions serve to establish the importance in understanding physical processes in the magnetospheric cusps and cusp diamagnetic cavities in particular, and the subsequent need therefore, to develop a model that is capable of appropriately investigating this physics. This thesis presents results from a local meso-scale model of the high-altitude magnetospheric cusp region which I have developed specifically in order to address these outstanding issues in cusp physics. The remaining chapters are in various stages of publication as indicated.

Chapter 2 has been published in *Annales Geophysicae* [Adamson et al., 2011]. It serves as an introduction to the high resolution local mesoscale model of the magnetospheric cusp region and provides more detailed information regarding the numerical method. The chapter is intended to illustrate the non-trivial construction of the local model and gives a detailed description of the numerical relaxation technique which generates the initial near-equilibrium configuration, complimented with an explanation of boundary conditions. Initial results for the case of strongly northward IMF are presented and compared with data from the Cluster 2 spacecraft constellation from February 14, 2003. Results show a cusp diamagnetic cavity (CDC) with depth normal to the magnetospheric boundary on the order of $1 - 2 R_E$ and a much larger extent of $\sim 5 - 9 R_E$ tangential to the boundary, bounded by a gradual inner boundary with the magnetospheric lobe and a more distinct

exterior boundary with the magnetosheath. These results are qualitatively consistent with observational data and serve as a supplemental verification of the simulation results.

Chapter 3 has been published in *Annales Geophysicae* [Adamson et al., 2012]. This chapter presents a more detailed analysis of simulation results. Specifically, it addresses the effect of varying solar wind conditions on the high-altitude cusp region. Results are presented for both strongly northward and strongly southward IMF conditions. Simulation results indicate an extended region of depressed magnetic field and strongly enhanced plasma β which exhibits a strong dependence on IMF orientation. These structures correspond to the Cusp Diamagnetic Cavities (CDC). The CDC region is described in detail, both for northward and for southward IMF. The typical features of these CDC's are generally well reproduced by the simulation. Further, the boundaries of the CDC are analyzed and the issue of the geometry of the external boundary and its relevance to the definition of the magnetopause is addressed. The inner boundaries between the CDC and the magnetosphere are gradual transitions which form a clear funnel shape, regardless of IMF orientation. The outer CDC/magnetosheath boundary exhibits a clear indentation in both the x - z and y - z planes for southward IMF, while it is only indented in the x - z plane for northward, with a convex geometry in the y - z plane. The outer boundary represents an Alfvénic transition, mostly consistent with a slow-shock, indicating that reconnection plays a important role in structuring the high-altitude cusp region. In summary, the simulation results paint a more complete three-dimensional picture of the high-altitude cusp region than has been possible as yet through global models and can provide further understanding of spacecraft data.

Chapter 4 has been prepared for submission to *Geophysical Review Letters*. The chapter explores the possibilities and implications of flux-tube entropy changes due to reconnection in the vicinity of CDC's, suggesting that this region is unique in its efficacy to realize changes in entropy due to the extended region of depressed magnetic field. Simulation results indicate that newly reconnected flux tubes can gain a significant amount of flux tube entropy through the reconnection process due to the topological change within the extended Diamagnetic Cavity Region (CDC). We argue that this is a property unique to this type of magnetic structure characterized by a magnetic null-point and an extended region of strongly depleted magnetic field. This effect has consequences regarding plasma

transport through the cusp region and may impose limits on the future evolution of cusp plasma.

Bibliography

- Adamson, E., Otto, A., and Nykyri, K.: 3-D mesoscale MHD simulations of a cusp-like magnetic configuration: method and first results, *Annales Geophysicae*, 29, 759–770, doi: 10.5194/angeo-29-759-2011, URL <http://www.ann-geophys.net/29/759/2011/>, 2011.
- Adamson, E., Otto, A., and Nykyri, K.: 3D mesoscale MHD simulations of magnetospheric cusp-like magnetic configurations: cusp diamagnetic cavities and boundary structure, *Annales Geophysicae*, pp. 325–341, doi:10.5194/angeo-30-325-2012, 2012.
- Alfvén, H.: On the existence of electromagnetic-hydrodynamic waves, *Arkiv foer Matematik, Astronomi och Fysik*, 39, 2, 1943.
- Baumjohann, W. and Truemann, R. A.: *Basic Space Plasma Physics*, Imperial College Press, 1997.
- Birn, J., Hesse, M., Schindler, K., and Zaharia, S.: Role of entropy in magnetotail dynamics, *J. Geophys. Res.*, 114, doi:0.1029/2008JA014015, 2009.
- Borovsky, J. E.: *Geospace Environment Modeling Meeting*, 2006.
- Borovsky, J. E., Thomsen, M. F., Elphic, R. C., Cayton, T. E., and McComas, D. J.: The transport of plasma sheet material from the distant tail to geosynchronous orbit, *J. Geophys. Res.*, 103, 20,297–20,331, 1998.
- Cargill, P. J., Dunlop, M. W., Lavraud, B., Elphic, R. C., Holland, D. L., Nykyri, K., Balogh, A., Dandouras, I., and Reme, H.: CLUSTER encounters with the high altitude cusp: boundary structure and magnetic field depletions, *Ann. Geophys.*, 22, 1739–1754, 2004.
- Cargill, P. J., Lavraud, B., Owen, C. J., Grison, B., Dunlop, M. W., Cornilleau-Wehrlin, N., Escoubet, C. P., Paschmann, G., Phan, T. D., Rezeau, L., et al.: *Cluster at the magnetospheric cusps*, vol. 20, Springer, 2005.
- Chang, S.-W., Scudder, J. D., Fuselier, S. A., Fennell, J. F., Trattner, K. J., Pickett, J. S., Spence, H. E., Menietti, J. D., Peterson, W. K., Lepping, R. P., and Friedel, R.: Cusp energetic ions: A bow shock source, *Geophys. Res. Lett.*, 25, 3729–3732, 1998.

- Chapman, S. and Ferraro, V. C. A.: A New Theory of Magnetic Storms, 1, The Initial Phase, *J. Geophys. Res.*, 36, 77, 1931a.
- Chapman, S. and Ferraro, V. C. A.: A New Theory of Magnetic Storms, 1, The Initial Phase (continued), *J. Geophys. Res.*, 36, 171, 1931b.
- Chen, J., Fritz, T. A., Sheldon, R. B., Spence, H. E., Spjeldvik, W. N., Fennell, J. F., and Livi, S.: A new, temporarily confined population in the polar cap during the August 27, 1996 geomagnetic field distortion period, *Geophys. Res. Lett.*, 24, 1447–1450, 1997.
- Chen, J., Fritz, T. A., Sheldon, R. B., Spence, H. E., Spjeldvik, W. N., Fennell, J. F., Livi, S., Russell, C., Pickett, J. S., and Gurnett, D. A.: Cusp energetic particle events: Implications for a major acceleration region of the magnetosphere, *J. Geophys. Res.*, 103, 69–78, 1998.
- Dunlop, M. W., Cargill, P. J., Stubbs, T. J., and Wooliams, P.: The high altitude cusps: HEOS 2, *J. Geophys. Res.*, 105, 27,509–27,517, 2000.
- Dunlop, M. W., Lavraud, B., Cargill, P., Taylor, M. G. G. T., Balogh, A., Reme, H., P., D., Glassmeier, K.-H., Elphic, R. C., Bosqued, J. M., Fazakerley, A., Dandouras, I., Escoubet, C. P., Laasko, H., and Marchaudon, A.: Cluster Observations of the Cusp: Magnetic Structure and Dynamics, Springer Netherlands, 2005.
- Eastman, T. E., Boardsen, S. A., Chen, S. H., Fung, S. F., and Kessel, R. L.: Configuration of high-latitude and high-latitude boundary layers, *J. Geophys. Res.*, 105, 23 221–23 238, 2000.
- Erickson, G. M.: A quasi-static magnetospheric convection model in two dimensions, *J. Geophys. Res.*, 97, 6505–6522, 1992.
- Erlanson, R. E., Zanetti, L. J., Potemra, T. A., Andre, M., and Matson, L.: Observation of electromagnetic ion cyclotron waves and hot plasma in the polar cusp, *Geophys. Res. Lett.*, 15, 412–424, 1988.
- Escoubet, C. P. and Bosqued, J. M.: The influence of IMF- B_z and/or AE on the polar cusp: An overview of observations from the AUREOL-3 satellite, *Planet. Space Sci.*, 37, 609–626, 1989.

- Fedder, J. A. and Lyon, J.: The Earth's Magnetosphere is 165 RE Long: Self-Consistent Currents, Convection, Magnetospheric Structure, and Processes for Northward Interplanetary Magnetic Field, *J. Geophys. Res.*, 100, 3623–3635, 1995.
- Frank, L. A.: Plasmas in the Earth's polar magnetosphere, *J. Geophys. Res.*, 76, 5202–5219, 1971.
- Fritz, T. A.: The Role of the Cusp as a Source for Magnetospheric Particles: a New Paradigm, in: Cluster-II Workshop: Multiscale/Multipoint Plasma Measurements, Proceedings of the Workshop held at Imperial College, London, UK, 22-24 September 1999. Paris: European Space Agency (ESA), vol. 449 of *ESA-SP*, p. 203, 2000.
- Fritz, T. A., Chen, J., and Siscoe, G. L.: Energetic ions, large diamagnetic cavities, and Chapman-Ferraro cusp, *J. Geophys. Res.*, 108, 1028, doi:10.1029/2002JA009476, 2003.
- Fuselier, S. A., Trattner, K. J., and Petrinec, S. M.: Cusp observations of high- and low-latitude reconnection for northward interplanetary magnetic field, *J. Geophys. Res.*, 105, 253–266, 2000.
- Gombosi, T. I., DeZeeuw, D. L., Groth, C. P. T., Powell, K. G., and Song, P.: The Length of the Magnetotail for Northward IMF: Results of a 3D MHD Simulation, *Physics of Space Plasmas*, 15, 121, 1998.
- Gosling, J. T., Thomsen, M. F., Bame, S. J., Elphic, R. C., and Russell, C. T.: Observations of reconnection of interplanetary and lobe magnetic field lines at the high-latitude magnetopause, *J. Geophys. Res.*, 96, 14,097, 1991.
- Haerendel, G., Paschmann, G., Sckopke, N., Rosenbauer, H., and Hedgecock, P.: The Frontside Boundary Layer of the Magnetosphere and the Problem of Reconnection, *J. Geophys. Res.*, 83, 3195–3216, 1978.
- Hansen, A. M., Bahnsen, A., and D'Angelo, N.: The Cusp-Magnetosheath Interface, *Journal of Geophysical Research*, 81, 556+, 1976.
- Heikkila, W. J. and Winningham, J. D.: Penetration of magnetosheath plasma to low latitudes through the dayside magnetospheric cusps, *J. Geophys. Res.*, 76, 883–891, 1971.

- Jackson, J. D.: *Classical Electrodynamics*, John Wiley & Sons, Inc., 111 River Street, Hoboken, NJ 07030, third edn., 1999.
- Johnson, J. R. and Wing, S.: Northward interplanetary magnetic field plasma sheet entropies, *J. Geophys. Res.*, 114, doi:10.1029/2008JA014017, 2009.
- Kessel, R. L., Chen, S. H., Green, S. F., Fung, S. F., Boardsen, S. A., Tan, L., Eastman, T. E., Craven, J. D., and Frank, L. A.: Evidence of high-latitude reconnection during northward IMF: Hawkeye observations, *Geophys. Res. Lett.*, 23, 583–586, 1996.
- Lavraud, B. and Cargill, P. J.: The magnetospheric cusps revealed: Results from the Cluster mission, *Astronomy and Geophysics*, 46, 1.32–1.35, 2005.
- Lavraud, B., Dunlop, M. W., Phan, T. D., Rème, H., Bosqued, J.-M., Dandouras, I., Sauvaud, J.-A., Lundin, R., Taylor, M. G. G. T., Cargill, P. J., Mazelle, C., Escoubet, C. P., Carlson, C. W., McFadden, J. P., Parks, G. K., Moebius, E., Kistler, L. M., Bavassano-Cattaneo, M.-B., Korth, A., Klecker, B., and Balogh, A.: Cluster observations of the exterior cusp and its surrounding boundaries under northward IMF, *Geophys. Res. Lett.*, 29, 2002.
- Lavraud, B., Fedorov, A., Budnik, E., Grigoriev, A., Cargill, P. J., Dunlop, M. W., Rème, H., Dandouras, I., and Balogh, A.: Cluster survey of the high-altitude cusp properties: A three-year statistical study, *Ann. Geophys.*, 22, 3009–3019, 2004a.
- Lavraud, B., Phan, T. D., Dunlop, M. W., Taylor, M. G. G. T., Cargill, P. J., Bosqued, J.-M., Dandouras, I., Rème, H., Sauvaud, J.-A., Escoubet, C. P., Balogh, A., and Fazakerley, A.: The exterior cusp and its boundary with the magnetosheath: Cluster multi-event analysis, *Ann. Geophys.*, 22, 3039–3054, 2004b.
- Lavraud, B., Fedorov, A., Budnik, E., Thomsen, M. F., Grigoriev, A., Cargill, P. J., Dunlop, M. W., Rème, H., Dandouras, I., and Balogh, A.: High altitude cusp flow dependence on IMF orientation: A 3 year Cluster statistical study, *J. Geophys. Res.*, 110, doi:10.1029/2004JA010804, 2005.

- Marshall Space Flight Center: A map of the magnetosphere, URL <http://xd12srv1.nsstc.nasa.gov/ssl/PAD/sppb/Edu/magnetosphere/mag5.html>, last accessed April 10, 2012, 2005.
- Mead, G. D.: Deformation of the geomagnetic field by the solar wind, *J. Geophys. Res.*, **69**, 1181, 1964.
- Měrka, J., Šafránková, J., and Němeček, Z.: Cusp-like plasma in high altitudes: a statistical study of the width and location of the cusp from Magion-4, *Ann. Geophys.*, **20**, 311–320, 2002.
- Midgley, J. E. and Davis, L.: Calculation by a moment technique of the perturbation of the geomagnetic field by the solar wind, *J. Geophys. Res.*, **68**, 5111, 1963.
- Newell, P., Meng, C.-I., Sibeck, D., and Lepping, R.: Some Low-Altitude Dependencies on the Interplanetary Magnetic Field, *J. Geophys. Res.*, **94**, 8921–8927, 1989.
- Newell, P. T. and Meng, C. I.: Cusp width and B_Z : Observations and a conceptual model, *J. Geophys. Res.*, **92**, 13,673–13,678, 1987.
- Niehof, J.: Diamagnetic Cavities and Energetic Particles in the Earth's Magnetospheric Cusps, Ph.D. thesis, Boston University, 2010.
- Nykyri, K., Otto, A., Adamson, E., Dougal, E., and Mumme, J.: Cluster observations of a cusp diamagnetic cavity: Structure, size and dynamics, *J. Geophys. Res.*, **116**, A03 228, doi:10.1029/2010JA015897, 2011a.
- Nykyri, K., Otto, A., Adamson, E., and Tjulin, A.: On the origin of fluctuations in the cusp diamagnetic cavity, *J. Geophys. Res.*, **116**, A06 208, doi:10.1029/2010JA015888, 2011b.
- Ogino, T.: A Three Dimensional MHD Simulation of the Interaction of the Solar Wind with the Earth's Magnetosphere: The Generation of Field Aligned Currents, *J. Geophys. Res.*, **91**, 6791–6806, 1986.
- Onsager, T., Scudder, J., Lockwood, M., and Russell, C.: Reconnection at the high latitude magnetopause during northward interplanetary magnetic field conditions, *J. Geophys. Res.*, **106**, doi:10.1029/2000JA000444, 2001.

- Otto, A.: Resistive MHD Computations of Magnetospheric Physics, *Computer Physics Communications*, pp. 185–195, 1990.
- Otto, A.: Geospace Environment Modeling (GEM) magnetic reconnection challenge: MHD and Hall MHD -constant and current dependent resistivity models, *J. Geophys. Res.*, 106, 3751–3757, 1999.
- Otto, A.: Cusp Tutorial, Geospace Environment Modeling Meeting, 2010.
- Otto, A.: Chapter 7 The Magnetopause, URL <http://how.gi.alaska.edu/ao/msp/chapters/chapter7.pdf>, last accessed April 10, 2012, 2010.
- Palmroth, M., Laasko, H., and Pulkkinen, T. I.: Location of high-altitude cusp during steady solar wind conditions, *J. Geophys. Res.*, 106, 21,109–21,122, doi: 10.1029/2001JA900073, 2001.
- Panov, E. V., Buchner, J., Franz, M., Korth, A., Savin, S. P., Reme, H., and Fornacon, K.-H.: High-latitude Earth's magnetopause outside the cusp: Cluster observations, *J. Geophys. Res.*, 113, 2008.
- Parker, E. N.: Dynamics of the interplanetary gas and magnetic fields, *Astrophys. J.*, 128, 664–676, doi:10.1086/146579, 1958.
- Paschmann, G., Haerendel, G., Sckopke, N., Rosenbauer, H., and Hedgecock, P.: Plasma and Magnetic Field Characteristics of the Distant Polar Cusp near Local Noon: The Entry Layer, *J. Geophys. Res.*, 81, 2883–2899, 1976.
- Pitout, F., Escoubet, C. P., Bogdanova, Y. V., Georgescu, E., Fazakerley, A. N., and Rème, H.: Response of the mid-altitude cusp to rapid rotations of the IMF, *Geophys. Res. Lett.*, 33, 2006a.
- Pitout, F., Escoubet, C. P., Klecker, B., and Rème, H.: Cluster survey of the mid-altitude cusp: 1. Size, location, and dynamics, *Ann. Geophys.*, 24, 3011–3026, 2006b.
- Potter, D.: *Computational Physics*, John Wiley and Sons Ltd., 1973.
- Raeder, J., Walker, R. J., and Ashour-Abdalla, M.: The structure of the distant geomagnetic tail during long periods of northward IMF, *Geophys. Res. Lett.*, 22, 349–352, 1995.

- Reiff, P. H., Hill, T. W., and Burch, J. L.: Solar wind plasma injection at the dayside magnetospheric cusp, *J. Geophys. Res.*, 82, 479–491, 1977.
- Russell, C. T.: Polar Eyes the Cusp, Cluster-II Workshop: Multiscale/Multipoint Plasma Measurements, Proceedings of the Workshop held at Imperial College, London, UK, 22–24 September 1999, 449, 47, 2000.
- Savin, S. P., Romanov, S. A., Fedorov, A., Zelenyi, L., Klimov, S. I., Yermolaev, Y. I., Budnik, E. Y., Nikolaeva, N. S., Russell, C. T., Zhou, X.-W., Urquhart, A. L., and Reiff, P. H.: The Cusp/Magnetosheath Interface on May 29, 1996: Interball 1 and Polar Observations, *Geophys. Res. Lett.*, 25, 2963–2966, 1998.
- Scarf, F. L., Fredricks, R. W., Neugebauer, M., and Russell, C. T.: Plasma Waves in the Dayside Polar Cusp, 2. Magnetopause and Polar Magnetosheath, *Journal of Geophysical Research*, 79, 1974.
- Schindler, K. and Birn, J.: MHD stability of magnetotail equilibria including a background pressure, *J. Geophys. Res.*, 109, doi:10.1029/2004JA010537, 2004.
- Schindler, K. and Otto, A.: Resistive Instability, *Geophysical Monograph*, pp. 51–61, 1989.
- Siscoe, G. L., Crooker, N., Siebert, K. D., Maynard, N. C., Weimer, D. R., and White, W. W.: Cusp geometry in MHD simulations, *Surveys in Geophysics*, 26, 387–407, doi: 10.1007/s10712-005-1902-4, 2005.
- Sonnerup, B. U. O. and Cahill, L. J.: Magnetopause Structure and Attitude from Explorer 12 Observations, *J. Geophys. Res.*, 72, 171–183, 1967.
- Spreiter, J. R. and Briggs, B. R.: Theoretical determination of the form of the boundary of the solar corpuscular stream produced by interaction with the magnetic dipole field of the Earth, *J. Geophys. Res.*, 67, 37–51, 1962.
- Tanaka, T.: Generation Mechanism for Magnetosphere-ionosphere Current Systems Deduced from a Three-dimensional MHD Simulation of the Solar-wind-magnetosphere-ionosphere Coupling Processes, *Journal of Geophysical Research*, 100, 12 057, 1995.

- Trattner, K. J., Fuselier, S. A., and Petrinec, S. M.: Location of the reconnection line for northward interplanetary magnetic field, *J. Geophys. Res.*, 109, doi: 10.1029/2003JA009975, 2004.
- Walters, G. K.: On the Existence of a second standing shock wave attached to the magnetosphere, *J. Geophys. Res.*, 71, 1341, 1966.
- White, W. W., Siscoe, G. L., Erickson, G. M., Kaymaz, Z., Maynard, N. C., Siebert, K. D., Sonnerup, B. U. O., and Weimer, D. R.: The Magnetospheric Sash and the Cross-tail S, *Geophysical Research Letters*, 25, 1605, 1998.
- Wing, S. and Johnson, J. R.: Introduction to the special section on entropy conservation and constraints related to space plasma transport, *J. Geophys. Res.*, 115, doi: 10.1029/2009JA014911, 2010.
- Yamauchi, M. and Lundin, R.: The Wave-Assisted Cusp Model: Comparison to Low-Altitude Observations, *Phys. Chem. Earth*, 22, 729–734, 1997.
- Zhang, H., Dunlop, M. W., Zong, Q.-G., Fritz, T. A., Balogh, A., and Wang, Y.: Geometry of the High-latitude Magnetopause as Observed by Cluster, *J. Geophys. Res.*, 112, 2007.
- Zhou, X. W. and Russell, C. T.: The location of the high-latitude polar cusp and the shape of the surrounding magnetopause, *J. Geophys. Res.*, 102, 105–110, 1997.
- Zhou, X.-W., Russell, C., Le, G., Fuselier, S. A., and Scudder, J. D.: The polar cusp location and its dependence on dipole tilt, *Geophys. Res. Lett.*, 26, 429–432, 1999.
- Zhou, X. W., Russell, C. T., Le, G., Fuselier, S. A., and Scudder, J. D.: Solar wind control of the polar cusp at high altitude, *J. Geophys. Res.*, 105, 245–251, 2000.

Chapter 2

3D Mesoscale MHD Simulations of a Cusp-Like Magnetic Configuration: Method and First Results¹

2.1 Abstract

We present a local mesoscale model of the magnetospheric cusp region with high resolution (up to 300 km). We discuss the construction and implementation of the initial configuration and give a detailed description of the numerical simulation. An overview of simulation results for the case of strongly northward interplanetary magnetic field (IMF) is then presented and compared with data from Cluster 2 spacecraft from February 14, 2003. Results show a cusp diamagnetic cavity (CDC) with depth normal to the magnetospheric boundary on the order of $1 - 2 R_E$ and a much larger extent of $\sim 5 - 9 R_E$ tangential to the boundary, bounded by a gradual inner boundary with the magnetospheric lobe and a more distinct exterior boundary with the magnetosheath. These results are qualitatively consistent with observational data.

2.2 Introduction

The magnetospheric cusps play a key role in plasma transport from the magnetosheath into the Earth's magnetosphere [Heikkila and Winningham, 1971; Frank, 1971]. The cusps are the regions extending from the magnetic poles out towards the magnetopause. These regions are very complex by nature, not simply in terms of their physical geometry, but also in terms of plasma dynamics and spatio-temporal variations. This complex nature has spawned a rich body of space science literature. Though these features were present in magnetospheric models as early as the papers of Chapman and Ferraro [Chapman and Ferraro, 1931a,b], there remain many outstanding questions with regard to these regions. Extensive research has focused on the low and mid altitude cusp [Newell et al., 1989; Lockwood and Smith, 1992; Yamauchi et al., 1996]. More recently, much research has focused on the exterior cusp. As research has progressed in this area, so has the general picture of the region. The exterior cusps have been identified as having three boundaries [Lavraud et al., 2004a; Paschmann et al., 1976; Haerendel et al., 1978; Onsager et al., 2001]: 1) the lobe/mantle, 2) the dayside plasma sheet, and 3) the magnetosheath. Due to the convergence (divergence)

¹Adamson, E., Otto, A., Nykyri, K., *Ann. Geophys.*, 29, 759-770, doi:10.5194/angeo-29-759-2011, 2011.

of the magnetic field into (out of) the cusp region in the northern (southern) hemisphere, the cusps act as focal regions for plasma flow and externally generated perturbations. The mapping of the open/closed boundary to the cusp region has enabled estimation of reconnection sites based on in situ cusp particle data [Fuselier et al., 2000; Trattner et al., 2004]. The magnetic field in the vicinity of the cusps rotates through a complete 360° about the dipolar axis. This ensures the existence of null-points where the dipolar magnetic field is bounded by an anti-parallel magnetosheath field. The complexity of the magnetic field orientation in the region suggests the presence of extended regions of significant magnetic shear. A typical feature of the exterior cusp is a region of extremely low magnetic field strength with respect to the surrounding field. These features have been descriptively referred to as cusp diamagnetic cavities (CDC's) due to the diamagnetic depression of the field [Erlandson et al., 1988]. These CDC's are also reported to exhibit enhanced plasma thermal pressure and density, as well as turbulent magnetic fluctuations [Savin et al., 1998; Chen and Fritz, 1998; Le et al., 2001; Savin et al., 2002, 2004; Nykyri et al., 2004, 2006]. Cusp energetic particles (CEP's) of up to at least 2 MeV were first reported in the high altitude polar cusp region by Chen et al. in 1996 [Chen et al., 1997]. The energization mechanism however, remains a topic of significant debate [Chen et al., 1998; Chang et al., 1998].

Modeling of the geomagnetic cusps is notoriously challenging. Global magnetospheric models have proven indispensable in the study of the interaction of the solar wind plasma with the Earth's magnetosphere [Fedder and Lyon, 1995; Raeder et al., 1995; Gombosi et al., 1998; White et al., 1998; Ogino, 1986; Tanaka, 1995]. However, the exterior cusp region poses a significant challenge for these models. While global models do reproduce the high altitude magnetospheric cusps (identified by the typical enhanced density and diamagnetic field regions), the resolution is too coarse to accurately model the small scale features. The exterior cusp is composed of the diamagnetic region extending $1 - 2 R_E$ normal to the magnetosheath boundary but much more expansive ($\sim 6 R_E$) in the transverse direction [Niehof, 2010], populated by largely stagnant plasma and bounded by a number of small scale features which vary depending on magnetosheath plasma conditions [Zhang et al., 2007]. For northward (southward) IMF, field aligned flows have been reported along the CDC-lobe [Lavraud et al., 2004b] (CDC-dayside plasma sheet) [Lavraud et al., 2005]

boundary, consistent with outflow from a high latitude (sub-solar) reconnection site. The magnetopause in the vicinity of the cusp region has been reported to range in thickness from $\sim 50 - 6000$ km, with an average thickness of ~ 1600 km and a median thickness of only 800 km [Panov et al., 2008]. Lavraud et al. [Lavraud et al., 2005] have associated sub-Alfvénic magnetosheath flows above the cusp with the existence of a plasma depletion layer adjacent to the cusp-magnetosheath interface. Global magnetospheric models typically consider a domain of some several $100 R_E$ in the sun-tail direction and some $50 R_E$ in the transverse direction. Even with the nonuniform grids commonly used in order to reduce the required grid densities in regions where lower resolution is possible, the simulations still require something on the order of 10^8 grid points, realizing a minimum resolution of $\sim .1 - .2 R_E$. At these resolutions, the cusp then poses a significant challenge for global models. It has also been noted by Siscoe et al. [Siscoe et al., 2005] that magnetic field depressions in the exterior cusp tend to be significantly greater than predicted by MHD models. This implies that the limited resolution of global models can not sufficiently reproduce the magnetic field gradients which define the diamagnetic currents within the cusp. Considering these small-scale features which add to the complexity of the cusp, it is clear that global magnetospheric models are presented with a significant challenge in modeling the region.

We have developed a mesoscale cusp-like magnetic field model in order to provide a better resolution of the entire cusp region than is possible in global models. The high resolution of the local model allows us to better reproduce the large gradients in the various plasma parameters which define the small scale features outlined above. The local model provides the additional benefit of allowing for the execution of controlled experiments. For instance, it provides a relatively easy means by which to examine the effects of variations in local plasma parameters. This paper introduces this model and presents first results in order to illustrate some model properties. In section 2 we discuss in detail the specifics of the model as well as the numerical methods implemented. Section 3 focuses on the method by which we generate an acceptable equilibrium configuration as an initial state for the dynamic simulation. In section 4, we present initial results for strongly northward IMF and section 5 consists of a summary of our results.

2.3 Numerical Simulation

2.3.1 Numerical Method

The evolution of a magnetized fluid is described by the full set of MHD equations. We implement these equations in the following form:

$$\begin{aligned}
 \frac{\partial \rho}{\partial t} &= -\nabla \cdot (\rho \mathbf{u}), \\
 \frac{\partial(\rho \mathbf{u})}{\partial t} &= -\nabla \cdot \left[\rho \mathbf{u} \mathbf{u} + \frac{1}{2} (p + B^2) \mathbf{I} - \mathbf{B} \mathbf{B} \right], \\
 \frac{\partial h}{\partial t} &= -\nabla \cdot (h \mathbf{u}) - \frac{\gamma - 1}{\gamma} h^{1-\gamma} \eta j^2, \\
 \frac{\partial \mathbf{B}}{\partial t} &= -\nabla \times (\mathbf{u} \times \mathbf{B} - \eta \mathbf{j}), \\
 \mathbf{j} &= \nabla \times \mathbf{B},
 \end{aligned} \tag{2.1}$$

where $h = (p/2)^{1/\gamma}$ and ρ , p , η , \mathbf{u} , and \mathbf{B} represent density, pressure, resistivity, velocity, and magnetic field. The ratio of specific heats (γ) is taken to be 5/3. All variables are normalized to typical system values, and are thus dimensionless. Length scale, density, and magnetic field strength are normalized to typical system values ($L_0 = 1 R_E$, $\rho_0 = 1 \text{ cm}^3$, and $B_0 = 50 \text{ nT}$). The pressure, velocity and time scale are then measured in units of normalized pressure $p_0 = B_0^2/8\pi = 1 \text{ nPa}$, Alfvén speed $u_A = B_0/\sqrt{4\pi\rho_0} = 1,090 \text{ km/s}$, and Alfvén time $\tau_A = L_0/u_A = 6 \text{ s}$, respectively.

We utilize a leapfrog discretization method for the integration of the MHD equations. This is a finite difference method of second order in both time and space. The method is relatively easy to implement and affords the possibility of using a nonuniform grid. This reduces the required number of grid points in the current configuration at this resolution by a factor of three. The simulations presented herein are comprised of $203 \times 203 \times 203$ grid points in x , y , and z , respectively.

The simulation code used here has been tested for conservation properties, varying grid and system size and compared with results from other methods (eg., [Schindler and Otto, 1989; Otto, 1990, 1999]). We are confident from the testing and various applications of the code that the results are reliable.

2.3.2 Model

We construct a local model of the magnetospheric cusp region by placing a dipole at $-10 R_E$ along the z -axis with the dipole axis anti-parallel to z (no dipole tilt). The coordinates are such that the x -axis is directed toward the sun and the y -axis completes the right-handed system. The simulation domain ranges from $-12 R_E$ to $12 R_E$ in both the x and y directions, while the z coordinate ranges from $-5 R_E$ to $6 R_E$, such that the dipole is $5 R_E$ below the lower z -boundary.

With $\nabla \cdot \mathbf{B} = 0$, the magnetic field may be represented by a vector potential \mathbf{A} , such that $\mathbf{B} = \nabla \times \mathbf{A}$. The dipole magnetic field is independent of the azimuthal angle, ϕ , lending a magnetic vector potential in cylindrical coordinates $\mathbf{A} = -\kappa(\sin \theta/r^2)\hat{\phi}$, where κ represents the dipole strength. By defining the original magnetic field in terms of a vector potential, it becomes straightforward to introduce a shielding current which effectively switches-off the magnetic field in the region $z > 0$, thus defining a magnetosheath region. This is accomplished through the inclusion of a hyperbolic tangent term in the vector potential. Modification of this dipolar magnetic vector potential to include the shielding current results in a vector potential of the form $\mathbf{A} = -\kappa(\sin \theta/r^2)[1 - \tanh(r \cos \theta/L)]\hat{\phi}$, where L controls the width of the transition region from dipolar field to no field. This current acts to magnetically shield the dipole magnetic field along the z direction. In Cartesian components, this yields a magnetic field with components:

$$\begin{aligned} B_x &= -\kappa \left\{ \frac{x \cosh^{-2}(z/L)}{r^3 L} + \frac{3xz[1 - \tanh(z/L)]}{r^5} \right\}, \\ B_y &= -\kappa \left\{ \frac{y \cosh^{-2}(z/L)}{r^3 L} + \frac{3yz[1 - \tanh(z/L)]}{r^5} \right\}, \\ B_z &= -\kappa \left(\frac{-1}{r^3} + \frac{3z^2}{r^5} \right) [1 - \tanh(z/L)]. \end{aligned}$$

A constant ‘‘draped’’ (no z -component) IMF may then be superposed in the magnetosheath region. The superposed model IMF is expressed as $B_{IMF_x} = -(B_{MSH}/2)[1 + \tanh(z/L)] \cos \phi$, $B_{IMF_y} = (B_{MSH}/2)[1 + \tanh(z/L)] \sin \phi$, where ϕ is the IMF clock angle. Thus the model IMF lies purely in the $x - y$ plane. The initial magnetic field configuration for the case of strongly northward IMF may be seen in Figure 2.1.

It remains to complete a prescription of the plasma density and pressure. We note here, that the superposition of these magnetic fields does not result in a configuration in force

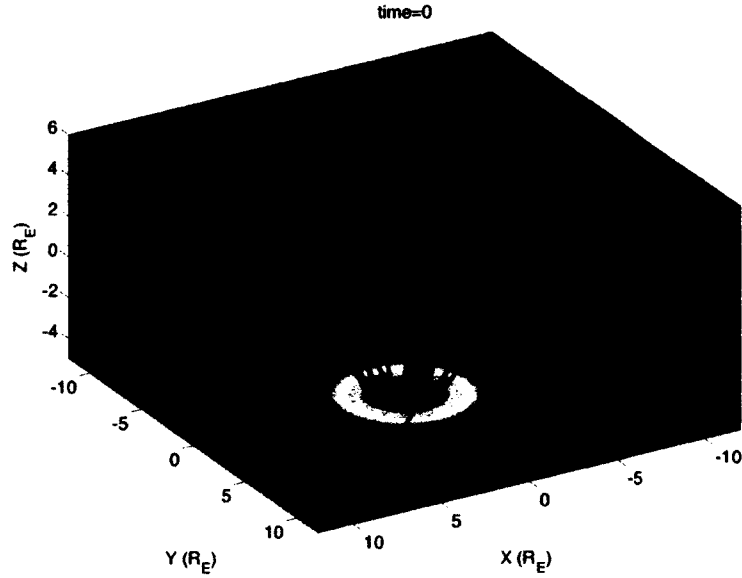


Figure 2.1. Initial magnetic field configuration under strongly northward IMF orientation. Dipolar magnetospheric field lines are shown in grey, while red lines represent the draped uniform magnetosheath field. The sun lies to the left of the figure such that the dayside (nightside) magnetosphere corresponds to $x > 0$ ($x < 0$).

balance, though this is the desired state of the initial configuration in order to insure that the plasma dynamics evolve as a result of the driving magnetosheath plasma flow and not due to the imbalance between forces in the initial construction of the fields. This initial non-equilibrium will be discussed later in this paper. This desire for force balance motivates our prescription of the pressure distribution.

Consider the MHD momentum equation (2.1). Static equilibrium requires:

$$\frac{\partial}{\partial t} = \mathbf{u} = 0.$$

With these assumptions, it is clear that the requirement of force-free static equilibrium results in the magnetohydrostatic equation:

$$0 = -\nabla p + \mathbf{j} \times \mathbf{B}. \quad (2.2)$$

As the magnetic field has already been prescribed, one is free to choose the pressure distribution. Consider the magnetohydrostatic equation (2.2). Taking the scalar product of this

equation with B :

$$0 = -B \cdot \nabla p$$

it follows that for a static equilibrium state, the pressure is constant on magnetic field lines. Thus, by expressing the initial pressure as a function of the field line equation, we ensure it's constancy on field lines. In three dimensional spherical coordinates, field lines are given by $r \sin \theta A_\phi = \text{constant}$. We therefore define the initial pressure distribution as

$$p = p_1 + p_2 \exp(\alpha r \sin \theta A_\phi)$$

where p_1 =typical magnetospheric thermal pressure, p_2 =typical magnetospheric magnetic pressure, and α is a parameter which controls the cross-field line gradient. This gives a pressure distribution with low pressure in the dayside plasma sheet and the lobe, but an enhanced pressure filling the throat of the cusp and into the magnetosheath.

Turning now to the treatment of the density distribution, we note that the plasma densities in the magnetosheath and the cusp proper are typically a factor of 10^2 larger than those in the magnetospheric lobes [Lavraud et al., 2002; Panov et al., 2008]. Thus, we choose a density distribution similar to that utilized for the pressure distribution:

$$\rho = \rho_0 + \delta\rho \exp(\alpha r \sin \theta A_\phi) + \delta\rho [1 + \tanh(z)],$$

where ρ_0 and $\delta\rho$ represent the background and maximally enhanced densities, respectively. Similar to the pressure distribution, the result is a system with enhanced density along field lines having foot-points in the throat of the cusp which map into the magnetosheath. The third term populates the magnetosheath with an increased density. The initial distribution of density and pressure is illustrated in Figure 2.2.

The largest gradients in the configuration discussed above are located in the center of the lower plane of the simulation domain, where the dipolar magnetic field lines converge. We reduce computational costs by using a nonuniform grid with highest grid resolution in this region of convergence. We define a grid in which the x - and y - resolutions are maximal ($\Delta x, \Delta y = 0.07$) in the center of the simulation domain, and lowest ($\Delta x, \Delta y = 0.168$) at the edges. The resolution in the z -direction is more uniform, with a maximum resolution of $\Delta z = 0.05$ at the lower boundary and minimum resolution of $\Delta z = 0.069$ at the top

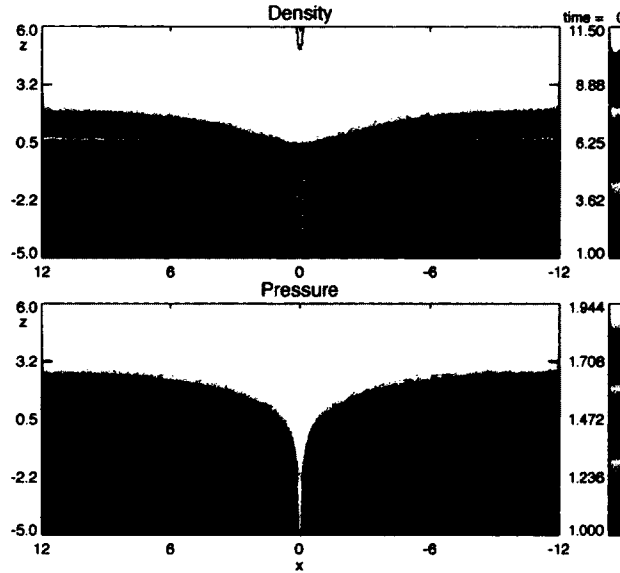


Figure 2.2. Illustration of the initial density (top) and pressure (bottom) distributions in the noon-midnight meridian ($y = 0.0$).

boundary. The grid is chosen to be more uniform in the z -direction in order to resolve not only the strong gradients toward the bottom of the domain where the field lines converge, but also to resolve the gradients within the magnetopause. The computational costs could be further reduced with the consideration of a more sophisticated grid with a high z -resolution within the magnetosphere and lower in the magnetosheath, for example.

Our initial configuration is not in equilibrium. We rely on a relaxation method to move the system towards force balance. The boundary conditions differ significantly between the relaxation and the dynamically evolving configurations. These differences will be discussed further in the respective sections of this paper. Here, it will suffice to mention the similarities in boundary conditions between the two configurations. Except where otherwise stated, Neumann boundary conditions are imposed, such that $\partial f / \partial x_n = 0$ (where f represents the general set of plasma parameters). The normal components of the magnetic field at the boundaries are calculated such that $\nabla \cdot \mathbf{B} = 0$, while a simple extrapolation method is applied to the transverse components. At the lower z -boundary, where the dipolar geomagnetic flux converges, this extrapolation does not strictly preserve the dipolar nature of the field. Rather, the approximation at the boundary results in a current sheet which generates

large $\mathbf{j} \times \mathbf{B}$ forces tending to evacuate plasma from the system on relatively short time scales. We resolve this issue by freezing the plasma at the lower z -boundary.

2.4 Relaxation Method

In this section, we discuss the method by which we relax the initial configuration towards force balance, resulting in a sufficient equilibrium state.

In order to investigate the plasma dynamics of the region, it is desired to begin the dynamic simulation with a force free equilibrium initial configuration such that any unbalanced forces present in the initial configuration do not contribute in any significant way to the ensuing dynamics. A simple superposition of magnetic fields however, does not in general result in an equilibrium configuration. The above ansatz is an effective means of producing the desired MHD model of the region under consideration (i.e., a magnetospheric cusp) however, the system which results is not in equilibrium. Such a prescription of the pressure distribution guarantees that the thermal pressure is constant on magnetic field lines. However, the magnetohydrostatic equation (2.2) requires that the pressure gradient be balanced by the Lorenz force. The net force ($\mathbf{F}_{\nabla p} + \mathbf{F}_{\mathbf{j} \times \mathbf{B}}$) is shown in the noon-midnight meridional plane for the initial state of the system in Figure 2.3.

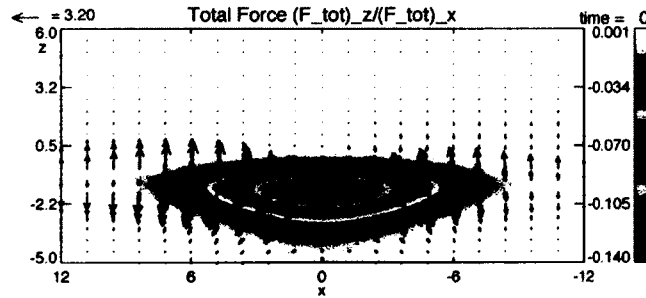


Figure 2.3. Illustration of the net force in the noon-midnight meridional plane ($y = 0$). Arrows indicate the z - x components within the plane, while the colors represent the y -component.

In order to reduce these forces and move toward an equilibrium state, a numerical relaxation is utilized, similar to that of Hesse and Birn [Hesse and Birn, 1993]. In their approach, the system was frozen when the kinetic energy reached a maximum. We do not employ this energy based method. A complicated three-dimensional system such as our

cusplike model has the tendency to realize a kinetic energy maximum far too frequently to make such an approach efficient. During the relaxation, the system is closed (no normal flow at the boundaries). As the system evolves, the forces accelerate the fluid, converting potential energy into kinetic energy. By periodically freezing the system, thus removing the kinetic energy, the system moves toward an equilibrium state. The initial system exhibits unbalanced forces which act over various scales. There are forces which act over relatively short scales (i.e., across a current sheet) and forces which act over larger scales (i.e., imbalance between the day and night sides of the magnetosphere). The various ranges over which these forces act necessitate freezing the system at different time intervals. Initially, the system is frozen on short time scales (every 100 time steps or 0.05 s). This is necessary due to the large forces present in the initial prescription of the system. If the system is allowed to evolve over longer periods initially (i.e., utilizing a lower frequency for the relaxation), the initial force imbalance drives the system so hard that the final relaxed state no longer represents an acceptable magnetic cusp model. A high frequency relaxation efficiently damps these initial local forces, but requires far more computation time in order to sufficiently relax the forces which act over larger distances. Thus, it is preferred to strike a balance between a short relaxation interval, which necessitates a long evolution in order to realize a sufficiently relaxed state, and a longer relaxation interval which may result in a significantly different final state. The cusp model must be relaxed on short timescales in order to reduce the larger local forces. Once this is accomplished, the system may be allowed to evolve on larger timescales to reduce the long-distance force imbalance and to realize the desired quasi-equilibrium more rapidly. The actual relaxation schedule employed has been devised through extensive testing. It was determined through this testing that the system requires a short initial relaxation interval, but after the strong small-scale forces have been relaxed, the system is relatively insensitive to the chosen relaxation interval, eventually realizing the same force balance. The decisive factor then becomes more a question of computation time. We employ a relaxation schedule which removes these initial small-scale forces through a short relaxation interval and then alternate between short intervals (400 time steps) and larger intervals (4,000 time steps), with preference given to the larger intervals in order to reduce computation time. Periodically reverting to short relaxation intervals ensures that small-scale forces remain damped.

Defining the density of unbalanced forces in the system as $F_u = \partial(\rho u)/\partial t + \nabla \cdot (\rho u u)$, the momentum equation (2.1) may be rewritten as $F_u = -\nabla p + j \times B$. The square of this unbalanced force density may then be integrated over the simulation domain to indicate the proximity of the system as a whole to force balance at a given time: $\mathcal{F}_n^2 = \int_v F_u^2 dv$. It is also useful to monitor the maximum force in the system as this allows for a comparison between remnant forces in the final relaxed state and initial forces present in the dynamic system.

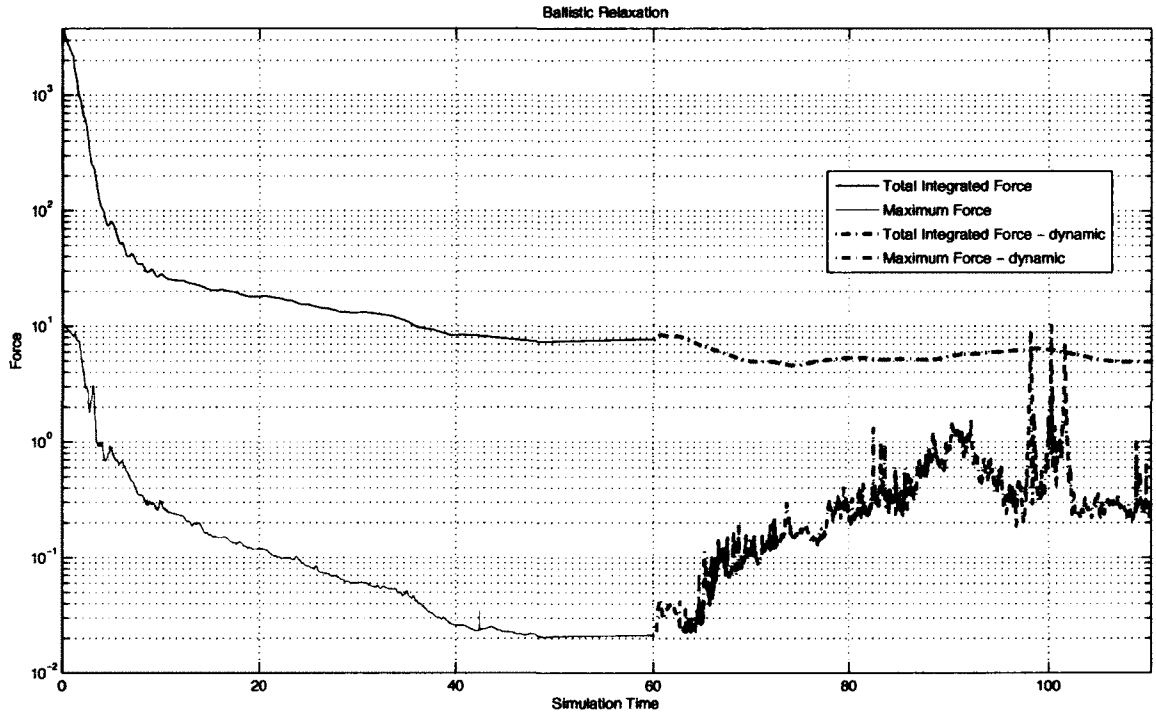


Figure 2.4. Temporal evolution of the maximum force and total integrated force through the entire system.

The results of this relaxation are shown in Figure 2.4 for the case of 10° IMF (strongly northward with a small positive B_y component). Both the maximum (blue) and total integrated (green) forces are plotted. The system is being relaxed only up to a time of 60 Alfvén times. The continuation of the line plot beyond this time represents the dynamic evolution of the system and will be addressed in the next section. Note that the previously mentioned $j \times B$ forces at the boundaries are not included in this calculation. The relaxation

reduces the total force in the system by roughly a factor of 500 and the maximum force by a factor of 250.

The initial configuration places a minimum in the magnetic field (which serves as a proxy for the magnetic null-point) at $(-11.74, 2.03, -0.06)$. This is the location within the magnetopause at which the magnetospheric and magnetosheath magnetic fields are most strongly anti-parallel. Through the relaxation, the magnetopause evolves from an initially flat current sheet in the $x - y$ plane, to a more hemispherical structure, bulging outward towards the center, and containing a slight dimple at the peak. The magnetic field in this relaxed state exhibits a minimum which has migrated sunward and slightly towards the noon-midnight meridian to $(-8.8, 1.6, 0.3)$. The converging dipolar field defining the “throat” of the cusp also begins to tilt slightly in the direction of the anti-parallel field. Figure 2.5 shows the relaxed magnetic field distribution and current density in the noon-midnight meridian plane. This plane is shown here in order to illustrate the general features of the magnetic field just described, though the magnetic null-point is not contained in this plane.

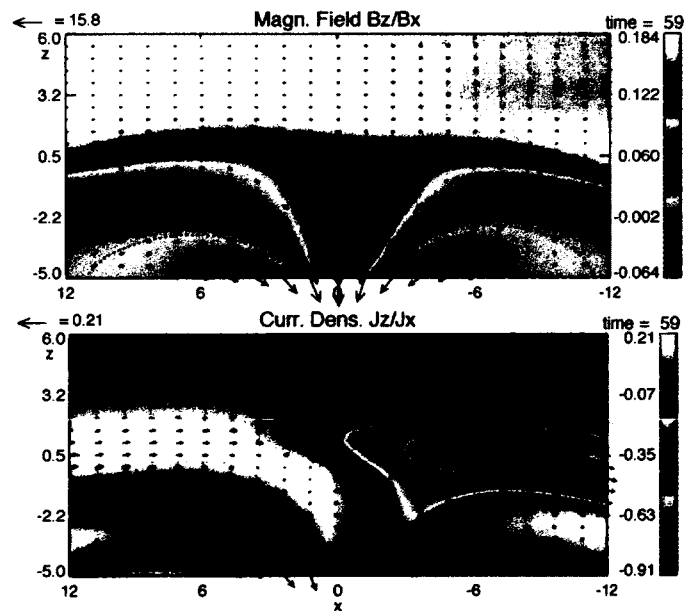


Figure 2.5. Distribution of the magnetic field (top) and current density (bottom) in the noon-midnight meridian plane ($y = 0$) for the final relaxed configuration. Arrows indicate the $z-x$ components within the plane, while colors represent the y -component.

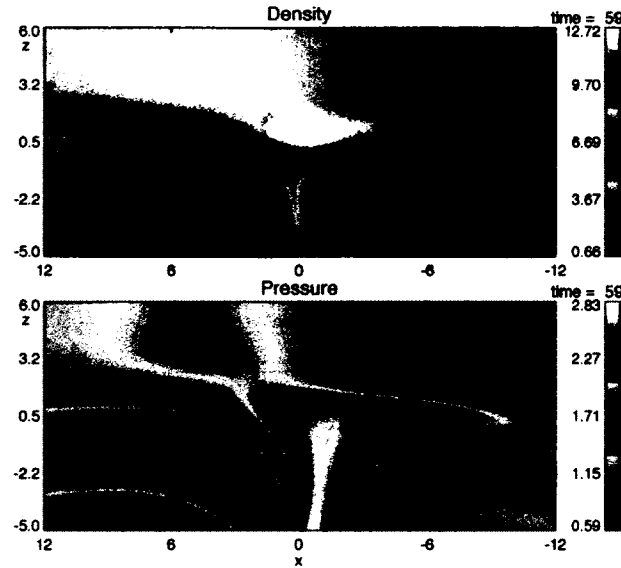


Figure 2.6. Distribution of the density and pressure in the noon-midnight meridian plane ($y = 0$) for the final relaxed configuration.

The resulting distributions of density and pressure also exhibit significant evolution (Figure 2.6). Both parameters have become enhanced in the throat and exterior of the cusp, while the range of values of each has roughly doubled. The x -gradient of both parameters in the magnetosheath is a direct consequence of the closed system relaxing toward force-balance. Note that the tilting of the cusp throat is also evidenced in the structure of the density and pressure.

2.5 Results

2.5.1 Dynamic Simulation

After the configuration has been sufficiently relaxed, a dynamic simulation may be initiated by imposing a homogeneous magnetosheath flow and modifying the boundary conditions. The boundary conditions are changed to allow inflow at the dayside boundary (maximum x -boundary) and outflow through the night-side boundary (minimum x -boundary). A position dependent (x, z) flow profile is constructed such that the streaming magnetosheath plasma flows over the top of the magnetopause current sheet. This initial flow profile is then used as the boundary condition for the flow at the dayside boundary, allowing for inflow

in the magnetosheath while maintaining no flow normal to the boundary within the magnetosphere. The night-side boundary differs in that the entire boundary is open to allow for motion of the magnetopause within this boundary. Note that these are initial results, meant only to give an overview of the general features present in the simulation, as such the boundary conditions are relatively simple, though more elaborate boundary conditions are planned for future work. The magnetosheath flow is initialized with a magnitude of ~ 220 km/s in the x -direction. The flow is sub-Alfvénic with an Alfvén Mach number of 0.7. For the following example, the resistivity is also increased by fifty percent over the value used during the relaxation in order to allow for a higher reconnection rate. The following results are from simulations with a 10° IMF (strongly northward with a small positive B_y component).

It is interesting in considering the previous plot of net forces throughout the relaxation to extend the plot so as to include the forces during the dynamic evolution of the system. This gives a means by which the remnant forces in the relaxed state may be compared with those during the dynamic evolution (see Figure 2.4). The line plots in the figure for times after 60 Alfvén times represent the maximum and total forces during the dynamics. The maximum force steadily increases after the magnetosheath flow is initiated, while the total integrated force gradually decreases over the first 10 Alfvén times (between 60 and 70 Alfvén times in the figure) and subsequently remains relatively constant. This suggests that, although the maximum force is increasing, the volume containing these contributive forces is actually decreasing, such that the total force decreases. This behavior suggests that the forces in the relaxed configuration are indeed sufficiently balanced such that they result in no significant contribution to the dynamics.

Typical characteristics of the external cusps are evident in Figures 2.5 and 2.6. The magnetic null-point is located on the night-side of the cusp, slightly offset from the noon-midnight meridian in the positive y -direction (eastward). This is a direct consequence of the IMF orientation as this is where the IMF is most strongly anti-parallel to the Magnetospheric field. This region corresponds to the largest magnetopause current due to the strong magnetic shear. The current sheet stretches out to both sides of this point around the surface of the magnetopause toward the dayside due to the anti-parallel projection of the field.

2.5.2 Comparison with Cluster 2 Data

Plots of Cluster 2 data are shown in Figure 2.7 for a cusp crossing on February 14, 2003. This event is quite interesting for a number of reasons and is discussed at length elsewhere [Nykyri et al., 2011a,b, submitted 2010]. Here, we discuss only the period from 18:30 - 19:30 for the purpose of comparison with our results from the local cusp simulation. The lagged IMF and solar wind dynamic pressure from ACE are shown in the bottom pane of Figure 2.7. The IMF is northward and relatively constant for the period shown. For simplicity, we present data only from spacecraft 4, as it traverses the CDC while encountering both the lobe-CDC boundary and the CDC-magnetosheath boundary once with the exception of a brief secondary traversal of the CDC-magnetosheath boundary during this interval.

Between 18:30 and 19:30, SC4 travels from the magnetospheric lobe into the CDC and finally exits into the magnetosheath. SC4 detects a gradual inner boundary between the magnetospheric lobe and the CDC. Densities increase from magnetospheric values of roughly $0.2 \text{ particles/cm}^3$ to values comparable to the magnetosheath ($20 \text{ particles/cm}^3$) by 18:53. This transition is accompanied by increasing plasma flows (up to 550 km/s) with proximity to the CDC-lobe boundary. The enhanced flows are largely field-aligned with a small convective component (velocity components are not shown here, see Nykyri et al.), consistent with outflow from a high-latitude reconnection site tailward of the cusp. The CDC is indicated by strongly depressed and fluctuating magnetic field accompanied by an increase in plasma density. It is difficult, however, to identify a clear boundary between the lobe and CDC, as all parameters converge gradually towards CDC values. It appears that SC4 enters the CDC proper by at least 18:50, corresponding to the inner edge of the enhanced flow region. Plasma flow in this region is only 50 km/s. At 18:53 the spacecraft encounters brief but significant fluctuations in all plasma parameters nearly simultaneously with an abrupt increase of the solar wind dynamic pressure. These fluctuations are consistent with magnetosheath values and likely represent an abrupt encounter with the CDC-magnetosheath boundary caused by a compression of the magnetosphere due to enhanced solar wind dynamic pressure or possibly an encounter with a flux transfer event. Immediately following this encounter with the magnetosheath, the solar wind dynamic pressure decreases and SC4 again measures flows consistent with the inner edge of the CDC. These flows persist until 19:05 at which point SC4 reenters the CDC and corresponding region of stagnant flow. SC4

appears to remain within the CDC until 19:19 at which point it clearly exits into the magnetosheath as indicated by the immediate drop in temperature and increase in magnetic field strength and bulk flow. This outer boundary of the CDC is much more distinct than the inner.

The traversal of spacecraft 4 may be summarized as follows:

1. A gradual lobe-CDC (inner) boundary marked by:
 - (a) density increase from typical magnetospheric values of 0.2 particles/cm³ to 20 particles/cm³
 - (b) Decreasing magnetic field
 - (c) enhanced (largely parallel) flows up to 550 km/s

2. Cusp diamagnetic cavity:
 - (a) magnetosheath-like density of 20 particles/cm³
 - (b) low average magnetic field strength of 30 nT with strong fluctuations between 5 – 40 nT
 - (c) low average plasma velocity of 50 km/s

3. Abrupt CDC-magnetosheath (outer) boundary:
 - (a) relatively stable (relative to CDC) magnetic field strength of 60 nT
 - (b) more steady plasma velocity of 150 km/s (largely $-v_x$)
 - (c) sudden decrease in temperature

Plots of simulated data are shown in Figure 2.8 for comparison with the Cluster data. The plots represent data generated along a cut in the noon-midnight meridian plane located at $x = -4 R_E$ after roughly two minutes of physical time. From top to bottom in the left pane of Figure 2.8, the plots represent density, velocity components, magnetic field components, Pressure, and current density, while the right pane shows electric field components, plasma β , and parallel current density (all in simulation units).

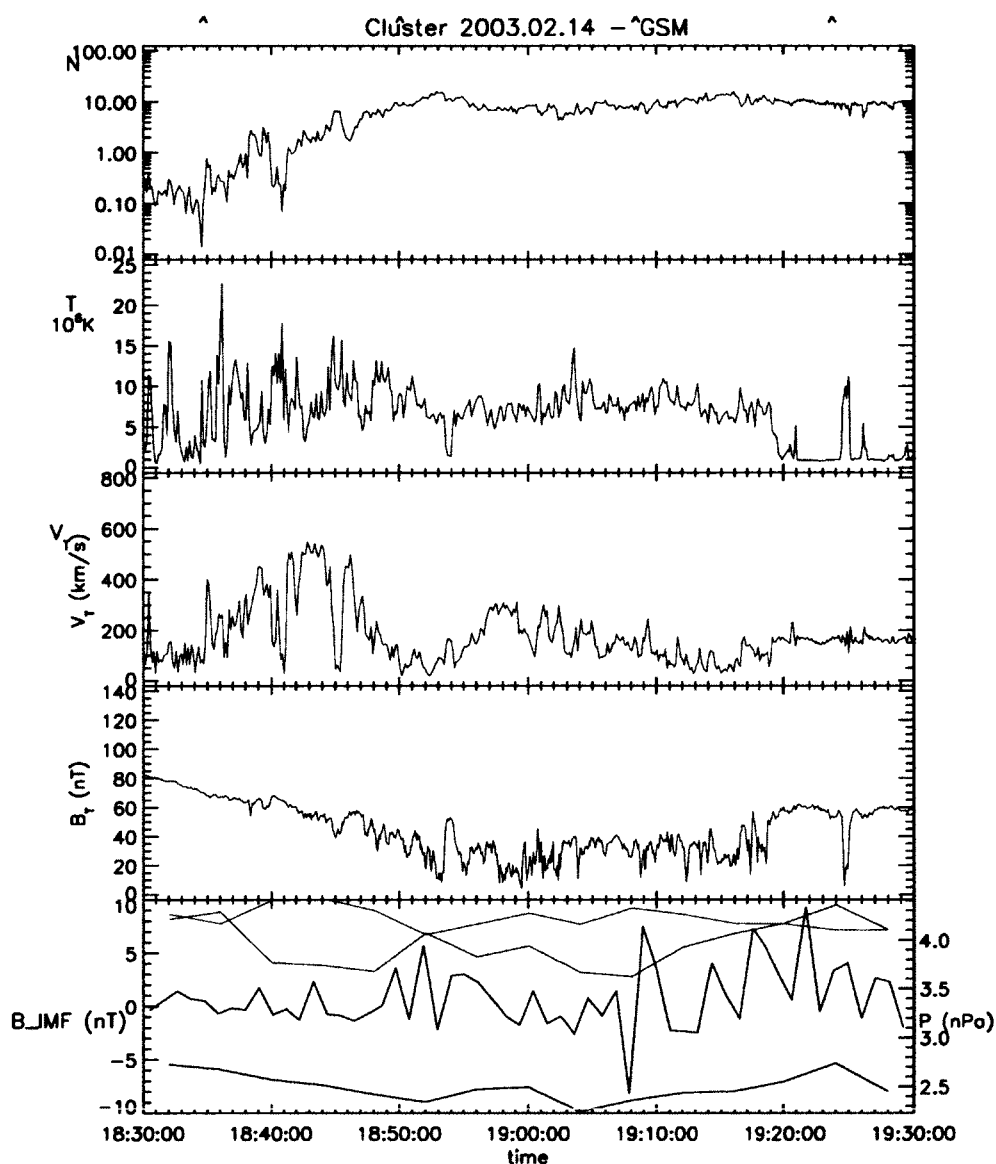


Figure 2.7. Plasma and magnetic field data from Cluster spacecraft 4 in GSM coordinates for a traversal of the cusp region on February 14, 2003. The solar wind dynamic pressure as well as all three components of the IMF measured by the ACE spacecraft and lagged 44.0 minutes are plotted in the bottom pane, with black, red, and blue corresponding to the x , y , and z components, respectively.

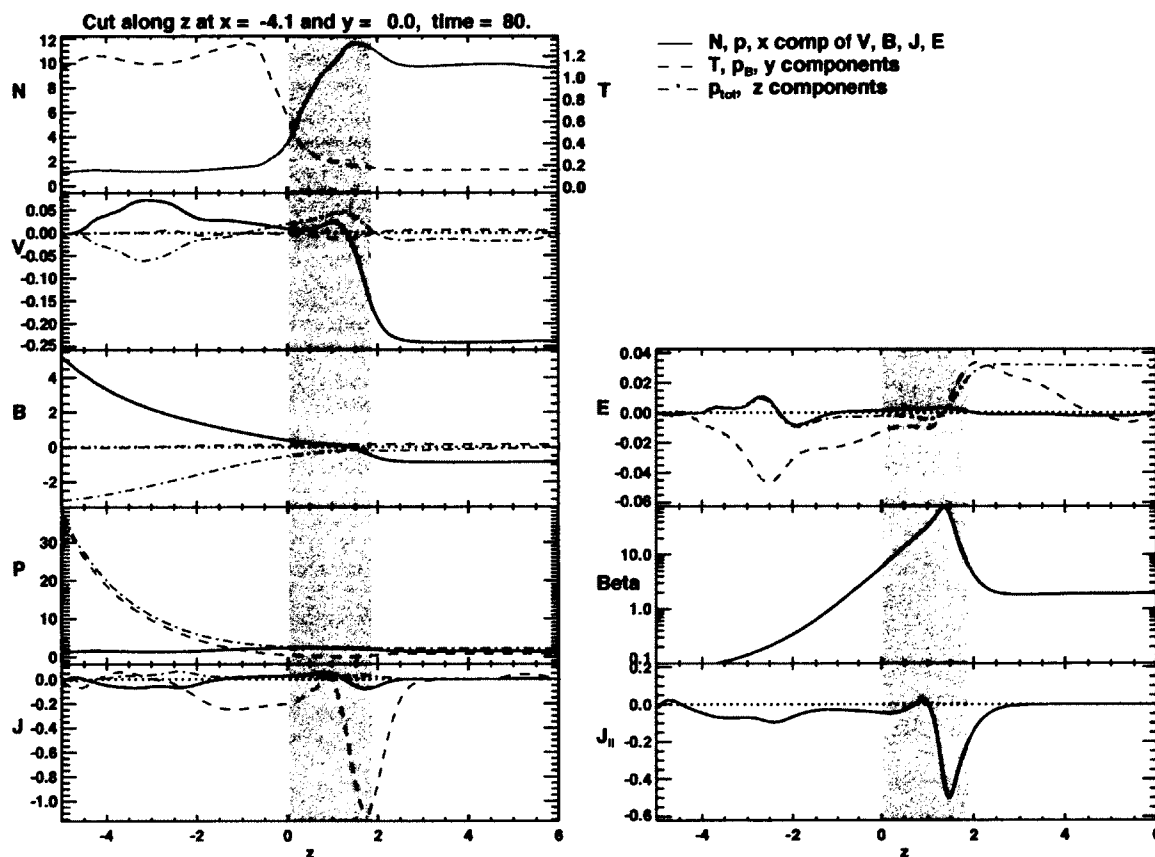


Figure 2.8. Simulated data (in normalized units) in the noon-midnight meridian plane along $x = -4.1 R_E$. The left pane shows (from top to bottom) number density (solid blue line) and temperature (dashed red line), velocity components (x - solid black, y - dashed blue, z - dash-dot red), magnetic field components, pressure (thermal pressure - black, magnetic pressure - blue, total pressure - red), current density components. The right pane shows (from top to bottom) the electric field components, plasma β , and the parallel current density. Shading represents the region of large plasma β indicating the CDC.

Towards the lower boundary of the simulation domain (between -5 and $-2 R_E$), field-aligned flows up to ~ 100 km/s are encountered, corresponding to the region of low density and high magnetic field strength. Adjacent to this region of enhanced flow is a region of relatively stagnant plasma ($20 - 30$ km/s) convecting sunward (Figure 2.8). Within this region of slow convection the magnetic field is reduced to a minimum of ~ 9 nT. The transition from magnetospheric lobe plasma to CDC plasma is very gradual making it difficult to identify a specific boundary (similar to the Cluster data presented previously).

The shaded section in the plots represents the CDC (indicated by a normalized plasma $\beta > 6$). The CDC spans a distance of at most $2 R_E$ in the z -direction (nearly normal to the magnetopause), but extends much farther in the transverse direction. This oblate geometry of the CDC may be seen in Figure 2.9. These figures are cuts in the noon-midnight meridian plane, roughly where the CDC realizes its maximal extent tailward. For northward IMF, the cavity is identified as the region of high plasma β extending from the reconnection line (indicated by the maximum current density in Figure 2.9), sunward. Plasma β ($\beta = p/(B^2/2\mu_o)$) is a useful indicator of the CDC due to the strongly depressed magnetic field and enhanced plasma pressure within.

The external boundary of the CDC with the magnetosheath is characterized by a much more abrupt transition than the inner boundary with the magnetosheath. The sunward directed outflow from the reconnection site bifurcates into two layers, one flowing parallel to the magnetic field earthward into the cusp, the other convecting sunward along the inner edge of the cusp-magnetosheath boundary (Figure 2.9). These flows are qualitatively consistent with those reported by Lavraud et al. [Lavraud et al., 2005] for instance. Enhanced sunward convection (~ 60 km/s) is evident along the inner edge of the CDC-magnetosheath boundary. Adjacent to this enhanced sunward convection, plasma parameters change relatively abruptly to magnetosheath values.

2.6 Discussion and Conclusion

We have presented a new mesoscale local simulation of a magnetospheric cusp-like configuration. This model has been developed in order to address the plasma dynamics in the cusp region which develop on scales which are too small to be sufficiently resolved in global magnetospheric models. A detailed discussion of the construction of the model has been

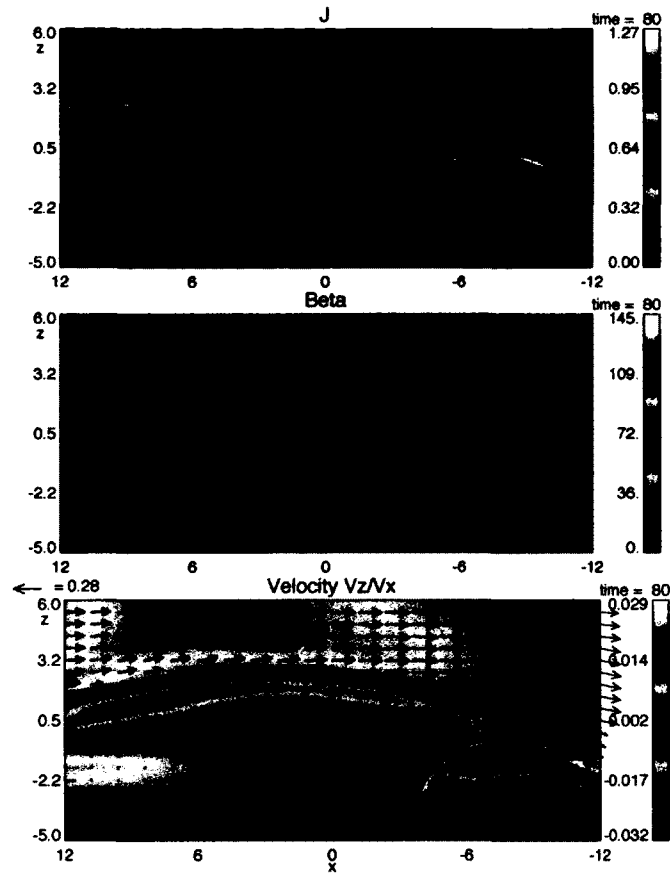


Figure 2.9. Distribution of the total current density, plasma beta, and velocity in the noon-midnight meridian plane ($y=0$). Arrows in the velocity plot indicate the z - x components within the plane, while colors represent the y -component.

given. The initial model requires the use of a relaxation method in order to realize a sufficiently force-balanced equilibrium state. The details of this method are presented herein, along with the specifics of the numerical method, grid and boundary conditions.

We have presented our model results in comparison with an overview of Cluster 2 data for an event on February 14, 2003. The general features modeled by the simulation are consistent with the overall view of the cusp represented by the Cluster 2 data for northward IMF. The simulation results are for the case of 10° IMF (strongly northward with a small positive B_y component). This places the null point in the tailward side of the cusp, slightly offset from the noon-midnight meridian in the positive y -direction.

The inner boundary between the magnetospheric lobe and the CDC is a gradual transition identified by increasing plasma density, decreasing magnetic field strength, enhanced (largely field-aligned) flow consistent with lobe reconnection, and increased temperature. The CDC is the region of depressed magnetic field strength, relatively stagnant plasma, and densities comparable to magnetosheath values. The cavity has a maximum depth of $\sim 2 R_E$ along CDC-magnetosheath boundary normal direction, decreasing with distance from the dipolar axis, consistent with the Cluster 2 data. The CDC has a much larger transverse extent of $\sim 5 - 9 R_E$. These dimensions and the shape of a relatively flat, but extended boundary agree well with observations [Nykyri et al., 2011a; Niehof, 2010]. The transition from CDC to magnetosheath is much more abrupt than the inner boundary, and is characterized by an increase in magnetic field strength, decrease in temperature, and increase in plasma flow (largely $-v_x$). Observations show a much stronger gradient at the cavity boundary to the magnetosphere. Currently, it is not clear whether the soft transition in the simulation is caused by the limited resolution (note that the simulation has already a much higher resolution than, for instance, global models) or by physics not contained within our model. The simulation also does not show the large amplitude fluctuations of observed cavities. The nature and cause of these fluctuations is also not clear in the observations and there are indications that several processes contribute such as rapid motion of cavity boundaries, transient events, such as magnetic flux bundles moving along the cavity, or waves within the cavity or at the cavity boundary. Several of these mechanisms can be explored in our model and it is conceivable that such inputs may indeed explain the observed fluctuations.

2.7 Acknowledgements

Support for the research of Eric Adamson and Antonius Otto was provided by NASA grants NNG06GG89Gprog07 and NNX09AI09Gprog2010 to the University of Alaska Fairbanks. K. Nykyri's work is supported by the National Science Foundation grant #0703327.

Bibliography

- Chang, S.-W., Scudder, J. D., Fuselier, S. A., Fennell, J. F., Trattner, K. J., Pickett, J. S., Spence, H. E., Menietti, J. D., Peterson, W. K., Lepping, R. P., and Friedel, R.: Cusp energetic ions: A bow shock source, *Geophys. Res. Lett.*, 25, 3729–3732, 1998.
- Chapman, S. and Ferraro, V. C. A.: A New Theory of Magnetic Storms, 1, The Initial Phase, *J. Geophys. Res.*, 36, 77–97, 1931a.
- Chapman, S. and Ferraro, V. C. A.: A New Theory of Magnetic Storms, 1, The Initial Phase (continued), *J. Geophys. Res.*, 36, 171–186, 1931b.
- Chen, J., Fritz, T. A., Sheldon, R. B., Spence, H. E., Spjeldvik, W. N., Fennell, J. F., and Livi, S.: A new, temporarily confined population in the polar cap during the August 27, 1996 geomagnetic field distortion period, *Geophys. Res. Lett.*, 24, 1447–1450, 1997.
- Chen, J., Fritz, T. A., Sheldon, R. B., Spence, H. E., Spjeldvik, W. N., Fennell, J. F., Livi, S., Russell, C., Pickett, J. S., and Gurnett, D. A.: Cusp energetic particle events: Implications for a major acceleration region of the magnetosphere, *J. Geophys. Res.*, 103, 69–78, 1998.
- Chen, J. S. and Fritz, T. A.: Correlation of cusp MeV helium with turbulent ULF power spectra and its implications, *Geophys. Res. Lett.*, 25, 4113–4116, 1998.
- Erlandson, R. E., Zanetti, L. J., Potemra, T. A., Andre, M., and Matson, L.: Observation of electromagnetic ion cyclotron waves and hot plasma in the polar cusp, *Geophys. Res. Lett.*, 15, 412–424, 1988.
- Fedder, J. A. and Lyon, J.: The Earth's Magnetosphere is 165 RE Long: Self-Consistent Currents, Convection, Magnetospheric Structure, and Processes for Northward Interplanetary Magnetic Field, *J. Geophys. Res.*, 100, 3623–3635, 1995.
- Frank, L. A.: Plasmas in the Earth's polar magnetosphere, *J. Geophys. Res.*, 76, 5202–5219, 1971.
- Fuselier, S. A., Trattner, K. J., and Petrinec, S. M.: Cusp observations of high- and low-latitude reconnection for northward interplanetary magnetic field, *J. Geophys. Res.*, 105, 253–266, 2000.

- Gombosi, T. I., DeZeeuw, D. L., Groth, C. P. T., Powell, K. G., and Song, P.: The Length of the Magnetotail for Northward IMF: Results of a 3D MHD Simulation, *Physics of Space Plasmas*, p. 121, 1998.
- Haerendel, G., Paschmann, G., Sckopke, N., Rosenbauer, H., and Hedgecock, P.: The Frontside Boundary Layer of the Magnetosphere and the Problem of Reconnection, *J. Geophys. Res.*, 83, 3195–3216, 1978.
- Heikkila, W. J. and Winningham, J. D.: Penetration of magnetosheath plasma to low latitudes through the dayside magnetospheric cusps, *J. Geophys. Res.*, 76, 883–891, 1971.
- Hesse, M. and Birn, J.: Three-Dimensional Magnetotail Equilibria by Numerical Relaxation Techniques, *Journal of Geophysical Research*, 98, 3973–3982, 1993.
- Lavraud, B., Dunlop, M. W., Phan, T. D., Rème, H., Bosqued, J.-M., Dandouras, I., Sauvaud, J.-A., Lundin, R., Taylor, M. G. G. T., Cargill, P. J., Mazelle, C., Escoubet, C. P., Carlson, C. W., McFadden, J. P., Parks, G. K., Moebius, E., Kistler, L. M., Bavassano-Cattaneo, M.-B., Korth, A., Klecker, B., and Balogh, A.: Cluster observations of the exterior cusp and its surrounding boundaries under northward IMF, *Geophys. Res. Lett.*, 29, 1995, doi:10.1029/2002GL015464, 2002.
- Lavraud, B., Fedorov, A., Budnik, E., Grigoriev, A., Cargill, P. J., Dunlop, M. W., Rème, H., Dandouras, I., and Balogh, A.: Cluster survey of the high-altitude cusp properties: A three-year statistical study, *Ann. Geophys.*, 22, 3009–3019, 2004a.
- Lavraud, B., Phan, T. D., Dunlop, M. W., Taylor, M. G. G. T., Cargill, P. J., Bosqued, J.-M., Dandouras, I., Rème, H., Sauvaud, J.-A., Escoubet, C. P., Balogh, A., and Fazakerley, A.: The exterior cusp and its boundary with the magnetosheath: Cluster multi-event analysis, *Ann. Geophys.*, 22, 3039–3054, 2004b.
- Lavraud, B., Fedorov, A., Budnik, E., Thomsen, M. F., Grigoriev, A., Cargill, P. J., Dunlop, M. W., Rème, H., Dandouras, I., and Balogh, A.: High altitude cusp flow dependence on IMF orientation: A 3 year Cluster statistical study, *J. Geophys. Res.*, 110, A02 209, doi:10.1029/2004JA010804, 2005.

- Le, G., Blanco-Cano, X., Russell, C., Zhou, X.-W., Mozer, F., Trattner, K. J., Fuselier, S. A., and Anderson, B. J.: Electromagnetic ion cyclotron waves in the high-altitude cusp: Polar observations, *J. Geophys. Res.*, 106, 19,067–19,079, 2001.
- Lockwood, M. and Smith, M.: The Variation of Reconnection Rate at the Dayside Magnetopause and Cusp Ion Precipitation, *J. Geophys. Res.*, 97, 14841–14847, 1992.
- Newell, P., Meng, C.-I., Sibeck, D., and Lepping, R.: Some Low-Altitude Dependencies on the Interplanetary Magnetic Field, *J. Geophys. Res.*, 94, 8921–8927, 1989.
- Niehof, J.: Diamagnetic Cavities and Energetic Particles in the Earth's Magnetospheric Cusps, Ph.D. thesis, Boston University, 2010.
- Nykyri, K., Cargill, P. J., Lucek, E., Horbury, T., Lavraud, B., Balogh, A., Dunlop, M. W., Bogdanova, Y., Fazakerley, A., Dandouras, I., and Rème, H.: Cluster observations of magnetic field fluctuations in the high-altitude cusp, *Ann. Geophys.*, 22, 2413–2429, 2004.
- Nykyri, K., Grison, B., Cargill, P. J., Lavraud, B., Lucek, E., Dandouras, I., Balogh, A., Cornilleau-Wehrin, N., and Rème, H.: Origin of the turbulent spectra in the high-altitude cusp: Cluster spacecraft observations, *Ann. Geophys.*, 24, 1057–1075, 2006.
- Nykyri, K., Otto, A., Adamson, E., Dougal, E., and Mumme, J.: Cluster observations of a cusp diamagnetic cavity: Structure, size and dynamics, *J. Geophys. Res.*, 116, A03228, doi:10.1029/2010JA015897, 2011a.
- Nykyri, K., Otto, A., Adamson, E., and Tjulin, A.: On the Origin of Fluctuations in the Cusp Diamagnetic Cavity, *J. Geophys. Res.*, 116, 6208, doi:10.1029/2010JA015888, 2011b.
- Nykyri, K., Otto, A., Adamson, E., Kronberg, E., and Daly, P.: Cluster Observations of High-Energy Particle Properties in Cusp Diamagnetic Cavity, *J. Geophys. Res.*, submitted 2010.
- Ogino, T.: A Three Dimensional MHD Simulation of the Interaction of the Solar Wind with the Earth's Magnetosphere: The Generation of Field Aligned Currents, *J. Geophys. Res.*, 91, 6791–6806, 1986.

- Onsager, T., Scudder, J., Lockwood, M., and Russell, C.: Reconnection at the high latitude magnetopause during northward interplanetary magnetic field conditions, *J. Geophys. Res.*, 106, 25 467–25 488, doi:10.1029/2000JA000444, 2001.
- Otto, A.: Resistive MHD Computations of Magnetospheric Physics, *Computer Physics Communications*, pp. 185–195, 1990.
- Otto, A.: Geospace Environment Modeling (GEM) magnetic reconnection challenge: MHD and Hall MHD -constant and current dependent resistivity models, *J. Geophys. Res.*, 106, 3751–3757, 1999.
- Panov, E. V., Buchner, J., Franz, M., Korth, A., Savin, S. P., Reme, H., and Fornacon, K.-H.: High-latitude Earth's magnetopause outside the cusp: Cluster observations, *J. Geophys. Res.*, 113, doi:10.1029/2006JA012123, 2008.
- Paschmann, G., Haerendel, G., Sckopke, N., Rosenbauer, H., and Hedgecock, P.: Plasma and Magnetic Field Characteristics of the Distant Polar Cusp near Local Noon: The Entry Layer, *J. Geophys. Res.*, 81, 2883–2899, 1976.
- Raeder, J., Walker, R. J., and Ashour-Abdalla, M.: The structure of the distant geomagnetic tail during long periods of northward IMF, *Geophys. Res. Lett.*, 22, 349–352, 1995.
- Savin, S. P., Romanov, S. A., Fedorov, A., Zelenyi, L., Klimov, S. I., Yermoleav, Y. I., Budnik, E. Y., Nikoleava, N. S., Russell, C., Zhou, X.-W., Urquhart, A. L., and Reiff, P. H.: The cusp/magnetosheath interface on May 29, 1996: Interball-1 and Polar observations, *Geophys. Res. Lett.*, 25, 2963–2966, 1998.
- Savin, S. P., Zelenyi, L., Maynard, N. C., Sandahl, I., Kawano, H., Russell, C., Romanov, S., Blecki, J., et al.: Multi-spacecraft tracing of turbulent boundary layers, *Adv. Space Res.*, 30, 2821–2830, 2002.
- Savin, S. P., Zelenyi, L., Romanov, S. A., Sandahl, I., Pickett, J., Amata, E., Avanov, L., Blecki, J., et al.: Magnetosheath-cusp interface, *Ann. Geophys.*, 22, 183–212, 2004.
- Schindler, K. and Otto, A.: Resistive Instability, *Geophysical Monograph*, pp. 51–61, 1989.

- Siscoe, G. L., Crooker, N., Siebert, K. D., Maynard, N. C., Weimer, D. R., and White, W. W.: Cusp geometry in MHD simulations, *Surveys in Geophysics*, 26, 387–407, doi:10.1007/s10712-005-1902-4, 2005.
- Tanaka, T.: Generation Mechanism for Magnetosphere-ionosphere Current Systems Deduced from a Three-dimensional MHD Simulation of the Solar-wind-magnetosphere-ionosphere Coupling Processes, *Journal of Geophysical Research*, 100, 12 057–12 074, 1995.
- Trattner, K. J., Fuselier, S. A., and Petrinec, S. M.: Location of the reconnection line for northward interplanetary magnetic field, *J. Geophys. Res.*, 109, A03 219, doi:10.1029/2003JA009975, 2004.
- White, W. W., Siscoe, G. L., Erickson, G. M., Kaymaz, Z., Maynard, N. C., Siebert, K. D., Sonnerup, B. U. O., and Weimer, D. R.: The Magnetospheric Sash and the Cross-tail S, *Geophysical Research Letters*, 25, 1605–1608, doi:10.1029/98GL50865, 1998.
- Yamauchi, M., Nilsson, H., Eliasson, L., Norberg, O., Boehm, M., Clemmons, J. H., Leping, R. P., Blomberg, L., Ohtani, S.-I., Yamamoto, T., Mukai, T., Terasawa, T., and Kokubun, S.: Dynamic response of the cusp morphology to the solar wind: A case study during passage of the solar wind plasma cloud on February 21, 1994, *J. Geophys. Res.*, 101, 24 675–24 687, doi:10.1029/96JA01873, 1996.
- Zhang, H., Dunlop, M. W., Zong, Q.-G., Fritz, T. A., Balogh, A., and Wang, Y.: Geometry of the High-latitude Magnetopause as Observed by Cluster, *J. Geophys. Res.*, 112, A02 204, doi:10.1029/2006JA011774, 2007.

Chapter 3

3D Mesoscale MHD Simulations of Magnetospheric Cusp-like Configurations: Cusp Diamagnetic Cavities and Boundary Structure¹

3.1 Abstract

We present results from mesoscale simulations of the magnetospheric cusp region for both strongly northward and strongly southward interplanetary magnetic field (IMF). Simulation results indicate an extended region of depressed magnetic field and strongly enhanced plasma β which exhibits a strong dependence on IMF orientation. These structures correspond to the Cusp Diamagnetic Cavities (CDC's). The typical features of these CDC's are generally well reproduced by the simulation. The inner boundaries between the CDC and the magnetosphere are gradual transitions which form a clear funnel shape, regardless of IMF orientation. The outer CDC/magnetosheath boundary exhibits a clear indentation in both the x - z and y - z planes for southward IMF, while it is only indented in the x - z plane for northward, with a convex geometry in the y - z plane. The outer boundary represents an Alfvénic transition, mostly consistent with a slow-shock, indicating that reconnection plays an important role in structuring the high-altitude cusp region.

3.2 Introduction

The interaction between the solar wind and the Earth's magnetosphere is characterized by processes which occur at the magnetopause boundary. The magnetospheric cusps play a pivotal role in understanding these processes, as the entire magnetopause maps through these key regions. Extensive research has focused on the low and mid altitude cusp [Newell et al., 1989; Lockwood and Smith, 1992; Yamauchi et al., 1996], but more recently research efforts have increased focus on the high-altitude cusp region. It is important to note that differing definitions of the high altitude cusp regions have lead to confusion in the past. For example, Trattner et al. [2006] identify the high altitude cusp by the presence of inflowing plasma resulting from reconnection as indicated by the time-of-flight effect or velocity filter effect [Rosenbauer et al., 1975; Onsager et al., 1993], while Peterson and Trattner [2011] identify the region by the presence of a mixture of boundary layer and newly reconnected

¹Adamson, E., Otto, A., Nykyri, K., *Ann. Geophys.*, 30, 325-341, doi:10.5194/angeo-30-325-2012, 2012.

solar wind plasma similar to the criteria used by Newell et al. [2004]. We focus our identification of the exterior cusp on the typical low magnetic field region or Cusp Diamagnetic Cavity (CDC) similar to Chen et al. [1998]; Fritz et al. [2003]; Niehof et al. [2008]; Lavraud et al. [2002]; Nykyri et al. [2011a]. These CDC's are characterized by magnetosheath-like plasma density, enhanced thermal pressure and low, fluctuating magnetic field. As a result of the relatively low magnetic field magnitude within these CDC's, they are highly dynamic regions. Both the location and structure of the high-altitude cusp are known to exhibit a strong dependence on the Interplanetary Magnetic Field (IMF) [Newell et al., 1989; Woch and Lundin, 1992; Newell and Meng, 1994; Yamauchi and Lundin, 1994; Yamauchi et al., 1996; Savin et al., 1998; Fedorov et al., 2000; Dubinin et al., 2002].

The exterior cusp has been shown to have three boundaries [Lavraud et al., 2004a; Paschmann et al., 1976; Haerendel et al., 1978; Onsager et al., 2001]: the day-side plasma sheet on the sunward side, the tail-lobe or mantle on the night-side, and the magnetosheath in the exterior. Though it has been suggested that the outer boundary may represent an intermediate or slow transition [Lavraud et al., 2002] the exact nature of these boundaries is not well understood [Walters, 1966; Scarf et al., 1974; Hansen et al., 1976; Yamauchi and Lundin, 1997; Savin et al., 1998]. It appears that the inner boundaries of the high-altitude cusp form a funnel shape and thus represent an indented surface which has been labelled as the magnetopause by some [Paschmann et al., 1976; Haerendel et al., 1978; Russell, 2000]. However, it is not clear whether the same is true of the outer boundary between the cusp and magnetosheath. This question regarding the shape of the magnetopause in the vicinity of the cusp has persisted for some time. While some results show clear evidence of an indented surface [Zhang et al., 2007; Dunlop et al., 2005; Eastman et al., 2000], others do not [Zhou and Russell, 1997; Lavraud et al., 2004a]. This debate is further complicated by the ambiguity of the definition of the magnetopause in the vicinity of the cusp, which may explain some of the disagreement.

In this paper, results are presented from a mesoscale cusp-like magnetic field model [Adamson et al., 2011]. The Earth's dipole tilt is neglected in the model. This simplification of the system is partially a consequence of the desired size of the simulation domain which enables a high resolution in comparison to global models, but also matter of convenience. We note that this simplification provides a convenient foundation for future work addressing

the effects of variations to the model such as the inclusion of the dipole tilt. As a result of the neglect of the dipole tilt the system has a tendency to localize the reconnection site somewhat closer to the cusp than is the case in the physical magnetosphere. Though the exact location of the reconnection site is not accurately represented in regards to the overall global structure of the Earth's magnetosphere, it is not the goal of this study to address plasma transport between the cusp and the magnetosphere on such a global scale, but rather to investigate the magnetospheric structures local to the cusp region. The physical processes responsible for the formation of the various boundary structures under investigation herein are the result of the local interaction of the shocked solar wind with the cusp region magnetosphere. Thus, it is expected that results do not exhibit any significant dependence on the geomagnetic dipole tilt other than possibly in regards to the geometry of the high latitude magnetopause.

Thus, particularly for southward IMF, the reconnection site is localized to high latitudes. Results focus on the high altitude cusp region for both strongly northward and strongly southward IMF orientations. A detailed comparison of the resulting cusp regions is presented. The boundaries of the CDC are discussed in detail and variance analysis methods [Sonnerup and Cahill, 1967] applied in order to address the nature of the boundaries. We utilize these methods to determine the boundary normals based on both the minimum variance of the magnetic field (MVAB) and on the maximum variance of the electric field (MVAE). We note that it is possible, due to the coplanarity of the magnetic field across a shock, that MVAB may determine the wrong normal eigenvector. For this reason, we give preference to the normal eigenvector resulting from MVAE.

The model and numerical method are reviewed in Section 3.3. Section 3.4 focuses on simulation results, separated by northward and southward IMF, followed by discussion in Section 3.5.

3.3 Numerical Procedure

3.3.1 Numerical Method

The presented simulation results employ the full set of MHD equations in the following form:

$$\begin{aligned}\frac{\partial \rho}{\partial t} &= -\nabla \cdot (\rho \mathbf{u}), \\ \frac{\partial(\rho \mathbf{u})}{\partial t} &= -\nabla \cdot \left[\rho \mathbf{u} \mathbf{u} + \frac{1}{2} (p + B^2) \mathbf{I} - B \mathbf{B} \right],\end{aligned}\quad (3.1)$$

$$\begin{aligned}\frac{\partial h}{\partial t} &= -\nabla \cdot (h \mathbf{u}) - \frac{\gamma - 1}{\gamma} h^{1-\gamma} \eta j^2, \\ \frac{\partial \mathbf{B}}{\partial t} &= -\nabla \times (\mathbf{u} \times \mathbf{B} - \eta \mathbf{j}), \\ \mathbf{j} &= \nabla \times \mathbf{B},\end{aligned}\quad (3.2)$$

where $h = (p/2)^{1/\gamma}$ and ρ , p , η , \mathbf{u} , and \mathbf{B} represent density, pressure, resistivity, velocity, and magnetic field. The ratio of specific heats (γ) is taken to be 5/3. The resistivity (η) is held constant and is defined according to:

$$\eta = \eta_o \left[\eta_1 + \frac{1}{2 \cosh((z_{min} - z)/2)} + \frac{1 - \tanh(z + .5)}{2 \cosh((x^2 + y^2)/2)} \right], \quad (3.3)$$

where $\eta_o = 0.015$ and $\eta_1 = 0.13$ in normalized simulation units. The first term defines a uniform background resistivity, while the second term prescribes a resistivity which falls off with increasing z , and the third term generates a column of resistivity aligned with the converging dipolar field in the center of the lower half of the simulation domain. As defined by this distribution, the resistivity ranges from a maximum value of 0.0245 at the center of the lower z -plane, to a minimum of 0.002 throughout the upper portion of the simulation domain towards the maximum z -boundary. This resistivity distribution improves code stability in the region of converging dipolar field while maintaining a relatively low resistivity (~ 0.002) near the x-line. All variables are normalized to typical system values, and thus dimensionless. Length scale, density, and magnetic field strength are normalized to typical system values ($L_0 = 1 R_E$, $\rho_0 = 2.0 \text{ cm}^{-3}$, and $B_0 = 40 \text{ nT}$). The pressure, velocity and time scale are then measured in units of normalized pressure $p_0 = B_0^2/8\pi = 0.64 \text{ nPa}$, Alfvén speed $u_A = B_0/\sqrt{4\pi\rho_0} = 616 \text{ km/s}$, and Alfvén time $\tau_A = L_0/u_A = 10 \text{ s}$, respectively.

The simulations use a Leapfrog/DuFort-Frankel finite difference scheme which is second order accurate, easy to implement, and has low numerical dissipation (the leading term in

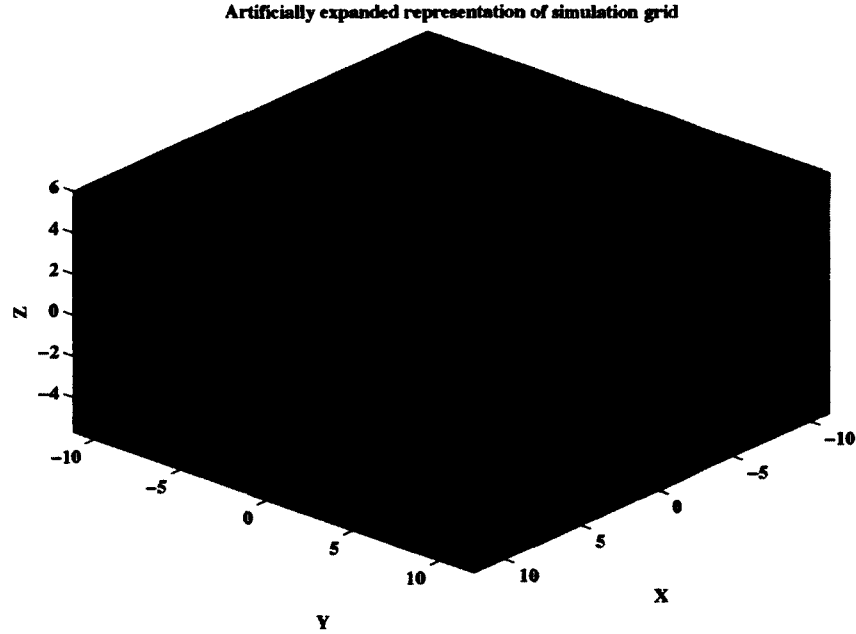


Figure 3.1. Illustration of the numerical grid. Note that only every fourth grid point is plotted in order to improve visual clarity.

the truncation error of the DuFort-Frankel scheme varies as Δx^2 , Δt^2 , but is also dependent on the diffusion coefficient η , ensuring that the physical resistivity η remains orders of magnitude larger than the numerical diffusion). The nonuniform grid has the best resolution in x and y -directions (Δx , $\Delta y = 0.08R_E$) in the center of the simulation domain, and the lowest (Δx , $\Delta y = 0.381R_E$) at the edges. The resolution in the z -direction is more uniform, with a maximum resolution of $\Delta z = 0.05R_E$ in the center and minimum resolution of $\Delta z = 0.163R_E$ at the boundaries. The grid is chosen to be more uniform in the z -direction in order to resolve not only the strong gradients toward the bottom of the domain where the field lines converge, but also the gradients within the magnetopause current sheet. The simulations presented herein are comprised of $153 \times 153 \times 153$ grid points in x , y , and z , respectively. Higher resolution ($253 \times 253 \times 203$ grid points) simulations were also undertaken in order to investigate the effect of larger density anisotropy between the magnetosphere and magnetosheath, the results of which are addressed in the next section.

The local model of the magnetospheric cusp region is constructed by placing a dipole at $-10R_E$ along the z -axis with the dipole axis anti-parallel to z (no dipole tilt). The

coordinates are such that the x -axis is directed toward the sun and the y -axis completes the right-handed system. The simulation domain ranges from $-12 R_E$ to $12 R_E$ in both the x and y directions and the z coordinate from $-6 R_E$ to $6 R_E$, such that the dipole is $4 R_E$ below the lower z -boundary. The dipolar magnetic field is effectively turned off in the upper region of the simulation domain ($z > 0$), thus defining the magnetosheath region. This is accomplished through the inclusion of a shielding current. A constant “draped” (no z -component) IMF may then be superposed in the magnetosheath region. The x -component of this “fully-draped” model IMF then represents the combined x - and z - components of the physical IMF. Finally, the density and pressure are prescribed as functions of the magnetic field-line equation. A ballistic relaxation is then applied in order to produce a near-equilibrium configuration. For further details on the model and relaxation method see Adamson et al. [2011].

Neumann boundary conditions are imposed, such that $\partial f / \partial x_n = 0$. The normal components of the magnetic field at the boundaries are calculated such that $\nabla \cdot \mathbf{B} = 0$ (excluding the lower z -boundary where \mathbf{B} is held fixed), while a simple extrapolation method is applied to the transverse components.

3.4 Results

Simulation results are presented, herein, for the cases of strongly northward and strongly southward IMF. Simulations are initialized with a uniform magnetosheath flow of local Alfvén Mach number (M_A) between .4 and 1 (specific values corresponding to the individual runs are indicated in the proceeding sections). The flow is prescribed as a slab corresponding to the region of draped IMF (magnetosheath).

We define the cusp to be the “funnel”-shaped region of the magnetosphere aligned with the magnetic dipole axis and exhibiting enhanced plasma density and thermal pressure. The CDC’s then, as features embedded within the cusp region must similarly satisfy the same criteria. In addition to these requirements, the CDC’s typically exhibit further increased (relative to the cusp proper) and varying densities as well as significantly reduced magnetic field strength. Typical features of CDC’s as identified from spacecraft observations may be summarized as follows:

1. Densities comparable to magnetosheath values (typically a factor of ten greater than

adjacent magnetospheric values)

2. Significantly depressed magnetic field
3. Pervasive magnetic field fluctuations
4. Relatively stagnant plasma (for northward IMF)
5. Gradual inner boundaries with magnetosphere exhibiting clear field-aligned plasma flows emanating from reconnection site
6. Often more abrupt outer boundary with magnetosheath

3.4.1 CDC dependence on IMF orientation

The orientation of the IMF is widely known to exert control over the location and dynamics of the polar cusp [Carbary and Meng, 1986; Escoubet and Bosqued, 1989; Woch and Lundin, 1992; Newell and Meng, 1994; Sandholt et al., 1994; Zhou et al., 2000; Bosqued et al., 2005; Pitout et al., 2006a,b; Escoubet et al., 2008]. This effect of IMF orientation on cusp location is clearly seen in the simulation results plotted in Figure 3.2. The figure shows isosurfaces encompassing the region of plasma $\beta > 30$ for three IMF orientations: 10° northward (green), 90° purely $+B(IMF)_y$ (magenta), and 170° southward (yellow). Plasma β is defined as the ratio of plasma thermal to magnetic pressure ($2\mu_0 P/B^2$) and is thus a useful parameter to employ in the identification of cusp diamagnetic cavities due to the characteristic enhanced plasma pressure and strongly depressed magnetic field strength within. These results indicate that the location of the CDC is strongly tied to the IMF orientation. The CDC's form due to the magnetic connection between the high-altitude geomagnetic field and the magnetosheath field. Where these fields are anti-parallel, a null-point is formed, embedded within a more extensive region of strong magnetic shear consistent with the expansive reconnection lines reported by Onsager et al. [2001]. Such a configuration enabling simultaneous anti-parallel and component reconnection has also been reported by Trattner et al. [2004]. This magnetic shear defines a current sheet bounding the geomagnetic field and enabling reconnection to transport plasma from the magnetosheath into the low field region of the magnetosphere. This accumulation of plasma resulting from the outflow from the reconnection site towards the converging dipolar geomagnetic field

generates the diamagnetic cavity. Thus, the cavity develops, offset from the dipolar axis in the direction of the IMF in agreement, for example, with the recent results of Nykyri et al. [2011a], who report results from a cluster event in which the position of the CDC moves in accordance with a rotation of the IMF. This behavior is evidenced in the model results as shown in Figure 3.2. For northward IMF, the cavity is located on the tailward edge of the converging geomagnetic field. The CDC then rotates clockwise with the IMF, generating CDC's on the dawn side for 90° IMF (shown here only for illustrative completeness), and on the dayside for southward IMF.

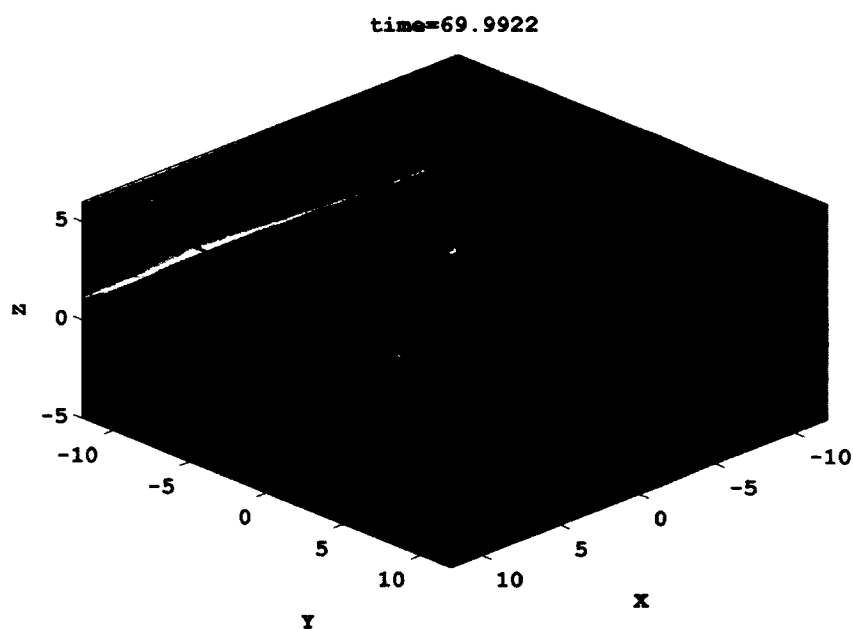


Figure 3.2. Cusp diamagnetic cavity position indicated by plasma β enhancement in cusp for strongly northward (green), purely $+B_{yIMF}$ (magenta), and strongly southward IMF (yellow).

Not only does the IMF orientation play a crucial role in determining the location of the CDC, but it also effects the overall structure of the CDC. This is not so much a direct result of adjacent magnetic field orientations across the magnetospheric boundary, but rather due to the direction of the streaming magnetosheath plasma relative to the convective motion of the newly reconnected magnetic flux. Figure 3.3 illustrates the differences in geometry between the cases of strongly northward and strongly southward IMF. For a

strongly southward IMF orientation, the reconnected flux tubes on the cusp-side of the x-line convect largely tailward, nearly parallel to the magnetosheath flow. Such is not the case for a strongly northward IMF. In this orientation, the reconnected flux tubes on the cusp-side of the x-line convect in the opposite direction of the streaming magnetosheath plasma. The result is a significantly larger CDC under Northward IMF conditions. Zhou et al. [2000] found a similar narrowing of the cusp under southward IMF conditions in agreement with Newell and Meng [1987], as well as a widening under northward IMF. The nature and geometry of this boundary is discussed in detail in the following sections.

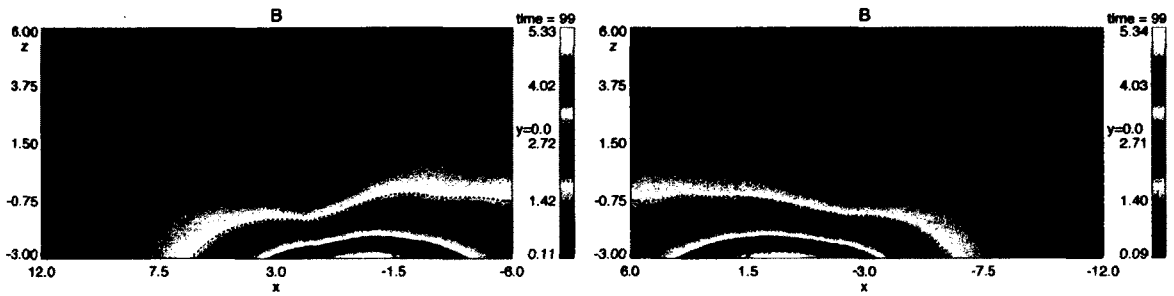


Figure 3.3. Total magnetic field strength indicating diamagnetic regions plotted near the noon-midnight meridian plane for the cases of strongly southward IMF (left) and strongly northward IMF (right).

3.4.2 Northward IMF

In this section we present simulation results for a strongly northward IMF orientation with a small positive B_y -component as defined by an IMF clock angle of 10° (IMF clock angle describes the deviation from the z -axis of the projection of the IMF into the x - z plane in a clockwise sense). This IMF orientation is chosen to include a small B_y -component simply to avoid the singular case of precisely Northward IMF which is highly unlikely in the physical system due to the dynamic nature of the interplanetary magnetic field. Plasma flow is initialized in the magnetosheath with $M_A \sim 0.5$. Resistivity is prescribed according to Equation 3.3. We begin with an overview of the cusp region with emphasis on the CDC and its boundaries. We then discuss the boundaries in more detail.

3.4.2.1 Cusp Overview

For northward IMF with clock angle of 10° , the null point is located on the tailward side of the converging dipolar field, offset slightly in the positive y -direction due to the positive y -component of the IMF. Figure 3.4 shows cuts of various plasma parameters in the noon-midnight meridian plane. The density (top left) and pressure (middle left) are enhanced (relative to the adjacent magnetosphere) within the cusp funnel. The density also shows significant variability (up to $\sim 50\%$ of typical CDC values) within the CDC. The enhanced current density (top right) indicating strong magnetic shear lies in the vicinity of the null-point, towards the minimum x -boundary in the plots. The plasma velocity (bottom) exhibits a clear field-aligned flow emanating from this region of enhanced current. The region of enhanced flow in the y -direction near the maximum x -boundary in the figure is due to the reconnected magnetospheric field convecting under the specific IMF conditions. A region of high plasma β (middle right) is clearly visible extending cuspward from the current sheet. The location and extent of this high β region agree well with that of the depleted magnetic field shown in Figure 3.3. These quantities both give reasonable indications of the CDC. The CDC is tilted anti-sunward (note the neglect of dipole tilt in the model) and is larger than for the southward case (discussed below).

Simulated “data” for a trajectory along z at $(x, y) = (-3.1, 0)$ in Figure 3.4 through the high-altitude cusp region is shown in Figure 3.5. The plot represents a traversal of the cusp region on the tailward edge of the cusp funnel. The transition from the strong dipolar field geometry accompanied by low density and plasma flow around $x = -.2 R_E$, to a lower magnetic field strength and higher density with enhanced flow, indicates the inner boundary between the magnetosphere and CDC. The CDC region is easily identified through the characteristically large plasma β . The highlighted area in the figure represents the region within which the normalized plasma $\beta > 5$ (there is no significance in the value of β chosen here, the intention is simply to give an indication of the approximate location of the CDC). The CDC is a region of enhanced density and temperature relative to magnetospheric values. Within the CDC is a region of relatively low plasma flow with increasing convection and enhanced density towards the exterior of the CDC. The outer boundary between the CDC and magnetosheath is quite abrupt in comparison to the inner boundary. This is clearly evident as the flow rotates to align with the orientation of the streaming magnetosheath

plasma concurrent with the magnetic field attaining IMF orientation.

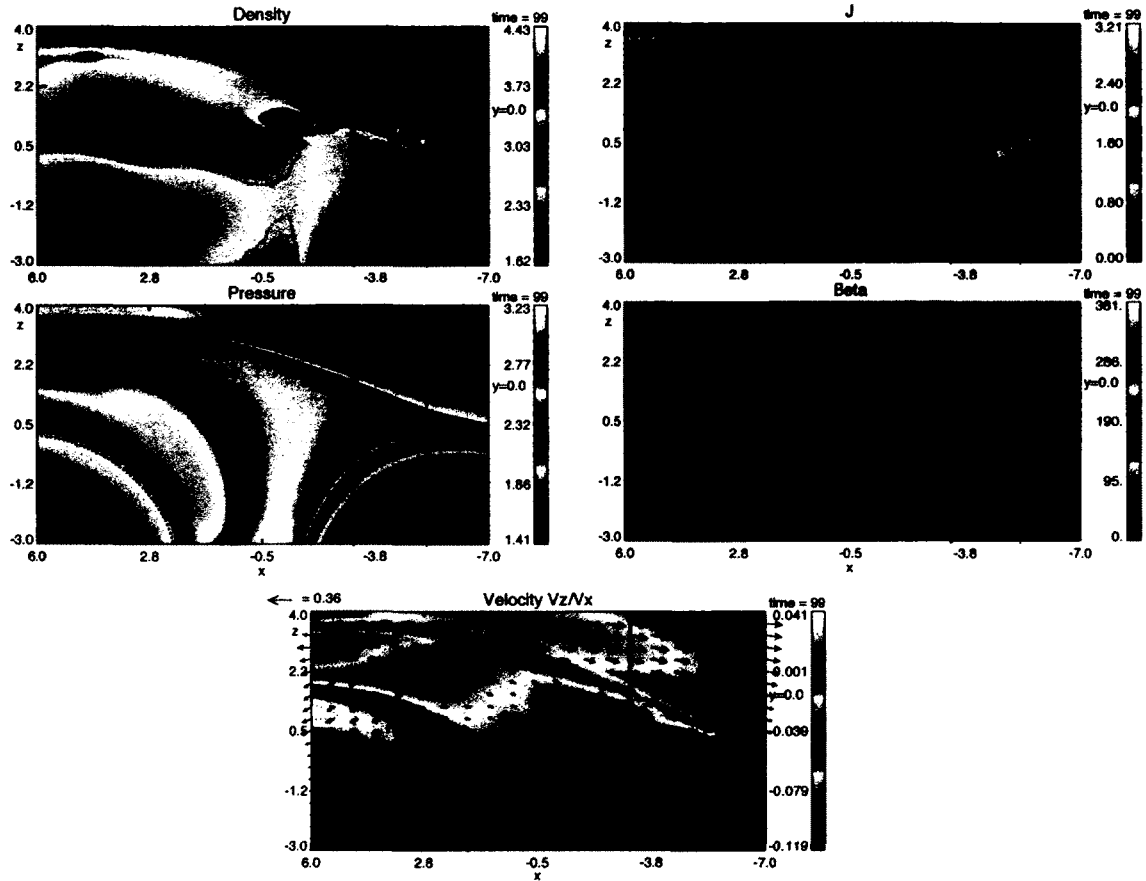


Figure 3.4. From top to bottom, the plots on the left display plasma density, thermal pressure, and plasma velocity, while those on the right display current density (J) and plasma β . All parameters are shown in the noon-midnight meridian plane. The black and red vertical lines indicate the trajectories along which simulated data is analyzed in Section 3.4.2.1 and 3.4.2.4, respectively.

Three boundaries are identified surrounding the CDC under northward IMF conditions: 1) the dayside plasma sheet/CDC boundary on the sunward side of the cusp, 2) the lobe/CDC boundary on the tailward side of the cusp, and 3) the CDC/magnetosheath boundary in the exterior. The following sections focus on the analysis of these boundaries.

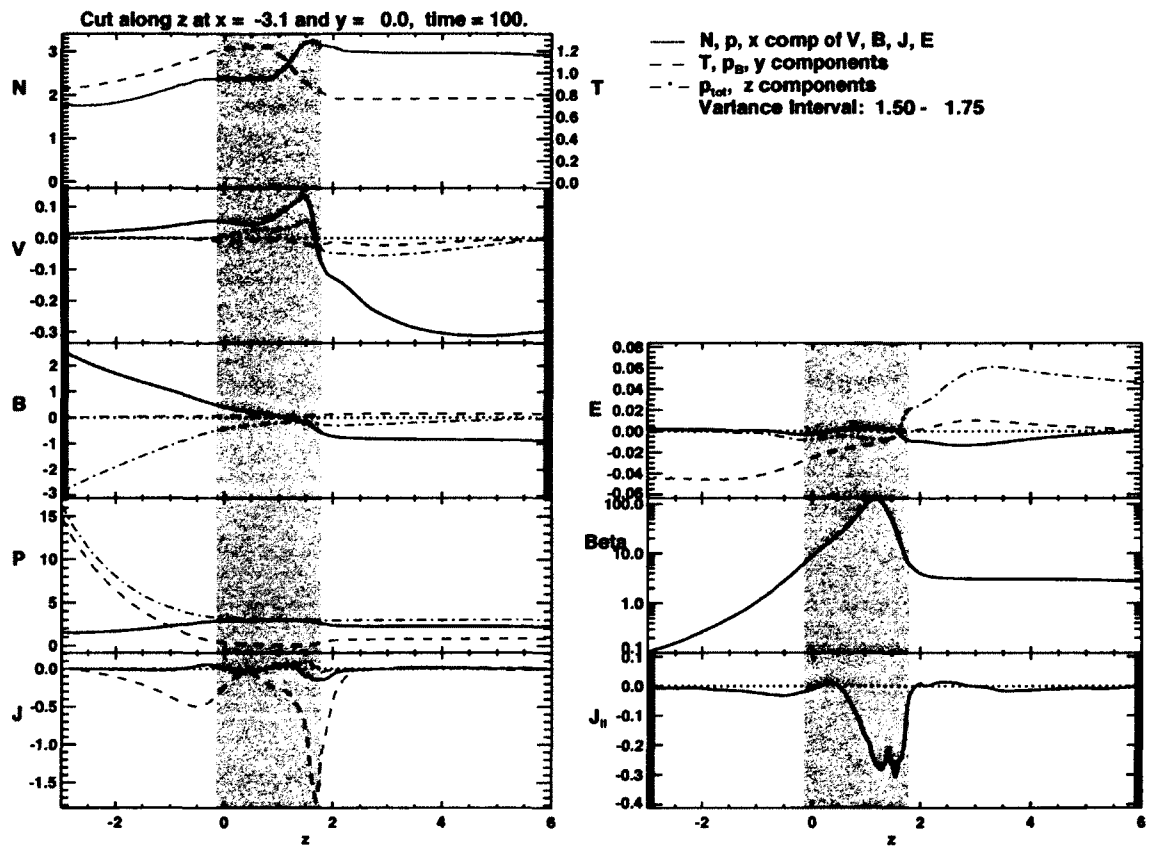


Figure 3.5. Simulated data for a cut along z at $(x, y) = (-3.1, 0)$. All quantities are plotted in normalized simulation units. Plotted in the left column from top to bottom are the density (solid blue line) and temperature (dashed red line), velocity components (x - solid black, y - dashed blue, z - dash-dot red), magnetic field components, pressure (thermal pressure - black, magnetic pressure - blue, total pressure - red), and current density components. The right column displays (from top to bottom) the electric field components, plasma β , and the parallel current density. The shading indicates regions of plasma $\beta > 6$.

3.4.2.2 Dayside Plasma Sheet/CDC Boundary

The inner dayside plasma sheet/CDC boundary is identified by a very gradual decrease in temperature and increase in density occurring over a span of roughly $2 R_E$. We were unable to find any intervals for this boundary which satisfied the Walén relation. This is not surprising, as it is not expected that this inner boundary represent an Alfvénic transition under northward IMF conditions. We were able to find good deHoffman-Teller frames for the inner transition with a typical velocity of $V_{HT} = (.02, -.01, -.02)$, indicating that the feature is steady-state. The sense and magnitude of convection is consistent with the expectations for flux convecting from a high-latitude reconnection site after having reached the inner boundary with the dayside plasma sheet.

3.4.2.3 Lobe/CDC Boundary

The inner boundary between the lobe and CDC is a similarly gradual transition, marked largely by increasing density and plasma flow when traversing from the magnetospheric side. The transition is less gradual than the inner boundary on the dayside, spanning a distance of roughly $1 R_E$. All traversals of the boundary yielded good deHoffman-Teller frames with typical velocities of $V_{HT} = (.2, .05, .2)$, indicating a convection away from the Earth and sunward, consistent with the expected convection for lobe reconnection. The boundary shows no indication of being Alfvénic in nature, as the Walén relation consistently yielded a slope of approximately $-.3$.

3.4.2.4 CDC/Magnetosheath Boundary

On exiting the CDC, the outer boundary with the magnetosheath is identified by the rotation of the magnetic field and plasma flow to magnetosheath values. This boundary is markedly more distinct than the inner boundaries. The boundary was analyzed at various locations yielding consistent deHoffman-Teller velocities and slopes of the Walén relation between $.8$ and 1.2 . The deHoffman-Teller and Walén analyses are shown in Figure 3.6 for a representative traversal at $(x, y) = (-5, 0)$.

A good deHoffman-Teller frame is found with a velocity $V_{HT} = (.09, -.07, .04)$. The slope of the Walén relation yields a value of 0.995 with corresponding correlation coefficient

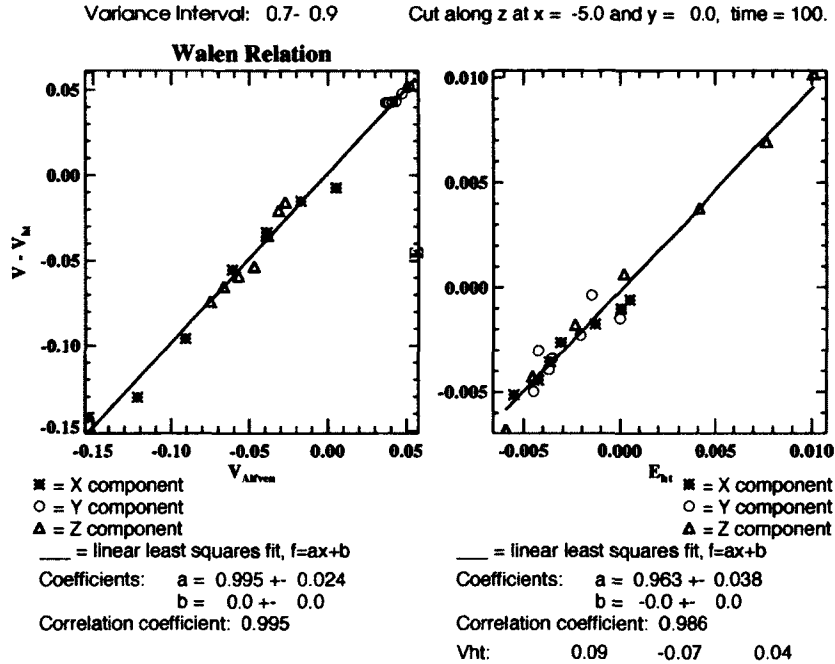


Figure 3.6. Walén relation (left) and deHoffman-Teller test (right) results for the CDC/magnetosheath boundary for the interval $z = [0.7 - 0.9]$ at $(x, y) = (-5, 0)$.

of 0.995, indicating that the boundary represents an Alfvénic transition resulting from lobe reconnection. MVA results are shown in Figure 3.7. MVAE gives a max/int eigenvalue ratio of 53.06 with a normal eigenvector $i_E = (-.33, .21, .92)$, while MVAB results in an int/min eigenvalue ratio of only 7.27. We therefore use the boundary normal coordinates determined through MVAE in the analysis of the discontinuity. The plasma data transformed in to MVAE coordinates are shown in Figure 3.8. The interval which was analyzed is $\Delta z = 0.7 - 0.9$.

The normal components of the magnetic field and velocity are negative. This indicates that the boundary is open and plasma is being transported from the magnetosheath into the CDC. Additionally, the density and pressure increase, while the tangential magnetic field decreases. This transition then is mostly consistent with a slow shock. Note that the magnetic field is nearly completely turned off across the transition as would be the case for a switch-off slow shock, and thus the agreement with the Walén relation.

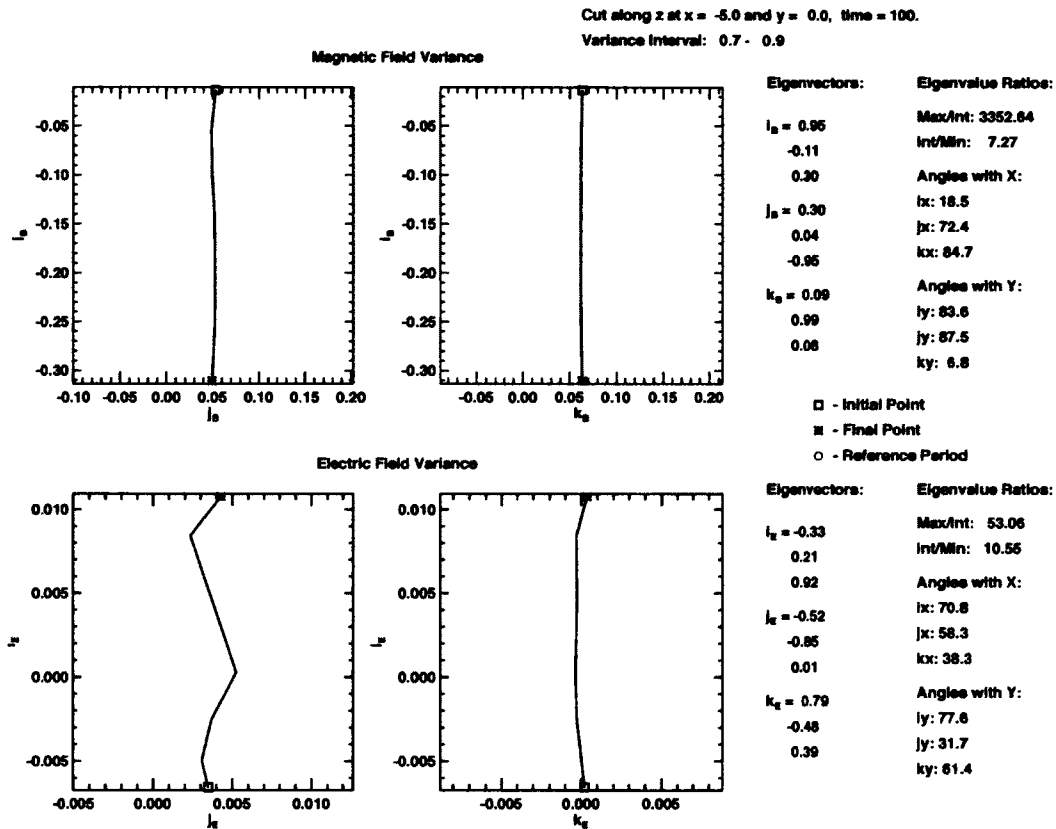


Figure 3.7. Results of the boundary normal calculation for the traversal of the CDC/magnetosheath boundary at $(x, y) = (-5, 0)$ under northward IMF conditions.

Normals resulting from MVA for the outer boundary were mostly oriented in the z -direction. The angle between normals computed for traversals of the outer boundary in the noon-midnight meridian plane at $x = -8 R_E$ and $-3 R_E$ is 17° , indicating that the outer boundary is indented in the x - z plane. Similar comparison for boundary normals along $x = -3 R_E$ at $y = 0 R_E$ and $3 R_E$ reveals that the boundary is convex between the two normals with an opening angle of 25° . A more detailed illustration of the geometry of this outer boundary is shown in Figure 3.9. The CDC bulges outward toward the magnetosheath in the y - z plane (left), while tilted tailward and indented in the x - z plane (right).

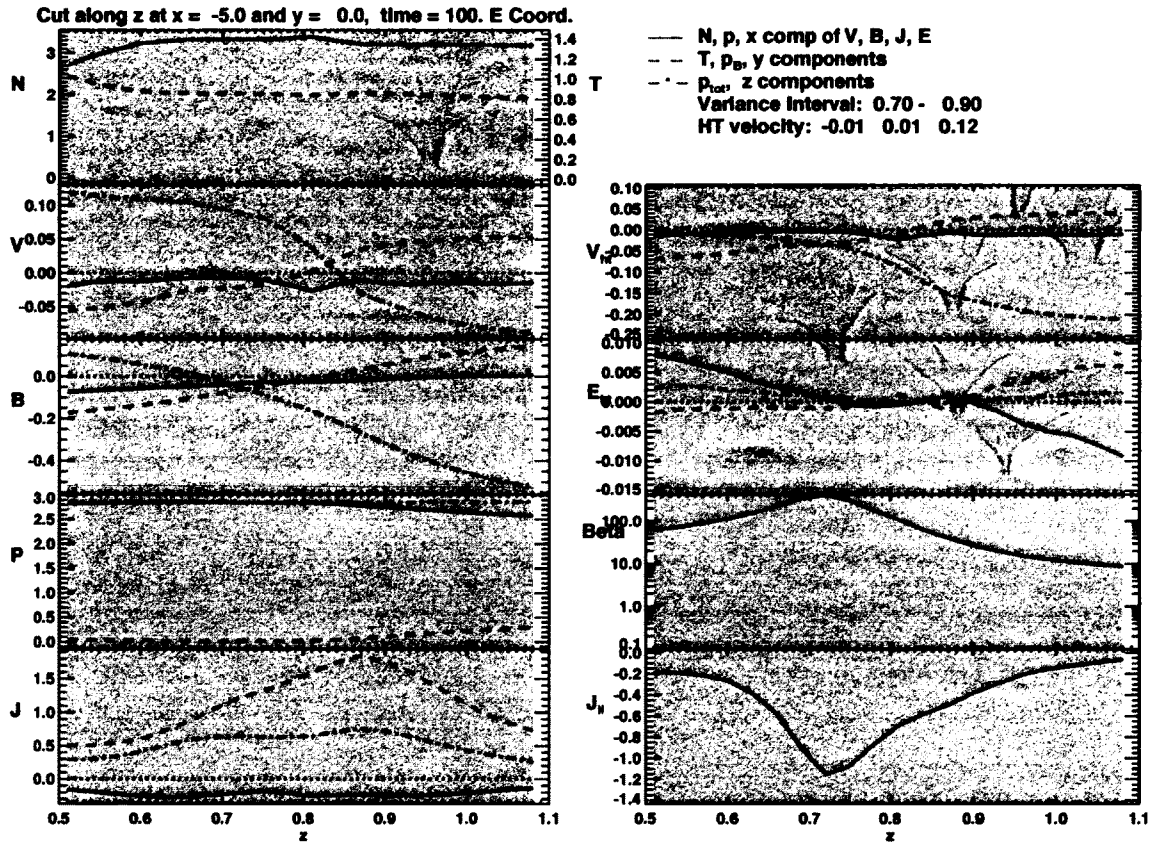


Figure 3.8. Simulated “data” for a cut along z at $(x, y) = (3, 0)$ transformed into MVAE boundary normal coordinates for outer CDC/magnetosheath boundary. All quantities are plotted in normalized simulation units. Plotted in the left column from top to bottom are the density (solid blue line) and temperature (dashed red line), velocity components (x - solid black, y - dashed blue, z - dash-dot red), magnetic field components, pressure (thermal pressure - black, magnetic pressure - blue, total pressure - red), and current density components. The right column displays the velocity and electric field components in the deHoffman-Teller frame, plasma β , and the parallel current density.

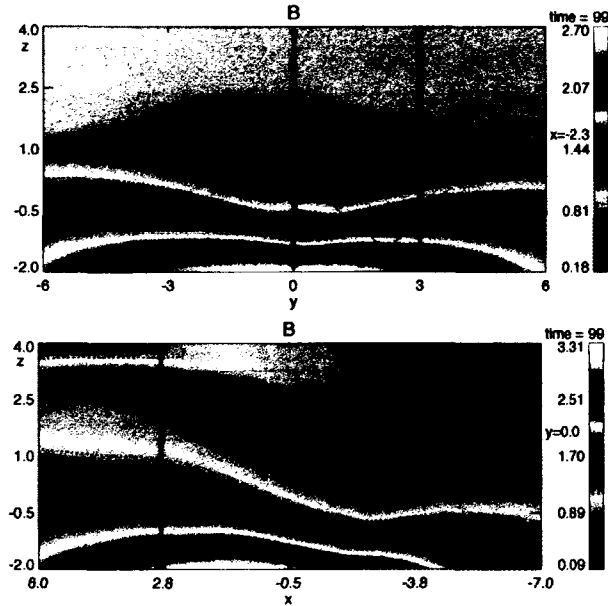


Figure 3.9. Total magnetic field ($|B|$) in the y - z plane (top), and x - z plane (bottom) for northward IMF. The CDC region is indicated by low magnetic field magnitude. The boundary normals used to address the geometry of the outer boundary are computed approximately along the vertical lines in the figures (note that the cut at $x = -8 R_E$ is not shown in the lower plot).

3.4.2.5 Discussion of Northward IMF cusp

The high-altitude cusp region under northward IMF conditions may be summarized as follows. The inner boundaries of the cusp form a funnel shape and are seen as gradual (occurring over the span of $1 - 2 R_E$) transitions in the density and temperature from typical magnetospheric values to those more comparable to the magnetosheath. This gradual nature of the inner lobe/CDC boundary under northward IMF conditions is in agreement observations [Lavraud et al., 2002; Nykyri et al., 2011a] however Lavraud et al. (2002) report a much more abrupt boundary between the dayside plasma sheet and CDC for the same IMF. The transition from the lobe is accompanied by increasing (largely field-aligned) flows on approach to the CDC region (see bottom plot in Figure 3.4). These flows are qualitatively consistent with reports in the literature of field aligned flows along the inner boundary for northward IMF [Lavraud et al., 2004b, 2005; Dunlop et al., 2005; Nykyri

et al., 2011a], though the results presented herein indicate significantly smaller flows. It should be noted, however, that the density asymmetry (between the magnetosphere and the magnetosheath) is rather small in this configuration, characterized by a change of only a factor of ~ 1.5 . Simulations with a more physical density distribution (realizing a change in density by a factor of ~ 50) and a higher resolution (however, a somewhat shorter physical duration) indicate parallel flows a factor of three larger than the bulk velocity in the CDC. Within the CDC, flows are significantly more moderate (60 km/s), in agreement with the stagnant exterior cusp (SEC) reported by Lavraud et al. (2002).

The exterior CDC/magnetosheath boundary is much more abrupt than the inner boundaries. The outer boundary is indented in the x - z plane, but is convex in the y - z plane. Analysis of the outer boundary reveals an Alfvénic transition (indicated by the slope of the Walén relation of 0.995 with $c.c. = 0.995$). The plasma parameters change in a manner mostly consistent with a slow-shock, often associated with reconnection.

3.4.3 Southward IMF

In this section we present simulation results for a strongly southward IMF orientation with IMF clock angle of 170° , resulting in a B_y -component identical to that for the northward case. Plasma flow for the southward case is initialized in the magnetosheath region with $M_A \approx 1$, while the resistivity is identical to the northward case (defined through Equation 3.3). We begin with an overview of the cusp region with emphasis on the CDC and its boundaries. We then discuss the boundaries in more detail, following the same format as in the previous section for northward IMF.

3.4.3.1 Cusp overview

For an IMF orientation of 170° , the CDC looks quite different from the northward IMF configuration. An IMF clock angle of 170° generates a null-point on the dayside of the cusp, slightly offset in the positive y -direction (duskward). Figure 3.10 shows cuts of various plasma parameters in the noon-midnight meridian plane. The density (top left) and pressure (middle left) are enhanced (relative to the adjacent magnetosphere) within the cusp funnel. The enhanced current density (top right) indicating strong magnetic shear lies in the vicinity of the null-point, towards the maximum x -boundary in the plots. The

plasma velocity (bottom) exhibits a clear field-aligned flow emanating from this region of enhanced current. A region of high plasma β (middle right) is clearly visible extending cusward from the current sheet. The location and extent this high β region agree well with that of the depleted magnetic field shown in Figure 3.3. The CDC is tilted sunward (note the neglect of dipole tilt in the model) and is significantly smaller than for the northward case. The cusward directed outflow from the reconnection site adjacent to the boundary with the magnetosheath is nearly parallel to the streaming magnetosheath flow. The newly reconnected magnetospheric field line is thus rapidly transported from the dayside, tailward, resulting in a relatively small CDC. The overall CDC is rather shallow, extending just over $1 R_E$ along the z -direction at its deepest extent into the cusp funnel, extending well past the central cusp region in a thin tailward structure compatible with the Cluster results for southward IMF cusp structure [Cargill et al., 2004]. In comparison, the CDC for the northward case shown in Figure 3.3 extends just more than $2 R_E$ along the z -direction. These results are consistent with reports of a smaller cusp under southward IMF conditions as evidenced by Cluster traversal of the high-altitude cusp region [Cargill et al., 2004] as well as mid-altitude cusp precipitation [Escoubet et al., 2008].

Simulated “data” for a trajectory along z at $(x, y) = (3, 0)$ in Figure 3.10 through the high-altitude cusp region is shown in Figure 3.11. The displayed “data” represents a cut through the dayside edge of the cusp region at $x = 3 R_E$. The dayside plasma sheet is evident from $z = -4 R_E$ until just above $z = -2 R_E$. This is indicated by the typical low density and plasma velocity, but strong, dipolar magnetic field geometry. Strong plasma flows are present near $z = -1 R_E$, along with increased density and a current sheet indicating the departure from a dipolar magnetic field geometry. The plasma flow in this layer has a significant field-aligned component, consistent with outflow from sub-solar reconnection. The CDC “proper” lies adjacent to this layer of strong plasma flow as indicated by the shaded region of large plasma β in the figure. The CDC is relatively shallow at this location, spanning a distance on the order of $.5 R_E$. The CDC is bounded in the exterior by a clear transition to magnetosheath plasma values.

We identify three boundaries of the CDC for southward IMF: 1) the dayside plasma sheet/CDC boundary on the sunward side of the cusp, 2) the lobe/CDC boundary on the tailward side of the cusp, and 3) the CDC/magnetosheath boundary in the exterior. The

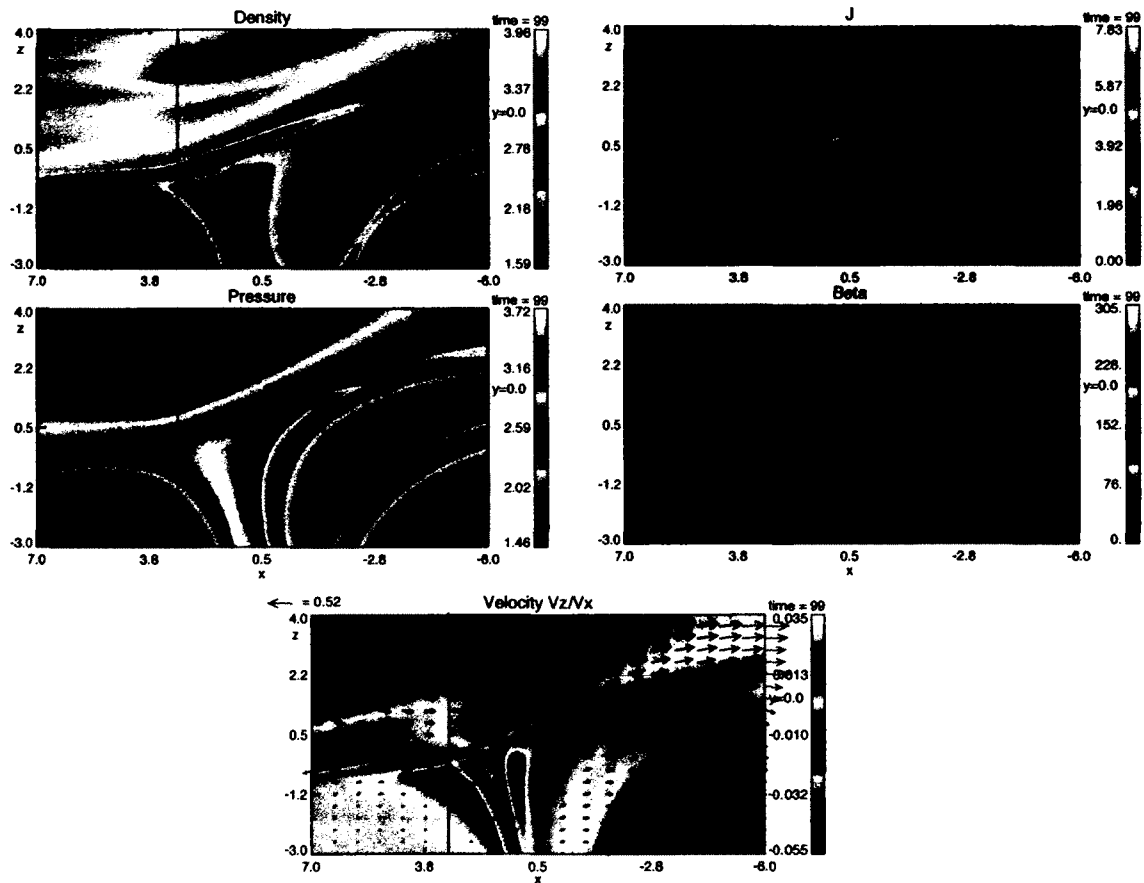


Figure 3.10. From top to bottom, the plots on the left display plasma density, thermal pressure, and plasma velocity, while those on the right display current density (J) and plasma β . All parameters are shown in the noon-midnight meridian plane. The green vertical lines indicate the trajectories along which simulated data is analyzed.

following sections focus on the analysis of these boundaries.

3.4.3.2 Dayside Plasma Sheet/CDC Boundary

The inner boundary between the dayside plasma sheet and the CDC is clearly identified by the deviation of the magnetic field (specifically B_x , B_y) from its dipolar geomagnetic values. We were able to find good a deHoffman-Teller frame (slope of 1.00 with $c.c. = 0.957$) for the inner boundary with a velocity (in normalized units) of $V_{HT} = (-.49, .08, -.18)$. This indicates that the structure is convecting largely tailward and towards the Earth, but with

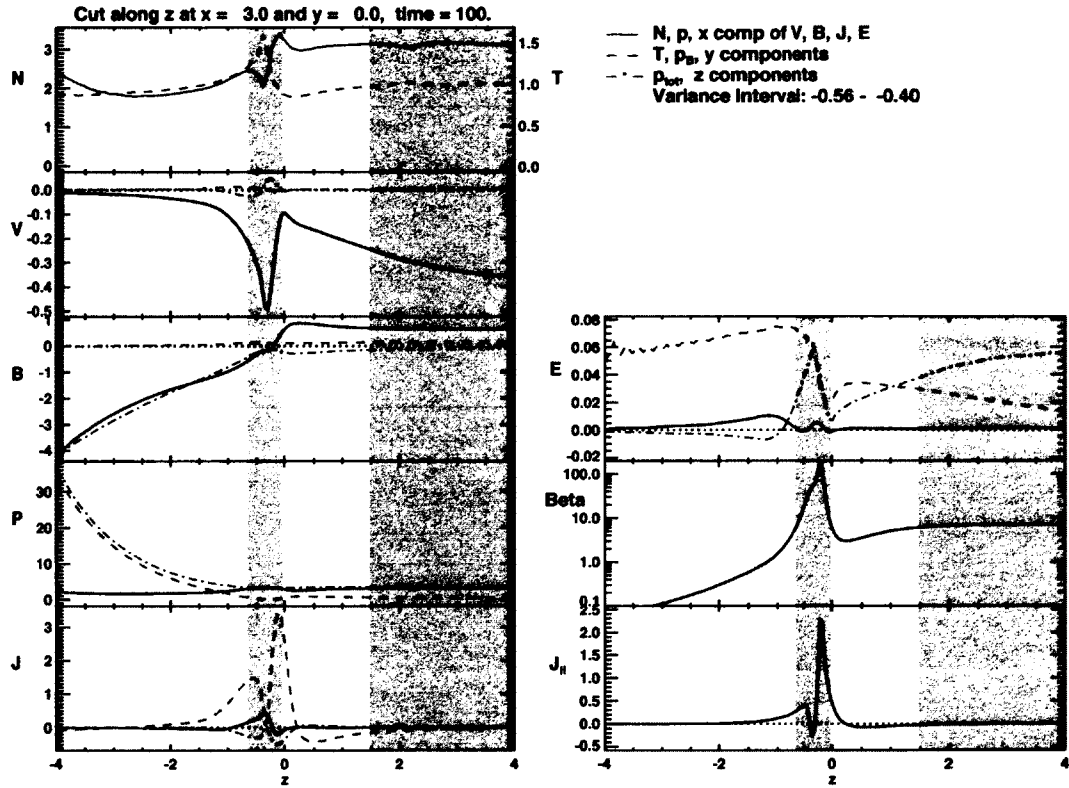


Figure 3.11. Simulated data for a cut along z at $(x, y) = (3, 0)$. All quantities are plotted in normalized simulation units. Plotted in the left column from top to bottom are the density, velocity components, magnetic field components, pressure, and current density. The right column displays the electric field, plasma β , and the parallel current density. The shading indicates regions of plasma $\beta > 6$.

a small duskward component, consistent with a dayside reconnection site. Plots of the deHoffman-Teller and Walén tests are displayed in Figure 3.12.

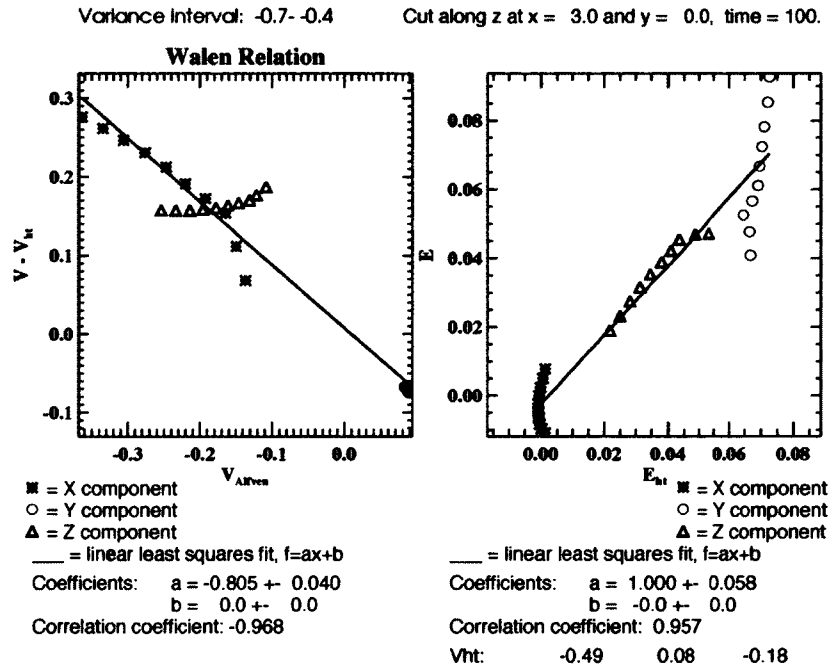


Figure 3.12. Walén relation and deHoffman-Teller test results for the dayside plasma sheet/CDC.

The transition from the dipolar geomagnetic field to the reduced diamagnetic region spans a much larger interval than the one analyzed above and generally does not satisfy the Walén relation. However, the interval analyzed above is mostly consistent with an Alfvénic transition, though the results are strongly dependent on the chosen interval. The positive result for the Walén relation shown in Figure 3.12 may be due to the interval of analysis not spanning the entire transition. There is evidence that this boundary may be a tangential discontinuity (TD) under northward IMF conditions ([Cargill et al., 2005], for instance), however this may not be the case for southward IMF. Under southward IMF, this transition which appears Alfvénic in the simulation may indeed be a reconnection associated shock extending from the reconnection site at the magnetopause towards the cusp funnel along the bottom edge of the CDC. Such a configuration would be reminiscent of the shocks in

the Petschek model [Petschek, 1964], but in a highly asymmetric configuration wherein the transition appears as a slow shock in the vicinity of the reconnection site, while farther away it appears more like a tangential discontinuity. Higher resolution in future work may allow for a more detailed analysis.

MVAB resulted in poor intermediate to minimum eigenvalue ratios ($int/min = 3.26$). Results of MVAE were better, with a maximum to intermediate ratio of 76.29, though the resolution of the transverse components remains ambiguous ($int/min : 3.26$). The boundary normal given by MVAE is $i_E = (-.01, -.23, .97)$. The simulated data (transformed into the basis resulting from MVAE) is plotted in Figure 3.13. In the framework of ideal MHD discontinuities, the increase in pressure from the magnetospheric side of the boundary towards the CDC implies the existence of a shock through which plasma is transported in the same sense as indicated by the positive normal component of the flow in the deHoffman-Teller frame (upper panel in the right of the figure). The concurrent variation of the magnetic field and velocity are suggestive of a slow-shock, though the normal component of the magnetic field decreases, inconsistent with the expectation for such a structure. This may be the result of inaccurate basis given by the MVAE method, or it may be that the gradual nature of the inner boundary in the simulation renders its classification as an ideal MHD discontinuity invalid.

3.4.3.3 Lobe/CDC Boundary

The inner boundary between the magnetospheric lobe and the CDC is a gradual and continuous transition marked largely by the slow transition from the dipolar geomagnetic field to the depressed field of the CDC region. This transition is similar to the inner boundary on the dayside as addressed in the previous section, but even more gradual spanning an interval of roughly $2 R_E$. No regions were found through which this boundary could be approximated as an MHD discontinuity, and thus no boundary analysis is presented here. This region is marked by steadily decreasing magnetic field on approach to the CDC from below, along with increasing plasma flow, while the density and thermal pressure remain relatively constant, consistent with the plasma mantle [Rosenbauer et al., 1975].

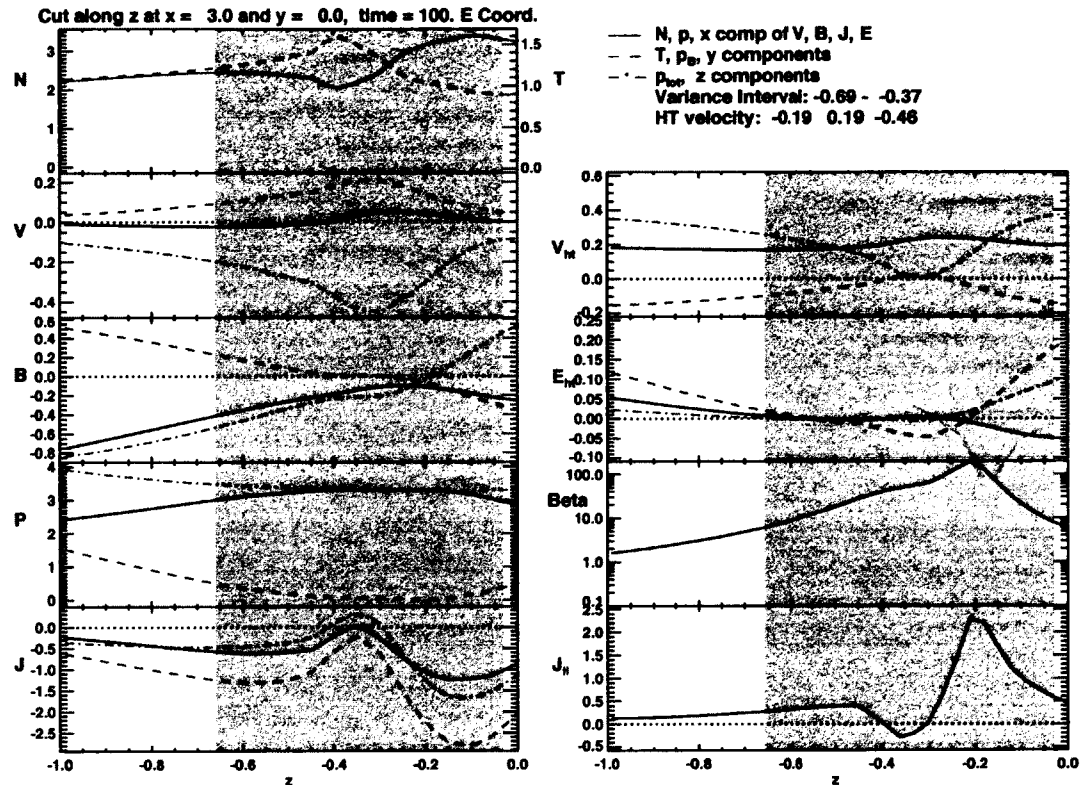


Figure 3.13. Simulated “data” transformed into MVAE boundary normal coordinates for the inner boundary transition. All quantities are plotted in normalized simulation units. Plotted in the left column from top to bottom are the density (solid blue line) and temperature (dashed red line), velocity components (x - solid black, y - dashed blue, z - dash-dot red), magnetic field components, pressure (thermal pressure - black, magnetic pressure - blue, total pressure - red), and current density components. The right column displays the velocity and electric field components in the deHoffman-Teller frame, plasma β , and the parallel current density.

3.4.3.4 CDC/Magnetosheath Boundary

The outer boundary between the CDC and the magnetosheath is most easily identified by the change in magnetic field from low CDC values to IMF values. Analysis of this exterior boundary at different locations along the noon-midnight meridian, both sunward and tailward of the cusp funnel, results in good deHoffman-Teller frames, moving largely in the $-x$ and $+z$ directions, consistent with tailward convection due to reconnection occurring on the dayside.

Searches were performed to identify intervals within which the Walén relation achieved a slope of between 0.85 and 1.15, while the slope of the deHoffman-Teller electric field versus the electric field in the simulation frame was between .90 and 1.1. In general, the outer boundary satisfies the Walén relation within the range previously stated. For the boundary crossing at $x = 3$, the slopes of the deHoffman-Teller and Walén tests were .993 and 1.035, respectively, with corresponding correlation coefficients of 0.997 and .991. The deHoffman-Teller velocity was found to be $V_{HT} = (-.34, -.07, .10)$. The boundary normal resulting from MVAE was $i_E = (.15, .52, .84)$. The plasma parameters transformed into this frame are plotted in Figure 3.14.

The normal components of both the velocity and magnetic field are negative, indicating an open boundary through which plasma is transported from the magnetosheath into the CDC. Variation of the remaining plasma parameters is consistent with a slow-shock: pressure increase, decrease in transverse components of magnetic field and velocity, and temperature increase. This indicates that the boundary is formed by reconnection processes at the magnetopause.

MVA resulted in normals with largest components aligned with the y - and z -directions. Comparison of normals given by MVAE for the boundary at $x = 5$ and $x = 2.8$ and projected into the x - z plane reveals that the boundary farther away from the reconnection site ($x = 2.8$) is oriented 25° towards the sun from the normal computed at $x = 5$. This indicates a clear indentation of the outer boundary under these IMF conditions. Similar analysis of boundary normals at $y = 0$ and $y = 1$, reveals that the computed normals open with an angle of 35° from each other. This indentation of the outer boundary is clearly visible in Figure 3.15. The figure displays the total magnetic field in the y - z (top) and x - z (bottom) planes.

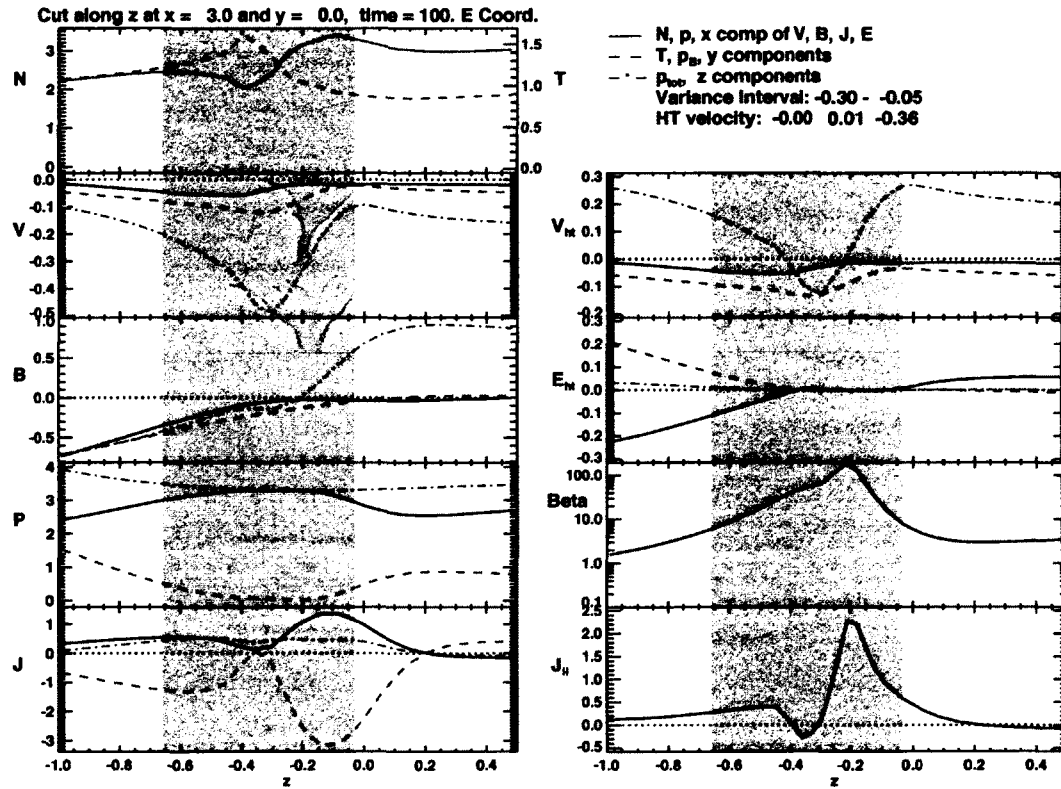


Figure 3.14. Plasma parameters transformed into the basis given by MVAE for the outer boundary between the CDC and magnetosheath at $x = 2.1$.

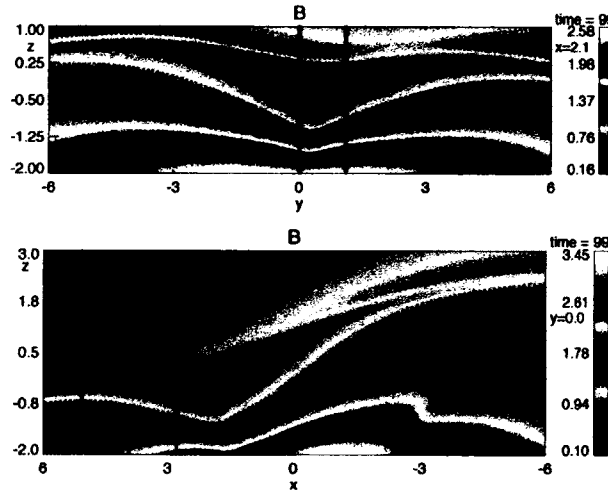


Figure 3.15. Total magnetic field ($|B|$) in the y - z plane (top), and x - z plane (bottom) for southward IMF. The CDC region is indicated by low magnetic field magnitude. The boundary normals used to address the geometry of the outer boundary are computed approximately along the vertical lines in the figures.

3.4.3.5 Discussion of Southward IMF cusp

The high-altitude cusp region is bounded by two gradual inner boundaries with the magnetosphere. These boundaries form a definite funnel shape (as for the northward case presented above). Though the inner boundaries are quite gradual, we were able to find an interval for the crossing of the inner CDC/dayside plasma sheet boundary which reasonably well satisfied the Walén relation (slope of -0.805 with $c.c. = 0.968$). Excluding the decrease in the normal component of the magnetic field (which may be the result of a poor normal determination), this transition is mostly consistent with a slow-shock. We note, however, that the gradual appearance of the transition from the dipolar geomagnetic field to the reduced diamagnetic region spans a much larger interval than the one analyzed above and it generally does not satisfy the Walén relation. This gradual nature of the inner boundary in the simulation may simply render its classification as an ideal MHD discontinuity invalid.

The CDC for southward IMF is filled with streaming plasma similar to that reported by Cargill et al. (2004) and Lavraud et al. (2005), as opposed to the results for northward IMF with a stagnant region [Lavraud et al., 2002, 2005]. This is not unexpected, due to the plasma flow in the sheath streaming in the same sense as the reconnected flux.

The outer CDC/magnetosheath boundary is much more abrupt than the inner boundaries and is indented in both the x - z and y - z planes. The boundary appears to be open (indicated by the $-B_n$) implying plasma transport from the magnetosheath into the CDC. The plasma characteristics across the boundary are consistent with a slow-shock suggesting that reconnection is the dominant process in the development of this boundary.

3.5 Discussion and Conclusion

We have presented results from local meso-scale resistive MHD simulations which address the effects of variations in the IMF orientation on the high-altitude cusp region. Typical observational features of CDC's are generally well reproduced in the simulation results:

1. Densities comparable to magnetosheath values
2. Strongly depressed magnetic field strength
3. Relatively stagnant plasma for northward IMF, but more convective flow for southward IMF
4. Gradual inner boundaries with a more abrupt boundary with the magnetosheath.

The high-altitude cusp has three boundaries: 1) the inner dayside plasma sheet boundary, 2) the inner lobe/mantle boundary, and 3) the outer magnetosheath boundary. The inner boundaries appear in the simulation as gradual transitions which exhibit field-aligned flows emanating from the side of the cusp where reconnection is occurring: the dayside plasma sheet boundary for southward IMF and the lobe boundary for northward IMF. The gradual appearance of the inner boundaries further supports the suggestion that it is appropriate to view the high-altitude cusp region containing the CDC and SEC as an extension of the magnetosphere [Russell, 2000; Lavraud et al., 2004b], and not as a detached structure as implied by the term "exterior".

Though the above features are reasonably well in agreement with observations, there remain a few aspects of the model results which disagree with some observational reports. These have to do with the inner boundaries between the magnetosphere and the CDC and with the presence of magnetic fluctuations within the CDC's.

The inner boundaries between the magnetosphere and CDC are represented by gradual transitions in the model. Though some observations agree with this gradual character for the inner transitions, for example Niehof et al. [2010]; Nykyri et al. [2011a], others describe a much more rapid transition [Lavraud et al., 2002]. This may be partly due to the dynamic nature of the cusp region, for instance Nykyri et al. [2011b] have shown that some of the local fluctuations in plasma parameters within the CDC may be attributed to the reaction of the CDC to solar wind changes on relatively short timescales. This gradual transition in the simulation may also be caused by limited resolution (note that the simulation already has a much higher resolution than typical global models) or by physics not contained within our model such as dipole tilt or inherent fluctuations within the solar wind plasma. These inner boundaries also exhibit significant field-aligned flows. These flows as seen in the simulation results, though qualitatively consistent with observations [Lavraud et al., 2004b, 2005; Dunlop et al., 2005; Nykyri et al., 2011a] are relatively small. It was previously noted that this appears to be the result of the low density asymmetry (between the magnetosphere and the magnetosheath) in this configuration. Simulations with a more physical density distribution and a higher resolution indicate parallel flows a factor of three larger than the bulk velocity in the CDC.

The other characteristic of CDC's that is not well represented in the model is the presence of magnetic fluctuations such as those reported by Chen and Fritz [1998]. The nature and cause of these fluctuations remains unclear in the observations and they may be the result of several processes such as rapid motion of cavity boundaries, transient events, such as magnetic flux bundles moving along the cavity, or waves within the region. It is possible that the consideration of such inputs in the model may indeed explain the observed fluctuations, however that is beyond the scope of this paper.

The main conclusions of this work may be summarized as follows:

1. Both the location and extent of the CDC exhibits a strong dependence on the IMF orientation. Results suggest that the extent of the high-altitude cusp, farthest from the dipole axis along the magnetopause, is anchored to the magnetopause through magnetic merging at the location of strongest magnetic shear. For northward IMF, the cusp is situated tailward of the dipole axis. Conversely, for southward IMF, the cusp is located on the sunward side of the dipole axis. Similar results were shown,

though not discussed in detail, for the case of 90° clock angle in Figure 3.2. These results are in agreement with the recent results of Nykyri et al. [2011a], who report results from a cluster event in which the position of the CDC moves in accordance with a rotation of the IMF.

The CDC appears significantly larger under northward IMF conditions than for southward IMF conditions. For a strongly southward IMF orientation, the reconnected flux tubes on the cusp-side of the x-line convect largely tailward, nearly parallel to the magnetosheath flow. Such is not the case for a strongly northward IMF. In this orientation, the reconnected flux tubes on the cusp-side of the x-line convect in the opposite direction of the streaming magnetosheath plasma. The result is a significantly larger CDC under Northward IMF conditions. Zhou et al. [2000] found a similar narrowing of the cusp under southward IMF conditions in agreement with Newell and Meng [1987], as well as a widening under northward IMF.

2. The location of the reconnection site is determined by the orientation of the IMF. Where the geomagnetic field and the IMF are anti-parallel, a null-point is formed, embedded within a more extensive region of strong magnetic shear consistent with the expansive reconnection lines reported by Onsager et al. [2001]. Such a configuration, enabling simultaneous anti-parallel and component reconnection has also been reported by Trattner et al. [2004].
3. The outer boundary between the CDC and magnetosheath appears mostly consistent with a slow-shock. Transformation of the plasma parameters near the boundary into the coordinate system defined through MVA methods applied to our simulation results indicate a boundary characterized by a negative normal component of both the magnetic field and velocity, accompanied by an increase in pressure and density, and a reduction in the tangential components of the magnetic field and velocity. The normal components of the magnetic field and velocity across the transition indicate an open boundary across which plasma is transported from the magnetosheath to the CDC. Similar open boundaries have been reported in case studies by Cargill et al. [2004] under southward IMF conditions and by Lavraud et al. [2002, 2004b] for northward IMF. The jump in plasma parameters across the transition are suggestive of a slow

shock. However, unexpectedly for a slow shock, the Walén test is well satisfied for the transition. Similar results were reported by Lavraud et al. [2002] and Cargill et al. [2004] for northward and southward IMF, respectively. Lavraud et al. [2002] found a value of .91 for the Walén relation, but noted that the change in plasma parameters was not consistent with a simple rotational discontinuity. They suggest that the boundary, though rotational-like, may be an intermediate or slow transition. Similarly, the results of Cargill et al. [2004] indicate a good value of the Walén relation of .8, but again note that the plasma parameter jumps across the boundary are inconsistent with a simple RD. They note that some characteristics of the transition are satisfied for a number of MHD discontinuities, however no simple discontinuity can explain them all. For instance, the good Walén relation is largely consistent with a rotational discontinuity, but such a transition does not exhibit the observed magnetic field and temperature changes. The authors also note that the parameter jumps are largely consistent with a slow shock if the Alfvénic character is neglected. We note that this apparent dual nature (Alfvénic and slow-shock like) may be explained in our simulation results through the fact that the tangential components of the magnetic field are nearly switched-off, whereas the Walén relation is approximately satisfied for switch-off slow shocks suggesting that magnetic reconnection is the dominant process in structuring this boundary.

4. We find the geometry of the magnetopause bounding the high-altitude cusp to differ based on IMF orientation. For northward IMF, the magnetopause exhibits an indentation in the x - z plane, but is convex in the y - z plane, whereas, the magnetopause appears indented in both x - z and y - z planes for southward IMF conditions. Numerous studies have presented evidence for an indented magnetopause [Eastman et al., 2000; Dunlop et al., 2005; Zhang et al., 2007], while others have identified no evidence for such a geometry [Zhou and Russell, 1997; Lavraud et al., 2004a; Cargill et al., 2004]. Our results exhibit clear indentation of the magnetopause bounding the high altitude cusp with the magnetosheath, with the exception of the y - z plane under northward IMF conditions which appears convex. In a statistical study Zhang et al. [2007] report an external cusp boundary which is clearly indented in the x - y plane, but less clearly indented in the x - z plane. It is unclear exactly how our results are to

be interpreted in terms of such observations due to the neglect of dipole tilt in our model. It is plausible that the consideration of dipole tilt in the model could alter the geometry of the magnetopause adjacent to the high-altitude cusp as the result of increased normal flow. In addition, results presented herein have considered sub-Alfvénic magnetosheath flow, whereas flow in the magnetosheath frequently realizes super-Alfvénic speeds. Consideration of magnetosheath flow with $M_A > 1$ may significantly alter results, particularly in terms of the geometry of the outer boundary. It is expected that the additional consideration of such effects would lead to further indentation of the magnetopause in the region (and thus possibly result in similar results also in the y - z plane under northward IMF). Thus our findings clearly support the existence of an indented magnetopause bounding the high altitude cusp region.

Our results paint a picture of the CDC as an attached feature of the high altitude cusp region, bounded on its exterior with the magnetopause. The magnetopause in the vicinity of the CDC appears Alfvénic in nature and exhibits characteristics consistent with a slow shock (nearly a switch-off slow shock). Additionally, the CDC exhibits a clear dependence on the IMF both in terms of its size and its location. These results suggest that the region is largely structured by reconnection processes (through concurrent anti-parallel and component merging) at the magnetopause largely under the control of the IMF. With evidence mounting for the role played by reconnection in forming this outer boundary, it may be more appropriately regarded as the magnetopause [Onsager et al., 2001; Lavraud et al., 2004b; Cargill et al., 2004], whereas the more gradual inner boundaries, as noted by Lavraud et al. (2004), appear more consistent with the traditional magnetopause [Paschmann et al., 1976; Haerendel et al., 1978; Russell, 2000].

3.6 Acknowledgements

Support for the research of Eric Adamson and Antonius Otto was provided by NASA grants NNG06GG89Gprog07 and NNX09AI09Gprog2010 to the University of Alaska Fairbanks. K. Nykyri's work is supported by National Science Foundation grant 0703327.

Bibliography

- Adamson, E., Otto, A., and Nykyri, K.: 3-D mesoscale MHD simulations of a cusp-like magnetic configuration: method and first results, *Ann. Geophys.*, 29, 759–770, doi:10.5194/angeo-29-759-2011, 2011.
- Bosqued, J. M., Escoubet, C. P., Frey, H. U., Dunlop, M., Berchem, J., Marchaudon, A., Cerisier, J. C., Fazakerley, A., Budnik, E., Lavraud, B., Rème, H., Laakso, H., and Balogh, A.: Multipoint observations of transient reconnection signatures in the cusp precipitation: A Cluster-IMAGE detailed case study, *Journal of Geophysical Research (Space Physics)*, 110, A03219, doi:10.1029/2004JA010621, 2005.
- Carbary, J. F. and Meng, C. I.: Relations between the interplanetary magnetic field B_z , AE index, and cusp latitude, *J. Geophys. Res.*, 91, 1549–1556, 1986.
- Cargill, P. J., Dunlop, M. W., Lavraud, B., Elphic, R. C., Holland, D. L., Nykyri, K., Balogh, A., Dandouras, I., and Reme, H.: CLUSTER encounters with the high altitude cusp: boundary structure and magnetic field depletions, *Ann. Geophys.*, 22, 1739–1754, 2004.
- Cargill, P. J., Lavraud, B., Owen, C. J., Grison, B., Dunlop, M. W., Cornilleau-Wehrlin, N., Escoubet, C. P., Paschmann, G., Phan, T. D., Rezeau, L., Bogdanova, Y., and Nykyri, K.: Cluster at the Magnetospheric Cusps, *Space Sci. Rev.*, 118, 321–366, doi:10.1007/s11214-005-3835-0, 2005.
- Chen, J. and Fritz, T. A.: Correlation of cusp MeV helium with turbulent ULF power spectra and its implications, *Geophys. Res. Lett.*, 25, 4113–4116, doi:10.1029/1998GL900122, 1998.
- Chen, J., Fritz, T. A., Sheldon, R. B., Spence, H. E., Spjeldvik, W. N., Fennell, J. F., Livi, S., Russell, C., Pickett, J. S., and Gurnett, D. A.: Cusp energetic particle events: Implications for a major acceleration region of the magnetosphere, *J. Geophys. Res.*, 103, 69–78, 1998.

- Dubinin, E., Skalsky, A., Song, P., Savin, S., Kozyra, J., Moore, T. E., Russell, C. T., Chandler, M. O., Fedorov, A., Avakov, L., Sauvaud, J.-A., and Friedel, R. H. W.: Polar-Interball coordinated observations of plasma and magnetic field characteristics in the regions of the northern and southern distant cusps, *Journal of Geophysical Research (Space Physics)*, 107, 1053, doi:10.1029/2001JA900068, 2002.
- Dunlop, M. W., Lavraud, B., Cargill, P., Taylor, M. G. G. T., Balogh, A., Reme, H., P., D., Glassmeier, K.-H., Elphic, R. C., Bosqued, J. M., Fazakerley, A., Dandouras, I., Escoubet, C. P., Laasko, H., and Marchaudon, A.: *Cluster Observations of the Cusp: Magnetic Structure and Dynamics*, Springer Netherlands, 2005.
- Eastman, T. E., Boardsen, S. A., Chen, S. H., Fung, S. F., and Kessel, R. L.: Configuration of high-latitude and high-latitude boundary layers, *J. Geophys. Res.*, 105, 23 221–23 238, 2000.
- Escoubet, C. P. and Bosqued, J. M.: The influence of IMF- B_z and/or AE on the polar cusp: An overview of observations from the AUREOL-3 satellite, *Planet. Space Sci.*, 37, 609–626, 1989.
- Escoubet, C. P., Berchem, J., Bosqued, J. M., Trattner, K. J., Taylor, M. G. G. T., Pitout, F., Laakso, H., Masson, A., Dunlop, M., Dandouras, I., Reme, H., Fazakerley, A. N., and Daly, P.: Effect of a northward turning of the interplanetary magnetic field on cusp precipitation as observed by Cluster, *Journal of Geophysical Research (Space Physics)*, 113, A07S13, doi:10.1029/2007JA012771, 2008.
- Fedorov, A., Dubinin, E., Song, P., Budnik, E., Larson, P., and Sauvaud, J.-A.: Characteristics of the Exterior Cusp for Steady Southward Interplanetary Magnetic Field: Interball Observations, *J. Geophys. Res.*, 105, 15 945–15 957, 2000.
- Fritz, T. A., Chen, J., and Siscoe, G. L.: Energetic ions, large diamagnetic cavities, and Chapman-Ferraro cusp, *J. Geophys. Res.*, 108, 1028, doi:10.1029/2002JA009476, 2003.
- Haerendel, G., Paschmann, G., Sckopke, N., Rosenbauer, H., and Hedgecock, P.: The Frontside Boundary Layer of the Magnetosphere and the Problem of Reconnection, *J. Geophys. Res.*, 83, 3195–3216, 1978.

- Hansen, A. M., Bahnsen, A., and D'Angelo, N.: The Cusp-Magnetosheath Interface, *Journal of Geophysical Research*, 81, 556–561, 1976.
- Lavraud, B., Dunlop, M. W., Phan, T. D., Rème, H., Bosqued, J.-M., Dandouras, I., Sauvaud, J.-A., Lundin, R., Taylor, M. G. G. T., Cargill, P. J., Mazelle, C., Escoubet, C. P., Carlson, C. W., McFadden, J. P., Parks, G. K., Moebius, E., Kistler, L. M., Bavassano-Cattaneo, M.-B., Korth, A., Klecker, B., and Balogh, A.: Cluster observations of the exterior cusp and its surrounding boundaries under northward IMF, *Geophys. Res. Lett.*, 29, 1995, 2002.
- Lavraud, B., Fedorov, A., Budnik, E., Grigoriev, A., Cargill, P. J., Dunlop, M. W., Rème, H., Dandouras, I., and Balogh, A.: Cluster survey of the high-altitude cusp properties: A three-year statistical study, *Ann. Geophys.*, 22, 3009–3019, 2004a.
- Lavraud, B., Phan, T. D., Dunlop, M. W., Taylor, M. G. G. T., Cargill, P. J., Bosqued, J.-M., Dandouras, I., Rème, H., Sauvaud, J.-A., Escoubet, C. P., Balogh, A., and Fazakerley, A.: The exterior cusp and its boundary with the magnetosheath: Cluster multi-event analysis, *Ann. Geophys.*, 22, 3039–3054, 2004b.
- Lavraud, B., Fedorov, A., Budnik, E., Thomsen, M. F., Grigoriev, A., Cargill, P. J., Dunlop, M. W., Rème, H., Dandouras, I., and Balogh, A.: High altitude cusp flow dependence on IMF orientation: A 3 year Cluster statistical study, *J. Geophys. Res.*, 110, doi:10.1029/2004JA010804, 2005.
- Lockwood, M. and Smith, M.: The Variation of Reconnection Rate at the Dayside Magnetopause and Cusp Ion Precipitation, *J. Geophys. Res.*, 97, 14 841–14 847, 1992.
- Newell, P., Meng, C.-I., Sibeck, D., and Lepping, R.: Some Low-Altitude Dependencies on the Interplanetary Magnetic Field, *J. Geophys. Res.*, 94, 8921–8927, 1989.
- Newell, P. T. and Meng, C.-I.: Cusp width and $B(z)$ - Observations and a conceptual model, *Journal of Geophysical Research*, 92, 13 673–13 678, doi:10.1029/JA092iA12p13673, 1987.
- Newell, P. T. and Meng, C. I.: Ionospheric Projections of Magnetospheric Regions under Low and High Solar Wind Pressure Conditions, *J. Geophys. Res.*, 99, 273–286, 1994.

- Newell, P. T., Ruohoniemi, J. M., and Meng, C.-I.: Maps of precipitation by source region, binned by IMF, with inertial convection streamlines, *Journal of Geophysical Research (Space Physics)*, 109, A10206, doi:10.1029/2004JA010499, 2004.
- Niehof, J. T., Fritz, T. A., Friedel, R. H. W., and Chen, J.: Interdependence of magnetic field and plasma pressures in cusp diamagnetic cavities, *J. Geophys. Res.*, 35, L11101, doi:10.1029/2008GL033589, 2008.
- Niehof, J. T., Fritz, T. A., Friedel, R. H. W., and Chen, J.: Size and location of cusp diamagnetic cavities observed by Polar, *Journal of Geophysical Research (Space Physics)*, 115, A07201, doi:10.1029/2009JA014827, 2010.
- Nykyri, K., Otto, A., Adamson, E., Dougal, E., and Mumme, J.: Cluster observations of a cusp diamagnetic cavity: Structure, size and dynamics, *J. Geophys. Res.*, 116, A03 228, doi:10.1029/2010JA015897, 2011a.
- Nykyri, K., Otto, A., Adamson, E., and Tjulin, A.: On the origin of fluctuations in the cusp diamagnetic cavity, *J. Geophys. Res.*, 116, A06208, doi:10.1029/2010JA015888, 2011b.
- Onsager, T., Scudder, J., Lockwood, M., and Russell, C.: Reconnection at the high latitude magnetopause during northward interplanetary magnetic field conditions, *J. Geophys. Res.*, 106, doi:10.1029/2000JA000444, 2001.
- Onsager, T. G., Kletzing, C. A., Austin, J. B., and Mackiernan, H.: Model of magnetosheath plasma in the magnetosphere - Cusp and mantle particles at low-altitudes, *J. Geophys. Res.*, 20, 479–482, doi:10.1029/93GL00596, 1993.
- Paschmann, G., Haerendel, G., Sckopke, N., Rosenbauer, H., and Hedgecock, P.: Plasma and Magnetic Field Characteristics of the Distant Polar Cusp near Local Noon: The Entry Layer, *J. Geophys. Res.*, 81, 2883–2899, 1976.
- Peterson, W. K. and Trattner, K. J.: Sources of plasma in the high altitude cusp, *Journal of Atmospheric and Solar-Terrestrial Physics*, doi:10.1016/j.jastp.2011.07.001, 2011.
- Petschek, H. E.: Magnetic Field Annihilation, *NASA Special Publication*, 50, 425, 1964.

- Pitout, F., Escoubet, C. P., Bogdanova, Y. V., Georgescu, E., Fazakerley, A. N., and Rème, H.: Response of the mid-altitude cusp to rapid rotations of the IMF, *Geophys. Res. Lett.*, **33**, 2006a.
- Pitout, F., Escoubet, C. P., Klecker, B., and Rème, H.: Cluster survey of the mid-altitude cusp: 1. Size, location, and dynamics, *Ann. Geophys.*, **24**, 3011–3026, 2006b.
- Rosenbauer, H., Gruenwaldt, H., Montgomery, M. D., Paschmann, G., and Sckopke, N.: Heos 2 plasma observations in the distant polar magnetosphere - The plasma mantle, *J. Geophys. Res.*, **80**, 2723–2737, doi:10.1029/JA080i019p02723, 1975.
- Russell, C. T.: Polar Eyes the Cusp, Cluster-II Workshop: Multiscale/Multipoint Plasma Measurements, Proceedings of the Workshop held at Imperial College, London, UK, 22-24 September 1999, 449, 47, 2000.
- Sandholt, P. E., Farrugia, C. J., Burlaga, L. F., Holtet, J. A., Moen, J., Lybekk, B., Jacobsen, B., Opsvik, D., Egeland, A., and Lepping, R.: Cusp/cleft auroral activity in relation to solar wind dynamic pressure, interplanetary magnetic field B_z and B_y , *J. Geophys. Res.*, **99**, 17,323–17,342, 1994.
- Savin, S. P., Romanov, S. A., Fedorov, A., Zelenyi, L., Klimov, S. I., Yermolaev, Y. I., Budnik, E. Y., Nikolaeva, N. S., Russell, C. T., Zhou, X.-W., Urquhart, A. L., and Reiff, P. H.: The Cusp/Magnetosheath Interface on May 29, 1996: Interball 1 and Polar Observations, *Geophys. Res. Lett.*, **25**, 2963–2966, 1998.
- Scarf, F. L., Fredricks, R. W., Neugebauer, M., and Russell, C. T.: Plasma Waves in the Dayside Polar Cusp, 2. Magnetopause and Polar Magnetosheath, *Journal of Geophysical Research*, **79**, 1974.
- Sonnerup, B. U. O. and Cahill, L. J.: Magnetopause Structure and Attitude from Explorer 12 Observations, *J. Geophys. Res.*, **72**, 171–183, 1967.
- Trattner, K. J., Fuselier, S. A., and Petrinec, S. M.: Location of the reconnection line for northward interplanetary magnetic field, *J. Geophys. Res.*, **109**, doi:10.1029/2003JA009975, 2004.

- Trattner, K. J., Petrinec, S. M., Peterson, W. K., Fuselier, S. A., and Reme, H.: Tracing the location of the reconnection site from the northern and southern cusps, *Journal of Geophysical Research (Space Physics)*, 111, A11211, doi:10.1029/2006JA011673, 2006.
- Walters, G. K.: On the Existence of a second standing shock wave attached to the magnetosphere, *J. Geophys. Res.*, 71, 1341, 1966.
- Woch, J. and Lundin, R.: Magnetosheath Plasma Precipitation in the Polar Cusp and its Control By the Interplanetary Magnetic Field, *J. Geophys. Res.*, 97, 1421–1430, 1992.
- Yamauchi, M. and Lundin, R.: Classification of Large-scale and Meso-scale Ion Dispersion Patterns Observed BY Viking over the Cusp-mantle Region, Kluwer Academic Publishers, 1994.
- Yamauchi, M. and Lundin, R.: The Wave-Assisted Cusp Model: Comparison to Low-Altitude Observations, *Phys. Chem. Earth*, 22, 729–734, 1997.
- Yamauchi, M., Nilsson, H., Eliasson, L., Norberg, O., Boehm, M., Clemmons, J. H., Leping, R. P., Blomberg, L., Ohtani, S.-I., Yamamoto, T., Mukai, T., Terasawa, T., and Kokburn, S.: Dynamic response of the cusp morphology to the solar wind: A case study during passage of the solar wind plasma cloud on February 21, 1994, *J. Geophys. Res.*, 101, 24 675–24 687, 1996.
- Zhang, H., Dunlop, M. W., Zong, Q.-G., Fritz, T. A., Balogh, A., and Wang, Y.: Geometry of the High-latitude Magnetopause as Observed by Cluster, *J. Geophys. Res.*, 112, 2007.
- Zhou, X. W. and Russell, C. T.: The location of the high-latitude polar cusp and the shape of the surrounding magnetopause, *J. Geophys. Res.*, 102, 105–110, 1997.
- Zhou, X. W., Russell, C. T., Le, G., Fuselier, S. A., and Scudder, J. D.: Solar wind control of the polar cusp at high altitude, *J. Geophys. Res.*, 105, 245–251, 2000.

Chapter 4

Entropy Change Through Reconnection in the Vicinity of Magnetic Cusps¹

4.1 Abstract

We present results from mesoscale simulations of magnetic reconnection in the vicinity of the magnetospheric cusp region. Results indicate that newly reconnected flux tubes can gain a significant amount of flux tube entropy through the reconnection process due to the topological change within the extended diamagnetic cavity region. We argue that this is a property unique to this type of magnetic structure characterized by a magnetic null-point and an extended region of strongly depleted magnetic field.

4.2 Introduction

The frozen-in condition is of fundamental importance in the framework of ideal MHD. The concept that plasma is frozen to the magnetic field results from the assumption that the electric field in the rest frame of the plasma vanishes:

$$\mathbf{E} + \mathbf{v} \times \mathbf{B} = 0$$

This allows for the definition of a flux tube as a bundle of magnetic flux to which the constituent plasma is ideally confined. We thus define the volume of said flux tube extending between footpoints l_1 and l_2 as:

$$V = \int_{l_1}^{l_2} \frac{dl}{B}$$

where the cross sectional area of the tube varies as $1/B$. Assuming no flux through the flux tube ends implies that the total number density is conserved. It can likewise be shown that any quantity which obeys a continuity equation is similarly conserved. Particularly relevant here is the conservation of entropy (assuming zero heat flux and isotropic pressure):

$$\frac{d(p\rho^{-\gamma})}{dt} + \mathbf{u} \cdot \nabla(p\rho^{-\gamma}) = 0$$

Further, for adiabatic changes, the pressure is constant on field lines. This enables the definition of a proxy for flux tube entropy (H), similar to that employed by *Birn et al.* [2006] which has the benefit of being additive:

¹Adamson, E., Otto, A., Prepared for submission to Geophys. Res. Lett.

$$H = p^{1/\gamma}V \quad (4.1)$$

The additive quality of equation (4.1) allows for the estimation of H along newly reconnected field lines by adding the contributions from the reconnecting sections of flux tubes. Though it has recently been shown that flux tube entropy is generally rather well preserved through reconnection in MHD (provided that resistivity is sufficiently localized) [Birn *et al.*, 2006], we suggest that magnetic cusps present a unique structure within which reconnection may effect significant changes to flux tube entropy.

The entropy on magnetic flux tubes is an important quantity for stability [Schindler and Birn, 2004; Birn *et al.*, 2009; Johnson and Wing, 2009] and convection [Erickson, 1992] in the magnetosphere. This particularly applies to newly reconnected (closed) magnetic flux. Provided that the entropy subsequent to reconnection is approximately invariant, the entropy content of a newly re-closed flux tube determines, to some degree, the downtail distance (from Earth) to which the flux tube should relax. Entropy may also be an important diagnostic tool for non-adiabatic processes participating in plasma transport [Borovsky *et al.*, 1998; Birn *et al.*, 2009; Wing and Johnson, 2010]. Knowledge of the expected flux tube entropy can aid to identify the importance of further non-adiabatic processes and possibly their nature.

We present results from a mesoscale resistive MHD simulation of reconnection in the vicinity of a magnetic cusp. Changes in flux tube entropy (H) are estimated by adding values of two sections of reconnecting flux tubes. The estimates are compared with the value along the newly reconnected flux tubes revealing a significant contribution from the section of flux tube threading the high β region of the cusp.

4.3 Numerical Procedure

4.3.1 Numerical Method and Model

Our simulation uses the full set of MHD equations in the following form:

$$\begin{aligned}\frac{\partial \rho}{\partial t} &= -\nabla \cdot (\rho \mathbf{u}), \\ \frac{\partial(\rho \mathbf{u})}{\partial t} &= -\nabla \cdot \left[\rho \mathbf{u} \mathbf{u} + \frac{1}{2} (p + B^2) \mathbf{I} - \mathbf{B} \mathbf{B} \right], \\ \frac{\partial h}{\partial t} &= -\nabla \cdot (h \mathbf{u}) - \frac{\gamma - 1}{\gamma} h^{1-\gamma} \eta j^2, \\ \frac{\partial \mathbf{B}}{\partial t} &= -\nabla \times (\mathbf{u} \times \mathbf{B} - \eta \mathbf{j}), \\ \mathbf{j} &= \nabla \times \mathbf{B},\end{aligned}$$

where $h = (p/2)^{1/\gamma}$ and ρ , p , η , \mathbf{u} , and \mathbf{B} represent density, pressure, resistivity, velocity, and magnetic field. The ratio of specific heats (γ) is taken to be 5/3. The resistivity (η) is homogeneous and constant for the results presented herein with a value of 0.015. All variables are normalized to typical system values, and thus dimensionless. Length scale, density, and magnetic field strength are normalized to typical system values ($L_0 = 1 R_E$, $\rho_0 = 0.1/\text{cm}^3$, and $B_0 = 50 \text{ nT}$). The pressure, velocity and time are then measured in units of normalized pressure $p_0 = B_0^2/8\pi = 1 \text{ nPa}$, Alfvén velocity $u_A = B_0/\sqrt{4\pi\rho_0} = 1100 \text{ km/s}$, and Alfvén time $\tau_A = L_0/u_A = 6 \text{ s}$, respectively.

We utilize a leapfrog/DuFort-Frankel discretization method for the integration of the MHD equations, as the method is relatively easy to implement and affords the benefit of using a nonuniform grid. The method is second order in space and time and uses a grid with a maximum resolution of 0.07 in x and y , and 0.05 in z . The grid is chosen to be more uniform in the z -direction in order to resolve not just the strong gradients toward the bottom of the domain where the field lines converge, but also to resolve the gradients within the magnetopause. The simulations presented herein are comprised of $203 \times 203 \times 203$ grid points in x , y , and z , respectively.

We construct a local model of the magnetospheric cusp region by placing a dipole at $-10 R_E$ along the z -axis with the dipole axis anti-parallel to z (no dipole tilt). The coordinates are such that the x -axis is directed toward the sun and the y -axis completes the right-handed system. The simulation domain ranges from $-12 R_E$ to $12 R_E$ in both the x

and y directions and the z coordinate from $-6 R_E$ to $6 R_E$, such that the dipole is $4 R_E$ below the lower z -boundary. The dipolar magnetic field is effectively turned off in the upper region of the simulation domain ($z > 0$), thus defining the magnetosheath region. This is accomplished through the inclusion of a shielding current. A constant “draped” (no z -component) IMF may then be superposed in the magnetosheath region. Results presented herein represent a magnetospheric cusp configuration with strongly northward IMF (10° clock angle). Finally, the density and pressure are prescribed as functions of the magnetic field-line equation. A ballistic relaxation is then applied in order to produce a near-equilibrium configuration.

Uniform flow is initialized in the equilibrium configuration throughout the magnetosheath region with Alfvén Mach number (M_A) of $\sim .7$. The position of the z -dependent flow transition is held fixed at the inflow boundary (x -min), while Neumann boundary conditions are imposed for the outflow (x -max) boundary such that $\partial f / \partial x_n = 0$, as well as for the other plasma quantities at all other boundaries (aside from the magnetic flux B). The normal components of the magnetic field at the boundaries are calculated such that $\nabla \cdot \mathbf{B} = 0$. A simple extrapolation method is employed at the minimum z -boundary where the plasma is also frozen. This is a convenient remedy which addresses the evacuation of plasma at the lower z -boundary where the simplistic boundary conditions lead to a departure from a strictly dipolar magnetic field geometry and, thus, large $\mathbf{j} \times \mathbf{B}$ forces. For further details on the simulation, see *Adamson et al.* [2011].

4.4 Results

Figure 4.1 shows a three-dimensional rendering of a magnetic cusp configuration after 10 Alfvén times.

The IMF clock angle of 10° results in a null-point located on the tailward side of the cusp ($x < 0$), slightly offset from the noon-midnight meridian. The surface in the Figure represents an arbitrary value of plasma β indicating the region of large thermal pressure collocated with low magnetic flux. This region is representative of the Cusp Diamagnetic Cavity (CDC), though the specific value of β chosen here is intended only to serve illustrative purposes. The field lines plotted in the Figure represent four topologically separate domains: red - magnetosheath, pink - magnetosphere, dark blue - reconnected flux tube

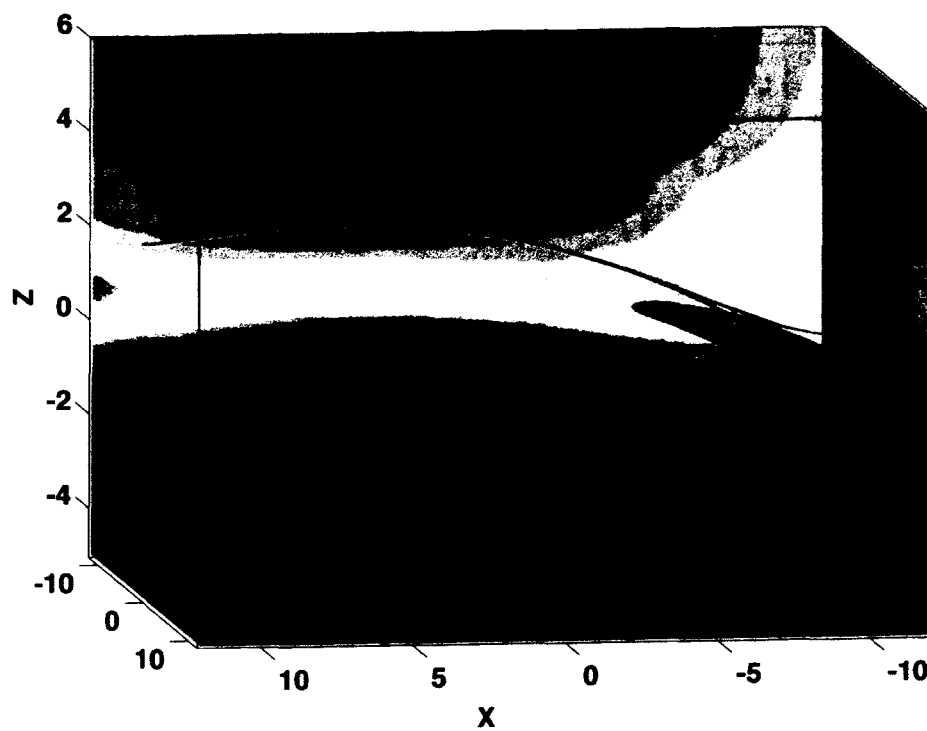


Figure 4.1. Illustration of the cusp reconnection geometry. The surface encompasses the region of high plasma β . The colored field lines represent: red - magnetosheath, pink - magnetosphere, dark blue - reconnected flux tube moving tailward, and light blue - magnetosheath field line newly reconnected to the dayside magnetosphere

moving tailward, and light blue - magnetosheath field line newly reconnected to the dayside magnetosphere. These flux tubes were chosen by eye, based on a plot of total magnetic flux in the x - y plane at $z \sim 0$, such that they represent the various regions of interest.

It is straightforward to estimate the flux tube entropy (H) of newly reconnected flux tubes by exploiting the additive property of the quantity. This estimation then, is dependent upon the assumptions that the pressure is constant on field lines, and that there are no losses or gains through the ends of the flux tubes.

Consider the flux tubes in Figure 4.1. The value of H for the newly reconnected light blue flux tube may be estimated by

$$H^* = H_{msp(z_{min} \rightarrow X)} + H_{msh(X \rightarrow x_{max})}, \quad (4.2)$$

where X represents the location of the x-point. Assuming no flow through the ends of the flux tubes, this should give a reasonable estimate of the entropy contained within the newly reconnected flux tube, and thus a means by which to estimate the effect of the reconnection process on flux tube entropy. Figure 4.2 displays cumulative values of both the flux tube volume and H along the flux tubes of Figure 4.1. The top plot in Figure 4.2 displays cumulative values of flux tube volume and H along the flux tube beginning at the minimum x -boundary and ending at the sunward boundary (x_{min}). There is a slight increase in the slope of both parameters beginning at a displacement of $\sim 15 R_E$ and extending to the sunward boundary. This is the effect of flow through the end of the flux tube, which has thus far been assumed negligible in the discussion. Though this suggests that the previous assumption of closed flux tubes in the system is invalid, we assert that this effect is irrelevant to our main results. This point is be addressed below.

Using values from Figure 4.2 in Equation (4.2) gives an estimate of the total flux tube entropy (H^*) contained within the newly reconnected flux tube (light blue in Figure 4.1):

$$\begin{aligned} H^* &= 2 \times 10^4 + 3.5 \times 10^4 \\ &= 5.5 \times 10^4, \end{aligned}$$

70% less than the results in the bottom plot of Figure 4.2.

The reconnected flux tube, similar to the magnetosheath flux tube shown in the top plot, exhibits a break in slope at $\sim 20 R_E$ towards the sunward boundary. This portion of

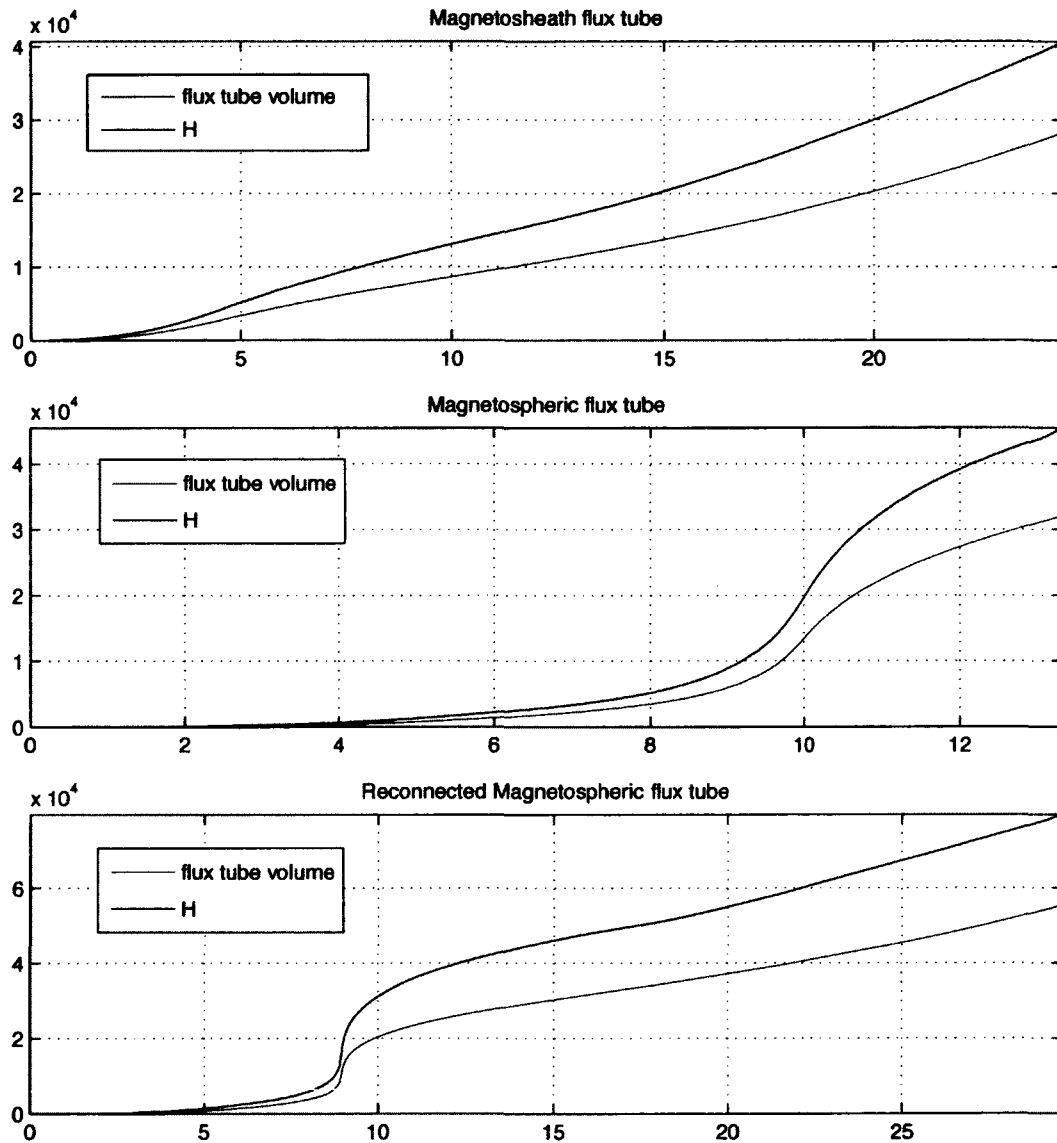


Figure 4.2. Cumulative flux tube entropy (H) and volume as a function of distance along a magnetic flux tube. Plots indicate the cumulative flux tube entropy (H) in blue and cumulative flux tube volume in red as a function of distance along the flux tube for a magnetosheath flux tube (top), magnetospheric flux tube (middle), and a reconnected flux tube (bottom).

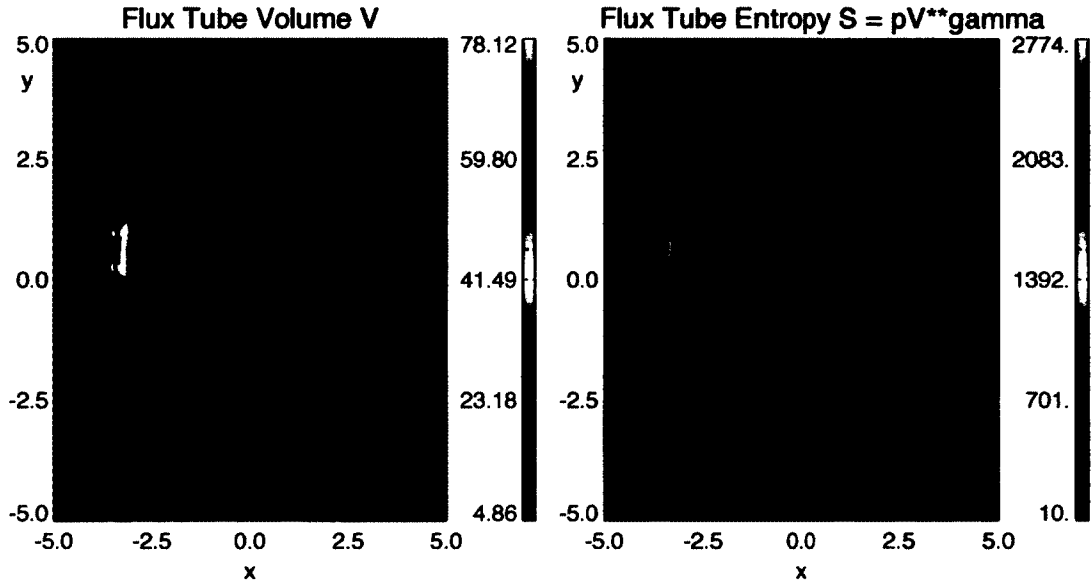


Figure 4.3. Total flux tube volume V (left) and field-line integrated entropy (pV^γ)(right) mapped into the $z = -2 R_E$ plane. The Sun is to the right of the plots ($+x$).

the flux tube contributes approximately 2.5×10^4 to the total flux tube entropy, comparable to the effect for the magnetosheath flux tube in the top plot. This affirms that the effect of flow through the flux tube end on the sunward side of the cusp is irrelevant to the present discussion provided that the flux tubes are chosen close enough together such that they reconnect sufficiently soon. Furthermore, the reconnected flux tube exhibits a substantial increase in H (and correspondingly, in flux tube volume) at a displacement of $\sim 9 R_E$ along the reconnected flux tube. This is indeed where the flux tube threads the region of high plasma β , indicating that discrepancy between the estimated flux tube entropy (H^*) and the actual flux tube entropy (H), is the result of the magnetosheath field line now being connected through this region of high plasma β to the dayside magnetosphere.

This effect is then clearly not limited to the null-point, but acts throughout the CDC region. Figure 4.3 shows the flux tube volume (V) and the frequently utilized entropy quantity PV^γ [Wolf *et al.*, 2006] integrated along field lines and mapped into the plane $z = -2 R_E$.

Both quantities exhibit clear maximal values localized around the region of large magnetic shear. In the $z = -2$ plane, this region extends $\sim 3 R_E$ in the y -direction (along

the current sheet), and approximately half that in the Sun-Earth direction. This rather large extent, particularly considering that this is mapped into a plane 1-2 R_E below the reconnection site, suggests that the effect is substantial in the cusp region and is not limited to the immediate vicinity of the null-point, but extends along the entire current sheet.

4.5 Discussion and Conclusion

The presence of the extended region of strongly depressed magnetic field in the high altitude magnetospheric cusp region (often referred to as the cusp diamagnetic cavity or CDC) presents a unique configuration in which reconnecting magnetic flux tubes may gain a significant amount of flux tube entropy ($H = p^{1/\gamma}V$) through topological changes, whereby the reconnected flux tubes thread the CDC. As evidenced by the extent of the region within which both the flux tube volume and the entropy quantity (PV^γ) exhibit enhancements in the mappings of Figure 4.3, the region over which the effect is appreciable is rather expansive. The obvious dependence on the magnetic field magnitude implies that the effect is far more pronounced for anti-parallel merging than for component merging, wherein, given a sufficiently strong guide field, the total magnetic field strength near the x-line need not present a significant reduction.

Strong agreement between recent MHD and PIC results indicate that flux tube entropy is well conserved so long as resistivity is sufficiently localized in the former [Birn *et al.*, 2006]. Assuming the conservation of flux tube entropy outside the diffusion region, this further implies that magnetospheric flux tubes reconnecting in the vicinity of the cusps may map farther into the tail than those undergoing component merging.

4.6 Acknowledgements

Support for this research was provided by NASA grants NNG06GG89Gprog07 and NNX09AI09Gprog2010 to the University of Alaska Fairbanks.

Bibliography

- Adamson, E., A. Otto, and K. Nykyri, 3-d mesoscale mhd simulations of a cusp-like magnetic configuration: method and first results, *Annales Geophysicae*, 29(5), 759–770, doi:10.5194/angeo-29-759-2011, 2011.
- Birn, J., M. Hesse, and K. Schindler, Entropy conservation in simulations of magnetic reconnection, *Physics of Plasmas*, 13(9), 2006.
- Birn, J., M. Hesse, K. Schindler, and S. Zaharia, Role of entropy in magnetotail dynamics, *J. Geophys. Res.*, 114(A00D03), doi:0.1029/2008JA014015, 2009.
- Borovsky, J. E., M. F. Thomsen, R. C. Elphic, T. E. Cayton, and D. J. McComas, The transport of plasma sheet material from the distant tail to geosynchronous orbit, *J. Geophys. Res.*, 103(A9), 20,297–20,331, 1998.
- Erickson, G. M., A quasi-static magnetospheric convection model in two dimensions, *J. Geophys. Res.*, 97(A5), 6505–6522, 1992.
- Johnson, J. R., and S. Wing, Northward interplanetary magnetic field plasma sheet entropies, *J. Geophys. Res.*, 114(A00D08), doi:10.1029/2008JA014017, 2009.
- Schindler, K., and J. Birn, MHD stability of magnetotail equilibria including a background pressure, *J. Geophys. Res.*, 109(A10208), doi:10.1029/2004JA010537, 2004.
- Wing, S., and J. R. Johnson, Introduction to the special section on entropy conservation and constraints related to space plasma transport, *J. Geophys. Res.*, 115(A00D00), doi:10.1029/2009JA014911, 2010.
- Wolf, R. A., V. Kumar, F. R. Toffoletto, G. M. Erickson, A. M. Savoie, C. X. Chen, and C. L. Lemon, Estimating local plasma sheet pv^γ from single-spacecraft measurements, *J. Geophys. Res.*, 111(A12218), 2006.

Chapter 5

Conclusions

Since their inception in early magnetospheric models [Chapman and Ferraro, 1931a,b], the magnetospheric cusps have been regarded as a key feature of the Earth's "magnetic oasis in space" (i.e., the magnetosphere). It was early suggested that these cusps represented the most direct point of entry for solar wind plasma, though the specifics of plasma entry and transport in the region have been controversial, particularly due to a lack of understanding of the physical structures governing the interaction of the cusp with the adjacent magnetosheath. Because of the reduced geomagnetic field in the high-altitude region, the magnetopause has been thought to sag inward, suggesting that the tailward edge of the cusp then represents a further obstacle in the path of the shocked solar wind streaming past the magnetopause in the magnetosheath region [Haerendel et al., 1978; Haerendel, 1978]. This concept led researchers to theorize the existence of a complicated system of shocks, and waves in order to accommodate the expected flow characteristics [Walters, 1966; Yamauchi and Lundin, 2001; Taylor and Cargill, 2002].

The Earth's magnetospheric cusp regions are quite complex, and thus rich in physics. The complexity of the region is largely due to the intricate structure of the local geomagnetic field, but is further complicated by variations in the adjacent solar wind plasma as well as through the process of magnetic reconnection which injects solar wind plasma into the magnetosphere. As a result of this plasma streaming into the high altitude cusp region, particle precipitation into the ionospheric footprint of the converging dipolar field lines is observed at high-latitudes, in the vicinity of observed ion outflows, suggesting a possible connection. Energetic particles in the cusps (CEP's) present a further challenge: the energization mechanism for these populations is not understood (though a number of theories have been asserted), nor is it known what implications they may have on the magnetosphere. It is however, well accepted that magnetic reconnection plays a critical role in the vicinity of the cusps and is likely responsible for much of the dynamics in the region, as this is commonly regarded as the dominant process allowing for plasma entry.

Our understanding of the cusp region has grown immensely through early satellite missions and theoretical work, and more recently as a result of the Polar and Cluster 2 missions. However there remain many outstanding questions with regard to these important regions:

- What is the exact structure of the high-altitude cusp region?
- How do solar wind parameters govern the dynamics of the region?
- To what extent does reconnection dictate the flow structure in the cusp?
- What is the physical nature of the CDC boundaries?
- CEP's
 - What is/are the acceleration mechanism(s)?
 - where do they go?
 - what effects do they have on the magnetosphere as a whole?
- What is the eventual fate of cusp plasma?

As satellite coverage of the region has improved, so has our understanding. However, spacecraft only record measurements along a one-dimensional trajectory in space-time. In recent years, with the advent of multi-spacecraft missions (e.g., Cluster, Double Star, THEMIS, etc.) we have been able to obtain multiple data-points concurrently from different spatial locations. This has greatly improved the ability of researchers to infer satellite locations with regards to specific magnetospheric structures, however it can still present a challenge: though a spacecraft may find itself in a relatively similar location relative to the Earth on consecutive orbits, it may be in an entirely different region of the magnetosphere due to the dynamic nature of the structure. To this end, magnetospheric models play a vital role in understanding the individual structures within the Earth's magnetosphere and it is extremely useful to address the region through the use of numerical simulations.

Reports of CDC size have varied significantly in the literature. For example, Lavraud et al. [2004] measured a width of $1.5 R_E$ with the Cluster spacecraft at an altitude of $\sim 8.8 R_E$, while Fritz et al. [2003] estimated the size to be as large as $6 R_E$ at an altitude of $6-8 R_E$. The CDC region as realized in the simulation results appears as a shallow structure on the order of $1-2 R_E$ normal to the magnetopause, but much more expansive ($\sim 5-9 R_E$) in the transverse direction. These results give a clear explanation for such large variations in reported CDC sizes from spacecraft at traversing the high altitude cusp at different altitudes and with differing trajectories. Indeed, Walsh et al. [2011] have recently

presented a case study based on simultaneous measurements of the cusp region from both the Cluster spacecraft constellation and the Polar spacecraft. Based on measurements from these five spacecraft, the authors describe a CDC spanning a distance of at least $4.5\text{--}9 R_E$ along the magnetopause with a depth of $1.3 R_E$.

The results presented herein paint a picture of the CDC as an attached feature of the high altitude cusp region, bounded on its exterior by a transition with the magnetosheath which is Alfvénic in nature and exhibits characteristics consistent with a slow shock (nearly a switch-off slow shock) across which plasma is transported from the magnetosheath into the magnetosphere. The nature of this outer boundary has remained elusive for some time. It was initially suggested that the region would require a number of shocks and waves in order to generate the observed local flow characteristics. However, more recent results, for instance those reported by Lavraud et al. [2002] and Cargill et al. [2004], have found evidence for an Alfvénic transition (though values of the Walén relation were not conclusive) suggesting that the boundary may be a rotational discontinuity (RD) typically associated with magnetic reconnection. However, the authors found that the variation of plasma parameters was not consistent with the expectations for a simple RD, but were more consistent with an intermediate transition or a slow-shock. Cargill et al. [2004] also noted that the parameter jumps were largely consistent with a slow shock if the Alfvénic character were neglected. We note that this apparent dual nature (Alfvénic and slow-shock-like) may be understood by noting that the tangential components of the magnetic field are nearly switched-off, as expected of a switch-off slow-shock, wherein the Walén relation is approximately satisfied.

While the outer boundary between the CDC and magnetosheath appears as a distinct transition, the inner boundaries of the cusp form a funnel shape and are seen as gradual transitions in plasma parameters from typical magnetospheric values to those more comparable with the magnetosheath. There is evidence that this boundary may be a tangential discontinuity (Cargill et al., 2005, for instance). However, simulation results suggest this may not be the case closer to the reconnection site where characteristics are more suggestive of reconnection associated shocks extending from the reconnection site at the magnetopause towards the cusp funnel along the bottom edge of the CDC. Such a configuration would be reminiscent of the shocks in the Petschek model of magnetic reconnection [Petschek, 1964],

but in a highly asymmetric configuration, wherein the transition appears as a slow shock in the vicinity of the reconnection site, while farther away it appears more like a tangential discontinuity. Higher resolution in future work may allow for a more detailed analysis of this structure.

Additionally, the CDC exhibits a clear dependence on the IMF both in terms of its size and its location. The simulation results presented herein reveal a larger CDC under northward IMF conditions in comparison with southward IMF conditions consistent with results of Zhou et al. [2000] and Newell and Meng [1987], which show a similar narrowing of the cusp under southward IMF conditions relative to northward IMF. This difference in size may be understood in terms of the direction of magnetosheath flow relative to the convective motion of newly reconnected magnetic flux. Under southward IMF orientation, the reconnection site is located on the dayside of the cusp. The reconnection process generates local $\mathbf{j} \times \mathbf{B}$ forces which eject plasma from the vicinity of the x-line, thus forming the outflow regions. Plasma on the sunward side of the x-line are swept around the flanks of the dayside magnetosphere due to the oncoming solar wind flow in the magnetosheath. The plasma outflow on the cuspward side of the x-line however is largely aligned with the streaming magnetosheath flow, and is thus swept along with it, tailward. Conversely, for northward IMF the reconnection site is located on the tailward edge of the cusp. The newly-reconnected magnetic field lines on the tailward edge of the reconnection site move further tailward with the streaming magnetosheath plasma, while the reconnected field lines on the cusp-side of the reconnection site are ejected towards the cusp, in opposition to the streaming magnetosheath plasma. Thus, the plasma tends to accumulate more within the high altitude cusp region under northward IMF conditions than under southward conditions. Of course, the IMF is not limited to northward and southward orientations, begging the question: "what about eastward or westward IMF?". Though strongly flank-oriented IMF orientations have not yet been examined in the model, it is of course possible. Results from simulations with a larger IMF y -component indicate that the reconnection site rotates around the cusp funnel with the IMF. This suggests the strong possibility for the growth of Kelvin-Helmholtz instabilities due to favorable local conditions ($\mathbf{v} \perp \mathbf{B}$). Indeed, these results reveal the growth of vortex-like structures along the magnetopause toward the flanks. The current grid specifications, however, render cases with a dominant y -component

somewhat challenging due to the rather small simulation domain, and it may be necessary to expand the domain in order to undertake simulations of such configurations in the future.

Due to the local nature of these cusp simulations, the transport of cusp plasma within the magnetosphere cannot be directly addressed. However, the results do have implications with regard to the eventual fate of cusp plasma. Simulation results have demonstrated that reconnection in the vicinity of the magnetospheric cusps can realize a significant increase in the entropy content of magnetic flux tubes as evidenced through the quantity $(p^{1/\gamma}V)$. In this configuration, field lines undergoing antiparallel reconnection near the null-point should relax further downtail than those undergoing component reconnection due to the differences in flux tube entropy.

The results presented herein suggest that the region is largely structured by reconnection processes (through concurrent anti-parallel and component merging) at the magnetopause, largely under the control of the IMF. With evidence mounting for the role played by reconnection in forming this outer boundary, it may be more appropriately regarded as the magnetopause [Onsager et al., 2001; Lavraud et al., 2004; Cargill et al., 2004], whereas the more gradual inner boundaries, as noted by Lavraud et al. (2004), appear more consistent with the traditional magnetopause [Paschmann et al., 1976; Haerendel et al., 1978; Russell, 2000].

5.1 Limitations of the Model and Future Considerations

The simulation results presented in this thesis are generally in good agreement with observations of the magnetospheric cusp region, with a few exceptions. Observations show a stronger gradient at the cavity boundary to the magnetosphere, though indeed typically more gradual than the outer boundary. Currently, it is not clear whether the more gradual transition in the simulation is caused by the limited resolution (note, however, that the simulation already has a much higher resolution than, for instance, global models) or by physics not contained within the model. It should be noted that the ion inertial scale in the CDC region is ~ 70 km, as compared to the typical system scale of 6000 km. Thus, the neglect of the Hall term is certainly justified in such an initial description of the system. However, inclusion of the Hall effect is the next logical enhancement to the simulation and it is expected that such a treatment would realize smaller scale current sheets and thus, possibly

less gradual transitions defining the inner boundaries of the CDC with the magnetosphere. The simulation also does not show the large amplitude fluctuations of observed cavities. The nature and cause of these fluctuations is also not clear in the observations and there are indications that several processes contribute such as rapid motion of cavity boundaries, transient events, such as magnetic flux bundles moving along the cavity, or waves within the cavity or at the cavity boundary. Several of these mechanisms can be explored in our model and it is conceivable that such inputs may indeed explain the observed fluctuations. It is worth noting that in the model the magnetosheath plasma has a very low perturbation level different from the actual magnetosheath where perturbations are typically of order 1.

The lack of dipole tilt in the model makes it somewhat unclear as to exactly how these results are to be interpreted in terms of observations with respect to magnetosheath flow. It is plausible that the inclusion of a more physical dipole tilt in the model could alter the geometry of the magnetopause adjacent to the high-altitude cusp as the result of increased normal flow. In addition, results presented herein have considered sub-Alfvénic to marginally-Alfvénic ($M_A \approx 1$) magnetosheath flow, whereas flow in the magnetosheath frequently realizes super-Alfvénic speeds. Further consideration of magnetosheath flow with $M_A > 1$ may significantly alter results, particularly in terms of the geometry of the outer boundary. Simulations realizing such flows are, however, more challenging to undertake, particularly for strongly northward IMF orientations wherein the super-fast flow can potentially sweep the reconnection site tailward and out of the simulation domain. In this sense, the simulations for southward IMF lie within a somewhat more physical parameter regime as the magnetosheath flow is slowed at the nose of the magnetosphere, but regains much of its magnitude with increasing latitude. Super-Alfvénic magnetosheath flows also complicate the consideration of boundary conditions as it becomes difficult to maintain an appropriate transition from magnetospheric plasma to the fast-flowing magnetosheath. Again here, a larger simulation domain may ease the constraints placed on the simulations due to these issues.

Additionally, the field-aligned flows observed for northward IMF appear to be of a significantly larger magnitude than those exhibited in the model. This is likely attributable to the low density asymmetry between the magnetosphere and magnetosheath. Results of simulations realizing a more physical density distribution exhibit flows which are consistent

with those observed in the region. These more asymmetric configurations, however result in a shorter physical evolution of the system (due to an increased normalized Alfvén speed and thus a reduced normalized Alfvén time). This initial density prescription could be modified in future work such that a larger value is employed for the density normalization, while retaining the larger (and thus more physical) asymmetry, resulting in a longer system time-scale.

Finally, a word in regard to the reported CEP's periodically mentioned throughout this thesis. The results presented herein are based on a single-fluid MHD description of the high-altitude cusp region and, thus, clearly can not directly address the issue of local ion or electron energization. However, the fields that result from the fluid dynamics described by this model are currently being employed in so-called test-particle simulations with this exact goal in mind, results of which indicate significant particle energization in the region [Otto et al., 2007; Bhattacharya et al., 2009]. This process is the focus of research being conducted by current graduate student Julia Pilchowski at the Geophysical Institute, at the University of Alaska, Fairbanks.

Bibliography

- Bhattacharya, T., Otto, A., Adamson, E., and Nykyri, K.: Particle energization in cusp-like diamagnetic cavities, *Eos Trans. AGU*, pp. Abstract SM33A-1546, 2009.
- Cargill, P. J., Dunlop, M. W., Lavraud, B., Elphic, R. C., Holland, D. L., Nykyri, K., Balogh, A., Dandouras, I., and Reme, H.: CLUSTER encounters with the high altitude cusp: boundary structure and magnetic field depletions, *Ann. Geophys.*, 22, 1739–1754, 2004.
- Cargill, P. J., Lavraud, B., Owen, C. J., Grison, B., Dunlop, M. W., Cornilleau-Wehrlin, N., Escoubet, C. P., Paschmann, G., Phan, T. D., Rezeau, L., Bogdanova, Y., and Nykyri, K.: Cluster at the Magnetospheric Cusps, *Space Sci. Rev.*, 118, 321–366, doi:10.1007/s11214-005-3835-0, 2005.
- Chapman, S. and Ferraro, V. C. A.: A New Theory of Magnetic Storms, 1, The Initial Phase, *J. Geophys. Res.*, 36, 77, 1931a.
- Chapman, S. and Ferraro, V. C. A.: A New Theory of Magnetic Storms, 1, The Initial Phase (continued), *J. Geophys. Res.*, 36, 171, 1931b.
- Fritz, T. A., Chen, J., and Siscoe, G. L.: Energetic ions, large diamagnetic cavities, and Chapman-Ferraro cusp, *J. Geophys. Res.*, 108, 1028, doi:10.1029/2002JA009476, 2003.
- Haerendel, G.: Microscopic plasma processes related to reconnection, *J. Atmos. Terr. Phys.*, 40, 343–353, 1978.
- Haerendel, G., Paschmann, G., Sckopke, N., Rosenbauer, H., and Hedgecock, P.: The Frontside Boundary Layer of the Magnetosphere and the Problem of Reconnection, *J. Geophys. Res.*, 83, 3195–3216, 1978.
- Lavraud, B., Dunlop, M. W., Phan, T. D., Rème, H., Bosqued, J.-M., Dandouras, I., Sauvaud, J.-A., Lundin, R., Taylor, M. G. G. T., Cargill, P. J., Mazelle, C., Escoubet, C. P., Carlson, C. W., McFadden, J. P., Parks, G. K., Moebius, E., Kistler, L. M., Bavassano-Cattaneo, M.-B., Korth, A., Klecker, B., and Balogh, A.: Cluster observations of the exterior cusp and its surrounding boundaries under northward IMF, *Geophys. Res. Lett.*, 29, 2002.

- Lavraud, B., Phan, T. D., Dunlop, M. W., Taylor, M. G. G. T., Cargill, P. J., Bosqued, J.-M., Dandouras, I., Rème, H., Sauvaud, J.-A., Escoubet, C. P., Balogh, A., and Fazakerley, A.: The exterior cusp and its boundary with the magnetosheath: Cluster multi-event analysis, *Ann. Geophys.*, 22, 3039–3054, 2004.
- Newell, P. T. and Meng, C.-I.: Cusp width and $B(z)$ - Observations and a conceptual model, *Journal of Geophysical Research*, 92, 13 673–13 678, doi:10.1029/JA092iA12p13673, 1987.
- Onsager, T., Scudder, J., Lockwood, M., and Russell, C.: Reconnection at the high latitude magnetopause during northward interplanetary magnetic field conditions, *J. Geophys. Res.*, 106, doi:10.1029/2000JA000444, 2001.
- Otto, A., Adamson, E., and Nykyri, K.: Particle acceleration in cusp diamagnetic cavities, *Eos Trans. AGU*, 88, Abstract SM31B–0458, 2007.
- Paschmann, G., Haerendel, G., Sckopke, N., Rosenbauer, H., and Hedgecock, P.: Plasma and Magnetic Field Characteristics of the Distant Polar Cusp near Local Noon: The Entry Layer, *J. Geophys. Res.*, 81, 2883–2899, 1976.
- Petschek, H. E.: Magnetic Field Annihilation, *NASA Special Publication*, 50, 425, 1964.
- Russell, C. T.: Polar Eyes the Cusp, Cluster-II Workshop: Multiscale/Multipoint Plasma Measurements, *Proceedings of the Workshop held at Imperial College, London, UK, 22-24 September 1999*, 449, 47, 2000.
- Taylor, M. G. G. T. and Cargill, P. J.: a magnetohydrodynamic model of plasma flow in the high-altitude cusp, *J. Geophys. Res.*, 107, 1084, doi:10.1029/2001JA900159, 2002.
- Walsh, B. M., Fritz, T. A., and Chen, J.: Simultaneous observations of the exterior cusp region, *Journal of Atmospheric and Solar-Terrestrial Physics*, doi:10.1016/j.jastp.2011.08.011, 2011.
- Walters, G. K.: On the Existence of a second standing shock wave attached to the magnetosphere, *J. Geophys. Res.*, 71, 1341, 1966.
- Yamauchi, M. and Lundin, R.: Comparison of various cusp models with high- and low-resolution observations, *Space Sci. Rev.*, 95, 457–468, 2001.

Zhou, X. W., Russell, C. T., Le, G., Fuselier, S. A., and Scudder, J. D.: Solar wind control of the polar cusp at high altitude, *J. Geophys. Res.*, 105, 245–251, 2000.

Appendix A

Cluster Observations of a Cusp Diamagnetic Cavity: Structure, Size and Dynamics¹

Abstract

We have analyzed Cluster magnetic field and plasma data during high-altitude cusp crossing and compared with high-resolution MHD simulations. Cluster encountered a diamagnetic cavity (DMC hereafter) during northward IMF conditions and as the IMF rotated southward, the spacecraft re-encountered the cavity more at the sunward side of the cusp because the reconnection site had changed location. We found evidence of magnetic reconnection both during northward and southward IMF conditions. The Cluster separation was ~ 5000 km enabling for the first time measurements both inside the DMC and surrounding boundaries that allowed us to construct the structure of the DMC and put the observations of ion pitch angle distributions in context of local reconnection topology and gradients of the boundaries. The cavity is characterized by strong magnetic field fluctuations and high energy particles. At the magnetosheath boundary the high energy particle (HEP) fluxes reduced several orders of magnitude. Throughout the magnetosheath, the high-energy proton fluxes remained low except during brief intervals when sc4 and sc1 dropped back into cavity due to changes in solar wind dynamic pressure. However, the high-energy O⁺ fluxes did not drop as much in the magnetosheath and were mostly at 60-120 degree pitch-angles, indicative of a trapped population in DMC which is observed in the magnetosheath due to large gyro radius. Significant fluxes of protons and ionized oxygen were also observed escaping from diamagnetic cavity anti-parallel to magnetic field in a time-scale consistent more with the local DMC source than reflected bow-shock source.

A.1 Introduction

The geomagnetic cusps are a key structural elements of the magnetospheric boundary layers and the magnetosheath plasma has the most direct access to the ionosphere through high-altitude cusps [Heikkilä and Winningham, 1971; Frank and Ackerson, 1971]. Prior to four spacecraft, multi-instrument Cluster mission, in situ measurements of the cusps and high-latitude magnetopause were provided by HEOS, ISEE2, Hawkeye, Polar and Interball

¹Nykyri, K., Otto, A., Adamson, E., Dougal, E., Mumme, J., J. Geophys. Res., 116, A03228, 2011.

missions [e.g. *Paschmann et al.*, 1976; *Gosling et al.*, 1991; *Kessel et al.*, 1996; *Dunlop et al.*, 2000]. Of particular interest has been the identification of lobe reconnection [*Gosling et al.*, 1991; *Kessel et al.*, 1996; *Scudder et al.*, 2002; *Fuselier et al.*, 2000; *Russell et al.*, 2000] and the spatial extent of the cusp [*Zhou et al.*, 1999, 2000]. The cusps also exhibit significant magnetic field fluctuations which can be created by solar wind (bow shock) perturbations, magnetic reconnection or intrinsic instabilities present in the cusp [*Savin et al.*, 1998; *Chen and Fritz*, 1998; *Le et al.*, 2001; *Savin et al.*, 2002, 2004].

Cluster has been ideal for studying the high- and mid-altitude cusps. Cluster has revealed for the first time many important observational aspects of the structure of the high-altitude cusps, and especially how they are related to the prevailing solar wind and IMF conditions [e.g. *Lavraud and Cargill*, 2005; *Cargill et al.*, 2005; *Lavraud et al.*, 2005]. For Northward IMF, a picture is emerging of a cusp influenced by lobe reconnection [*Vontrat-Reberac et al.*, 2003; *Twitty et al.*, 2004; *Lavraud et al.*, 2005] with Earthward-directed plasma jets being observed, but also containing regions of stagnant plasma [*Lavraud et al.*, 2002, 2004]. On the other hand, for Southward IMF, the cusp is dominated by tailward convection due to sub-solar reconnection [*Cargill et al.*, 2004].

One particularly interesting aspect of the cusp encounters have been the observations of extensive regions of magnetic field fluctuations seemingly associated with Earthward-directed plasma flows generated by lobe reconnection. These flows are observed near the boundary between the cusp and lobe, where the magnetic field is still quite large ~ 100 -60 nT [*Nykyri et al.*, 2003a, 2004; *Sundkvist et al.*, 2005; *Nykyri et al.*, 2006a]. The level of fluctuations appears to correlate with the magnitude of the flows and the ion number flux, and also shows wave activity with strong peaks at the ion cyclotron frequency. The role that these waves play in heating, scattering and transport is still unclear. The energy level in these waves close to ion cyclotron frequency is small and assuming a complete dissipation of the wave with an amplitude of 5 nT in plasma density of $10/\text{cm}^3$, one would expect a temperature increase of 10^5 K which is insignificant compared to measured temperatures in the cusp which are typically 2-10 MK. However, these waves may have sufficient energy to accelerate a small fraction of the distribution. In addition statistical study of the properties of the exterior cusp has shown that the magnetic field fluctuations are closely associated with the magnetic shear angle, which indicates that the large-amplitude fluctuations in the

high-latitude exterior cusp region are mainly produced by the high-latitude reconnection process [Zhang *et al.*, 2005]. Our observations of reconnection signatures in the present paper and in Nykyri *et al.* 2010b (submitted to JGR) are in agreement with this result.

Despite these advances, there are still unresolved questions concerning the cusp physics. Probably the biggest is on the origin of cusp energetic particles (CEPs) observed at the high-altitude cusp during intervals of strongly depressed magnetic field [Chen and Fritz, 1998]. These regions of depressed magnetic field at high-altitude cusp are called diamagnetic cavities, DMC hereafter and they are frequently occupied by high-energy particle populations [Chen and Fritz, 1998; Fritz *et al.*, 1999; Chen and Fritz, 2001; Zhang *et al.*, 2005; Whitaker *et al.*, 2006, 2007; Walsh *et al.*, 2007; Niehof *et al.*, 2008; Walsh *et al.*, 2010]. Zhang *et al.* [2005] showed that high energy ions above 28 keV are present most of the time while high-energy electrons are less frequent. Currently there are three schools of thought on the origin of these high-energy populations: 1) Local acceleration [Chen and Fritz, 1998; Chen, 2008], 2) bow-shock source [Chang *et al.*, 1998, 2000; Trattner *et al.*, 2001], 3) Magnetospheric source [Sibeck *et al.*, 1987; Fuselier *et al.*, 1991; Asikainen and Mursula, 2005, 2006].

Chen and Fritz [1998] have suggested that energetic ion populations are generated by acceleration via ULF wave turbulence present in DMC's. In order to understand the physical mechanisms that could accelerate the ions in the cusp one needs first to identify what is the 'turbulence' in the DMCs. We demonstrate in this paper and in Nykyri *et al.* 2010b (submitted to JGR) that what looks like 'turbulence' in the time series is in fact mostly motion of the structure by spacecraft.

Our motivation for the present study has been to identify the source for the high-energy particles in the cusp diamagnetic cavity and obtain a better understanding of reconnection dynamics, structure, fluctuations in the cavity, formation and re-formation of the cavity for changing IMF orientation, and properties of ion distribution functions and high-energy particles in relation to cavity boundaries. In order to find an event with simultaneous measurements in the cavity and surrounding magnetosheath we searched through Cluster spacecraft orbits between 2001-2005 in order to find a perfect event where the IMF changes from northward to southward and spacecraft separation is large enough to study plasma properties simultaneously in the DMC and in the magnetosheath.

Our survey indicates that Cluster encountered clear DMC's only when the dynamic pressure of the solar wind was high enough (typically above ~ 2 nPa). During many (about one third) of the high-altitude cusp crossings Cluster observes a magnetic field that is not depressed like during DMC's but gradually decreases from ~ 100 nT to ~ 20 nT. This is due to the Cluster orbit. For Polar spacecraft, that observes DMC's most of the time during high-altitude cusp crossing and for extended time periods, the DMC is in the apogee of the orbit so Polar moves very slowly through this region. Cluster moves faster through this region and at lower altitude during part of the orbit, so it only 'sees' clear diamagnetic cavity during intervals of enhanced dynamic pressure.

We have divided the material of this study into three papers. The present paper discusses the structure, size and dynamics of cusp diamagnetic cavity, the second paper focuses on analysis of the magnetic field fluctuations in the DMC [Nykyri *et al.*, 2010b, submitted to *JGR*], and the third paper discusses the high-energy particle observations in the DMC [Nykyri *et al.*, 2010c, submitted to *JGR*]. In order to explain the high-energy particle observations a good understanding of reconnection structure, dynamics and boundary normal orientations is needed.

The paper is organized as follows. Section 2 describes the instrumentation and data-analysis tools, section 3 discusses an overview of the event, section 4 describes the reconnection dynamics and observations, section 5 describes the structure of the cavity and analysis of 'sheath intervals' that show presence of high-energy particles, section 6 concludes the study and Appendix illustrates the method used in determination of stability and error estimates of the boundary normals that are used in determining the size and orientation of the boundaries in the DMC.

A.2 Instrumentation and Data-Analysis Tools

We use data from four instruments on Cluster. From each spacecraft, we use magnetic field measurements from the Flux Gate Magnetometer (FGM) [Balogh *et al.*, 2001], with a sampling rate of 4 vectors /sec; ion spectra and moments from the Cluster Ion Spectrometer (CIS) [Rème *et al.*, 2001] from spacecraft 1 (sc1), 3 (sc3) and 4 (sc4) and energetic particle data from RAPID (Research with Adaptive Particle Imaging Detectors) spectrometer [Wilken *et al.*, 2001]. We use 4 second time resolution data for temperature, velocity and

density from the Hot Ion Analyzes (HIA) on sc1 and sc3. The HIA data has some data gaps that are linearly interpolated. The longest (shortest) data-gaps are 48 seconds (4 seconds) in duration. The proton velocity, temperature and densities for sc4 are obtained from the ion COmposition and DIstribution Function analyser (CODIF) for every 4 seconds and 8 seconds during some intervals. Our data analysis tools use the deHoffman-Teller (HT) analysis and the Walén relation [Sonnerup *et al.*, 1995]. The HT frame is a frame where the convection electric field vanishes, thus indicating an approximately steady state plasma configuration. The electric field for the HT plots is calculated from $-\mathbf{v}_{\text{obs}} \times \mathbf{b}_{\text{obs}}$, where \mathbf{b}_{obs} and \mathbf{v}_{obs} are obtained from FGM and CIS data, respectively. The HT velocity, \mathbf{v}_{HT} , is determined by minimizing $|(\mathbf{v} - \mathbf{v}_{\text{obs}}) \times \mathbf{b}_{\text{obs}}|^2$ in terms of the constant transformation velocity \mathbf{v} for a given data-set [Sonnerup *et al.*, 1995]. In order to obtain a slope for the HT frame a linear least squares fit is calculated for the data set: electric field components on the y -axis and HT-electric field on the x -axis.

The Walén relation is calculated in the HT frame as $\mathbf{v} - \mathbf{v}_{\text{HT}} = \pm C \mathbf{v}_A$ and implies that in the HT -frame the plasma flow velocity is Alfvénic [Sonnerup *et al.*, 1995]. The Alfvén velocity, $\mathbf{v}_A = \mathbf{B} / \sqrt{(\mu_0 n_p m_p)}$, is corrected by factor $C = \sqrt{(1 - \alpha)}$, where $\alpha = (T_{\parallel} - T_{\perp}) n_p k_B \mu_0 / B^2$ is the pressure anisotropy correction [e.g. Sonnerup *et al.*, 1981]. The Walén relation is satisfied for Alfvén waves, rotational discontinuities, but also approximately for intermediate and switch-off slow shocks. These phenomena are often associated with magnetic reconnection.

The boundary normal directions are calculated using the minimum variance of the magnetic field (MVAB), maximum variance of the electric field (MVAE) [Sonnerup and Scheible, 1998] and Minimum Faraday Residue (MFR) method [Khrabrov and Sonnerup, 1998]. Haaland *et al.* [2004] used MFR method and compared it with other single- and multi-spacecraft methods for the magnetopause event. They found that multi-spacecraft technique Constant Thickness Approach (CTA) and a hybrid technique CTAM gave reasonably good agreement ($\approx 5^\circ$) with MFR -method. For our event, the dominant magnetic field and the dominant plasma velocity are tangential to the boundary layer such that the maximum variance for the convection electric field should be normal to the layer.

A.3 Overview of the Cusp Encounter

The DMC crossings are on the outbound leg of Cluster orbit in the Northern hemisphere at $\sim 8 R_E$ altitude. Cluster trajectory and constellation (magnified by factor of 3) in GSM coordinates are presented in Figure A.1. Cluster spacecraft separation is ~ 5000 km enabling simultaneous multi-point observations of plasma and magnetic field properties both inside and outside the cusp DMC. Spacecraft 4 (sc4 hereafter) is leading the constellation (blue), followed by sc2 (red), sc1 (black) and sc3 (green), respectively.

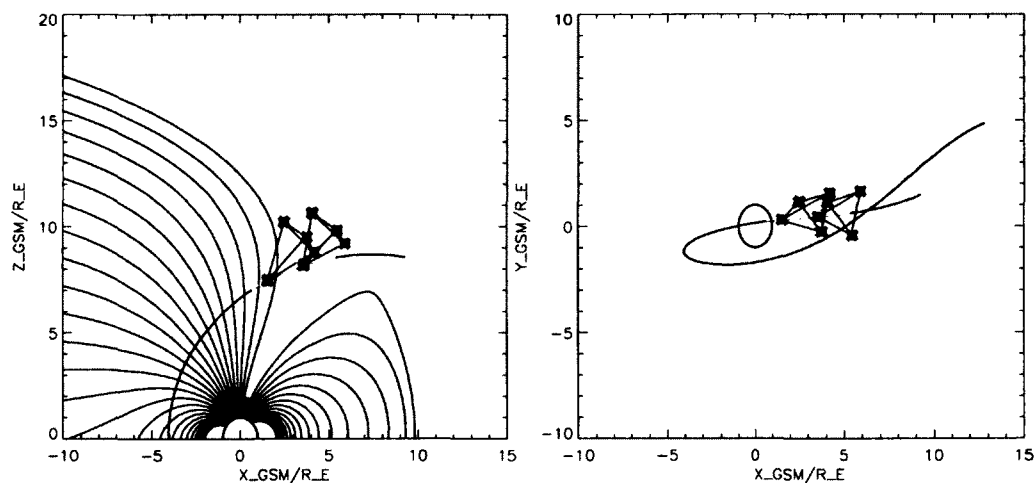


Figure A.1. Cluster trajectory on 14th of February 2003 is plotted on top of the magnetic field lines from Tsyganenko 89 model (T89) in GSM coordinates in xz -plane (left) and trajectory and constellation are plotted in xy -plane (right). The T89 model uses the Kp -index of four. The circle is the Earth, the yellow line depicts Cluster trajectory between 18:00-21:00 UT and Cluster constellation (magnified by factor of 3) is drawn with respect to sc3 position at 18:30 UT and at 19:45 UT.

The overview of the Cluster observations between 18:18-20:45 UT on 14th of February 2003 is presented in Figure A.2. The measurements of spacecraft 1, 2, 3 and 4 are marked with black, red, green and blue respectively. The plasma observations show from top to bottom ion number density, three components of the ion velocity, total ion velocity and ion temperature. The magnetic field components and total magnetic field measured by Cluster are plotted on top four panels of Figure A.2. Three components of the interplanetary magnetic field (IMF) (b_x , b_y , and b_z are marked with black, red and blue respectively) and

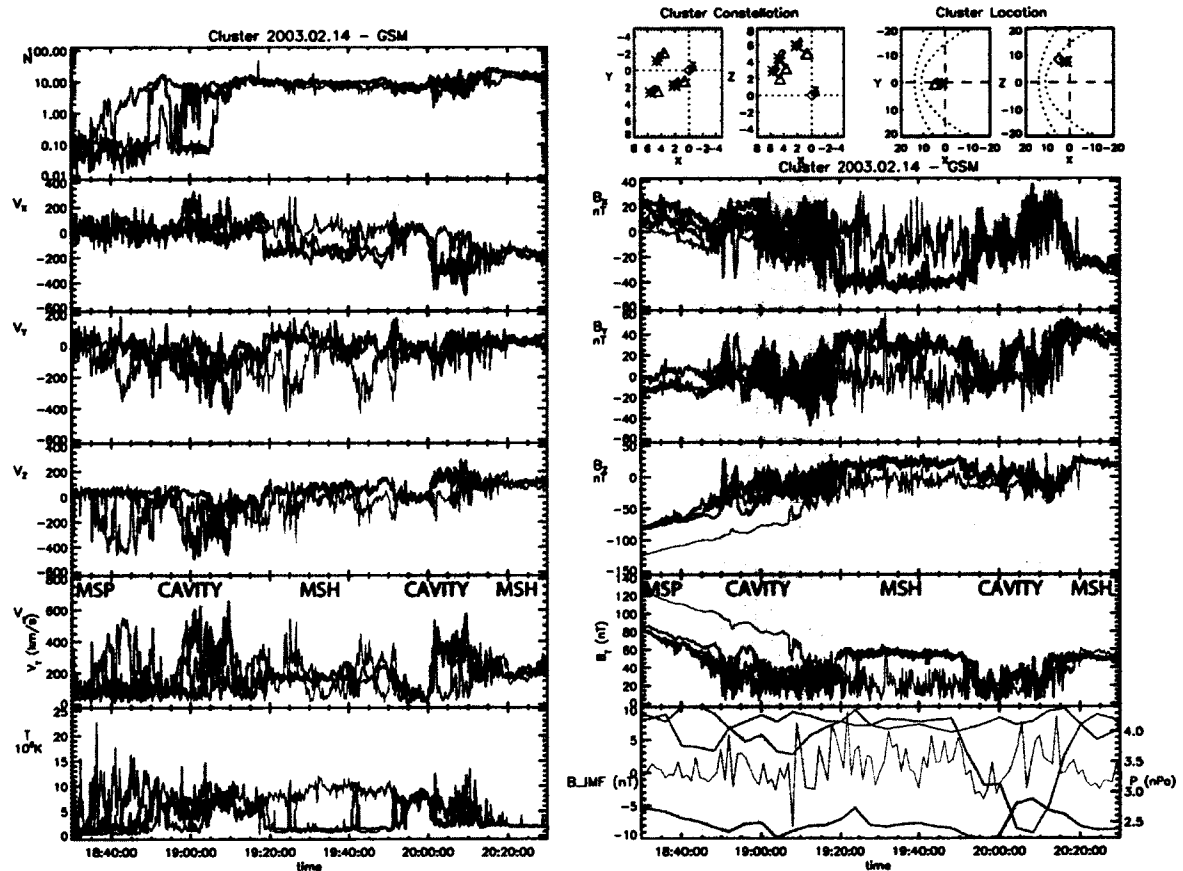


Figure A.2. Cluster plasma (on left) and magnetic field (on right) observations on 14th of February 2003. The four boxes at the top right show Cluster separation (units are in thousands of kilometers) from sc3 projected at *xy*-plane (1st box) and *xz*-plane (2nd box), and Cluster location (units are in Earth radius) at *xy*-plane (3rd box) and *xz*-plane (4th box). The approximate magnetopause and bow-shock locations are drawn as parabolas. The dynamic pressure of the solar wind (orange line) and the three components of the IMF measured by ACE spacecraft lagged by 44.0 minutes are plotted on the bottom right panel with black, red and blue corresponding to *x*, *y* and *z* components respectively.

dynamic pressure (orange line) measured by ACE spacecraft and lagged by 44.0 minutes are plotted on the bottom right side panel of Figure A.2. Initial timelag is calculated between 18:30-20:30 UT from $\Delta t = \Delta x / \langle v_x \rangle$ where Δx is the distance between ACE and Cluster along x -direction and $\langle v_x \rangle$ is the average of the x -component of the solar wind speed. This gives a timelag of ~ 49.1 minutes. This procedure is repeated for the ACE data that has been shifted by 49.1 minutes and this gives a new time lag of 48.9 minutes, which indicates that there was no big discontinuity in solar wind speed between 17:41-20:30 UT. The v_x in the solar wind during this shifted two hour interval varies between ~ -455 km/s and -515 km/s which can cause a difference of ~ 6 minutes in timelag estimates. We have used the time lag of 44 minutes in order to better match the main features in the Cluster data.

The lagged ACE data indicates that the IMF was strongly northward up to 19:48 UT, after which it starts to rotate southward reaching -9 nT at 20:06 UT. The IMF returns back northward reaching 7 nT by $\sim 20:19$ UT. The solar wind speed (not shown) is ~ 500 km/s and the dynamic pressure varies between 2.5-4.3 nPa.

The transition from the tail lobe magnetosphere (MSP) to the DMC is characterized by an increase of plasma density, enhanced magnetic field fluctuations, depressed total magnetic field, appearance of large field aligned plasma flows associated with lobe reconnection during prevailing northward IMF conditions and enhanced plasma temperature. Note that the cavity region is more pronounced here and the observed plasma temperatures are much higher than for the cusp crossing reported by *Lavraud et al.* [2002], which occurred during a low dynamic pressure of the solar wind. They also did not report any observations of high-energy particles during this crossing.

This transition from MSP to DMC occurs first for sc4 between 18:30-18:50 UT, followed by sc1 at 18:50 UT and finally by sc3 at 19:05 UT. There are no CIS measurements for sc2, but based on the magnetic field signatures, the transition to diamagnetic cavity occurs slightly earlier for sc2 than for sc1. This can be most easily seen as a sharp decrease of total magnetic field at 18:50 UT (at sc2) and at 18:51 UT (at sc1). Based on the density measurements, the transition from MSP to cusp is gradual at sc4, but is more abrupt at sc1 and at sc3. One can also notice that sc1 returns briefly back to the MSP at $\sim 18:55$ UT before finally returning back to the cavity. This is produced by back and forth motion

of the cavity boundary by sc1 due to dynamic pressure variations [Nykyri *et al.*, 2010b, submitted to JGR].

Sc1 and sc4 are in the cavity until $\sim 19:18$ UT after which they move to the magnetosheath. The transition into magnetosheath is probably mostly produced by dynamic pressure enhancement in the solar wind: during the first magnetosheath interval the average level of the dynamic pressure is higher than during the cavity intervals. The sharp pressure enhancement at 19:17-19:18 UT seem to be associated with sc1 and sc4 transition into magnetosheath which is followed by another pressure enhancement 19:21-19:22 UT which may be associated with sc2 transition into magnetosheath. The transition into magnetosheath may also be associated with the slight change in reconnection site because b_z is increased from previous cavity interval and the spacecraft have moved further sunward. For more northward IMF the cavity is formed more tailward (see later discussion on FigureA.3) which could partly explain (together with dynamic pressure enhancement) why three of the spacecraft move into magnetosheath. Note that sc3 remains in the cavity because it is furthest tailward but is also furthest away from magnetosheath along z -direction (is deepest in the cavity), so pressure variation does not move it into magnetosheath compared to those spacecraft that have a higher z -coordinate. Evidence for the change of reconnection site may be the fast flows observed by sc3 at $\sim 19:25$ UT. The magnetosheath is characterized as a steady tailward ion velocity (negative v_x), decreased ion temperature and increased magnetic field. The draping of the IMF around the magnetopause generates a strong negative b_x in the magnetosheath.

The lagged ACE data shows that IMF starts to rotate from northward to southward at $\sim 19:47$ which is also accompanied by the dynamic pressure decrease of 40 percent. The change of the reconnection site and dynamic pressure decrease can cause a motion of magnetopause and cavity boundaries such that sc1, sc2 and sc4 re-encounter the region of the depressed field. It seems that the transition into cavity is mostly due to changing IMF because the subsequent pressure increase that starts at $\sim 20:00$ UT is not adequate to move the spacecraft back into magnetosheath. The change of the reconnection site is further demonstrated with Walén relations and Hoffman Teller frame velocities in Section 4.

The last transition into magnetosheath seems to be associated with both: the sharp pressure increase at $\sim 20:14$ UT and the change of b_z from southward to zero. Note that

when pressure reduces by 20:15 UT, sc4 which is closest to cavity boundary drops back to weak field region but finally returns back to magnetosheath as the IMF has rotated more northward. During this strong northward IMF the cavity has moved so much tailward that even the large pressure decrease after 20:18 UT is not adequate to bring the spacecraft back into cavity.

We have used high-resolution local MHD cusp model [*Adamson et al., 2010a and b, submitted to JGR*] in order to see how the DMC depends on IMF orientation. Figure A.3 presents simulation results for northward (right) and southward (left) IMF orientation. The background color is magnetic field strength and sun is to the left. One can see that the region of depressed field is forming more sunward for southward IMF compared to northward IMF orientation. This can be explained by reconnection site changing location when IMF b_z turns from northward to southward. Note that these results are presented in simulation coordinates. Qualitatively this movement of DMC sunward with southward turning IMF agrees with the Cluster observations. Numerous studies have shown the motion of the cusp sunward with southward IMF in observations [*Burch, 1973; Newell and Meng, 1987; Palmroth et al., 2001b; Pitout et al., 2006; Niehof et al., 2010*] and in global MHD simulations [*Palmroth et al., 2001a*]. In our event sc3 remains in the cavity the entire time so the reformed cavity must overlap with the original one that was formed during $b_z > 0$.

Energy-time spectrograms of the high-energy particles measured by sc4 are presented in Figure A.4. The panels show omni-directional fluxes of electrons (top), protons (middle) and helium ions (bottom). Comparison of this figure with the total magnetic field measurements shown in Figure A.2 reveals that the high energy particles up to few hundred keV are present during the intervals with depressed magnetic field. The spacecraft have also brief re-encounters with the cavity-like plasma and high-energy particles during the 'sheath' intervals. An example of such interval can be seen between 19:45-19:50 UT at sc4 (also sc1 re-encounters the cavity during this interval (not shown)).

We have found several reconnection intervals with good HT frames satisfying the Walén relation for both northward and southward IMF orientation. In next section we will discuss the reconnection geometry and search for reconnection intervals in more detail.

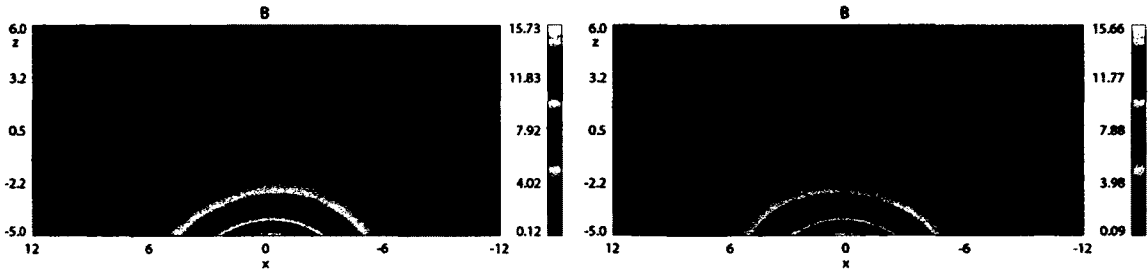


Figure A.3. MHD simulations of the cusp for southward (left) and northward (right) IMF. Sun is to the left. Background color is the total magnetic field strength. The region of depressed magnetic field (cavity) is forming more sunward when IMF is southward.

A.4 Fluid and Particle Evidence for Magnetic Reconnection

We have automated the search for reconnection intervals by applying a sliding window over the data between 18:30-20:30 UT and testing for a reconnection criteria. In order to ensure that we find most of the reconnection intervals, we have used window sizes of 90, 80, 70, 60, 54, 48, 42, 36, 30, 24, 18 and 12 seconds. A six second sliding is used for 30-90 second searches and a four second sliding for 12-24 second searches. We have required that the Walén slopes are between 0.7-1.1 for 30-90 second search intervals and 0.8-1.1 for 12-24 second search intervals, and that HT frame slopes are between 0.8-1.2. In addition we have required that the correlation coefficients for both tests are at least 0.9. The scatter plots, hodograms, and ion distribution functions of the search results are then examined. Because the data sampling frequency is 4 seconds, and magnetic field and plasma data is interpolated before calculating Walén relation and HT-frame velocity, some interval lengths recorded in Table 1 can be few seconds shorter or longer than length of the search window size. We have recorded information of the good reconnection intervals into Table 1 and have eliminated those intervals from the table that had a longer duration data-gap. If a 48 second window is embedded inside a 54 second window, so that both of these satisfy the search criteria, we have recorded the information of the interval having the better slopes and less scatter in Walén and HT-frame plots into Table 1. In case two intervals are partially overlapping, we have recorded information of the both. We have applied this search method for reconnection intervals before at the low latitude boundary layer [Nykyri *et al.*, 2006b].

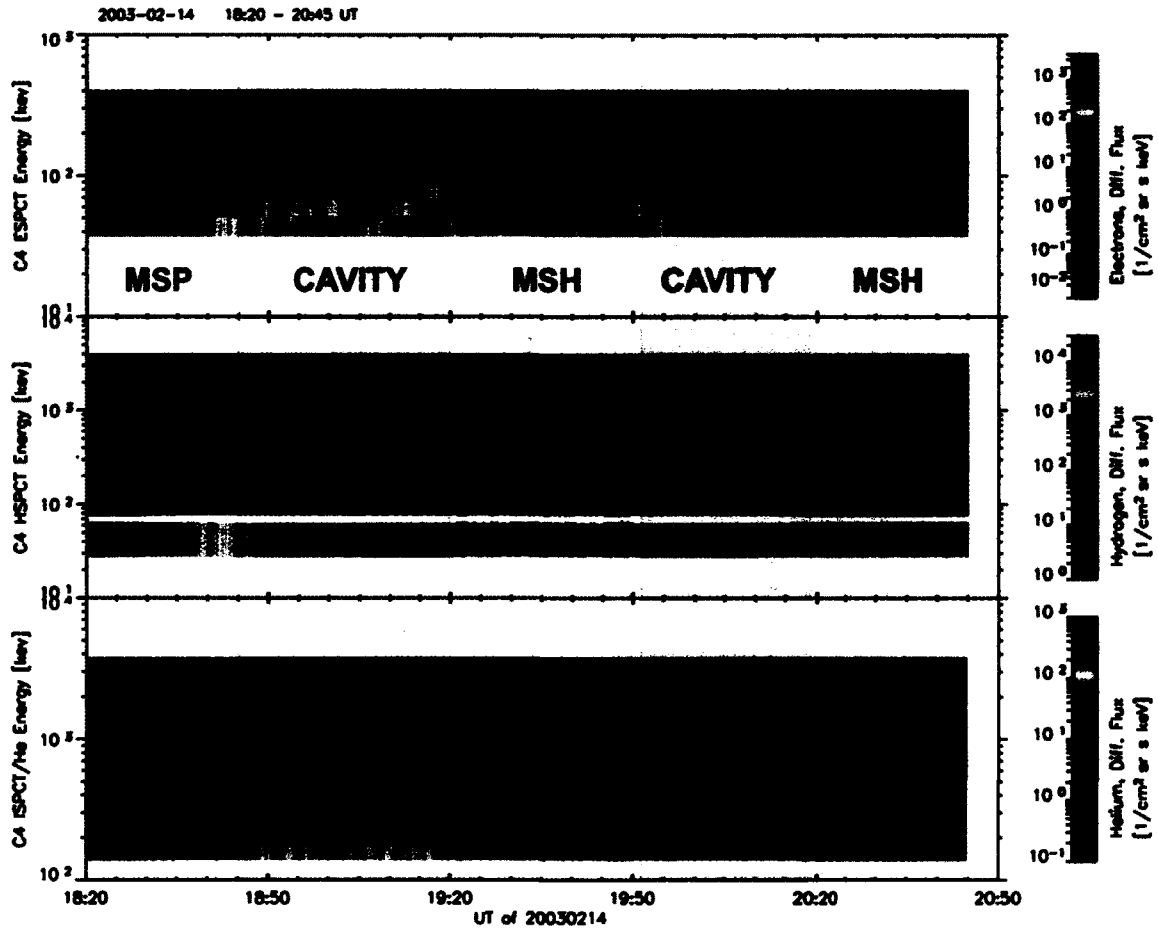


Figure A.4. Sc4 measurements of electron (top panel), proton (middle), helium (bottom) omni-directional fluxes at different energies between 18:20-20:45 UT.

A.4.1 Reconnection Signatures During Northward IMF

A.4.1.1 de Hoffman-Teller frame velocities and slopes of the Walén relations

One typical feature that this table shows is that most intervals during the first period of northward IMF (intervals up to $\sim 19:58$ UT) have HT velocities with positive v_x -component, negative v_y -component, and negative v_z -component, and most of the intervals during southward IMF (intervals between 19:58-20:15 UT) have HT velocities with negative v_x and v_y -components, and positive v_z components. The last three intervals after 20:15 UT are again during northward IMF but have negative v_x -components and positive v_y components of the

HT-velocity. These HT-velocities can be explained by the motion of the reconnected flux tubes originating from different reconnection sites surrounding the cusp funnel. Up to 19:58 UT and after 20:15 UT the IMF is northward and duskside (corresponding to a clock angle of ~ 45 degrees) and has a strong negative b_x -component, generating a region of largest magnetic shear at the tailward-duskside northern cusp. Reconnection in this geometry will result in two flux tubes moving approximately in opposite directions: one moving sunward and dawnward with positive v_x and negative v_y (type A), and another moving tailward and duskside with negative v_x and positive v_y (type B). The most intervals observed up to 19:58 UT are type A. All intervals after 20:15 UT have the slopes and v_x and v_y components consistent with type B reconnection, but the very large v_z and the spacecraft location are not consistent with type B lobe reconnection (see more discussion in section 4.3).

The v_z -components of the HT velocities for the type A intervals are mostly negative, although there are few intervals where they are positive. The angle between dipole tilt and z_{GSM} -axis is -3 degrees at 18:30 UT so the dipole points away from the sun, which together with the fact that dynamic pressure is high and variable may explain the observed positive v_z components during some of the type A-events: a pressure pulse can locally compress the magnetopause generating a magnetic tension force with positive z -component. This may also depend on what altitude the spacecraft are crossing the flux tube and how 'fresh' (e.g. how long ago it has reconnected) the flux tube is. For example sc4 observes a HT velocity of [77,-41,197] km/s at 19:05-19:06 UT when the SW dynamic pressure (shown in Figure 2), P_{dyn} , increases by 10 percent. P_{dyn} actually shows even larger 75 percent variations between 19:06-19:09 UT. Considering that solar wind v_x is also varying between -515 km and -455 km, some inaccuracies (order of 2-3 minutes) will follow when average solar wind speed is used in time lag estimation, so that this signature may be associated with the 75 percent pressure variation.

The slopes of the Walén relations depend on from which side of the x -line the spacecraft cross the reconnected flux tube. Crossing (or partial crossing) of the sunward moving flux tube originating from lobe reconnection (type A) would result in a positive slope, since the normal component of plasma velocity, v_N , and magnetic field, b_N , have the same sign. Most of the intervals have positive slopes during northward IMF.

A.4.1.2 Example of the reconnection interval during northward IMF

An example of a typical reconnection interval during northward IMF measured by sc1 is shown in Figure A.5. Panel a) is in the same format as Figure A.2 and shows plasma (left) and magnetic field (right) observations between 19:06-19:12 UT. A cartoon in Figure 6a shows how sc1 might be crossing the reconnected flux tube in xz -plane in order to explain the observed signatures in magnetic field and ion distribution functions (see caption for more details). The highlighted column in Figure A.5 depicts a 44 second time interval measured by sc1 satisfying the reconnection criteria. Because the flow in the magnetosheath is sub-Alfvénic and the IMF orientation is quite steady during 19:06-19:12 UT, the reconnection is occurring somewhat continuously generating flux tubes moving earthward and dawnward (type A) and tailward and duskside (type B). The observed HT-frame velocity has the strongest $-y$ -component, ~ -200 km/s, positive v_x and negative v_z , which is a signature of type A flux tube. During the 44 seconds, a single flux tube moves earthward a distance of $V_{HT} \cdot 44s = 1 - 1.65 R_E$ (probably feeling some resistance by the magnetosheath flow), so it is likely that several reconnected flux tubes are swept by sc1 during this interval.

Figure A.6a shows a cartoon of a time history of reconnected field lines ('1' refers to field line that reconnected first and '3' to a field line that is just reconnecting), relative trajectory of sc1 with respect to reconnected flux tubes and numbers c-e referring to measured distribution functions in Figure A.5. The ion distribution functions (panels c-f) show most flux in quadrants 1 and 2 (numbering scheme for quadrants is illustrated in panel c), indicating that particles are moving parallel to magnetic field and that the mirrored population is absent, which indicates that field lines are freshly reconnected. Eventually the sunward motion of the reconnected field lines gets reduced, which may explain the relatively small v_x component during the beginning of the interval and some reflected particles in ion distribution functions c)-e). As sc1 crosses more freshly reconnected field lines the v_x increases to 275 km/s and simultaneously the b_x rotates from -7 to 15 nT. One should also remember that the reconnection is happening at the duskside of the cusp so the actual motion of the field lines has the largest $-y$ -component. Finally we would like to note that highly variable dynamic pressure of the solar wind will make this entire region to oscillate in a time scale of 3-5 minutes, which would also result in relative motion of the reconnected flux tubes by the spacecraft. However, the b_z and b_y remain negative during this interval,

so sc1 is not crossing into the magnetosheath -side of the reconnected flux tube where the b_z and b_y should be positive for the prevailing draping geometry of the IMF. This is also consistent with the absence of anti-parallel ion population in distribution function f).

A larger interval around the interval in Figure A.5 from 19:08:36-19:10:12 also yields a reasonable Walén relation with a positive slope of 0.74 and HT frame of 0.89. The MVAB and MFR tests show a hodogram that is a mirror image of letter 'S' and MVAE test shows a 'S' shaped hodogram (see Figure A.7 and caption for more details). The S-shaped hodograms have been observed at the magnetopause [Berchem and Russell, 1982], and could be associated with the Alfvén (intermediate) shocks [Lyu and Kan, 1989].

A.4.2 Reconnection Signatures During Southward IMF

A.4.2.1 de Hoffman Teller frame velocities and slopes of the Walén relations

Between 19:54-20:15 UT, the IMF remained duskward and IMF b_z turns gradually from 0 nT to -10 nT and then gradually back up to 0 nT. When the IMF clock angle becomes 135 degrees, the most anti-parallel region forms at sunward, duskside cusp, so the reconnection site is expected to move from duskside cusp (approximate location during $b_z \sim 0$ nT) further sunward (in MLT). Table 2 indicates that the HT velocities change and increase after 20:04 UT compared to two intervals observed by sc4 at $\sim 20:00$ UT and 20:01 UT when b_z is closer to zero. These changing HT velocities are likely to be evidence for reconnection site moving sunward. However, throughout 19:54-20:15 UT, the reconnection region remains somewhere between duskside-sunward cusp. In this geometry the reconnected flux tubes will move tailward and dawnward (type C), and duskside and sunward (type D). Table 2 indicates that nearly all of the intervals between 19:58-20:15 UT have HT velocities consistent with type C reconnection (see discussion on abnormalities in section 4.3).

A.4.2.2 Example of the reconnection interval during southward IMF

Figure A.8 is in same format as Figure A.5 and shows a typical example of a reconnection interval (Type C) between 20:07:40-20:08:00 UT measured by sc3 during southward IMF. The HT frame velocity of the tailward moving flux tube is [-250,-20,31] km/s, and compared to previous sc1 interval illustrated in Figure A.5 the particle distribution functions show

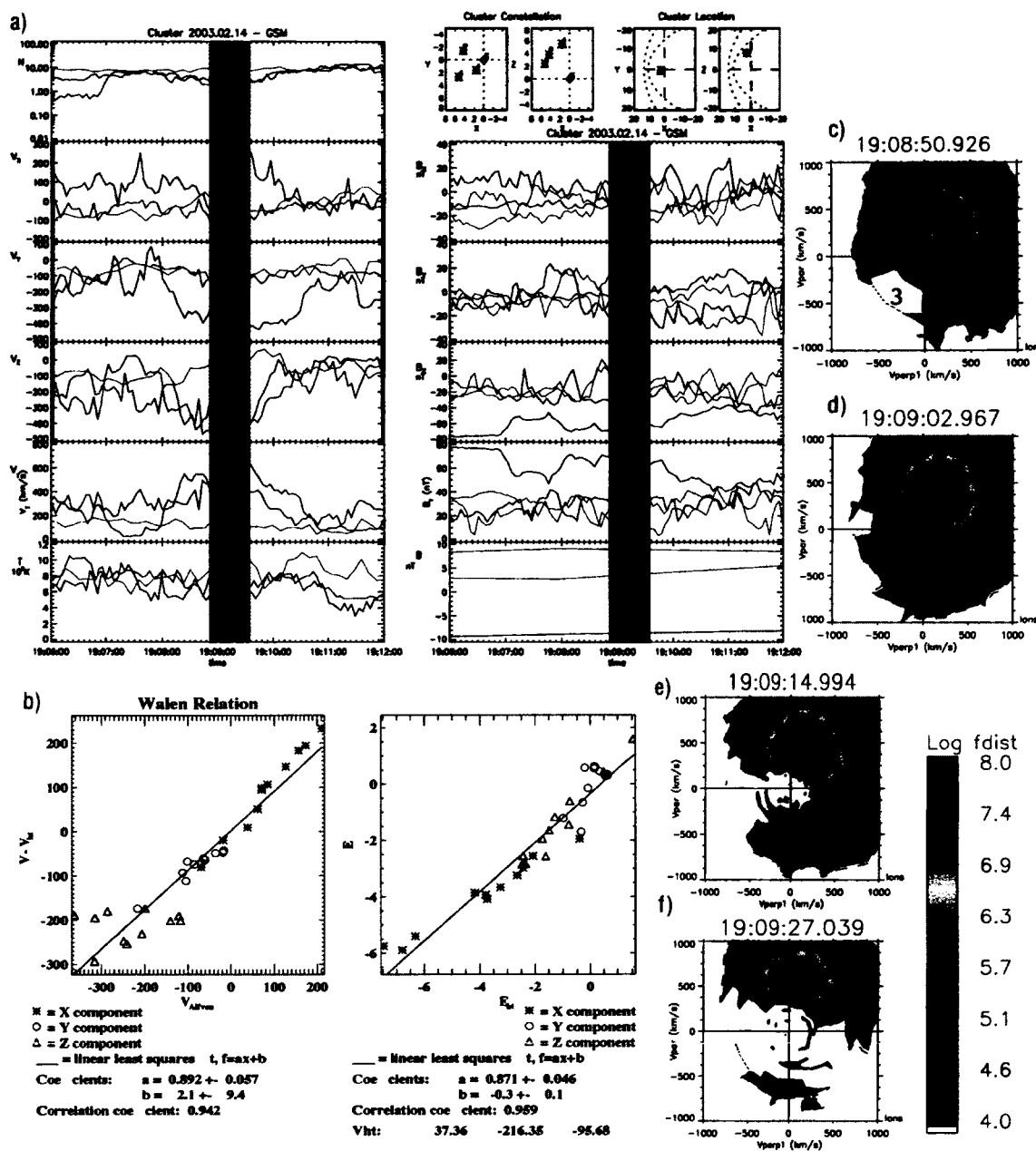


Figure A.5. A) shows plasma (left) and magnetic field (right) observations between 19:06-19:12 UT during northward IMF. B) shows Walén relations and HT-frames during the highlighted interval between 19:08:50-19:09:34 UT (19.1474-19.1596 UT) measured by sc1. The panels c-f show evolution of the ion distribution functions measured by sc1 in parallel-perpendicular plane between 19:08:50-19:09:27 UT.

more variability: At the beginning of the interval (panel c) most flux is in the 1st and 4th quadrant indicating that particles are streaming both parallel and anti-parallel to magnetic field; at the center of the interval (panel d) the parallel population becomes more dominant and at the end of the interval ions propagate mostly anti-parallel to magnetic field. During this interval the b_x rotates from positive to negative to positive and simultaneously plasma flow speed increases first from ~ 100 km/s to 325 km/s and then drops back to ~ 250 km/s. There are also strong variations in other components, but the rotation of b_x gives the clearest signature in order to interpret how sc3 might be moving with respect to the reconnected flux tube. The cartoon in Figure A.6b illustrates the relative trajectory of sc3 by the reconnected flux tube in order to explain the observed signature: 1) this field line reconnected first which is indicated by reduced tailward flow, presence of both incoming and reflected ion population (see Figure A.8c), positive b_x and negative b_z ; 2) this field line reconnected later having larger tailward flow, larger incoming ion population, smaller reflected population, small negative b_x and b_z indicating that sc3 is crossing that close to the middle; 3) this field line reconnected last which is indicated by tailward flow with positive v_z . Positive b_x , negative b_z , reduced plasma temperature and strong anti-parallel population indicate that sc3 crossed this field line into the magnetosheath side. Here also the variable dynamic pressure of the solar wind can result in relative motion of the flux tubes by the spacecraft. The MVAE hodogram (not shown) of the extended interval (20:07:40-20:08:24) measured by sc3 shows an S-shaped hodogram, similar to sc1 interval in Figure A.7, while MVAB and MFR tests show an upper curve of S-shape and a squeezed lower arc of the S.

A.4.3 Abnormalities in Observations of Reconnection Signatures

Most of the reconnection signatures were consistent with expected reconnection geometry during northward and southward IMF with strong b_y but we also encountered some puzzling observations. Sc3 observes a negative slope during southward IMF with strongly enhanced negative v_y -component of the HT-frame velocity (see sc3 interval in Table 2 at 20:05:39-20:05:51 UT). Examination of plasma and magnetic field data (not shown) indicates that during this interval plasma density gets reduced from $\sim 10/\text{cc}$ to $\sim 3/\text{cc}$; b_x changes from ~ -30 nT to -18 nT; b_y varies between -30 nT to -20 nT; b_z changes from $+19$ nT to 5 nT and plasma velocity gets reduced from 330 km/s to 100 km/s. This may suggest that sc3

Table A.1. Properties of Reconnection Intervals between 18:53-19:25 UT

Interval (hh:mm:ss)	(Decimal hour)	Sc	Walén slope	Walén cc.	HT slope	HT cc.	HT velocity (km/s)
18:53:20-18:53:38	18.8890-18.8940	4	1.01	0.99	0.90	0.96	[96,-199,-1]
18:56:30-18:56:54	18.9417-18.9484	4	0.86	1.00	0.96	0.98	[9,-60,25]
18:59:15-18:59:34	18.9875-18.9930	1	0.81	0.99	0.95	0.98	[-39,-153,-15]
18:59:45-18:59:57	18.9960-18.9993	1	0.85	0.97	1.00	1.00	[51,-35,44]
19:01:48-19:01:59	19.0300-19.0333	1	0.87	0.97	0.91	0.94	[52,-106,-57]
19:02:56-19:03:11	19.0490-19.0533	1	0.96	0.96	0.94	0.98	[53,-218,-30]
19:03:14-19:03:26	19.0540-19.0573	1	1.10	0.97	0.93	0.96	[87,-349,-223]
19:05:16-19:05:35	19.0880-19.0933	4	1.01	0.99	0.98	0.99	[77,-41,197]
19:05:27-19:05:39	19.0910-19.0943	1	0.82	0.94	0.97	0.98	[30,-161,-67]
19:06:28-19:06:40	19.1080-19.1113	1	0.81	0.96	0.97	0.99	[8,-114,19]
19:06:43-19:07:04	19.1120-19.1180	4	0.86	0.99	0.99	1.00	[93,3,74]
19:07:19-19:07:44	19.1222-19.1289	1	0.72	0.92	0.84	0.91	[70,-130,-84]
19:07:44-19:08:00	19.1290-19.1334	4	0.88	0.99	0.98	0.99	[62,-10,7]
19:07:44-19:07:56	19.1290-19.1323	1	0.82	0.99	0.92	0.96	[36,-123,-12]
19:08:16-19:08:32	19.1380-19.1424	4	1.08	0.98	0.95	0.98	[138,-17,132]
19:08:38-19:08:50	19.1440-19.1473	1	0.92	0.99	0.99	0.99	[93,-215,-18]
19:08:49-19:09:07	19.1470-19.1520	1	0.94	0.91	0.96	0.98	[8,-240,6]
19:09:21-19:09:33	19.1560-19.1593	1	0.82	0.99	0.96	0.99	[97,-218,-142]
19:08:50-19:09:34	19.1474-19.1598	1	0.89	0.94	0.87	0.96	[37,-216,-96]
19:11:27-19:11:39	19.1910-19.1943	1	0.98	0.97	0.94	0.96	[-32,-262,91]
19:15:12-19:15:24	19.2536-19.2569	3	0.99	0.99	0.97	0.99	[60,-73,-14]
19:17:45-19:18:09	19.2960-19.3027	3	0.93	0.99	0.96	0.97	[62,-107,-33]
19:17:48-19:18:12	19.2967-19.3034	3	0.98	0.99	0.95	0.97	[60,-106,-32]
19:19:37-19:19:52	19.3270-19.3313	1	0.80	1.00	0.96	0.98	[47,-162,25]
19:23:53-19:24:24	19.3981-19.4069	3	0.75	0.94	0.95	0.97	[46,-208,-46]
19:24:07-19:25:42	19.4020-19.4286	1	0.92	1.00	0.87	0.93	[91,-166,-86]
19:24:16-19:24:29	19.4047-19.4081	4	0.90	1.00	0.81	0.90	[213,-113,-55]
19:24:59-19:25:27	19.4164-19.4242	1	0.95	1.00	0.87	0.93	[106,-164,-95]

Table A.2. Properties of Reconnection Intervals between 19:25-20:25 UT

Interval (hh:mm:ss)	(Decimal hour)	Sc	Walén slope	Walén cc.	HT slope	HT cc.	HT velocity (km/s)
19:25:01-19:25:16	19.4170-19.4213	4	0.94	1.00	0.99	0.99	[200,-151,-165]
19:25:35-19:26:26	19.4264-19.4408	1	1.12	1.00	0.93	0.96	[138,-230,-129]
19:28:01-19:28:18	19.4672-19.4717	4	0.87	1.00	0.94	0.97	[166,-184,-83]
19:28:00-19:28:55	19.4669-19.4820	1	0.86	1.00	0.89	0.95	[60,-134,-67]
19:30:28-19:31:01	19.5079-19.5170	1	0.95	0.97	0.82	0.91	[40,-262,-113]
19:40:18-19:41:31	19.6719-19.6920	1	0.91	0.99	0.87	0.93	[69,-256,-87]
19:41:45-19:42:10	19.6961-19.7028	1	0.74	0.99	0.90	0.96	[127,-184,-76]
19:50:45-19:50:57	19.8461-19.8494	4	1.07	0.99	0.91	0.95	[262,-232,-81]
19:50:56-19:51:50	19.8490-19.8640	1	1.16	0.97	0.85	0.92	[244,-185,-96]
19:51:46-19:51:58	19.8630-19.8663	1	0.90	0.99	0.99	1.00	[172,-154,-84]
19:52:04-19:52:16	19.8680-19.8713	1	1.12	1.00	0.95	0.98	[199,-150,-144]
19:52:36-19:53:20	19.8767-19.8889	1	0.86	1.00	0.87	0.93	[139,-146,-79]
20:00:36-20:01:23	20.0100-20.0245	4	0.74	0.92	0.82	0.93	[-116,-83,76]
20:01:19-20:01:44	20.0222-20.0289	4	0.79	0.97	0.86	0.93	[-155,-59,99]
20:04:37-20:05:06	20.0772-20.0850	1	0.79	0.96	1.00	1.00	[-304,-124,196]
20:05:39-20:05:51	20.0942-20.0975	3	-0.87	-0.96	0.95	0.98	[-270,-327,156]
20:06:34-20:06:46	20.1097-20.1130	3	0.97	0.91	0.97	0.98	[-203,-33,391]
20:07:39-20:07:51	20.1275-20.1311	3	0.87	0.90	0.98	0.99	[-179,-45,15]
20:07:40-20:08:12	20.1280-20.1369	1	0.85	0.96	0.91	0.96	[-225,-21,277]
20:07:37-20:07:49	20.1270-20.1303	4	0.84	1.00	0.96	0.98	[-386,-60,185]
20:07:40-20:07:53	20.1280-20.1330	3	1.00	1.86	0.96	0.98	[-252,-20,31]
20:09:39-20:10:12	20.1610-20.1702	1	0.99	0.94	0.97	0.99	[-342,10,215]
20:10:26-20:10:38	20.1740-20.1773	3	0.81	0.96	0.92	0.96	[-129,15,144]
20:10:33-20:11:01	20.1760-20.1838	3	0.79	0.94	0.89	0.94	[-218,43,202]
20:12:25-20:12:37	20.2070-20.2103	1	-1.08	-1.00	0.93	0.96	[-22,242,-97]
20:16:54-20:17:34	20.2818-20.2929	3	-0.79	-0.99	0.93	0.97	[-262,210,130]
20:23:44-20:24:12	20.3958-20.4036	1	-0.73	-1.00	0.98	0.99	[-281,185,205]

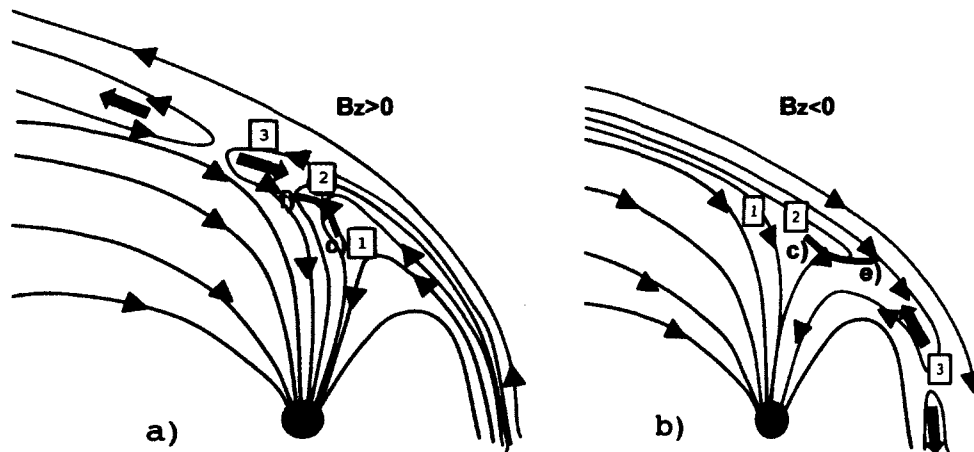


Figure A.6. a) shows a cartoon of reconnection topology during northward IMF and b) during southward IMF. The blue line is the solar wind magnetic field line, the red lines are reconnected field lines and black lines depict closed magnetic field lines. Numbering shows the time sequence of the events, where 1 refers to a field line that reconnected first and 3 to a field line that is just reconnecting. The purple curve and letters c-e illustrate how spacecraft might be moving relative to reconnected field lines in order to explain the observed HT-frame velocities, magnetic and velocity fields and ion distribution functions presented in Figure A.5 and A.8. The letters refer to corresponding intervals at Figures A.5 and A.8. Note that although Cluster is traveling from left to right with ~ 3 km/s, the motion of the flux tubes by the spacecraft both naturally and due to variations of P_{dyn} in solar wind is much faster resulting possibly in observed sequence of events in the time series.

crossed a reconnected flux tube (type C) more at the magnetospheric side (see cartoon of the magnetic field geometry in Figure A.6b, which shows that b_x (b_z) should be negative (positive) on magnetospheric side of reconnected flux tube #3).

The last two intervals with northward IMF showed a strongly positive v_z -component of the HT-velocity. Considering the spacecraft have moved more sunward it first seems unlikely that they are observing the tailward moving flux tube originating from lobe reconnection at dusk-side cusp, also the observed v_z -components should be smaller. Understanding these last intervals in Table 2 requires further work -but they might be signatures of day-side component merging or merging between IMF and magnetic flux generated during previous southward IMF interval. During southward IMF more magnetic flux has piled up at high-latitudes (see red field lines in Figure A.6b), so when IMF turns northward reconnection

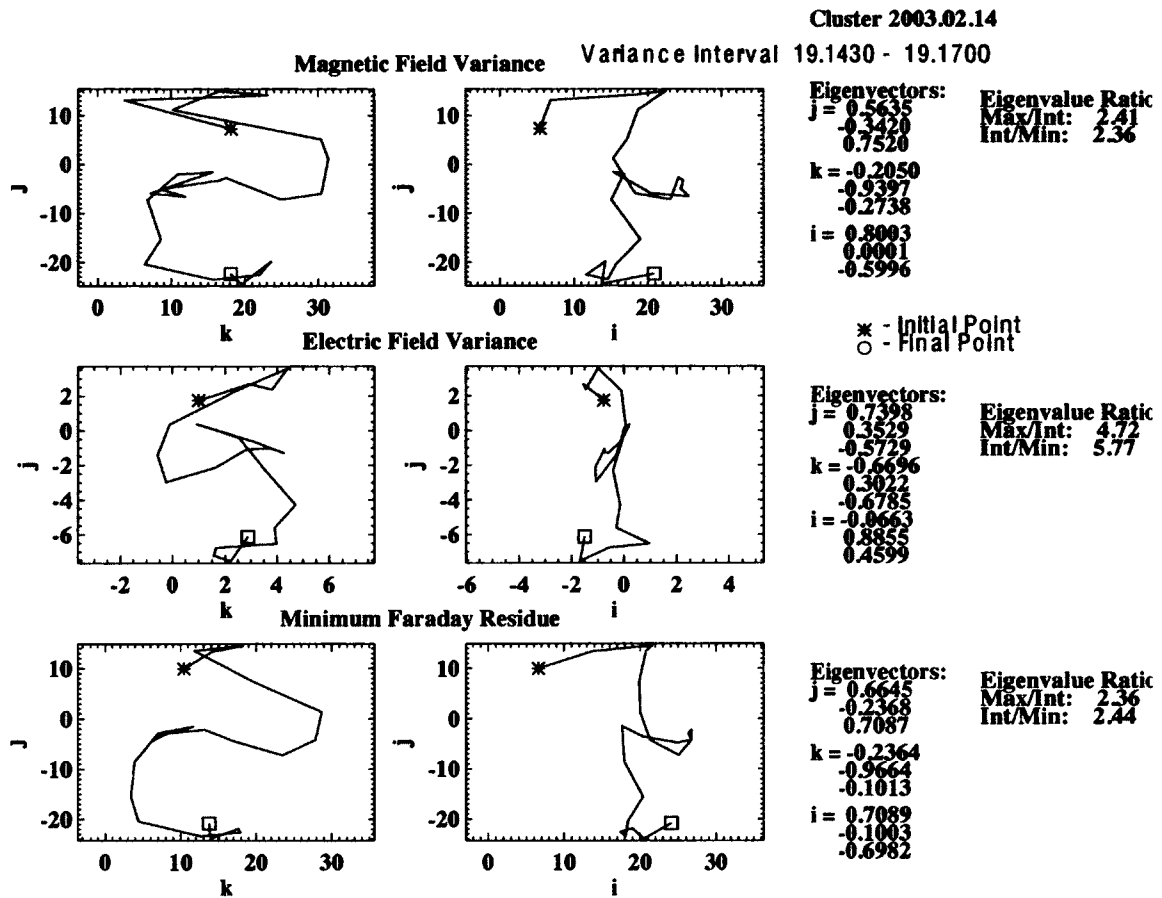


Figure A.7. MVAB (top), MVAE (middle) and MFR (bottom) hodograms during extended reconnection interval at 19:08:34-19:10:12 UT presented in Figure A.5.

occurs between this newly generated (red) flux and IMF resulting in tailward moving flux tubes with positive v_z originating from more dayside (compared to location of the tailward moving flux tube in Figure A.6a)) and it would explain why Cluster can observe these closer to dayside.

A.5 Structure and Size of the Cavity

The size and structure of the DMC is calculated by estimating boundary normal orientations and projecting the spacecraft separation pairs along these boundary normal directions. We have calculated the normals with three different methods: minimum variance of the magnetic field (MVAB), maximum variance of $-\mathbf{V} \times \mathbf{B}$ -electric field (MVAE) and minimum

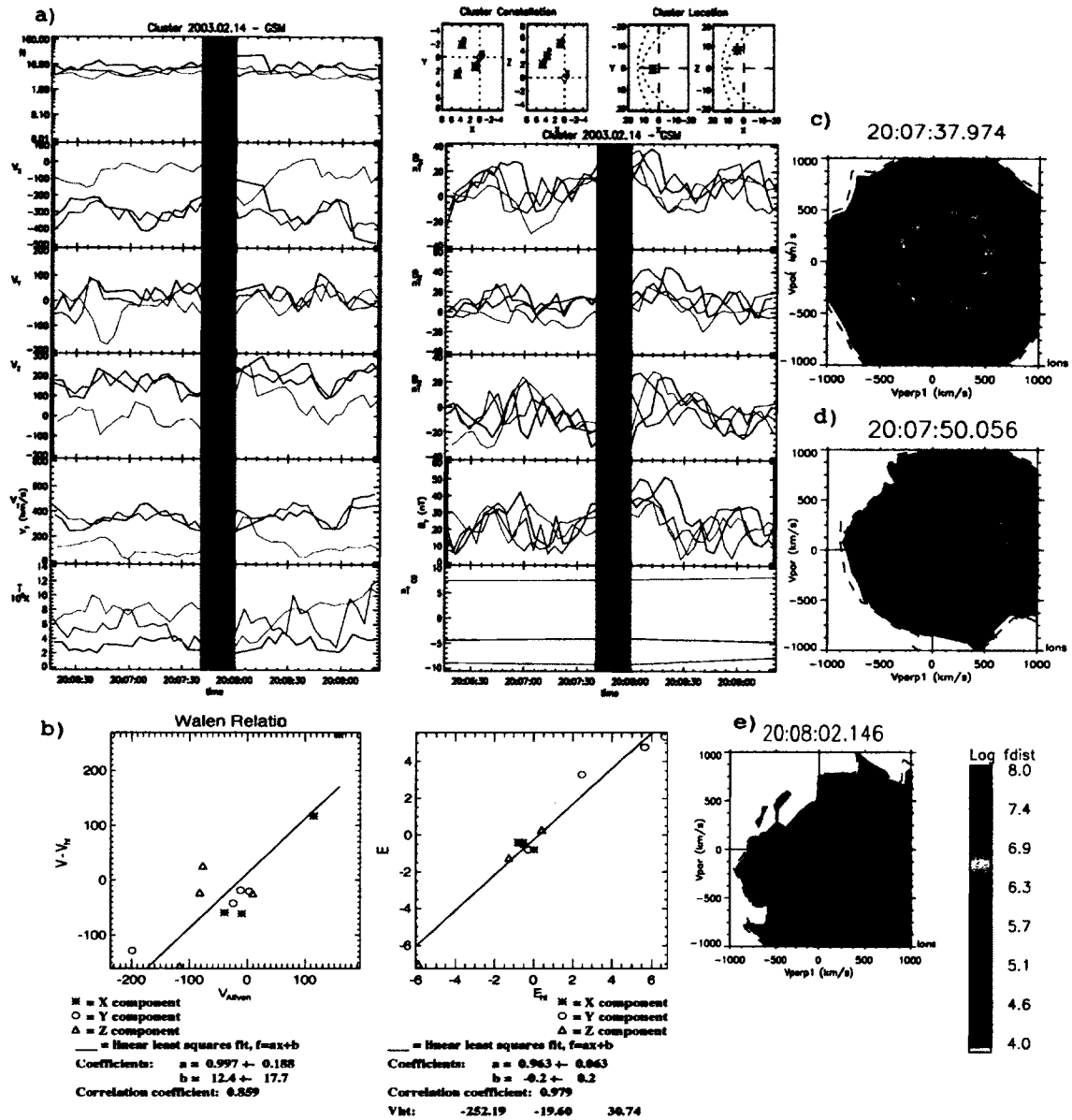


Figure A.8. a) shows plasma (left) and magnetic field (right) observations between 20:06:15-20:09:24 UT during southward IMF. b) shows Walén relations and HT-frames during high-lighted interval between 20:07:40-20:08:00 UT measured by sc3. The panels c-e show evolution of the ion distribution functions measured by sc3 in parallel-perpendicular plane between 20:07:37-20:08:02 UT.

Faraday residue method (MFR), except that for sc2 we only use MVAB technique due to lack of plasma data.

We have not used multi-spacecraft techniques such as Constant Thickness Approach (CTA) [e.g. *Haaland et al.*, 2004] for determining boundary orientation due to following reasons: 1) The spacecraft separation is so large that during the magnetosphere-cavity crossing ($\approx 18:40-19:00$ UT at sc1, sc2 and sc3) sc3 crosses the cavity 30 minutes later than other spacecraft and at different altitude so there is not good correlation between four spacecraft measurements, 2) IMF conditions have changed during this 30 minute interval, so that by the time sc3 gets into the cavity the b_z is dominating over b_y so the reconnection site and thus the boundary normal orientation have possibly changed as sc3 crosses the boundary, 3) When determining the orientation of the cavity-magnetosheath boundary only three of the spacecraft are doing the transition from cavity to sheath.

Because the normal calculations are sensitive to the fluctuations in the data and length of the analysis window we have checked the time-stationarity and error estimates for the normals by doing MVAB, MVAE, MFR on sets of nested data segments centered at the middle (or close to middle) of the current sheet [*Sonnerup and Scheible*, 1998]. The smallest segment has only three data points (M-value of 3), and then each subsequent segment has one additional data point added at both ends (M-value increases by increments of two). Appendix 1 shows an example of plateau normal calculation with error estimates.

Tables 3 and 4 present the results of the average plateau normals measured by different spacecraft during different current sheet crossings and lists the spacecraft separation vectors (rounded to nearest ten) projected along Average Plateau Normals (APN). The time denotes the reference interval for reference normal (see Appendix1 for more details) and approximate central current sheet time at the middle of each nested segment. The M-value lists the segment used for plateau normal calculation. If no good plateau normal is obtained the time interval and normal yielding the best eigenvalue ratio is marked. For interval 19:24:50-19:25:12 UT, the intermediate direction of the MVAE normal is marked because it seems that maximum and intermediate eigenvector of MVAE-test had switched places.

A.5.1 Magnetosphere-Cavity Transition

The first crossing is the magnetosphere-cavity (MSP-DMC) transition that occurs gradually at all spacecraft. For sc1 this transition is from 18:48:00-18:51:35 UT and both MVAE and MFR yield a stable plateau normal with very similar eigenvectors which have a dominant x -component of 0.96. The MVAB test has the smallest eigenvalue ratio but the normal is still not significantly different from those calculated from MVAE and MFR tests: the angle between MVAB normal is MFR normal is ~ 9 degrees. Sc1 is briefly swept back to the magnetosphere due to pressure increase at $\sim 18:53$ -18:55 UT after which it returns back to cavity when dynamic pressure decreases measuring a normal (although still with the largest x -component) tilted more toward positive z -direction. Sc4 which is at lower altitude and further duskside observes at 18:36-18:53 UT also stable MFR and MVAE normals with largest x -component (0.95 and 0.97, respectively), but now the normals are tilted more toward positive y -direction than measured at sc1 location (the normal from MVAB test has the lowest eigenvalue ratio and yields a completely different normal: the angle between MVAB and MFR normal is ~ 84 degrees). Sc2 which is furthest dawnward also observes a normal with largest x -component but now with a strong tilt toward negative y -direction. For sc3 which is at lowest altitude and between sc1 and sc2 in y -direction, the transition from MSP to cavity occurs last at 19:03-19:17 UT and it also observes the largest x -component but now the normal is slightly tilted toward positive y and negative z -direction. The observations of normals with the largest x -component and tilt toward positive (negative) z -direction at higher (lower) altitude are consistent with Cluster location with respect to magnetic field line topology from T89-model (see later Figure A.13 and discussion on the cavity structure). The differing y -components of the normals indicate that magnetosphere-cavity boundary has curvature in $x - y$ -plane within spacecraft separation.

By 19:15 UT all the spacecraft have moved from magnetosphere into cavity which allows us to calculate the minimum extent of the cavity by choosing the maximum value of projected spacecraft pair distances along various directions. From now on we discuss only the projected distances along the plateau normals (if they exist) obtained with the test that returns best eigenvalue ratios during plateau observations. The maximum extent (width) along sc3 normal vector [0.94, 0.16, -0.30] (sc3 and sc4 separation projected along this normal) is 4680 km and 6090 km along sc1 normal vector (see Table 3). The projection

of sc4 and sc3 separation vectors along z -direction of the cavity at 19:15 UT is 5440 km. The extent along x -direction (projection of sc4 and sc3 separation vectors along x -direction) is 5230 km and along y -direction 4170 km which is measured between sc2 and sc4. The actual extent of the cavity may be even larger than this as sc1 and sc4 move from cavity into magnetosheath at $\sim 19:17$ UT due to enhanced dynamic pressure (see lowest panel in Figure A.2). Although the dynamic pressure shows lots of variations, the average pressure is much higher during the magnetosheath interval compared to cavity interval.

A.5.2 1st Cavity-Magnetosheath Transition

Velocity and magnetic field data indicate that the transition from diamagnetic cavity to the magnetosheath occurs almost simultaneously for sc1 and sc4, except that for sc1 the gradients are slightly sharper. However, the temperature data shows that sc1 leads sc4 by one minute in the transition. Table 1 indicates that for sc1 this transition satisfies the reconnection criteria, suggesting that diamagnetic cavity-magnetosheath (DMC-MSH) boundary is a rotational discontinuity. The orientation of this DMC-MSH boundary is tilted more toward positive z -direction compared to MSP-DMC-boundary. The MVAE test returns eigenvectors with the best eigenvalue ratios for plateau normals. The normals that sc1 and sc4 measure are very similar: $[0.67, 0.43, 0.60]$ for sc1 and $[0.67, 0.54, 0.52]$ for sc4. Examination of Cluster constellation in Figure 1 indicates that sc1 and sc4 separation vector is almost perpendicular to these normals in $x - z$ -plane, which at first would seem to explain why an increased dynamic pressure would move the DMC-MSH boundary over these spacecraft nearly simultaneously. However, Sc2 is much closer to sc1 and sc4 along these boundary normals compared to mutual separation between sc1 and sc4, so it is surprising that it enters to the magnetosheath about three minutes later than sc4. This can be either if the cavity-magnetosheath boundary is further outward at the location of sc2 or the cavity boundary moves toward negative y -direction instead of purely along boundary normal direction. The strong peak at solar wind dynamic pressure coincides with sc2 transition into the magnetosheath which may explain the sideways motion of the cavity boundary. Sc3 remains in the cavity during the entire cavity interval which allows us to calculate the minimum extent of the cavity along the boundary normals measured by sc1, sc2 and sc4. These depths are 6060, 5940 and 6100 km for sc1, sc2 and sc4, respectively. However, it

unclear how far below sc3 the cavity actually extends.

A.5.3 Observations of Cavity-like Plasma during Magnetosheath Intervals

During the magnetosheath interval at $\sim 19:17-19:52$ UT, spacecraft have brief encounters with the cavity-like plasma. At $19:24:18-19:25:12$ UT as the dynamic pressure drops from a peak value measured at $\sim 19:22:00$ UT, the magnetopause moves outward and sc4 drops briefly back into cavity like plasma characterized by depressed field, increased plasma temperature of 10-11 MK and departure from magnetosheath-like flow. RAPID data in Figure A.4 shows significant fluxes of ~ 200 keV electrons, ~ 300 keV protons and ~ 400 keV Helium (We can not say whether this is Helium+ or Helium ++) during this interval. See *Nykyri et al. 2010c (submitted to JGR)* for detailed analysis of high-energy particle observations. Table 1 and Table 2 indicate that parts of this interval satisfy the reconnection criteria for sc4 indicating that this signature is a rotational discontinuity.

Magenta colored column in Figure A.9a shows plasma and magnetic field measurements and b) shows hodograms during $19:24:18-19:25:16$ UT during sc4 encounter with cavity like plasma. The de Hoffman Teller-frame velocities measured by sc4 at $19:24:16-19:24:29$ UT and $19:25:01-19:25:16$ UT are $[213, -112, -55]$ km/s and $[200, -151, -165]$ km /s, respectively, which are consistent with flux tubes moving sunward (toward positive x), earthward (decreasing z) and dawnward (toward negative y) from reconnection site at the duskside of the cusp. We have compared the plasma and magnetic field observations by sc4 with 2.5-D MHD simulations of the FTE. The simulation code and application for dayside reconnection is explained in *Nykyri et al. [2003b]* and *Otto [1995]* and here it is run for the magnetic field and plasma parameters observed during magnetosheath/cavity crossing in high-altitude cusp: number density is normalized to $10/cm^3$, magnetic field, B_0 is 50 nT, Alfvén speed is 345 km/s, length scale, L_0 , is 400 km and time unit, t_0 is 1.16 seconds. The density is higher on magnetosheath side and magnetic field is larger on magnetospheric side. Figure A.10a) and b) show simulation results (see caption for more details) at $t=159.96 t_0$ and at $t=219.97 t_0$ together with cartoon (c) depicting the FTE geometry together with sc4 trajectory relative to FTE structure.

The normal component of magnetic field and plasma velocity in Figure A.10a) and b) is the x -component in simulation units and the FTE is propagating toward positive

z -direction. The x -coordinate of the simulation box corresponds roughly to z_{GSM} , the z -coordinate of the simulation box corresponds roughly to direction of the deHoffman-Teller frame velocity which is mostly into direction of x_{GSM} and $-y_{GSM}$, the y -coordinate of the simulation box goes into the paper (right-handed coordinate system) and points roughly out of the FTE-cartoon (Figure A.10c) tilted more toward y_{GSM} . The simulation indicates that the reconnection flow is stronger on the magnetospheric side of the reconnected field line consistent with Cluster observations and that magnetic field is rather weak inside the FTE (green bubble). This region of depressed field essentially is the diamagnetic cavity.

The MVAB analysis (Figure A.9b) gives the best eigenvalue ratio for the interval 19:24:18-19:25:16 UT and shows a clearly polarized ellipse in maximum-intermediate plane. The normal is $[0.38, 0.0, 0.92]$ so it is mostly along positive z_{GSM} -direction tilted slightly toward positive x_{GSM} , which corresponds to x -component in simulation coordinates. Projecting the average magnetosheath magnetic field, $[-40.16, 34.55, 20.25]$ nT measured by sc4 between 19:22-19:24 UT along the boundary normal direction yields a normal component of 3.42 nT. A cut along x -direction at $z = 25$ in Figure A.10b (mimicking sc4 trajectory over this structure (see yellow path in c)) shows first a normal component that is closely zero but then it becomes negative inside the FTE. Rotating Cluster data into boundary normal coordinates shows that inside FTE the normal component becomes negative reaching the maximum value of -14 nT. Also the magnetic field along the intermediate variance direction which is mostly along y -direction changes from positive to negative. This corresponds to the color coded out of the plane magnetic field component (b_y) in Figure A.10 which shows that it also changes from positive to negative as one crosses from magnetosheath into the FTE (the color code changes from negative to positive because positive y points into the paper). These observations are in excellent agreement with the simulations of a FTE which support our hypothesis that sc4 indeed crosses into diamagnetic cavity bounded by the FTE structure between 19:24:18-19:25:16 UT. Note that during the entire sheath interval sc3 remains in the cavity and observes similar plasma and magnetic field characteristics during part of the FTE interval as sc4. The sc3 separation from sc4 projected along boundary normals (for the tests yielding the best eigenvalue ratios) measured by sc4 at the inbound and outbound transition of this FTE (see Table 3) varies between 3660-3920 km which indicates that cavity may be extending at least 3660 km below sc4 along boundary normal

direction. The separation between sc3 and sc4 along normal, $[0.38, 0.0, 0.92]$, measured during the entire FTE interval is even larger, 4180 km. The separation between sc4 and sc3 during this interval is 6220 km.

An immediate question is if this FTE is releasing hot magnetospheric or magnetosheath plasma into cavity or does the FTE open up the cavity and let cavity-like plasma escape anti-parallel to magnetic field. The ion distribution functions are presented in Figure A.11 and Figure A.10c shows a cartoon depicting the FTE geometry together with letters a)-g) marking the intervals when the distribution functions were observed relative to FTE structure along sc4 trajectory. In the following we will describe the magnetic field and plasma observations along sc4 orbit at points a)-g) and utilizing information presented at Figures A.9, A.11 and A.10.

a) At 19:24:04 UT Sc4 is in the magnetosheath field line that has not yet reconnected and has negative b_x , positive b_y and b_z , and a magnetosheath like flow of ~ 200 km/s. The ion distribution function is showing in addition to the typical D-shaped magnetosheath population a higher energy population at very oblique and perpendicular pitch angles, some of which are propagating anti-parallel to the magnetic field. These high energy particles with velocities of ~ 1000 km/s could either be particles that are trapped in the cavity but are observed in the limited region in the magnetosheath due to their larger gyro-radius or they could be particles of bow-shock origin. Indeed it has been shown that quasi-parallel bow shock maps to the cusp during this event [Trattner et al., 2010, submitted to JGR]. The gyro radius of the proton that is trapped in the cavity at 10 nT field and has perpendicular velocity of 1000 km/s is 1044 km, so it is well possible that these trapped cavity particles are observed in the limited region at the magnetosheath up to 1000 km from cavity boundary.

If indeed sc4 is on the field line that has not yet reconnected, the positive parallel distribution at higher energies could be of bow-shock origin. However, bow-shock source would not explain the high-energy, anti-parallel population.

b) At 19:24:15 UT sc4 is closer to the cavity boundary on magnetosheath (MSH) field line and shows a more pronounced butterfly shape of the distribution.

c) At 19:24:27 UT sc4 encounters the field line at the outer edge of the DMC: magnetic field starts to rotate, plasma temperature starts to increase and the distribution shows a large quantity of particles up to 1000 km/s streaming also anti-parallel to magnetic field.

The high-energy proton fluxes are larger and there is a significant increase in perpendicular energy.

d) By 19:24:39 UT sc4 moves deeper into DMC and observes a more symmetric distribution function with enhanced high-energy fluxes. The magnetic field becomes more distorted from magnetosheath values and is close to its minimum value observed at 19:24:36 UT. The proton gyro-radius in this weak field region is larger than the gradient of the boundary which is calculated to be 810-1330 km (separation between sc2 and sc4 along boundary normal directions calculated during the crossing of the FTE structure, see Table 3). The protons become strongly non-adiabatic and can be pitch angle scattered into the loss-cone. This is qualitatively consistent with the observed distribution function which shows that the loss cone is filled, which enables cavity particles to leak into magnetosheath or ionosphere. However, because the magnetic field in the cavity is much weaker than in the magnetosphere or magnetosheath, the loss cone is small. Particles with oblique pitch angles are outside the loss-cone and are trapped.

Applying the conservation of the first adiabatic invariant for electrons, shows that the loss cone into the magnetosheath or magnetosphere is extremely narrow and the electron pitch-angle distributions show that the majority of the electrons are trapped [Nykkyri *et al.*, 2010c, submitted to JGR].

e) At 19:24:51 UT sc4 is still inside DMC and observes higher fluxes of more energetic particles streaming anti-parallel than parallel to magnetic field. The loss cone is still filled.

f) At 19:25:03 sc4 is close to DMC-MSH boundary and observes the more typical magnetosheath distribution but also more higher energy particles at oblique pitch angles and energetic beam propagating anti-parallel to this field.

g) At 19:25:15 sc4 has moved into magnetosheath and observes a magnetosheath-like distribution but still some fluxes anti-parallel to magnetic field.

h) and i) At 19:25:28 and 19:25:39 UT sc4 has moved closer to the DMC-MSH boundary due to decrease in dynamic pressure of solar wind so the distributions show more higher energy particles similar to those observed at a) and b).

Figure A.12 shows a summary of these sheath interval observations measured by sc4 (see caption for more details). Proton pitch angles vary from 0-180 degrees showing clearly more fluxes anti-parallel to magnetic field at 19:24:18-19:25:16 UT which is the first sheath

Table A.3. Boundary normals, average plateau eigenvalue ratios and average of spacecraft separation projections along plateau-normals measured by four Cluster spacecraft during boundary crossings. MSP-DMC denotes magnetosphere-diamagnetic cavity crossing and DMC-MSH denotes cavity -magnetosheath crossings between 18:48-19:26 UT

Spacecraft Ref.Interval Central time	Avg. of plateau MVAB normals Avg. of plateau MVAE normals Avg. of plateau MFR normals	λ_2/λ_3 λ_1/λ_2 λ_2/λ_3	ΔRN_{14}	ΔRN_{24}	ΔRN_{34}	ΔRN_{12}	ΔRN_{23}	ΔRN_{13}	M-range
Sc1, (1) MSP-DMC 18:48:00-18:51:35 18:49:47	0.99,-0.03, 0.14 0.96, 0.04, 0.28 0.96, 0.03, 0.27	1.4 4.7 4.1	3130 2670 2680	570 600 560	5700 6080 6050	2570 2070 2110	5130 5490 5470	2560 3420 3380	no plateau 53-79 53-79
Sc4, (1) MSP-DMC 18:36:00-18:53:00 18:44:30	-0.36,0.91,-0.20 0.95, 0.30,-0.03 0.97, 0.26,-0.03	2.5 4.1 2.7	120 3760 3650	3490 2060 1920	150 6010 5990	3390 1700 1830	3650 3950 4070	260 2260 2240	243-273 243-273 243-273
Sc2, (1) MSP-DMC 18:42:00-18:50:06 18:46:02	0.79,-0.60, 0.14 no plasma data no plasma data	2.9	1840	1860	3130	3710	5000	1290	73-83
Sc1, (1) MSP-DMC 18:55:47-19:06:00 19:00:53	0.88,-0.10, 0.46 0.87,-0.15, 0.46 0.88,-0.19, 0.44	2.8 2.1 1.9	1710 1650 1720	290 500 610	5680 5510 5380	2010 2150 2330	5980 6010 5990	3970 3860 3660	151-159 149-158 149-158
Sc3, (1) MSP-DMC 19:03:00-19:21:00 19:12:00	0.94,0.16,-0.30 0.97,0.18,-0.15 0.96,0.22,-0.145	4.9 2.9 2.1	4520 4220 4210	1950 1850 2010	4680 5250 5350	3710 2370 2200	2740 3400 3340	160 1030 1140	253-281 253-281 253-281
Sc1, (2) DMC-MSH 19:17:00-19:20:00 19:18:30	0.69, 0.40, 0.60 0.67, 0.43, 0.60 0.68, 0.47, 0.57	3.3 6.8 3.8	1150 1110 1290	1430 1560 1780	6070 6060 6100	290 450 490	4640 4500 4320	4930 4940 4810	no plateau 39-45 39-45
Sc4, (2) DMC-MSH 19:17:00-19:21:00 19:19:00	0.81, 0.34, 0.46 0.67, 0.54, 0.52 0.62, 0.58, 0.53	4.3 5.4 4.0	2010 1470 1320	1520 2120 2250	6260 6100 6000	500 660 930	4740 3980 3760	4240 4630 4690	59-69 59-69 59-69
Sc2, (2) DMC-MSH 19:18:35-19:23:24 19:21:00	0.75, 0.21, 0.62 no plasma data no plasma data	3.7	1150	690	5940	460	5250	4790	61-71
Sc4, (3) MSH-DMC 19:24:18-19:24:50	0.40, 0.07, 0.92 0.36,-0.03, 0.93 0.39,-0.09, 0.92	19.4 21.5 28.2	1200 1480 1400	620 1120 1330	4380 3970 3920	590 360 70	4990 5100 5250	5580 5450 5320	no plateau no plateau no plateau
Sc4, (4) DMC-MSH 19:24:50-19:25:12	0.23, 0.08, 0.97 0.15, 0.17, 0.97 (int) 0.14, -0.02,0.99	27 1.9 10.7	1990 2200 2470	810 510 1370	3660 3490 2990	1190 1690 1100	4460 4000 4360	5650 5690 5470	no plateau no plateau no plateau

Table A.4. Boundary normals, average plateau eigenvalue ratios and average of spacecraft separation projections along plateau-normals measured by four Cluster spacecraft during boundary crossings. MSP-DMC denotes magnetosphere-diamagnetic cavity crossing and DMC-MSH denotes cavity -magnetosheath crossings between 19:40-20:30 UT

Spacecraft Ref.Interval Central time	Avg. of plateau MVAB normals Avg. of plateau MVAE normals Avg. of plateau MFR normals	λ_2/λ_3 λ_1/λ_2 λ_2/λ_3	ΔRN_{14}	ΔRN_{24}	ΔRN_{34}	ΔRN_{12}	ΔRN_{23}	ΔRN_{13}	M-range
Sc1, (5) MSH-DMC-MSH 19:40:28-19:42:28 19:41:28	0.53, -0.10, 0.84 0.52, -0.06, 0.85	14.4 9.6	640 660	1090 950	4290 4350	450 300	5370 5310	4920 5010	no plateau 33-39 33-39
Sc4, (5) MSH-DMC-MSH 19:40:12-19:41:42 19:40:57	0.54, 0.28, 0.79 0.55, 0.28, 0.79	4.8 4.6	60 70	650 640	5200 5230	670 610	4550 4590	5230 5200	no plateau 23-35 23-35
Sc1, (6) MSH-DMC 19:42:00-20:00:00 19:51:00	0.56, 0.06, 0.83 0.44, -0.10, 0.89 0.46, -0.05, 0.89	4.4 13.07 8.0	310 1120 970	350 1240 1010	4760 3920 4130	50 110 40	5120 5160 5140	5070 5050 5100	251-281 251-281 251-281
Sc2, (6) MSH-DMC 19:42:00-20:00:00 19:51:00	0.57, 0.00, 0.82 no plasma data no plasma data	3.7	290	580	4690	290	5270	4970	261-279
Sc4, (6) MSH-DMC 19:45:00-19:59:23 19:52:12	0.31, -0.41, 0.86 0.56, 0.07, 0.81 0.56, 0.02, 0.83	1.7 12.42 6.5	1840 110 340	2660 230 530	2400 4880 4650	820 120 190	5070 5100 5180	4250 4990 4990	218-231 218-231 218-231
Sc1, (7) DMC-MSH 19:57:00-20:27:00 20:12:00	0.76, -0.025, 0.64 0.55, -0.10, 0.83 0.74, -0.07, 0.67	6.3 3.0 3.5	960 500 730	250 1040 530	5020 4180 4830	1220 530 1260	5280 5220 5360	4060 4690 4100	451-481 451-481 451-481
Sc2, (7) DMC-MSH 19:54:00-20:27:00 20:10:30	0.70, -0.11, 0.70 no plasma data no plasma data	6.0	440	780	4650	1220	5440	4220	481-509
Sc3, (7) DMC-MSH 19:54:00-20:30:00 20:12:00	0.50, -0.34, 0.80 0.55, -0.07, 0.83 0.67, 0.03, 0.72	2.0 5.6 3.2	850 460 530	2080 900 200	3310 4300 4990	1230 440 720	5390 5200 5190	4160 4760 4470	501-551 501-551 501-551
Sc4, (7) DMC-MSH 19:54:00-20:27:00 20:10:30	0.60, -0.22, 0.77 0.53, -0.12, 0.84 0.60, -0.13, 0.79	7.0 3.9 3.4	270 650 220	1460 1180 1060	4020 4080 4310	1190 530 830	5470 5250 5360	4280 4720 4530	481-521 481-521 481-521

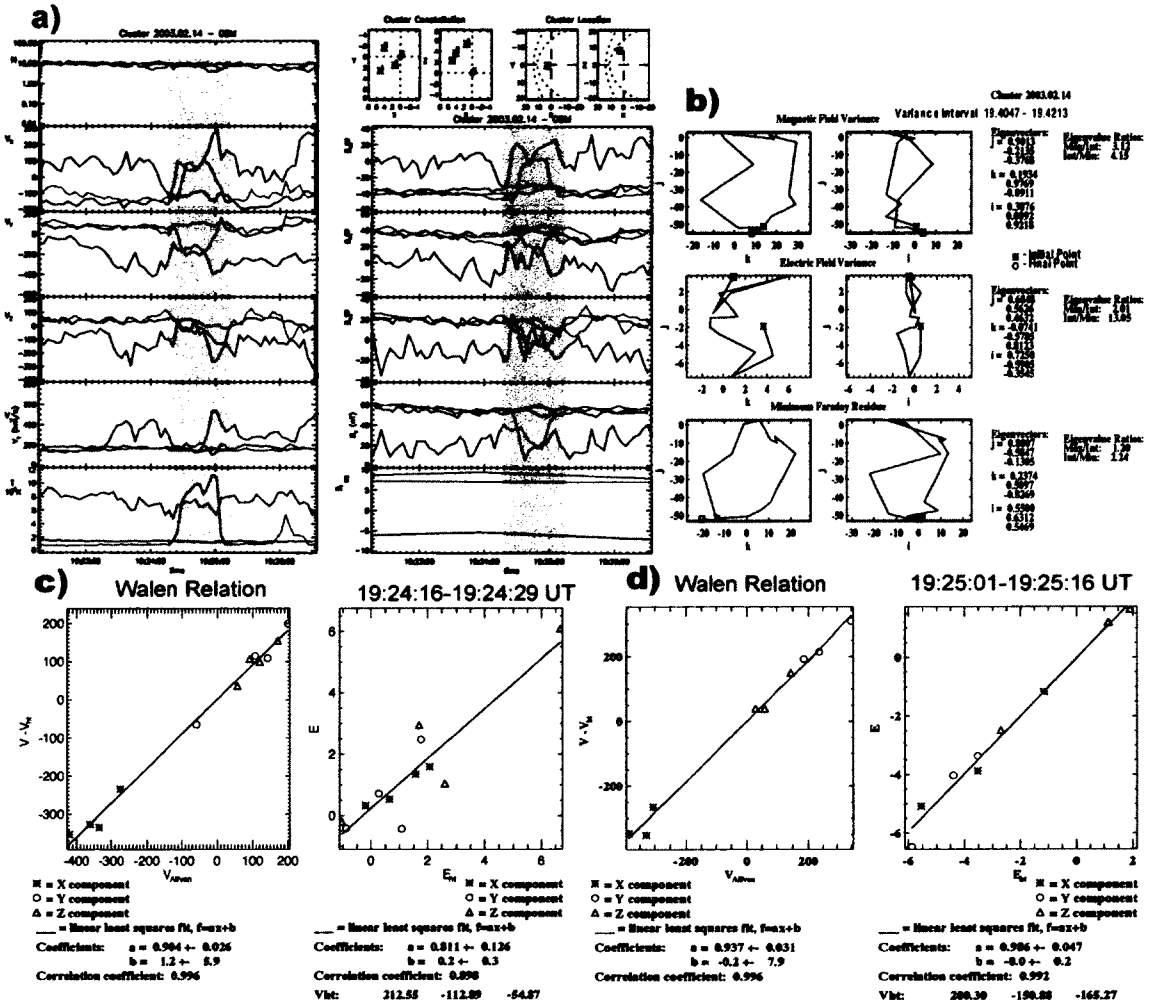


Figure A.9. Plasma and magnetic field observations (a) and hodograms (b) during cavity interval measured by sc4 between 19:24:18-19:25:16 UT. The Walén relations and HT-frames are satisfied at both edges of depressed B -field signature at 19:24:16-19:24:29 UT (c) and at 19:25:01-19:25:16 UT (d) but not during the entire interval at 19:24:18-19:25:16 UT (not shown).

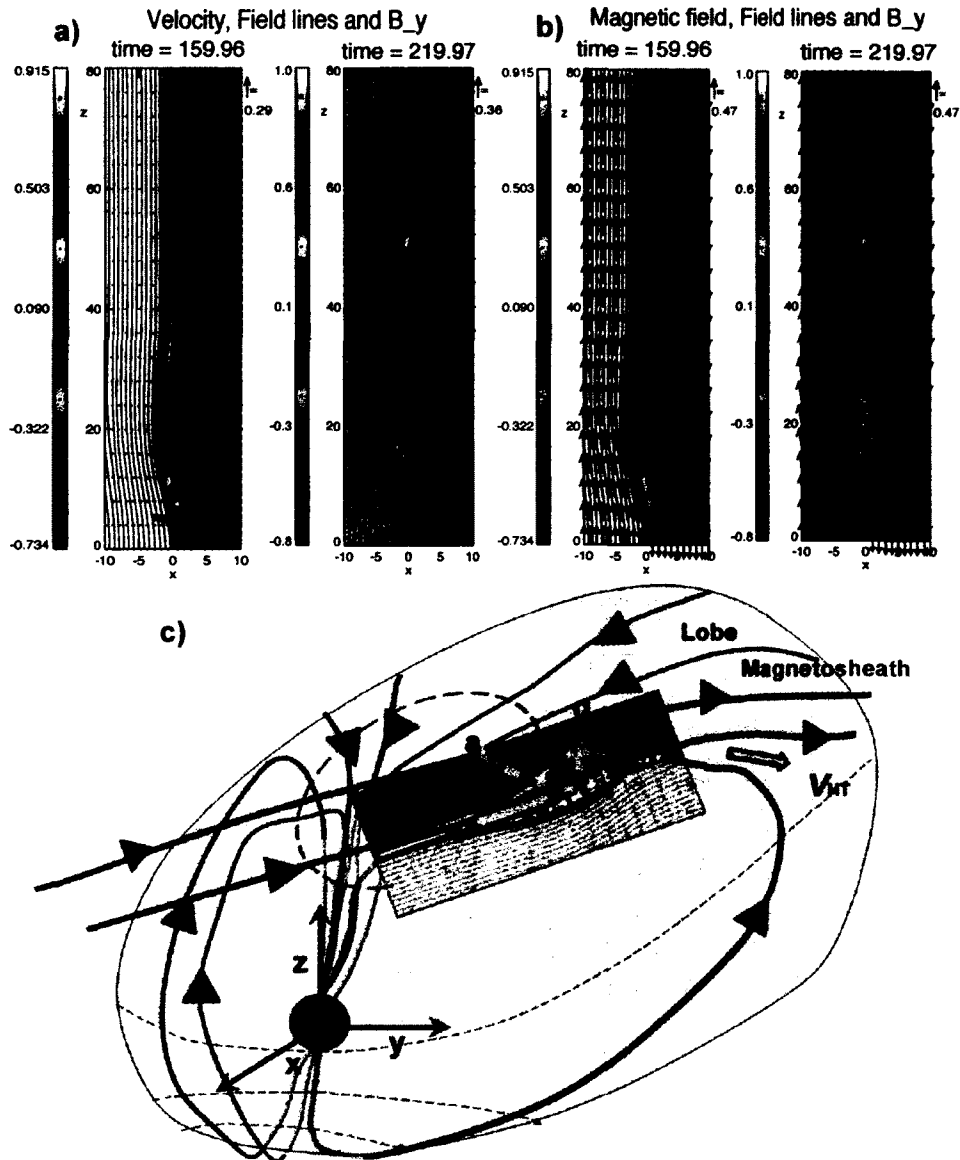


Figure A.10. 2-D MHD simulation of the Flux-Transfer event originating from duskside of the cusp. Time evolution of velocity field vectors and magnetic field lines are plotted in a) and magnetic field vectors and magnetic field lines are plotted in b). The background color in both plots depicts the into-the-plane magnetic field component. 3-D cartoon of the reconnection geometry is plotted in c). The relative trajectory of Cluster sc4 with respect to FTE is plotted with yellow curve together with letters a)-g) illustrating times when ion distribution functions shown in Figure A.11 are observed.

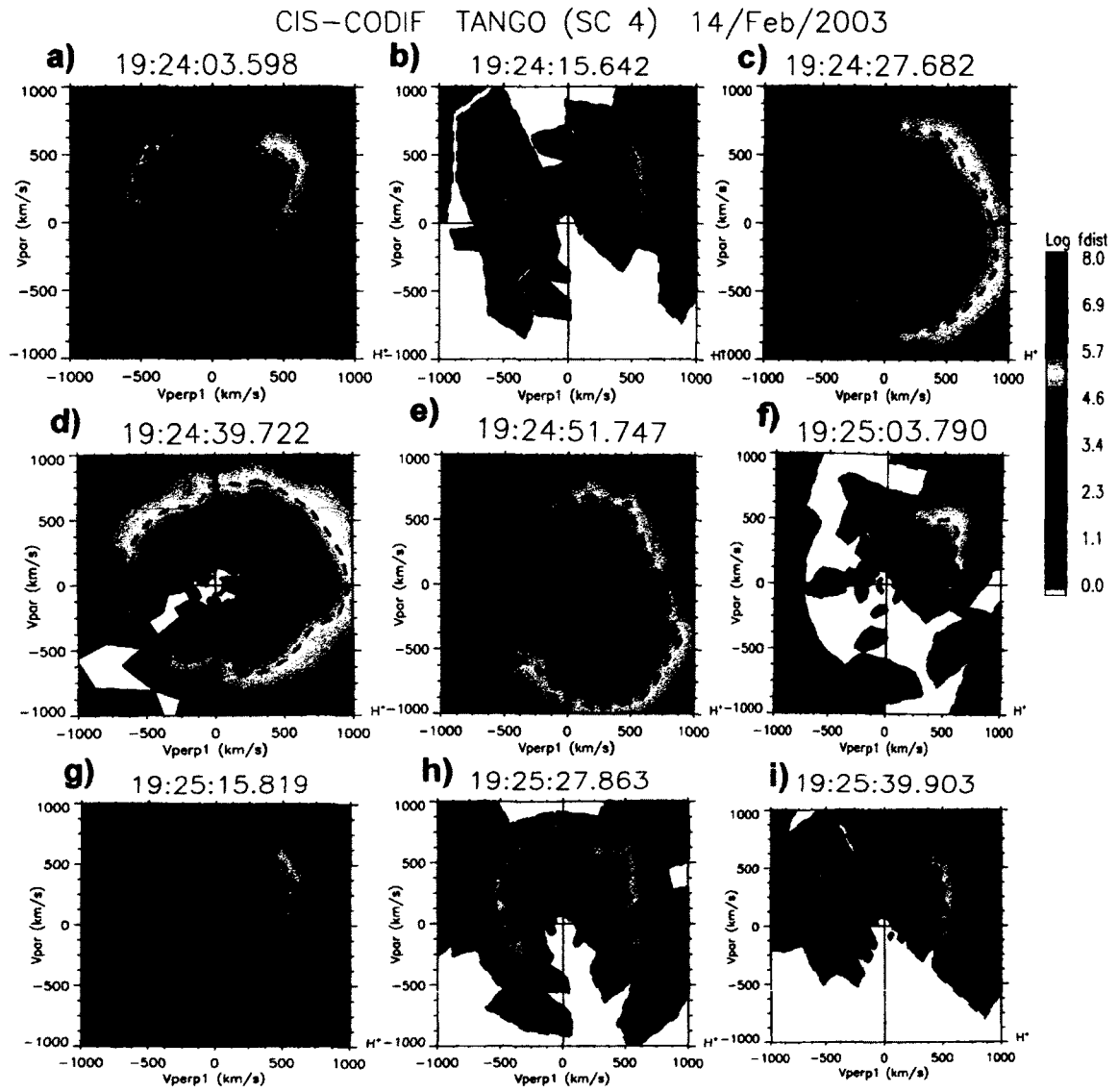


Figure A.11. Ion distribution functions measured by sc4 before, after and during the DMC interval between 19:24:18-19:25:16 UT.

interval exhibiting the FTE signature. In addition this interval shows enhanced fluxes of 10-20 keV O⁺ ions at 0-90 degree pitch angles at the beginning of the interval (corresponding to locations c-d in Figure A.10) and 10-40 keV fluxes at 90-180 degree pitch angles during the exit from the cavity (corresponding to locations e-f in Figure A.10).

O⁺ could come from magnetosphere into the cavity but because during the beginning of interval the sc4 is on field lines c)-d) in Figure A.10, the population of magnetospheric origin should propagate anti-parallel to magnetic field -not parallel. The fact that this is not observed indicates that O⁺ could originate from DMC. Indeed, during the rest of the magnetosheath crossing, most 30-40 keV O⁺ is at 60-120 degree pitch angles, which would be consistent with leakage from DMC due to large gyro-radius of energetic O⁺.

For the interval corresponding to field lines e-f sc4 observes a trapped population and particles propagating-anti-parallel to magnetic field which could be of cavity or magnetospheric origin. Note that the O⁺ fluxes at ~ 180 degree pitch angles at 19:24:51-19:25:04 UT are larger and at higher energies than at other pitch-angles and also co-exist with the maximum anti-parallel proton fluxes. This signature indicates that the source region for O⁺ and H⁺ fluxes during this interval may be the same and based on lack of anti-parallel O⁺ fluxes during the beginning of the interval the most likely source is the DMC. *Chang et al. [2000]* showed that there are two types of energetic ions observed in the magnetosheath, one type for H⁺, He⁺⁺, and O^{>2+} and the other for He⁺. Based on spectral properties they suggested that the acceleration region for He⁺ ions is different from the one(s) for He⁺⁺, and O^{>2+} ions that were of solar wind origin. Unfortunately the RAPID instrument cannot distinguish the charge state of the observed He-ions, so we can not say whether the observed He-ions were of solar wind or ionospheric origin. However, the singly ionized energetic O⁺-ions have been observed in the DMCs before and they are thought to be of ionospheric origin [*Chen and Fritz, 2001*].

For protons the pitch angle scattering fills the loss cone on a time-scale that is faster than the time scale one would see the loss cone emptied. On the other hand, the pitch angle scattering for oxygen within one gyro-period can get O⁺ either parallel or anti-parallel to magnetic field and can be either swept into ionosphere or lost into magnetosheath. These asymmetric O⁺ distributions are also observed during other DMC intervals which may suggest that O⁺ can be energized in the DMC and portion of the distribution can be lost

either into the ionosphere or magnetosheath via pitch angle scattering.

We think that the highly oblique and perpendicular high-energy populations that are observed at the boundaries at the DMC could be either the high-energy particles trapped in the cavity but that are observed due to their higher gyro-radius at the cavity boundary or they could originate from the bow-shock. The large fluxes of ions streaming anti-parallel to the magnetic field at 19:24:27 UT are ions escaping the DMC: they appear only 12 seconds after the observations of streaming in distribution on the field line that is just about to reconnect and the counter streaming population is immediately present when the field line is opened. A particle with 500 km/s travels 6000 km in 12 seconds, so it is unlikely that these could be particles that enter the cavity from the magnetosheath, propagate to mirror-point and reflect back. If this was the case, the mirror point should be only 3000 km below sc4. Considering the z -coordinate for sc4 is ~ 53000 km this is very unlikely. We also showed that sc3 has remained in the cavity during the entire sheath interval so the cavity with hot plasma extends likely at least 3660 km along boundary normal direction and 6220 km from sc4 toward sc3, so the cavity is the closest reservoir to explain the immediate presence of these anti-parallel particles.

Also during remaining of the magnetosheath interval sc4 remains close to the cavity boundary: it continues to measure lower v_x compared to sc1 that is at higher z -coordinate than sc4. Note that as sc4 travels at the vicinity of the DMC boundary in the magnetosheath, it continues to observe the 20-40 keV oxygen ions at very oblique pitch-angles. This further supports the idea that oxygen ions of cavity origin are observed in the magnetosheath due to their large gyro-radius.

Sc4 has another encounter of hotter cavity-like plasma with reduced v_x and b_t between 19:40:24-19:42:03 UT and sc1 observes this region of hotter plasma at 19:41:42-19:42:30 UT. Any parts of this sc4 interval are not picked up by the automated search for reconnection intervals. The Walén relation and HT frames are poorly satisfied at both edges of this structure for sc4, which may indicate that sc4 is not fully crossing the reconnected field line. However, throughout this interval sc4 is measuring ion distribution functions (not shown) similar to Figure A.11c and e which indicates that it might be observing particles on field line that reconnected recently in the past and therefore shows both parallel and anti-parallel population. Interestingly, the anti-parallel population is at higher energies than

the parallel population (D-shape is larger at quadrants 3 and 4 compared to quadrants 1 and 2). For sc1 the Walén relation and HT-frame velocity are well satisfied at the inbound edge of this structure at 19:41:45-19:42:10 UT (see Table 2) and it observes a distribution function where the parallel population is dominating but the anti-parallel population at higher energy is immediately present at 19:41:53 UT and gets stronger at the center of this interval. The boundary normals measured by sc1 and sc4 during these intervals (see Table 4) are now tilted more toward x -direction compared to previous sheath interval. Sc3 that remains in the cavity during the sheath interval is located 4290-5230 km (4920-5230 km) below sc4 (sc1) along the boundary normal directions measured by sc4 (sc1). Note that now the sc1 rather than sc2 is closer to sc4 along these boundary normal directions measured by sc1 and sc4. The high-energy particles signatures during these sheath intervals are discussed elsewhere [Nykyri *et al.*, 2010c, submitted to JGR].

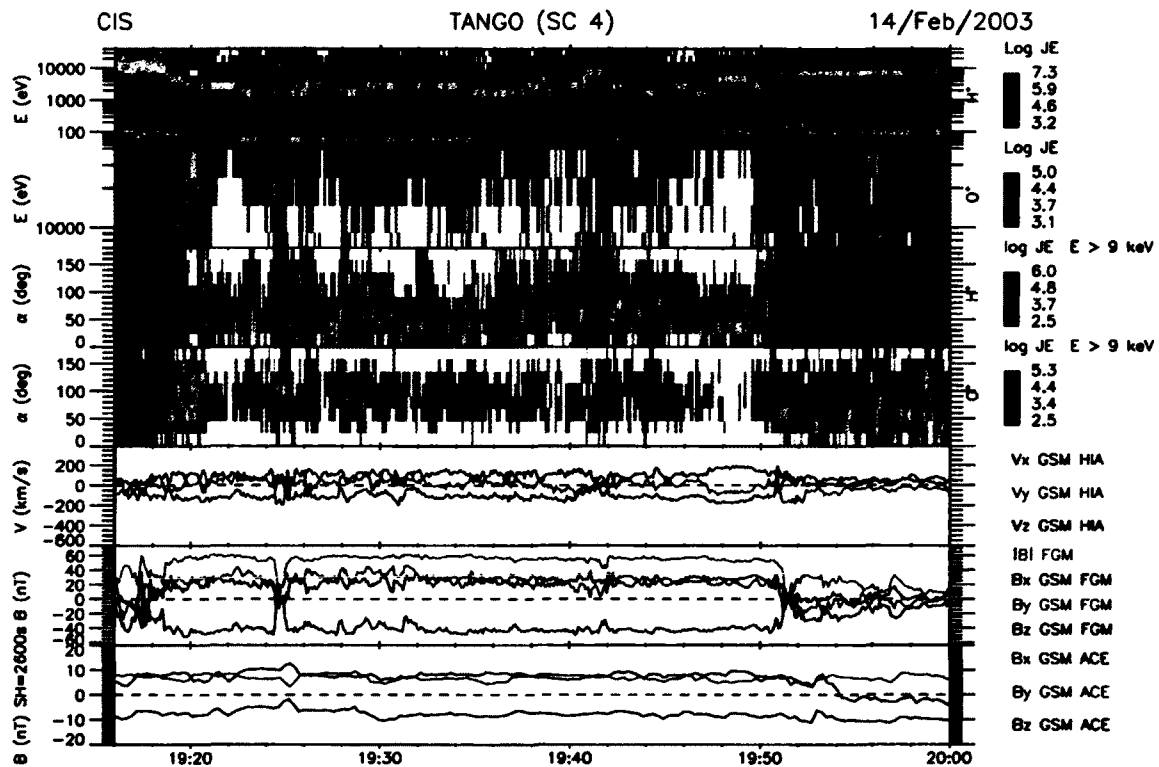


Figure A.12. Sc4 observations at 19:08-20:00 UT during and surrounding the magnetosheath. The panels show from top to bottom proton energy, O+ energy, proton pitch angles, O+ pitch angles, velocity vector, magnetic field, and IMF.

A.5.4 Magnetosheath-Cavity Transition

Figure A.2 shows that as the dynamic pressure of the SW drops by 30 percent, all spacecraft that were in the magnetosheath are swept back into cavity at $\sim 19:52$ UT. Note that the IMF is rotating from northward to southward so the reconnection site moves to the sunward side of the duskside cusp and the region of depressed field forms now more sunward compared to the first cavity interval. At the magnetosheath cavity boundary there is a FTE signature observed by sc1, sc2 and sc4. The orientation of the boundary normal measured during the longer interval at $\sim 19:45:00$ - $20:00$ UT from the magnetosheath into the second cavity interval is quite similar (except for one test with poor eigenvalue ratio) at sc1, sc2 and sc4 (interval 6 at Table 4) and also similar to the orientation of the boundary during the second sheath interval (interval 5 at Table 4). For example sc4 measures a MVAE normal of $[0.56, 0.07, 0.81]$ and sc2 a MVAB normal of $[0.57, 0.00, 0.80]$. We chose this longer interval for boundary normal determination as the FTE would cause a stronger perturbation to the normal if the interval was shorter. This FTE signature is discussed in detail in *Nykyri et al. 2010b (submitted to JGR)*

A.5.5 Cavity-Magnetosheath Transition

After 20:00 UT the dynamic pressure starts to increase and finally after few oscillations as it reaches the peak value of 4.4 nPa at 20:15 UT, all spacecraft move back to the magnetosheath. This final transition into magnetosheath shows more variability in boundary structure within Cluster separation. Sc1 and sc2 measure similar normals (for the tests with best eigenvalue ratios) that are tilted more toward x -direction compared to the previous interval: for example the normal measured by sc2 is $[0.70, -0.11, 0.70]$. Sc3 and sc4 that are below sc1 and sc2 along the z -direction measure higher z -components of the normals. For example sc4 MVAB normal is $[0.60, -0.22, 0.77]$. When the dynamic pressure reduces again after 20:15 UT sc4 briefly drops back into the region of more depressed field. At first it may seem surprising that as the dynamic pressure reaches the bottom value of ~ 3 nPa at $\sim 20:25$ UT none of the spacecraft are swept back into cavity. This is because now the IMF has returned back northward so the reconnection site is moved back tailward of the duskside cusp (see Figure A.3 for the motion of the diamagnetic cavity with respect to IMF

orientation), so the DMC is expected more tailward.

A.5.6 Summary of the Large-Scale Cavity Structure

Summary of the boundary normal analysis is shown in Figure A.13 (see caption for more details). The normals for MSP-DMC transition are plotted at each spacecraft location corresponding to the time at the beginning of the data interval used for normal determination. For example, the first transition for sc1 occurs between 18:48-18:51:35 UT, so we have plotted the normal in xz -plane at 18:48 UT along sc1 trajectory. Normals for DMC-MSH transition are plotted at each spacecraft location at the end of each crossing, normals for MSH-DMC transition are plotted at the center of the each crossing and the normals for the last DMC-MSH transition are plotted ~ 10 minutes before the end of the analysis interval because the end of the interval is already quite far in the magnetosheath. We chose to plot the normals at these times because the interval lengths for normal determination using the stability analysis are different for each crossing and sometimes the central time of the interval is far off from the time when spacecraft actually enter (leave) a new (the old) region.

In addition to boundary normals we have plotted short black lines perpendicular to each normal in order to better visualize the boundary structure. The curvature of the magnetosphere cavity boundary agrees quite nicely with the field line curvature from T89 model. The angle between sc1 MSP-DMC and DMC-MSH normals is 35.9 degrees and is denoted as the wedge-angle. Sc1, sc2 and sc4 travel to the magnetosheath $\sim 19:21$ UT and when IMF starts turning southward $\sim 19:52$ UT sc1, sc2 and sc4 re-encounter the cavity more sunward. Note that sc3 remains in the cavity the entire time indicating that the new cavity must overlap with the old-one. By 20:25 UT all spacecraft get into magnetosheath. Note that Figure A.13 illustrates the cavity structure only in xz -plane. Tables 3 and 4 indicate that boundary normals for these crossings can have sometimes significant y -components.

A.6 Conclusions and Discussion

In the present study we have analyzed Cluster spacecraft data during a diamagnetic cavity (DMC) crossing at the northern high-altitude cusp characterized by depressed magnetic field and magnetic field fluctuations. The diamagnetic cavity is a highly-dynamic region and its location is dependent on the IMF orientation and dynamic pressure. In this section

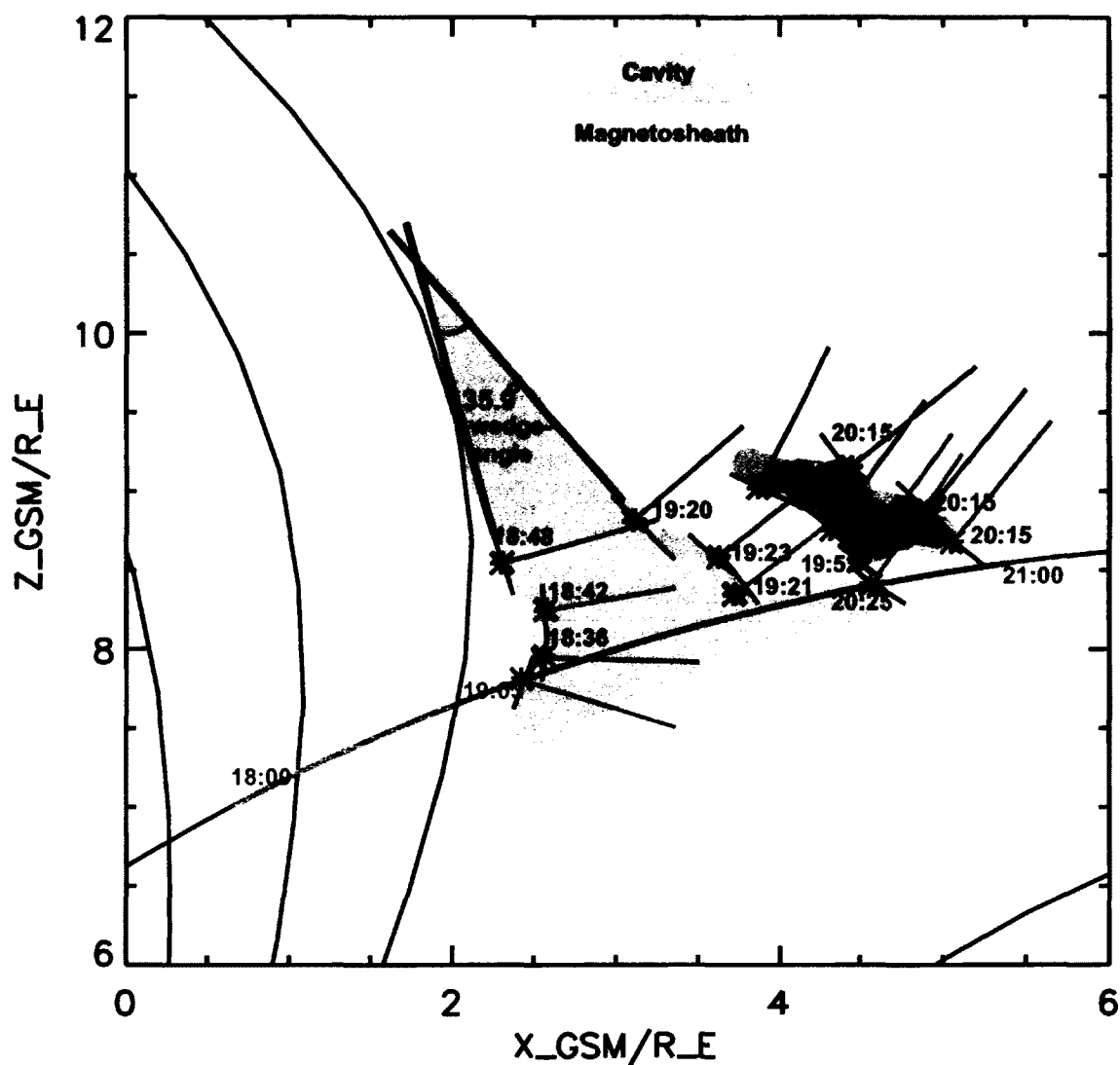


Figure A.13. Cavity structure determined from Cluster boundary normal analysis in xz -plane superposed on T89 model. Boundary normals from Tables 3 and 4 are plotted along sc1 (black), sc2 (red), sc4 (blue) orbits at times corresponding to i) magnetosphere-cavity, ii) DMC-magnetosheath, iii) magnetosheath-cavity and iv) DMC-magnetosheath crossings. For sc3 only crossings i) and iv) are marked as it remains in the cavity up to $\sim 20:25$ UT. The angle between sc1 normals for crossings i) and ii) is 35.9 degrees and is denoted as the wedge-angle. The thick yellow line shows sc3 trajectory between 18:00 UT-21:00 UT. Approximate cavity and magnetosheath areas are shaded with light magenta and light blue colors, respectively.

we conclude the main findings of the study and discuss the viability of different sources for high-energy particles.

1. We have demonstrated that as the IMF changes from northward to southward, the diamagnetic cavity reforms more sunward. We found fluid and particle evidence of magnetic reconnection that showed flux tubes moving tailward during southward IMF and sunward during northward IMF. Most of the reconnection signatures were consistent with lobe reconnection and sub-solar reconnection, but also some puzzling intervals with negative slopes were found (see section 4.3).

2. The orientations of the boundary normals measured by Cluster are tilted mostly sunward for magnetosphere-cavity (MSP-DMC) boundary and get tilted more toward z -direction for cavity-magnetosheath (DMC-MSH) boundary.

3. The extent of the cavity along the MSP-DMC-normal direction at sc3 is at least 4680 km and 6090 km at sc1. The extent of the 1st cavity along DMC-MSH normal at sc4 location is at least 6100 km.

4. The cavity is filled with high-energy electrons, protons and oxygen ions and high-energy particle fluxes drop several orders of magnitude as spacecraft cross into the magnetosheath.

5. At the magnetosheath the ion distribution functions show a typical magnetosheath population with no high-energy particles but closer to the DMC boundary a higher energy population at very oblique pitch-angles becomes present.

6. Throughout the magnetosheath, the high-energy proton fluxes remained low except during brief intervals when sc4 and sc1 dropped back into cavity due to changes in solar wind dynamic pressure. However, the high-energy O⁺ fluxes did not drop as much in the magnetosheath as the proton fluxes and were mostly at 60-120 degree pitch-angles, consistent with leakage from DMC due to large gyro radius of the oxygen ions.

7. Comparison between sc4 data during the brief cavity encounter at 19:24 UT and 2.5 D MHD simulations indicates that this interval exhibits a FTE structure. RAPID data shows that this FTE is filled with high-energy electrons, protons and helium and CODIF data showed that in addition to H⁺ also O⁺ ions at higher energy are present. Inside the FTE significant fluxes of energized protons and oxygen ions were propagating anti-parallel to the magnetic field, and the anti-parallel protons appeared immediately when sc4

encountered the reconnected field line, consistent more with the local DMC source than reflected bow-shock source. This further demonstrates that the formation of the DMC is controlled by magnetic reconnection, which generates freshly reconnected flux tubes that subsequently end up as stagnant fossil flux tubes in the DMC that had reconnected some time ago. So the extended DMCs are formed by various reconnected flux tubes, where the newly generated flux is modifying the existing DMC. It is shown here that when IMF was first northward the DMC formed more tailward and as IMF turned southward the new cavity formed more sunward but overlapping with the old cavity as sc3 remained in the cavity the entire time.

8. The large-amplitude 'turbulence' observed in the cavity can be a consequence of spacecraft crossing flux tubes generated by the reconnection process (see for example fluctuating magnetic field during reconnection intervals in Figures A.5, A.8 and A.9) and back and forth motion of the boundaries over the spacecraft (see repeated transitions for sc1 from magnetosphere to cavity due to dynamic pressure variations of solar wind at 18:45-19:05 UT in Figure A.2). Three things can contribute to this relative motion over the flux tubes: a) spacecraft motion, b) flux tube motion, c) motion of the entire DMC due to highly variable dynamic pressure of the solar wind. The more detailed description on the analysis of magnetic field fluctuations in the cavity is given in *Nykyri et al. 2010b (submitted to JGR)*.

Possible Source for High-Energy Particles in The Cavity

The origin of high-energy particles in the cusp diamagnetic cavities has been a longstanding and controversial topic. The present study does not exclude the bow-shock or magnetospheric source for energetic ions but rather adds new constraints to these sources:

1. At the very close vicinity to the DMC boundary there are some particles streaming parallel but also anti-parallel to magnetosheath field lines. If the anti-parallel energetic population is on the magnetosheath field line that has not yet reconnected these particles can not directly originate from quasi-parallel bow shock.

2. The region of energetic protons forms a very narrow layer at the magnetosheath close to DMC boundary characterized by butterfly shape distribution function at high-energies continuing to anti-parallel direction. This signature in the magnetosheath can be caused by the leakage of energetic particles to the magnetosheath due to their large gyro-

radius. The fact that fluxes of high-energy (20-40 keV) O⁺ are observed during most of the magnetosheath crossing at very oblique pitch angles is also consistent with DMC source, since the O⁺ has larger gyro-radius than H⁺.

3. Because the field in the DMC is weak, the loss cone into the magnetosheath and magnetosphere is small. Therefore, the adiabatic access from magnetosheath or magnetosphere would not explain the trapped population with closely perpendicular pitch-angles observed in the cavity.

4. Previous studies [*Chang et al.*, 1998, 2000; *Trattner et al.*, 2001, e.g] have not quantitatively shown the width of the magnetosheath layer surrounding the DMC that maps to the quasi-parallel bow-shock. Determining the width of this layer along the cavity boundary normal direction is important as it would help clarify the energetic ion source: if this width is wider than the gradients, L , (for example sc1 and sc4 separation along boundary normal at ~19:24 UT is around 1200-2470 km) calculated in this paper (Tables 3 and 4), then the high-energy particle fluxes should not drop in distance L (see *Nykyri et al. 2010c (submitted to JGR)*), if the energetic ion source for the DMC is the quasi-parallel bow-shock.

5. Bow-shock source does not explain the energetic electrons (see top panel of Figure A.4) and O⁺ ions (see 2nd panel in Figure A.12) observed in the cavity.

Our detailed analysis of high-energy particle observations from RAPID instrument during this event implies even stronger constraints for magnetospheric and magnetosheath sources [*Nykyri et al., 2010c, submitted to JGR*]. Based on these constraints the most simple explanation on the origin for high-energy particles observed in the DMC is the local source. We will also discuss the acceleration mechanism that works both for electrons and protons in *Nykyri et al. 2010c (submitted to JGR)*.

Appendix: Example Calculation of Boundary Normals and Error Estimates

Examination of the Cluster data indicates that boundary crossings and areas surrounding the crossings at the high-altitude cusp are not smooth but show fluctuations at different frequencies. Therefore the calculations of the boundary normals are sensitive to the length of window that is used in variance analysis. In order to test the time-stationarity and calculate the error estimates of the MVAB, MVAE and MFR normals and normal component of B -field we have utilized a technique described in *Sonnerup and Scheible [1998]*. Figure A.14a

illustrates an example of a calculation of a reference normal using MVAB, MVAE and MFR-tests, A.14b shows time stationarity of MVAE normals measured by sc1 during a current sheet crossing centered at 19:18:30 UT and 7c shows spacecraft separations along sc1 plateau normals. The second and third panel in A.14b show the angular deviations, $\Delta\phi_{13}$ and $\Delta\phi_{12}$ (in radians) between individual normal x_1 and the reference normal $x'_1 = [0.66, 0.44, 0.61]$ toward x'_3 and x'_2 , respectively, where the set (x'_1, x'_2, x'_3) is specified in middle panel of A.14a. The Plateau (light blue column) is defined as a region having approximately a constant normal component of the magnetic field and smallest $\Delta\phi_{13}$ and $\Delta\phi_{12}$ -values. For MFR and MVAB tests the deviation between individual normal x_3 and the reference normal x'_3 toward x'_1 is calculated as

$$\Delta\phi_{31} = \cos^{-1}\left(\frac{x_3 \cdot x'_3}{\sin(\cos^{-1}(x_3 \cdot x'_2))}\right) \quad (\text{A.1})$$

with error bars calculated from

$$\sqrt{\frac{\lambda_3 \lambda_1}{(m-1)(\lambda_3 - \lambda_1)^2}} \quad (\text{A.2})$$

Figure A.15 illustrates the calculation of $\Delta\phi_{31}$. Deviation toward x'_2 and error bars are calculated from

$$\Delta\phi_{32} = \cos^{-1}\left(\frac{x_3 \cdot x'_3}{\sin(\cos^{-1}(x_3 \cdot x'_1))}\right), \sqrt{\frac{\lambda_3 \lambda_2}{(m-1)(\lambda_3 - \lambda_2)^2}} \quad (\text{A.3})$$

For MVAE test the deviation from x'_1 toward x'_3 and error bars are calculated as

$$\Delta\phi_{13} = \cos^{-1}\left(\frac{x_1 \cdot x'_1}{\sin(\cos^{-1}(x_1 \cdot x'_2))}\right), \sqrt{\frac{\lambda_1 \lambda_3}{(m-1)(\lambda_1 - \lambda_3)^2}} \quad (\text{A.4})$$

Deviation toward x'_2 with error bars are calculated from

$$\Delta\phi_{12} = \cos^{-1}\left(\frac{x_1 \cdot x'_1}{\sin(\cos^{-1}(x_1 \cdot x'_3))}\right), \sqrt{\frac{\lambda_1 \lambda_2}{(m-1)(\lambda_1 - \lambda_2)^2}} \quad (\text{A.5})$$

The MVAB and MFR error bars for the normal component of the magnetic field are calculated from

$$|\Delta \langle \mathbf{B} \cdot \mathbf{x}_3 \rangle| = \sqrt{\frac{\lambda_3}{m-1} + (\Delta\phi_{32} \langle \mathbf{B} \rangle \cdot \mathbf{x}_2)^2 + (\Delta\phi_{31} \langle \mathbf{B} \rangle \cdot \mathbf{x}_1)^2} \quad (\text{A.6})$$

and the MVAE error bars for the normal component of the magnetic field are

$$|\Delta \langle \mathbf{B} \cdot \mathbf{x}_1 \rangle| = \sqrt{\frac{\lambda_1}{m-1} + (\Delta\phi_{12} \langle \mathbf{B} \rangle \cdot \mathbf{x}_2)^2 + (\Delta\phi_{13} \langle \mathbf{B} \rangle \cdot \mathbf{x}_3)^2} \quad (\text{A.7})$$

where $\langle \mathbf{B} \rangle$ is the average magnetic field vector during interval.

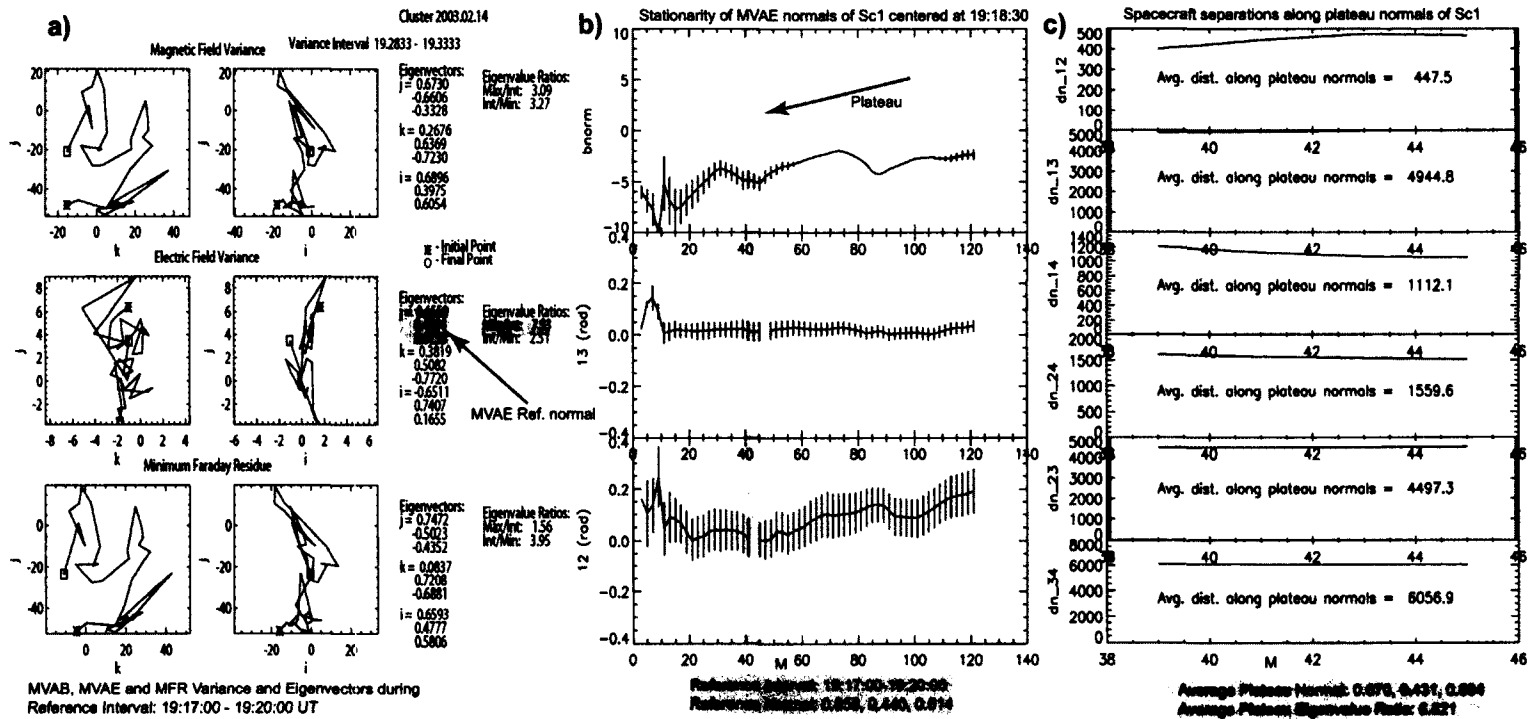


Figure A.14. A) Presents hodograms, eigenvectors and eigenvalues of MVAB, MVAE and MFR-analysis during reference interval 19:17:00-19:19:30 UT. The MVAE maximum eigenvector (reference normal) and λ_1/λ_2 -ratio are highlighted in pink. B) shows stationarity of MVAE normals calculated during nested segments around 19:18:30 UT: top panel shows the normal component of the magnetic field, the quantities 13 and 12 indicate angular deviations (in radians) from the reference normal $x1' = [0.66, 0.44, 0.61]$ toward $x3'$ and $x2'$, respectively, where the set $(x1', x2', x3')$ is specified in middle panel of A). The plateau is defined as an interval having the smallest angular deviations and constant normal component of magnetic field and is highlighted with light blue. C) shows projected spacecraft distances (in km) along plateau normals, for example average distance between sc3 and sc4 along the measured plateau normals is 6057 km.

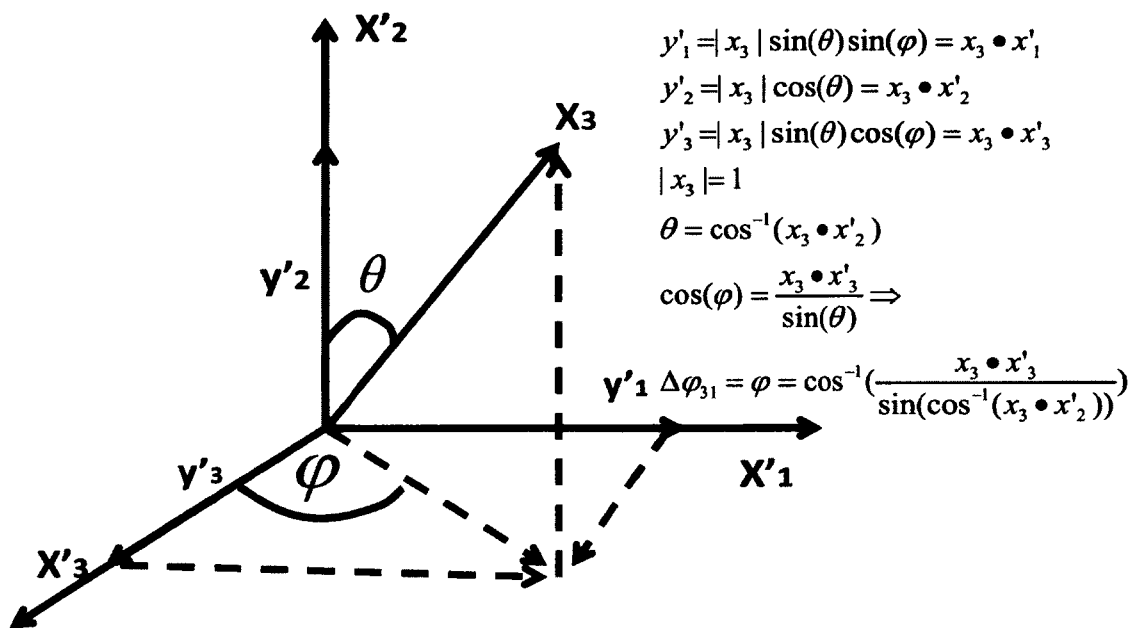


Figure A.15. Illustration of calculation of $\Delta\phi_{13}$: Deviation between individual normal x_3 and the reference normal x'_3 toward x'_1 .

Bibliography

- Asikainen, T., and K. Mursula, Energetic particle fluxes in the exterior cusp and the high-latitude dayside magnetosphere: statistical results from the Cluster/RAPID instrument, *Annales Geophysicae*, *23*, 2217–2230, 2005.
- Asikainen, T., and K. Mursula, Reconnection and energetic particles at the edge of the exterior cusp, *Annales Geophysicae*, pp. 1949–1956, 2006.
- Balogh, A., et al., The Cluster magnetic field investigation: overview of in-flight performance and initial results, *Ann. Geophys.*, *19*, 1207–1217, 2001.
- Berchem, J., and C. T. Russell, Magnetic field rotation through the magnetopause - ISEE 1 and 2 observations, *J. Geophys. Res.*, *87*, 8139–8148, doi:10.1029/JA087iA10p08139, 1982.
- Burch, J. L., Rate of erosion of dayside magnetic flux based on a quantitative study of the dependence of polar cusp latitude on the interplanetary magnetic field, *Radio Science*, *8*, 955–+, 1973.
- Cargill, P. J., M. W. Dunlop, B. Lavraud, R. C. Elphic, D. L. Holland, K. Nykyri, A. Balogh, I. Dandouras, and H. Réme, CLUSTER encounters with the high altitude cusp: Boundary structure and magnetic field depletions, *Ann. Geophys.*, *22(5)*, 1739–1754, 2004.
- Cargill, P. J., et al., *The Cusp, Outer Magnetospheric Boundaries: Cluster Results*, ISSI, Bern, 2005.
- Chang, S., et al., Cusp energetic ions: A bow shock source, *J. Geophys. Res.*, *25*, 3729–3732, 1998.
- Chang, S., et al., Energetic magnetosheath ions connected to the Earth's bow shock: Possible source of cusp energetic ions, *J. Geophys. Res.*, *105*, 5471–5488, doi: 10.1029/1999JA900468, 2000.
- Chen, J., Evidence for particle acceleration in the magnetospheric cusp, *Annales Geophysicae*, *26*, 1993–1997, 2008.

- Chen, J., and T. A. Fritz, Energetic oxygen ions of ionospheric origin observed in the cusp, *Geophys. Res. Lett.*, *28*, 1459–1462, 2001.
- Chen, J. S., and T. A. Fritz, Correlation of cusp mev helium with turbulent ULF power spectra and its implications, *Geophys. Res. Lett.*, *25*, 4113–4116, 1998.
- Dunlop, M. W., P. J. Cargill, T. J. Stubbs, and P. Woolliams, The high altitude cusps: Heos 2, *J. Geophys. Res.*, *105*, 27,509–27,517, 2000.
- Frank, L. A., and K. L. Ackerson, Observations of charged particle precipitation into the auroral oval, *J. Geophys. Res.*, *76*, 3612, 1971.
- Fritz, T., J. Chen, R. Sheldon, H. Spence, J. Fennell, S. Livi, C. Russell, and J. Pickett, Cusp energetic particle events measured by POLAR spacecraft, *Physics and Chemistry of the Earth C*, *24*, 135–140, 1999.
- Fuselier, S. A., D. M. Klumpar, and E. G. Shelley, On the origins of energetic ions in the earth's dayside magnetosheath, *J. Geophys. Res.*, *96*, 47–56, 1991.
- Fuselier, S. A., K. J. Trattner, and S. M. Petriner, Cusp observations of high- and low-latitude reconnection for northward interplanetary magnetic field, *J. Geophys. Res.*, *105*, 253–266, 2000.
- Gosling, J. T., M. F. Thomsen, S. J. Bame, R. C. Elphic, and C. T. Russell, Observations of reconnection of interplanetary and lobe magnetic field lines at the high-latitude magnetopause, *J. Geophys. Res.*, *96*, 14,097–+, doi:10.1029/91JA01139, 1991.
- Haaland, S. E., et al., Four-spacecraft determination of magnetopause orientation, motion and thickness: comparison with results from single-spacecraft methods, *Ann. Geophys.*, *22*, 1347–1365, 2004.
- Heikkilä, W. J., and J. D. Winningham, Penetration of magnetosheath plasma to low altitudes through the dayside magnetospheric cusps, *J. Geophys. Res.*, *76*, 883, 1971.
- Kessel, R. L., S.-H. Chen, J. L. Green, S. F. Fung, S. A. Boardsen, L. Tan, T. E. Eastman, J. D. Craven, and L. A. Frank, Evidence of high-latitude reconnection during northward IMF: HAWKEYE observations, *Geophys. Res. Lett.*, *23*, 583–586, 1996.

- Khrabrov, A. V., and B. Sonnerup, Orientation and motion of current layers: Minimization of the faraday residue, *Geophys. Res. Lett.*, *25*, 2373–2376, 1998.
- Lavraud, B., and P. J. Cargill, The magnetospheric cusps revealed: Results from the cluster mission, *Astronomy and Geophysics*, *46*, 1.32–1.35, 2005.
- Lavraud, B., M. W. Dunlop, T. D. Phan, and et. al., Cluster observations of the exterior cusp and its surrounding boundaries under northward IMF, *Geophys. Res. Lett.*, *29* (20), doi:10.1029/2002GL015464, 2002.
- Lavraud, B., et al., The exterior cusp and its boundary with the magnetosheath under northward IMF: Cluster multi-event analysis, *Ann. Geophys.*, *22*(8), 3039–3054, 2004.
- Lavraud, B., et al., High-altitude cusp flow dependence on IMF orientation: A 3-year cluster statistical study, *J. Geophys. Res.*, *110*, A02,209,doi:10.1029/2004JA010804, 2005.
- Le, G., X. Blanco-Cano, C. T. Russell, X. W. Zhou, F. Mozer, K. J. Trattner, S. A. Fuselier, and B. J. Anderson, Electromagnetic ion cyclotron waves in the high-altitude cusp: Polar observations, *J. Geophys. Res.*, *106*, 19,067–19,079, 2001.
- Lyu, L. H., and J. R. Kan, Structures of Alfvén shocks - S-shaped magnetic hodogram observed at the magnetopause, *Geophys. Res. Lett.*, *16*, 349–352, doi: 10.1029/GL016i005p00349, 1989.
- Newell, P. T., and C. Meng, Cusp width and $B(z)$ - Observations and a conceptual model, *J. Geophys. Res.*, *92*, 13,673–13,678, 1987.
- Niehof, J. T., T. A. Fritz, R. H. W. Friedel, and J. Chen, Interdependence of magnetic field and plasma pressures in cusp diamagnetic cavities, *Geophys. Res. Lett.*, *35*, 11,101–+, 2008.
- Niehof, J. T., T. A. Fritz, R. H. W. Friedel, and J. Chen, Size and location of cusp diamagnetic cavities observed by Polar, *Journal of Geophysical Research (Space Physics)*, *115*, 7201–+, 2010.

- Nykyri, K., P. J. Cargill, E. Lucek, T. S. Horbury, A. Balogh, B. Lavraud, I. Dandouras, and H. Rème, Ion cyclotron waves in the high altitude cusp: Cluster observations at varying spacecraft separations, *Geophys. Res. Lett.*, *30(24)*, 2263–2269, doi: 10.1029/2003GL018594, 2003a.
- Nykyri, K., A. Otto, J. Büchner, B. Nikutowski, W. Baumjohann, L. M. Kistler, and C. Mouikis, Equator-S observations of boundary signatures: FTE's or Kelvin-Helmholtz waves?, *Geophysical Monograph 133, Earth's Low Latitude Boundary Layer*, 205–210, 2003b.
- Nykyri, K., B. Grison, P. J. Cargill, B. Lavraud, E. Lucek, I. Dandouras, A. Balogh, N. Cornilleau-Wehrin, and H. Réme, Origin of the turbulent spectra in the high-altitude cusp: Cluster spacecraft observations, *Ann. Geophys.*, *24*, 1057–1075, 2006a.
- Nykyri, K., A. Otto, B. Lavraud, C. Mouikis, L. Kistler, A. Balogh, and H. Réme, Cluster observations of reconnection due to the Kelvin-Helmholtz instability at the dawn side magnetospheric flank, *Ann. Geophys.*, *24*, 2619–2643, 2006b.
- Nykyri, K., et al., Cluster observations of magnetic field fluctuations in the high-altitude cusp, *Ann. Geophys.*, *22*, 2413–2429, 2004.
- Otto, A., Magnetic reconnection at the magnetopause: A fundamental process and manifold properties, *Reviews of Geophysics*, *33*, 657–663, 1995.
- Palmroth, M., P. Janhunen, T. I. Pulkkinen, and W. K. Peterson, Cusp and magnetopause locations in global MHD simulation, *J. Geophys. Res.*, *106*, 29,435–29,450, 2001a.
- Palmroth, M., H. Laakso, and T. I. Pulkkinen, Location of high-altitude cusp during steady solar wind conditions, *J. Geophys. Res.*, *106*, 21,109–21,122, 2001b.
- Paschmann, G., G. Haerendel, N. Sckopke, H. Rosenbauer, and P. C. Hedgecock, Magnetic field characteristics of the distant polar cusp near local noon: the entry layer, *J. Geophys. Res.*, *81*, 2883–2899, 1976.
- Pitout, F., C. P. Escoubet, B. Klecker, and H. Rème, Cluster survey of the mid-altitude cusp: 1. size, location, and dynamics, *Annales Geophysicae*, *24*, 2006.

- Rème, H., C. Aoustin, J. M. Bosqued, I. Dandouras, B. Lavraud, and et. al., First multi-spacecraft ion measurements in and near the Earth's magnetosphere with the identical Cluster ion spectrometry (CIS) experiment, *Ann. Geophys.*, *19*, 1303–1354, 2001.
- Russell, C. T., G. Le, and S. M. Petrinec, Cusp observations of high-and low-latitude reconnection for northward IMF: An alternate view, *J. Geophys. Res.*, *105*, 5489–5495, 2000.
- Savin, S. P., L. Zelenyi, N. C. Maynard, I. Sandahl, H. Kawano, C. T. Russell, S. Romanov, J. Blecki, and et al., Multi-spacecraft tracing of turbulent boundary layer, *Adv. Space Res.*, *30(12)*, 2821–2830, 2002.
- Savin, S. P., L. Zelenyi, S. A. Romanov, I. Sandahl, J. Pickett, E. Amata, L. Avanov, J. Blecki, and et al., Magnetosheath-cusp interface, *Ann. Geophys.*, *22*, 183–212, 2004.
- Savin, S. P., et al., The cusp/magnetosheath interface on may 29, 1996: Interball-1 and Polar observations, *Geophys. Res. Lett.*, pp. 3015–3018, 1998.
- Scudder, J. D., F. S. Mozer, N. C. Maynard, and C. T. Russell, Fingerprints of collisionless reconnection at the separator, *J. Geophys. Res.*, *107*, SMP13–1 to SMP13–38, 2002.
- Sibeck, D. G., R. W. McEntire, A. T. Y. Lui, R. E. Lopez, and S. M. Krimigis, Energetic magnetospheric ions at the dayside magnetopause - Leakage or merging?, *J. Geophys. Res.*, *92*, 12,097–12,114, 1987.
- Sonnerup, B. U. Ö., and M. Scheible, Minimum and maximum variance analysis, in *Analysis methods for multi-spacecraft data, ISSI Scientific Report*, edited by G. Paschmann and P. W. Daly, p. 185, The International Space Science Institute, Hallerstrasse 6, CH-3012 Bern, Switzerland, 1998.
- Sonnerup, B. U. Ö., G. Paschmann, I. Papamastorakis, N. Sckopke, G. Haerendel, S. J. Bame, J. R. Asbridge, J. T. Gosling, and C. T. Russell, Evidence for magnetic reconnection at the earth's magnetopause, *J. Geophys. Res.*, *86*, 10,049–10,067, 1981.
- Sonnerup, B. U. Ö., G. Paschmann, and T.-D. Phan, Fluid aspects of reconnection at the magnetopause: In situ observations, in *Physics of the Magnetopause*, Geophys. Monogr.

- Ser., vol. 90, edited by P. Song, B. U. Ö. Sonnerup, and M. F. Thomsen, p. 167, AGU, Washington, D. C., 1995.
- Sundkvist, D., et al., Multi-spacecraft determination of wave characteristics near the proton gyrofrequency in high-altitude cusp, *Ann. Geophys.*, *23*, 983–995, 2005.
- Trattner, K. J., S. A. Fuselier, W. K. Peterson, S.-W. Chang, R. Friedel, and M. R. Aellig, Origins of energetic ions in the cusp, *J. Geophys. Res.*, *106*, 5967–5976, doi: 10.1029/2000JA003005, 2001.
- Twitty, C., T. D. Phan, G. Paschmann, B. Lavraud, H. Rème, and M. Dunlop, Cluster survey of cusp reconnection and its IMF dependence, *Geophys. Res. Lett.*, *31*, L19,808, doi:10.1029/2004GL020,646, 2004.
- Vontrat-Reberac, A., et al., Cluster observations of the high-altitude cusp for northward interplanetary magnetic field: a case study, *J. Geophys. Res.*, *108(A9)*, doi: 10.1029/2002JA001717, 2003.
- Walsh, B. M., T. A. Fritz, N. M. Lender, J. Chen, and K. E. Whitaker, Energetic particles observed by ISEE-1 and ISEE-2 in a cusp diamagnetic cavity on 29 September 1978, *Annales Geophysicae*, *25*, 2633–2640, 2007.
- Walsh, B. M., T. A. Fritz, M. M. Klida, and J. Chen, Energetic electrons in the exterior cusp: identifying the source, *Annales Geophysicae*, *28*, 983–992, 2010.
- Whitaker, K. E., J. Chen, and T. A. Fritz, CEP populations observed by ISEE 1, *Geophys. Res. Lett.*, *33*, 23,105, 2006.
- Whitaker, K. E., T. A. Fritz, J. Chen, and M. Klida, Energetic particle sounding of the magnetospheric cusp with ISEE-1, *Annales Geophysicae*, *25*, 1175–1182, 2007.
- Wilken, B., et al., First results from the RAPID imaging energetic particle spectrometer on board Cluster, *Annales Geophysicae*, *19*, 1355–1366, 2001.
- Zhang, H., T. A. Fritz, Q. Zong, and P. W. Daly, Stagnant exterior cusp region as viewed by energetic electrons and ions: A statistical study using Cluster Research with Adap-

tive Particle Imaging Detectors (RAPID) data, *Journal of Geophysical Research (Space Physics)*, *110*, 5211, 2005.

Zhou, X. W., C. T. Russell, G. Le, S. A. Fuselier, and J. D. Scudder, The polar cusp location and its dependence on dipole tilt, *Geophys. Res. Lett.*, *26*, 429–432, 1999.

Zhou, X. W., C. T. Russell, G. Le, S. A. Fuselier, and J. D. Scudder, Solar wind control of the polar cusp at high altitude, *J. Geophys. Res.*, *105*, 245–251, 2000.

